Fog from the Ground Up

Investigating the Conditions Under Which Fog Forms and Evolves Within the Nocturnal Boundary Layer

Izett, J.G.

DOI
10.4233/uuid:7c413cdf-1cd0-44e8-b1f5-347a8f888166

Publication date
2020

Document Version
Final published version

Citation (APA)
Izett, J. G. (2020). *Fog from the Ground Up: Investigating the Conditions Under Which Fog Forms and Evolves Within the Nocturnal Boundary Layer*. [Dissertation (TU Delft), Delft University of Technology]. https://doi.org/10.4233/uuid:7c413cdf-1cd0-44e8-b1f5-347a8f888166

Important note
To cite this publication, please use the final published version (if applicable).
Please check the document version above.

Fog
from the Ground Up

Jonathan George Izett

Fog from the Ground Up

Investigating the Conditions Under Which Fog Forms and Evolves Within the Nocturnal Boundary Layer.

PROEFSCHRIFT

ter verkrijging van de graad van doctor
aan de Technische Universiteit Delft,
op gezag van de Rector Magnificus prof. dr. ir. T.H.J.J. van der Hagen,
voorzitter van het College voor Promoties,
in het openbaar te verdedigen op
1 september 2020

door

Jonathan George IZETT

Master of Science in Oceanografie,
Dalhousie University, Canada
geboren te Chester, Verenigde Koninkrijk.

Dit proefschrift is goedgekeurd door de promotor.

Samenstelling promotiecommissie:

Rector Magnificus,	voorzitter	
Prof.dr.ir. Bas J. H. van de Wiel	Promotor	TU Delft
Prof.dr.ir. Herman W. J. Russchenberg	Twede Promotor	TU Delft
Onafhankelijke leden:		
Prof. Adam H. Monahan	University of Victoria	
Prof.dr.ir. Susan C. Steele-Dunne	TU Delft	
Prof.dr. A. Pier Siebesma	TU Delft	
Dr.ir. Gert-Jan Steeneveld	Wageningen University and Research	
Dr. Wim D. van den Berg	DTN	

Dit onderzoek is financieel mogelijk gemaakt door de Europese Onderzoeksraad (ERC) door middel van een *Consolidator Grant* (nummer 648666).

Keywords: Analytical analysis, Atmospheric science, CESAR, Clouds, Fog, Meteorology, Mist, Observational analysis, Stable boundary layer, Weather

ISBN 978-94-6366-295-6

Typeset by the author with the LaTeX Documentation System.
This is the electronic version.

You'll Never Walk Alone

From the beginning of my PhD, it was often said that I would become an "independent researcher". However, while the research itself can be independently driven, there is in reality no such thing as a researcher who is independent. We all have our own support networks and teams of people—colleagues, friends, family—who help us through. The work contained in this thesis has my name on it, but it would not have been possible without many others. I have placed my acknowledgements at the beginning as without these people, this book would have never been compiled. As I go through, please excuse me if I get a bit misty eyed.

First and foremost, **Bas**. Dankuwel voor u vertrouwen in mij, zelfs na slechts één Skype gesprek! Volgens mij bent u een echte leider: aardig, nederig, enthousiast, ondersteunend, bemoedigend en nog veel meer. Bedankt voor onze vele discussies, over onderzoek en wetenschap, maar ook over voetbal. Tijdens mijn PhD werd u benoemd tot hoogleraar. Het is een welverdiende eer die u goed draagt.

Prof. Adam Monahan (University of Victoria) first put me in contact with Bas four years ago and has served as a mentor and role model since my very first class at UVic. I am honoured that he sits on my examination committee. I am also exceedingly grateful to **Prof. Katja Fennel** (Dalhousie University) who supervised my MSc research, teaching me how to conduct research and write scientific articles, and providing a daily example of strong leadership and scientific excellence from which I continue benefit.

I would like to thank **the examination committee** for the time they have taken to assess this thesis, as well as for the interactions I had with each of them over the past four years. I am particularly grateful to **Herman Russchenberg** for his role as the "second promotor" and for all of his efforts in leading GRS. I was also fortunate to have many **collaborations and discussions** with excellent scientists, including: Bart Schilperoort, Fred Bosveld, Harm Jonker (and the WHIFFLE team), Jelle Wisse, Justus van Ramshorst, Maurice van Tiggelen, Miriam Coenders-Gerrits, Rini Hoevenaren, Stephan de Roode, and many more. Thank you for your input, assistance, and discussion.

If I had hand-picked my colleagues, I doubt I would have been able to come up with a better bunch. In **the SBL group**, Steven, my officemate, sounding board, and walking encyclopædia; Antoon, my Iceland companion, comic relief, Mandela-effect inducer, and most critical reviewer; Peter, my source of data, and all-around meteorological expert—I lost track of the number of times I heard the phrase, "Peter will know" (and, of course, always did!). Further: Ivo van Hooijdonk, Ruben Schulte, and Vincent Heusinkveld.

The wider **GRS community** has been a supportive and nurturing environment, with such an open and engaging atmosphere making it a pleasure to head to work. I would have been particularly lost without **my fellow PhDs**. Thank you for your friendship; I wish you all nothing but success! And, of course, I will be forever grateful to the most important people in GRS: **the support staff**. In particular, the present staff of Debbie Rietdijk, Josine Kelling, Lidwien de Jong, Suzanne de Hoog-Dollée, as well as, Erwin de Beus, Irma Zomerdijk, Minke Regenboog, and Sylvia van Willigen. The Department would fall apart without such fantastic people.

Throughout my time in Delft, I had the pleasure of serving as "PhD representative" in different groups. I am grateful to everyone—including members of the **CiTG PhD Council**, **Faculty Graduate School**, and GRS staff—who took the time to constructively discuss and implement strategies aimed at optimizing the PhD experience.

Beyond academia, I am exceedingly grateful for the support of **my friends**, both here and abroad. Especially Esther, Joel, Katie, Mike, Nannika, Niels, and Phil who have been by my side throughout this entire process.

Above all, I must acknowledge the support and love I have received from **my family** during this process and throughout my "academic career" to date: Mum, Dad, Robert*, Kelly, Alex, Trish, Dave, Tasha, and the extended van Kooten *familie*. The distance between us these past several years has been great, but your love and support has always been greater. I am particularly grateful for your efforts to see that, while my head may be in the clouds, my feet remain firmly on the ground.

Finally, **Maaike**: the twinkling star in my foggy night. Thank you for bringing me with you to the Netherlands on this adventure. Without your brave first step, I would never have experienced what has been an incredible four years full of so many wonderful experiences and opportunities. Thank you for your continued love and support through it all, and for putting up with all of my idiosyncrasies, flaws, and fog puns. Completing my PhD is great, but a better achievement was somehow convincing you to marry me.

*The reader of this thesis may also be interested to know that Robert—my twin brother—and my parents are now famous in the world of fog research. In honour of their importance in my life; *RWI* (Chapter 4), and the AEI, EMI, and RWI simulations in Chapter 6 are directly derived from their initials.

Contents

Summary

In J. K. Jerome's *Three Men in a Boat*, the narrator asks, "*...who wants to be foretold the weather? It is bad enough when it comes without us having the misery of knowing it beforehand*." While a satirical work, I think many would agree with that sentiment, particularly in the case of fog, which is often deemed to be dull, depressing, and boring[†]. Fog is, however, of critical importance to forecast accurately, not least because of the hazard it presents to human safety. Yet, while weather forecasts have improved significantly over recent decades—and continue to improve—fog remains a particularly challenging phenomenon to predict. The research presented within this thesis takes a step back from prediction, and aims to better understand the conditions under which fog forms. Topics investigated include the observational likelihood of fog, the near-surface conditions during the infancy of a fog layer, the spatial variability of fog (and the influences thereon), and the growth and evolution of a fog layer.

One simple method of fog prediction is to use statistical relationships between observed variables in order to identify periods when fog is most likely to occur. However, such methods must accept high false-alarm rates (fog predicted, but does not occur) in order to obtain high hit rates (fog occurs when predicted). To investigate how false alarms may be reduced using statistical methods, five years of observations from the Cabauw Experimental Site for Atmospheric Research (CESAR) were analyzed. Forecasts were assessed for different lead times, and using different optimization methods. Prediction scores are shown to improve significantly with decreased lead time, with the possibility of achieving a hit rate of over 90% and a false-alarm rate of just 13%. Testing different predictive variables, little change to the prediction scores indicates any appropriate combination of variables that measure saturation, turbulence, and near-surface cooling can be used. Ultimately, the lack of spatio–temporal information employed in statistical forecasting is the limiting factor in predictive capability.

From the investigation of observational forecasting, it was noted that fog may be present, but unobserved by traditional meteorological sensors (e.g., a fog layer may be shallower than the sensor height). As a result, a two-week field campaign was conducted in November 2017 at the CESAR facility with the aim of observing the growth of very shallow fog layers. Distributed temperature sensing (DTS) and a novel method for detecting fog from camera images were used to provide high-resolution observations of the near-surface. Large temperature inversions in the lowest metre (up to 5 K) were observed, along with corresponding regions of (super)saturation

[†]One particular interaction stands out. Upon meeting someone, their reaction to what I do was jarring: "Fog? Wow! ...*That's* boring!"

where the fog formed. The camera methodology also allowed for detection of very shallow radiation fog, forming in the lowest 0.5 m as early as two hours before it was observed at the conventional height of 2.0 m.

Moving from localized observations of fog, this thesis also investigates the role of spatial and temporal influences in determining a region's fog climate. Using observations from a dense network of weather stations throughout the country, the climatology of fog in the Netherlands was assessed over a period of 45 years. On a national scale, inter-annual variability is related to synoptic pressure-gradient forcing, while, within the country, regional variability is strongly related to the influences of urbanization and the North Sea. A simple "Regionally Weighted Index" (*RWI*) was distilled that accurately sorts the stations according to their relative fogginess.

Throughout this thesis, the formation of fog is shown to be highly sensitive to observed and simulated conditions. A simple explanation of this sensitivity is presented based on analysis of the propagation of errors within the mathematical formulae describing relative humidity. Overall, relative humidity is shown to be most sensitive to temperature, errors of which contribute roughly 20 times as strongly to uncertainty in relative humidity as other variables. Yet, errors in specific humidity are on the order of 10–20 times greater than those in temperature, meaning they may contribute equally to the resulting error in relative humidity. This allows for the ability to assign priority to different model processes in order to better represent the specific variable that contributes most to errors in estimating saturation. It also stresses the need to further improve representations of the (stable) atmospheric boundary layer in simulations, while also continuing to improve our observational capabilities, including the use of newer techniques such as DTS.

The rate at which a fog layer deepens is also investigated. An analytical expression is derived to describe the rate at which a fog layer will deepen or erode, dependent upon the ratio of the relative moistening at fog top to the relative drying of the air with increased height. The derived expression is then compared against the high-resolution observations taken during the field experiment, as well as against numerical output of a simulated fog event. For both the observational and numerical comparisons, the expression is shown to accurately estimate the growth rate, and subsequent fog depth over many hours, allowing for greater understanding of the processes that lead to fog growth, as well as a better diagnosis of the fog interface in coarse-resolution settings.

Building upon the description of fog growth, the foundations for a simple conceptual model are presented in the final chapter. The model explains both the initial growth of a radiation fog layer, as well as its transition from a shallow, stably stratified fog layer, into one that is deep with well-mixed temperature and moisture profiles. The conceptual framework allows for *a priori* estimates of fog depth, liquid water content, and transition to deep fog. The work is still in its infancy, however, is presented here as a foundation for future research.

Ultimately, fog is, and remains, a challenge to forecast and predict. This thesis, however, builds toward further understanding of fog events. The conditions under which fog forms (or does not form) are further highlighted, along with reasons that

seemingly ideal conditions do not lead to a fog layer. The spatial characteristics that are (un)favourable for fog formation are also determined. Fog events were observed in their earliest stages through the use of emerging technology, which provides a foundation for future observational studies that investigate fog at higher resolution. The reasons fog is so sensitive in numerical simulation are highlighted, enabling greater insight when assessing numerical output in the future. Finally, the evolution of fog, including the rate at—and conditions under—which fog grows, is described through conceptual analysis.

Samenvatting[‡]

In het boek *Three Men in a Boat* geschreven door J. K. Jerome, vraagt de verteller: '*...wil iemand wel weten wat voor weer er op komst is? Het is al erg genoeg als het komt zonder de ellende om het van tevoren te weten*.' Hoewel het een satirisch werk is, zouden volgens mij veel mensen het met dat gevoel eens zijn. Vooral als het gaat om mist, waarvan vaak wordt gedacht dat het een deprimerend en saai fenomeen is[§]. Maar mist is erg belangrijk om nauwkeurig te voorspellen, want het kan een groot gevaar voor menselijke activiteit opleveren. En hoewel het voorspellen van het weer aanzienlijk verbeterd is over de afgelopen decaden (en nog steeds verbeterd wordt), blijft mist nog steeds moeilijk om te voorspellen. Het onderzoek dat in dit proefschrift wordt gepresenteerd heeft als doel de omstandigheden waaronder mist ontstaat beter te begrijpen. De onderwerpen zijn onder meer: hoe waarschijnlijk is het dat mist ontstaat onder bepaalde waargenomen omstandigheden, onder welke condities vindt misvorming nabij de grond plaats en hoe groeit een mistlaag?

Een eenvoudige methode om mist te voorspellen is het gebruik van statistische relaties tussen waargenomen variabelen. Met een idee van de omstandigheden bijvoorbeeld temperatuur en vochtigheid is het mogelijk om te identificeren hoe waarschijnlijk het is dat mist zal vormen. Echter, die methode staat hoge "false alarm rates" (mist voorspeld, maar vormt niet) toe om hoge "hit rates" (mist voorspeld en opgetreden) te krijgen. Om te weten hoe false alarms kunnen worden verminderd, zijn vijf jaar aan observaties geanalyseerd van het observatorium voor atmosferisch onderzoek dichtbij Cabauw (CESAR). Met de statistische methode werden misvoorspellingen geproduceerd voor verschillende doorlooptijden en met gebruik van verschillende optimalisatie methoden. De kwaliteit van de voorspellingen verbetert met kortere doorlooptijden, met de mogelijkheid van een hit rate van meer dan 90%, met een false alarm rate van slechts 13%. De methode blijkt succesvol, zolang er gebruik gemaakt wordt van een combinatie van variabelen die karakteristiek zijn voor de vochtigheid, turbulentie, en koeling. Uiteindelijk is het het gebrek aan ruimtelijke en temporele informatie datgene wat de mogelijkheden van statistische methoden beperkt.

Bij het onderzoek van statistische methoden, werd reeds vermoed dat een zeer ondiepe mistlaag zou kunnen bestaan, maar dat deze te laag zou zijn om te meten met de huidige standaardapparatuur. Dat wil zeggen: de meetapparatuur is doorgaans hoger opgesteld (>1.5 m boven de grond). Dit vermoeden is onderzocht in

[‡]Met veel dank aan Bas en Steven voor hun hulp bij het vertalen vanuit het Engels... of nog moeilijker, vertalen vanuit mijn Nederlands naar iets die op echte Nederlands lijkt!

[§]Ik heb ooit iemand ontmoet die riep bij het leren van wat ik doe: "Mist? Wow! ...*Dat* is saai!"

een veldcampagne bij CESAR van twee weken lang in november 2017 om hoge resolutie waarnemingen te krijgen bij de grond tijdens mist. Hierbij werden "Distributed Temperature Sensing"(DTS) en een nieuwe camera methode gebruikt. Er bleek inderdaad mistvorming net boven het aardoppervlak op te treden, welke pas veel later op grotere hoogte gedetecteerd werd door de traditionale instrumenten. Zo werd mist op 0.5 m gedetecteerd twee uur voordat deze op 2 m waargenomen kon worden. Bovendien werd met de DTS een zeer nauwkeurig beeld verkregen van de sterke temperatuurinversies nabij het aardoppervlak.

Waar het veldexperiment lokaal uitgevoerd was op de Cabauw site van het KNMI, is vervolgens het Nederlandse mistklimaat over het gehele land bekeken. Een dicht netwerk van weerstations werd gebruikt om te bepalen hoe het mistklimaat ruimtelijk varieert over het land als functie van lokale omgevingsfactoren. Allereerst bleek dat op landelijke schaal grote interjaarlijkse veranderingen optreden in mistfrequentie, doordat er veranderingen optreden in grootschalige atmosferische drukpatronen. Los hiervan treden binnen Nederland zelf grote verschillen op die relateerd kunnen worden aan lokale verstedelijking en de invloed van water, bijvoorbeeld de Noordzee. Vervolgens is er een eenvoudige parameter geïdentificeerd, de “Regionally Weighted Index” (*RWI*), die locaties nauwkeurig sorteert op basis van hun relatieve mistgevoeligheid, welke dus een functie is van lokale omstandigheden.

In dit proefschrift is het aangetoond dat mist zeer gevoelig is voor temperatuur en vochtigheid in zowel observaties als simulaties. De reden voor deze gevoeligheid kan verklaard worden door analyse van foutenpropagatie in de wiskundige formules voor verzadiging. Relatieve vochtigheid is het meest gevoelig voor temperatuur. Fouten in temperatuur hebben een 20 keer grotere impact op de relatieve luchtvochtigheid dan fouten gemaakt in de specifieke vochtigheid. Aan de andere kant zijn de typische fouten in absolute vochtigheid ongeveer 10–20 keer zo groot als de fouten in temperatuur. Al met al, lijken ze dus toch eenzelfde impact te hebben op fouten in relatieve vochtigheid. Met dit inzicht is het mogelijk om te zeggen waar de prioriteit(en) moet(en) zijn om mistvoorspelling te verbeteren: in de temperatuur of in de vochtigheid. Het versterkt ook de behoefte voor het verbeteren van voorstellingen van de (stabiele) atmosferische grenslaag in modellen, net zoals het verbeteren van observatiemogelijkheden (inclusief het gebruik van bijvoorbeeld DTS).

Vervolgens is onderzocht hoe snel de dikte van een mistlaag groeit en van welke factoren dit afhankelijk is. Een analytische uitdrukking is afgeleid die de groei van mist beschrijft. Deze uitdrukking is de ratio van de relatieve bevochtiging bovenaan de mist met de verticale vochtgradiënten op het grensvlak. De analytische voorspellingen zijn vergeleken met de hoge resolutie observaties van de veldcampagne en resultaten van numerieke simulaties. Voor zowel de observationele als de gesimuleerde mistlagen is de vergelijking zeer goed zelfs met een voorspellingstermijn van enkele uren. Het analytische perspectief zorgt voor een beter begrip van de processen die tot mistgroei leiden, evenals een betere diagnose van het mistinterface in omstandigheden met een grove resolutie.

Ten slotte wordt een eenvoudig conceptueel model gepresenteerd. Dit model beschrijft zowel de initiële groei van een stralingsmistlaag als de overgang van een

ondiepe, stabiel gestratificeerde mistlaag naar één die diep is met goed gemengde temperatuur- en vochtprofielen. Het conceptuele kader maakt het mogelijk *a priori* schattingen van de mistdiepte, de hoevelheid water en de overgang naar diepe mist te geven. Hoewel het werk nog in de kinderschoenen staat, is het hier opgenomen als basis voor toekomstig onderzoek.

Mist is zeer lastig te voorspellen en dat zal voorlopig zo blijven. Maar dit proefschrift heeft geleid tot meer begrip rondom het voorkomen van mist. De omstandigheden waarin mist vormt en groeit (of niet), en ook de reden waarom soms geen mist vormt in wat anders ideale omstandigheden zijn, worden beter geïdentificeerd. De ruimtelijke kenmerken die gunstig zijn voor mist zijn ook bepaald. Mistlagen werden waargenomen vanaf hun allereerste begin nabij de grond met gebruik van nieuwe methoden en technologieën; dit biedt een basis voor toekomstige observationele studies van mist op hoge resolutie. De theoretische inzichten rondom foutenpropagatie kunnen van pas komen bij de beoordeling van numerieke output in de toekomst. Ten slotte is de evolutie van mist beschreven door conceptuele analyse.

Chapter 1

Introduction

> . . . and the pillar of cloud went from before them and stood behind them.
>
> Exodus 14:19 *NKJV*

Fog, *from the ground up*. There are two reasons behind this title. First, it reflects my research approach, seeking to build understanding from the bottom-up, and including greater complexity with each step. The second refers to the nature of the type of fog on which most of my focus was placed; radiation fog grows upwards from the ground. More on that in the following.

1.1 The Nature of Fog and Associated Challenges

To most living in a temperate environment, fog is a well-known phenomenon. In literature and popular culture it is linked to mystery and suspense (as some of the chapter quotes indicate). It can also be seen as a hazard to transportation, or a depressing day at the beach. However, fog has a bright side as an important source of water in arid, or drought-prone regions both for plants (e.g., Huang 2019; Raux et al. 2020), as well as for remote communities (e.g., Schemenauer 1988).

Colloquially, the term "fog" is often used to refer to conditions of reduced visibility in general. Formally, however, a distinction is made between fog, mist[§], haze, and smog, although their qualitative differences may be unclear. From the perspective of visibility reduction, fog and smog are the most severe of the phenomena, with fog defined as a surface cloud where visibility is reduced below 1 km due to the presence of suspended water droplets/particulates (NOAA 2005; Figure 1.1). Fog can further be categorized according to its severity, with "dense" or "thick" often used to describe visibility conditions of just a few tens to hundreds of metres. Smog is fog induced—or aggravated—by pollution as, for example, witnessed in London during the previous centuries (including the infamous "Great Smog of London"; Martinez 2019), and can have a significant impact on human health (e.g., Pérez-Díaz et al. 2017). Mist is when visibility is between 1–2 km, while haze consists of dry aerosols

[§]Don't be confused; in Dutch, the word "mist" means "fog"!

Figure 1.1: A typical "Dutch fog" observed in the morning between Leiden and Den Haag, The Netherlands. Fog is defined as visibility below 1 km.

(e.g., dust or pollutants) reducing visibility below 7 km. The reason for reduced visibility is that water droplets (fog and mist) or dry particles (haze) scatter and absorb light, reducing the distance that it can travel.

1.1.1 How Does Fog Form?

Unless in a particularly arid environment, the air contains a certain amount of water vapour (i.e., water in its gaseous, invisible state). Air can only hold so much of this water vapour at a given temperature and pressure before it becomes saturated (saturation is commonly measured in terms of relative humidity, *RH*; when air reaches an *RH* value of 100%, it is saturated). At its simplest, saturation—and subsequent condensation of water vapour into liquid water that forms fog or dew—can therefore be brought about in two ways. Either an air mass cools (reaching what is known as the "dew point temperature" when $RH = 100\%$), or more water is added (for example, due to advection from upwind, rainfall, or evaporation from a moist surface). The point of saturation is, however, neither necessary nor sufficient in some cases. For example, the condensation of water can occur at less than 100% saturation if there is a surface onto which the water can be deposited (Köhler 1936); think, for example, of your bathroom mirror when you take a shower. In the air, there are small particles—called aerosols—that can act as such deposition surfaces for the formation of water droplets. These are known as "cloud condensation nuclei" (CCN), of which sea salt (NaCl) and other polar molecules are particularly efficient. This is why polluted environments experience significant smog, with many particles present to allow for water condensation and deposition. On the other hand, in the absence CCN (either too few, or the particles themselves repel water), then air can be supersaturated ($RH > 100\%$) before condensation occurs (because the water has nothing

onto which it can deposit; e.g., high in the troposphere, or in Antarctica).

While all fog forms through condensation of water, several types of fog are commonly distinguished according to the processes that lead to onset. Radiation fog, for example (the primary focus of this research) is formed during low wind speed, clear-sky nights, when strong near-surface cooling occurs. Under such stable boundary-layer conditions, the cooling of the air results in saturation. Advection fog, on the other hand, occurs when moist air (or cold air) is blown into an undersaturated region. The mixing of air masses, or the passage of warm, moist air over a cold surface, results in condensation. Further types of fog include cloud base lowering fog (a cloud sinks to the surface from above), precipitation fog (reduced visibility due to rain or snow), and upslope fog (as air moves up a slope, it cools due to expansion under reduced atmospheric pressure, causing the dewpoint to be reached; this type of fog is not common in the Netherlands!).

1.1.2 Fog as a Hazard

When one thinks of an atmospheric hazard, they will often think of heavy rain, hail, tornadoes, and hurricanes. The "impressive" hazards. In contrast, fog is a seemingly docile phenomenon. It is, essentially, a "passive hazard" in that it does not cause damage of its own accord. Rather, it is only a problem when human activities are involved.

Due to the accompanying reduction in visibility, fog impacts all modes of surface transport. Economically, fog is an expensive problem for commercial operations, particularly at airports when low-visibility conditions reduce the capacity for aircraft movements. With cost of delay expensive for both passenger and airline (costs of €1 000 per airplane after just 30 minutes, and in the tens of thousands of Euros after just 90; Cook and Tanner 2015), the economic cost can grow rapidly, and can even be equivalent to that of more "extreme" weather events such as tornadoes and winter storms (e.g., Gultepe et al. 2007). For this reason, extending the accurate window of a fog forecast by as little as half an hour may already have a significant impact (Valdez 2000). Of course, cost cannot be measured in currency alone, with fog being responsible for transportation accidents across the globe. Some notable examples include the Tenerife Air Disaster, where two Boeing 747 aircraft collided on the runway (Ministeria de Transportes y Communicaciones 1978); the sinking of the SS Andrea Doria after collision with the MV Stockholm (Andrews 2019); and, at the end of last year, the fatal multi-vehicle collison near Akkrum in Friesland (Dupuy 2019).

1.1.3 Observing Fog

Due to the hazard presented by low-visibility events, monitoring and accurate forecasting of fog is essential. Visibility—and therefore fog—can be observed in many ways. Historically, dedicated observers determined visibility based on the distance that could be viewed (e.g., can a tree 1 km away from the observer be seen?). Hu-

man vision, however, depends on the individual observer, and the ambient light conditions. In a modern meteorological sense, "visibility" is defined according to the maximum distance that a black object can be distinguished against the horizon during daylight conditions (WMO 2014). With more particles blocking/scattering light, the contrast is reduced such that the distance becomes smaller.

Given that the reduction in visibility caused by fog is due to the scattering and absorption of light by the water droplets and other particles along the optical path, visibility can also be measured based on the properties of light transmission and scattering. Transmissometers, for example, measure the relative reduction in intensity between a light source and sensor (this is the basis of the camera method used in Chapter 3). Most modern in situ sensors rely on the scattering of light from particles to infer the visibility, such as the Biral-SWS sensors used at the Cabauw site in the Netherlands (Monna and Bosveld 2013). A more objective measure of visibility is "meteorological optical range" (MOR), which is a quantitative description of light propagation, absorption, and scattering (WMO 2014). Depending on the purpose, other definitions and observation methods may be used (e.g., runway optical range).

In situ observations are essentially restricted to single-point observations. As such, the three-dimensional features of a fog layer cannot be accurately mapped without using an increasingly large number of sensors. This makes process-based studies, as well as the comparison of observations with numerical output, challenging. More spatially continuous measurement techniques, such as distributed temperature sensing (DTS) and photograph-based visibility monitoring (Chapter 3), as well as infra-red imaging (e.g., Price and Stokkereit 2020) are therefore desirable.

Rather than observe at a single, localized position, remote sensing of fog can provide greater spatial coverage. Ground-based remote sensing has achieved some success through the use of RADAR (e.g., Li 2016). Satellites have also been used to observe fog (e.g., Bendix 2002; Egli et al. 2017, 2019). However, ground-based and satellite remote-sensing methods of fog detection are primarily restricted by limits in achieving near-surface resolution to observe shallow fog layers (e.g., due to ground clutter and/or sampling resolution on the order of tens of metres). Satellite methods often further require clear-sky conditions (i.e., no upper-level clouds obscuring what lies below), and ambient daylight (in order to have a light source for satellite images). However, if such challenges can be overcome, there is great potential of remote sensing techniques to improve our understanding of fog in space and time, as evidenced by Egli et al. (2019) who generated spatial climatologies of fog over Europe.

1.1.4 Simulating and Forecasting Fog

While weather forecasts continue to improve (gaining roughly one day of skill every 10 years; Hollingsworth et al. 2003), forecasting fog remains challenging (e.g., Steeneveld et al. 2015). This is due to the complex interplay of many different processes in advance of fog formation, as well as technical limitations.

Essentially, fog is a "secondary" process; the correct simulation of which first de-

pends upon correctly simulating the underlying temperature, wind, and radiation conditions. As a result, any errors in other fields can have a significant impact on whether or not fog will form within a simulation environment. Even then, if all ambient conditions are perfectly simulated, fog forms as the result of sometimes complex microphysical interactions, and depending on the aerosol composition of the airmass, can form anywhere from under-saturated to over-saturated conditions. Given factors such as temperature are already challenging to forecast to 100% accuracy, particularly within the stable boundary layer, forecasting fog inherits these challenges.

Radiation fog is particularly difficult to forecast. Unlike advection fog, for example, radiation fog forms primarily as the result of highly localized conditions. It is also a fine balance between competing processes of radiation and turbulent transport. Such conditions are extremely difficult to simulate accurately, as the balance of forces is so fine. During the day, solar radiation and turbulent fluxes are dominant factors in determining the near-surface conditions. At night, however, with the sun absent and turbulent motions suppressed by increasingly stable conditions, small errors can make a big difference, with the end result particularly sensitive to accurate simulation. Simulating stable nocturnal conditions is challenging enough; (e.g., Mahrt 2014), even without the further difficulty of adding fog.

In part, the simulation of fog is restricted by the grid resolution achievable in numerical models (which is most often limited by computational resources). In general, weather forecasts operate with horizontal resolutions on the order of a few kilometers, and their lowest vertical level on the order of 10 m (e.g., ECMWF 2018). As a result, the small-scale processes involved in the formation of fog are often "sub-grid" features. This is, again, particularly true for radiation fog that forms initially as a very shallow ground layer and grows over time. Tardif (2007) and Maronga and Bosveld (2017) have shown the importance of employing fine vertical grid resolution on the formation of radiation fog, with resolutions on the order of 1 m or less required to accurately capture the timing of onset. Similarly, Bergot et al. (2015) demonstrated the importance of having finer horizontal resolution, particularly in heterogeneous domains such as at airports. Nested grid approaches (where a coarse numerical grid is used to provide boundary conditions to a smaller, finer-resolution grid) are commonly used to improve horizontal resolution in earth-system models without incurring too great an additional computational cost; however, Steeneveld et al. (2015) showed that nesting—because the boundary conditions inherited from the larger, coarse domain, are incorrect—does not improve the simulation of fog, and may in fact be detrimental.

1.2 Research objectives

This thesis aims to improve our understanding of fog and the conditions under which it forms and grows. Specific questions include:

1. Under what conditions does fog form? Why does fog not always form under

otherwise favourable conditions?

2. Can the initial growth stages of radiation fog be accurately observed?
3. What determines regional variability in fog occurrence?
4. To what factors is the simulation of fog most sensitive?
5. How does a fog layer evolve in time? What determines its evolution?

1.3 Outline

The remainder of this thesis is structured as follows. In **Chapter 2**, the challenges associated with observational prediction are investigated, including identifying why so many "false alarms" occur. **Chapter 3** addresses some of the observational limitations identified in the first two chapters by presenting the results of a field campaign designed to observe (very) shallow fog during its formation and growth stages. **Chapter 4** shifts focus from local to mesoscale observations, presenting the results of a climatological analysis of fog throughout the Netherlands. In an effort to understand the significance of errors and different processes for the formation and simulation of fog, **Chapter 5** presents an analysis of the saturation equations, highlighting the sensitivity of saturation to different physical parameters. Continuing the analytical assessment, and building upon the observations of Chapter 3, **Chapter 6**, presents an analytical description of the growth of an existing fog layer, which is compared with observed and simulated fog layers. Finally, **Chapter 7** outlines a simple conceptualization of a growing fog layer, providing a means of estimating the evolution of a stably stratified fog layer from its onset. The individual chapters are summarized and discussed in context in **Chapter 8**, along with recommendations and implications for future research.

Chapters 2–4 and 6 have been published in peer-reviewed academic journals, while Chapter 6 is under revision. Appropriate references have been placed at the start of each chapter.

How much fog does it take to turn on a light bulb?

If you have ever placed your hand over a boiling kettle, you know that a large amount of energy is released when water changes phase from gas to liquid (condenses), as in the case of fog formation. The energy released is proportional to the latent heat of vaporization/condensation, which is roughly 2.3×10^6 J kg^{-1}. If we assume a fog liquid water content of roughly 0.15 g m^{-3} (e.g., Pilie et al. 1972), that means a release of 344 J of energy per every cubic metre of fog that forms. Let us then then assume a fog layer covering the entire Netherlands (a land area of just less than 35 000 km^2). Assuming it is 1 m deep, that means an energy release during its formation of roughly 1.2×10^{13} J, or, to put it in terms of your energy bill, 3.2×10^6 kWh.

Now, some context. Our hypothetical fog layer would be able to provide electricity for 6100 60-W light bulbs for one whole year. Or, if you prefer, electricity to all households in the Netherlands for approximately 75 minutes*! The resulting energy scales linearly with the depth of our fog layer, as shown in the figure below.

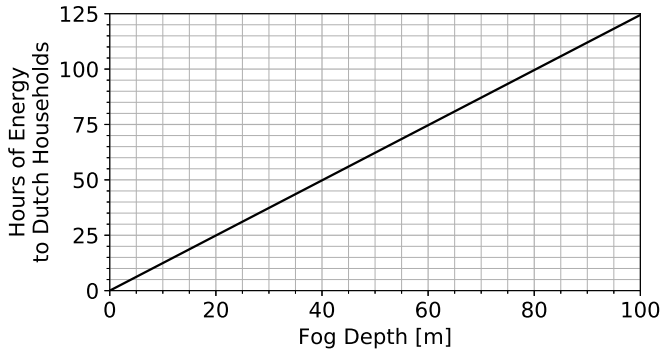

The energy released due to the formation of fog over the Netherlands.

So, is fog a good source of renewable energy, particularly to supplement solar energy under cloudy skies? Unfortunately, no. The energy is never truly available, with the evaporation of fog requiring the same amount of energy. Therefore, our analysis remains purely hypothetical. It does, however, raise questions about the impact phase change might have on a juvenile fog layer. Might some of the latent heat release counteract the cooling of a fog layer, leading to a slight delay in its formation and/or growth?

*assuming an annual average consumption of 2.3×10^{10} kWh (CBS 2019)

Chapter 2

Understanding and Reducing False Alarms in Observational Fog Prediction

> . . . there hung a dense, white fog. . . low, but thick and well-defined
>
> Sir A. C. Doyle, *The Hound of the Baskervilles*

Summary

Five years of observations from the Cabauw Experimental Site for Atmospheric Research are used to further investigate how false alarms may be reduced using the statistical method for diagnosing radiation-fog events from observations developed by Menut et al. (2014). The method is assessed for forecast lead times of 1–6 h and implementing four optimization schemes to tune the prediction for different needs, compromising between confidence and risk. Prediction scores improve significantly with decreased lead time, with the possibility of achieving a hit rate of over 90% and a false-alarm rate of just 13%. In total, a further 31 combinations of predictive variables beyond the original combination are explored (including mostly, e.g., variables related to moisture and static stability of the boundary layer). Little change to the prediction scores indicates any appropriate combination of variables that measure saturation, turbulence, and near-surface cooling can be used. The remaining false-alarm periods are manually assessed, identifying the lack of spatio–temporal information (such as the temporal evolution of the local conditions and the advective history of the airmass) as the ultimate limiting factor in the methodology's predictive capabilities. Future observational studies are recommended that investigate the near-surface evolution of fog and the role of non-local heterogeneity on fog formation.

This chapter has been published as:

Izett JG, van de Wiel BJH, Baas P, Bosveld FC (2018) Understanding and reducing false alarms in observational fog prediction. Boundary-Layer Meteorol 169(2):347–372, doi:10.1007/s10546-018-0374-2

2.1 Introduction

We use the diagnostic observational fog-prediction method described by Menut et al. (2014) to predict fog events over a five-year period at the Cabauw Experimental Site for Atmospheric Research (CESAR) in the Netherlands. Our goal is to identify where the method is limited, why it is limited, and how it may be further improved, particularly with respect to reducing the overall number of false alarms. We test different forecast lead times from 1–6 h, along with different optimization schemes and predictive variables. We further look to understand the underlying reasons for the occurrence of false alarms in the prediction: are they due to an incomplete representation of fog-formation processes, or due to limitations of the methodology itself, which uses only local information in both space and time?

Fog is a meteorological phenomenon that is particularly common in the Netherlands where high humidity and a distinct seasonal cycle provide favourable conditions for its formation. The reduction in visibility that accompanies fog makes it a hazard for navigation, and can be a major cause of motor-vehicle accidents (Bartok et al. 2012) as well as a disruption to maritime shipping operations (e.g., Alpert and Feit 1990; Fu et al. 2010). Fog disruptions to air travel can also have a high economic impact (e.g., Fabbian et al. 2007; Gultepe et al. 2007; Stolaki et al. 2012), with more time needed between plane takeoffs and landings causing delays, as well as the need to cancel flights.

Fog forms when water vapour in the air condenses to form droplets, leading to a reduction in visibility as increasing numbers of water droplets block the optical path via the scattering and absorption of light. Regional and application-based definitions of fog vary; however, for consistency with previous studies (Menut et al. 2014; Román-Cascón et al. 2016a), we use the accepted meteorological definition of fog, i.e., when visibility is below 1 km at the surface (NOAA 2005).

There are several types of fog, and while each is the result of the basic process of droplet formation, the differences in formation conditions and environments are used to distinguish them. Our focus is on radiation fog since this is a common fog type in the Netherlands (e.g., Duynkerke 1999), and its primarily localized nature makes it easier to study the dynamics involved. Radiation fog typically forms at night under calm, clear conditions as the result of radiative cooling of the surface due to an imbalance in the net radiation and subsequent saturation of moist air.

The study of fog has a long history (for a detailed review, see Gultepe et al. 2007), with considerable investigation into the key processes for fog formation and the ability of different methods to predict fog. For example, Duynkerke (1991, 1999) investigated fog in the Netherlands, identifying conditions favourable for the formation of radiation fog (such as the need for a calm, stable boundary layer), as well as the need for reliable physical parametrizations in numerical models. The simulation of fog formation, for instance, is particularly sensitive to the surface roughness, requiring careful attention in models. More recently, Maronga and Bosveld (2017) investigated the sensitivity of a radiation-fog event's life cycle to various parameters through sensitivity tests and idealized simulations using the Paralellized Large-Eddy

Simulation Model (PALM; Maronga et al. 2015). They found the timing of fog onset to be sensitive to turbulent mixing, cold-air advection, and soil temperature, with overall duration and intensity of the fog event additionally sensitive to soil moisture. Further international studies at a range of sites include: the ParisFog experiments (Haeffelin et al. 2010) regarding fog in a semi-urban area around Paris, France; and the Fog Remote Sensing and Modelling (FRAM) project in Canada (Gultepe and Milbrandt 2007), among many others (e.g., Fabbian et al. 2007; Tardif and Rasmussen 2007; Bartok et al. 2012; Boneh et al. 2015; Huang and Chen 2016).

While fog has been studied for many years and it is of clear societal relevance, the accurate prediction of fog events remains elusive (Steeneveld et al. 2015). In part, this is due to the complex interplay between many different processes during formation, and the need to capture not only large-scale dynamics (such as wind speed and the synoptic conditions), but also small-scale processes such as droplet microphysics (e.g., Gultepe et al. 2007). Numerical models are often unable to capture the timing and duration of fog events (e.g., Steeneveld et al. 2015; Román-Cascón et al. 2016a,b). In many cases, this is the result of deficiencies in subgrid-scale parametrizations (Steeneveld et al. 2015), as well as the vertical and horizontal resolutions being too coarse to fully model the necessary scales of relevance and heterogeneity (e.g., Tardif 2007; Bergot et al. 2015; Philip et al. 2016; Maronga and Bosveld 2017). A further challenge for numerical simulations is in deriving estimates of visibility. Both liquid-water content and droplet-number concentration are needed to accurately estimate visibility in models; often, however, only the droplet-number concentration is included (Gultepe et al. 2006, 2007). At the same time, the relationship between droplet properties and visibility is complex and dependent on whether a fog layer is growing or dissipating (Boers et al. 2013). As a result, a combination of process-based numerical forecasts and a rule-based fog diagnosis may be useful (Zhou et al. 2012).

The prediction of fog from observations dates back at least one century, with Taylor (1917) outlining a simple method for nocturnal fog predition in England based on observations at 2000 local time the evening before. The simple methodology—comparing wind speed and humidity to empirical threshold functions—resulted in a hit rate of roughly 80%, and a false-alarm rate of around 50%. Recently, Menut et al. (2014) developed a similarly straightforward statistical approach with which to forecast radiation-fog events at the ParisFog site using observations of key variables (such as relative humidity) and comparing them to threshold values that indicate the onset of fog in the coming 6 h. Their method was subsequently applied by Román-Cascón et al. (2016a) at the Spanish Research Centre for the Lower Atmosphere (CIBA) and at the CESAR facility. In both studies, the statistical method proved successful in capturing at least 90% of all fog cases analyzed; however, the high rate of correct prediction is still accompanied by a correspondingly high rate of false alarms: almost 40%. It is this method outlined by Menut et al. (2014), hereafter referred to as the M14 method, which we also use to predict fog events at Cabauw and assess the impact of different optimization schemes and the role of different factors leading to false alarms.

While the M14 method has been well-documented at different sites, including Cabauw, the reasons for false-alarm occurrence—and correspondingly, means of reducing false alarms—have not been reported in great detail. We look to fill this gap by investigating the role of various forecast windows on the overall predictability—comparing the performance at the suggested lead time of up to 6 h to shorter lead times of 3 h and 1 h—in order to assess whether the loss in lead time is compensated by a significant improvement in forecast skill. We also test the ability of different optimization schemes to improve performance, by accepting increased risk (reduced identification of events) in order to increase the confidence of the predictions (reduced false alarms), tuning the methodology for different needs and uses. Further, the potential of other predictive variables (particularly the inclusion of vertical information as opposed to purely near-surface observations) is investigated to determine whether a key process has been ignored in the formulation. Finally, we focus on the reasons why false alarms occur when using the methodology. In part this is related to the search for a previously ignored factor in fog formation. It is also aimed at assessing the impact that the method's lack of spatio–temporal information has on the prediction; for example, its inability to account for temporal evolution of the system and the advective history of the airmass.

A brief introduction to the CESAR facility follows, with an overview of the M14 methodology and optimization schemes in Sect. 2.2. The results of applying the methodology with different lead times and optimization schemes are presented in Sect. 2.3, followed by an analysis of the remaining false alarms in Sect. 2.4. Finally, a discussion follows in Sect. 2.5.

2.2 Observations and Methodology

2.2.1 The CESAR Facility and Observational Data

The CESAR facility (e.g., Monna and Bosveld 2013) is located near Lopik in the province of Utrecht, the Netherlands (51.971 °N, 4.927 °E). It is operated by the Royal Netherlands Meteorological Institute (KNMI) and a consortium of research institutes and universities. The site is surrounded by predominantly agricultural fields and small waterways, and is in fairly homogeneously flat terrain, broken occasionally by small villages. The nearest major city is Utrecht, located roughly 20 km to the north-east, with the industrial city of Rotterdam approximately 35 km to the west-south-west. Amsterdam, The Hague and the North Sea are located roughly 50 km to the north and west, respectively. The water table is maintained approximately 1 m below the surface, except during periods of heavy or extended rainfall.

The primary feature of the CESAR facility is the 213-m tall instrument mast, which, in addition to other instruments around the site, including a series of smaller masts and an automatic weather station, measures the vertical profiles of various meteorological variables including temperature, wind speed, and visibility. Data from the site are publicly and freely available through the KNMI data centre (https://data.knmi.nl/datasets?q=CESAR).

Visibility—which we use as our primary indicator of fog—is measured at the site with Biral SWS-100 forward-scatter visibility sensors at seven heights: 2 m, 10 m, 20 m, 40 m, 80 m, 140 m, and 200 m. The visibility range of the sensors is 10 m to 20 km. Air temperature and dewpoint temperature are also measured at these seven heights (replacing the measurement at 2 m with one at 1.5 m), with air temperature additionally measured at 0.1 m. Relative humidity is calculated at seven heights from both temperatures, and wind speed and direction are measured along the mast at six heights: 10 m and above. Net radiation is measured as the total (longwave and shortwave) upwelling and downwelling radiation at 1.5-m height. For other variables, the reader is encouraged to visit the CESAR website and accompanying documentation. We use the 10-min averaged observations.

We restrict our analysis to the five years 2012—2016 (inclusive) when visibility data are available at all seven heights at the tower location. An independent fog event is classified as when conditions are foggy (visibility < 1 km) at the 2-m level for at least 50 min out of every 1 h, and separated from a previous event by at least 2 h as in Román-Cascón et al. (2016a). Of all 254 fog events between 2012—2016, the most common type of fog at the CESAR facility according to the classification algorithm of Tardif and Rasmussen (2007) was radiation fog, making up roughly 63% of all events. Twenty percent of the events could not be classified with the algorithm and may include further radiative events. These and the non-radiative events are not considered in this analysis. It should be noted that the classification is for the CESAR facility alone, and is likely different for other locations around the country, particularly at the coast.

Fog at the CESAR facility occurs throughout the year, with the greatest number of all fog events occurring in autumn (Fig. 2.1a). Due to the nature of formation, the radiative events form mostly in the middle of the night (Fig. 2.1b), when radiative cooling has led to a significant reduction in temperature at the surface. With a typical duration of around 1—3 h (Fig. 2.1c), only a few events persist beyond sunrise. For most fog events the mean visibility for the duration of the event is below 500 m (Fig. 2.1c) regardless of the duration, with the minimum visibility as low as tens of metres.

2.2.2 Prediction of Fog from Observations

In the most naïve sense, radiation fog forms when the air cools to saturation (the air temperature is equal to the dewpoint temperature; a relative humidity of 100%). Given that, the simplest prediction of radiation fog would be to compare the air temperature at a given time to the dewpoint temperature (how much cooling is needed for fog to occur), and then predict the amount of cooling that will occur. If the predicted cooling is greater than the cooling required, fog would be expected to form. However, Fig. 2.2a shows that, for the 1.5-m level at sunset, while it may be a necessary condition that the air temperature must reach (or be very close to) the dewpoint temperature, it is not a sufficient condition for fog formation. Therefore, such a simple prediction cannot be reliably employed.

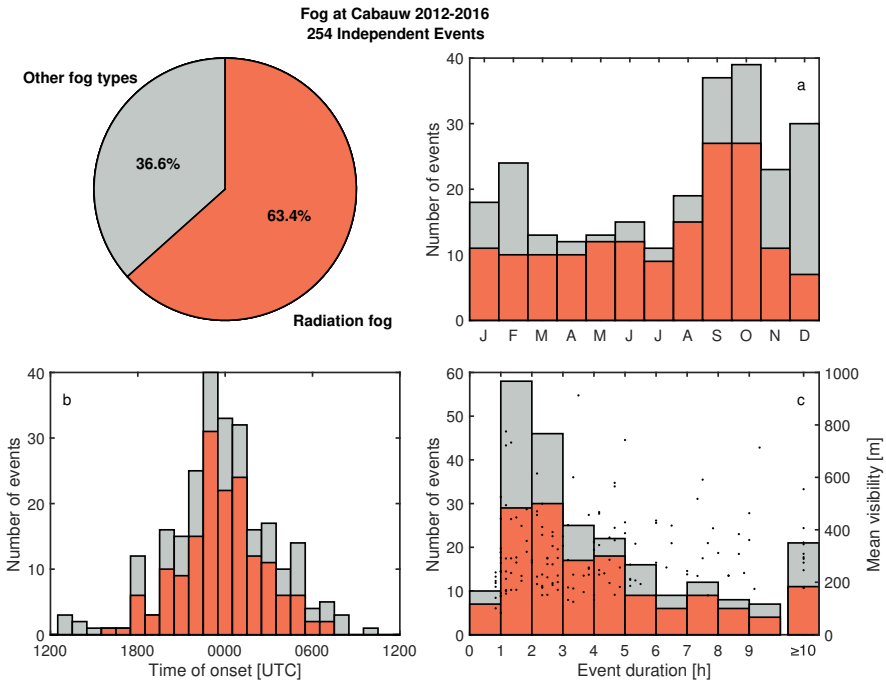

Figure 2.1: Fog at the CESAR facility between 2012—2016. Out of 254 events, radiation-fog events contribute the greatest portion. a) Total number of fog events per month, b) time of onset of fog events, and c) duration of fog events by type with the dots indicating the mean visibility for radiative events.

The conditions before the onset of the radiative events are fairly consistent, however, pointing toward the possibility of prediction based on observations and providing the foundation for statistical-observational methods, such as by Taylor (1917) and Menut et al. (2014). In part, this is due to the classification of events using the Tardif and Rasmussen (2007) algorithm, which identifies radiation fog based on low wind speeds and clear skies; however, it also points to the underlying dynamical processes under which fog events occur. For example, the probability density functions in Fig. 2.2b—d show almost all of the radiation-fog events occur when the net radiation is strongly negative, wind speed is low, relative humidity is high, and the boundary layer is stable, with the distributions becomming increasingly distinct toward the time of onset. Relative humidity, in particular, exceeds the 95-percentile of all observed values as onset approaches. Likewise, calm conditions and strong radiative cooling are preferred for radiation fog.

While not as distinct as the approach to fog onset, the conditions before dissipation begin to return toward the underlying distribution as dissipation approaches (not shown). For example, the wind speed increases and the temperature inversion weakens. All of this is generally initiated by an increase in net radiation (a warming) at the surface, usually as the result of sunrise, though also from the formation and/or

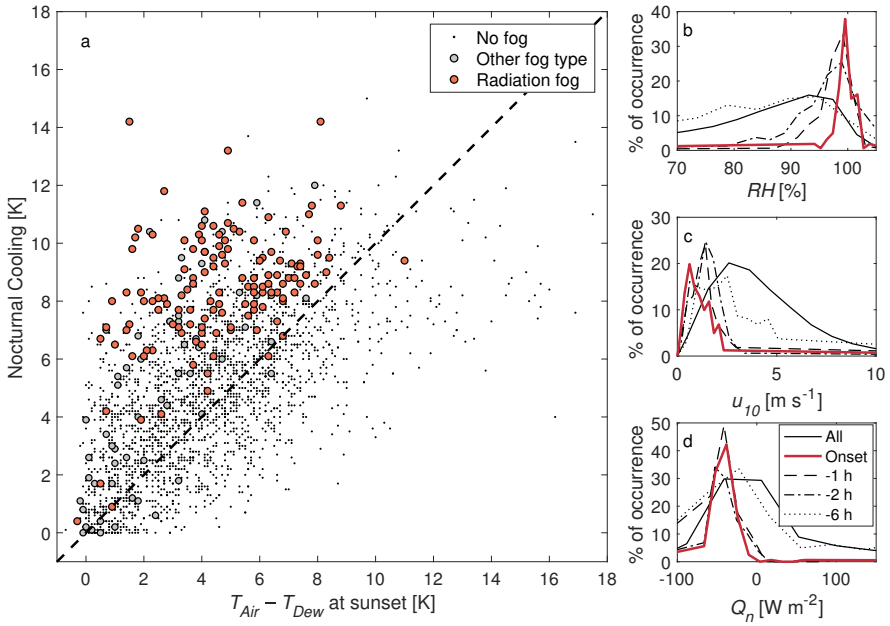

Figure 2.2: a) Amount of cooling at 1.5 m over a given night (temperature sunset minus minimum nocturnal temperature) compared to the amount of cooling needed to reach saturation at sunset. Nights with radiation fog events are in orange, nights with other fog types are grey. Nights on which no fog was observed are represented by the black dots. The dashed line indicates the 1:1 equivalency, above which cooling is sufficient to reach saturation and fog events are expected to occur. b—d) Probability density functions of relative humidity at 1.5 m, 10-m wind speed, and net radiation, respectively, up to 6 h before the onset of radiation-fog events. The solid black lines indicate the overall distributions in the data.

passage of clouds.

2.2.3 M14 Methodology

We investigated strategies for reducing false alarms in observational fog prediction using the M14 methodology. We tested shortened forecast lead times, along with a range of additional predictive variables beyond the original methodology. This section briefly outlines the steps employed by the M14 method, with the reader directed to Menut et al. (2014) for more detail on its development.

Given that the conditions preceding radiation-fog events are, in general, distinct, the M14 method assigns a probability of pre-fog conditions based on how close current observations are to the fog-favourable conditions, which is then used to diagnose the likelihood of fog forming within the next 6 h (Fig. 2.3).

Menut et al. (2014) identified four key variables for the diagnosis of pre-fog conditions: relative humidity (RH), net radiation (Q_n), wind speed at 10-m height (u_{10}), and the overall trend in surface temperature from 3 h prior ($\Delta T_{1.5}^{3\ h}$). They

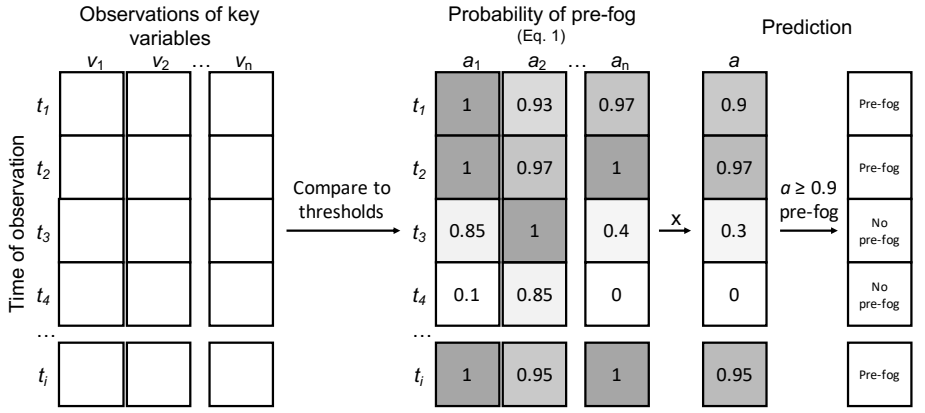

Figure 2.3: Overview of the M14 method.

then define thresholds for each variable (v) for which fog conditions are favourable. If the threshold (v_T) is met for a given variable, its prediction score, $a_v = 1$. If it is not met, the probability is calculated from a tapered normal distribution, allowing for conditions which are close to favourable to still influence the prediction score positively,

$$a_v = \begin{cases} 1 & \text{if threshold met} \\ \frac{1}{\sqrt{2\pi\sigma_v}} \exp\left[\frac{-(v-v_T)^2}{2\sigma_v}\right] & \text{otherwise} \end{cases}, \tag{2.1}$$

where σ_v is the standard deviation of the observed variable, v. The overall probability of pre-fog is then calculated as the product of each individual prediction score at each time step for the variables considered,

$$a = \prod_{v=1}^{n_v} a_v. \tag{2.2}$$

If $a \geq 0.9$, then pre-fog is diagnosed and fog is expected in the next 6 h. This is predominantly an engineering aproach, rather than a physically robust approach (as the properties are not independent and the real likelihood of fog is not necessarily a strict multiplication), but it does provide a means of estimating the statistical likelihood of fog formation based on the observed variables.

The thresholds determined by Menut et al. (2014) for the Paris site are presented in Table 2.1, along with site-specific thresholds for the CESAR facility as determined by Román-Cascón et al. (2016a) (identified as RC16). RC16-H is the threshold set found to achieve the highest hit rate, and RC16-F is the result of minimizing the false-alarm rate, both over the period from 2008–2011. It should be noted that RC16-F is inherently stricter than RC16-H as the aim is to exclude the highest proportion of false alarms.

In Sect. 2.3, the results of applying the M14 method at Cabauw using the original

Variable	Thresholds		
	M14	RC16-H	RC16-F
RH [%] $\geq$	90	88	98
Q_n [W m^{-2}] $\leq$	-10	5	-20
u_{10} [m s^{-1}] $\leq$	3	4	1.5
$\Delta T^{3\ h}_{1.5\ m}$ [K] $\leq$	-0.5	0	-1.5

Table 2.1: The M14 method thresholds (v_T in Eq. 2.1) as defined by Menut et al. (2014) for the ParisFog site, and the thresholds for the CESAR facility to achieve maximum hit rate or minimum false-alarm rate from Román-Cascón et al. (2016a).

thresholds are presented for a prediction window of 6 h as well as shorter windows of 3 h and 1 h, with a diagnosis made at each 10-min observation. From the PDFs in Fig. 2.2b-d, the shorter windows should lead to improved performance of the method; however, naturally, the degree to which the method is improved may not be sufficient to outweigh the loss of lead time. Only radiation-fog events lasting more than 2 h are considered (as with Román-Cascón et al. 2016a).

Further to the proposed combination of four variables, we investigated a total of 31 further variable combinations in addition to, and in replacement of, the original variables. The additional criteria include thresholds on such variables as the friction velocity (u_*) and the trend in visibility over the past 1 h as proposed by Román-Cascón et al. (2016a), as well as those that include not only surface observations, but vertical information as well (such as the temperature inversion between the surface and aloft, and the relative humidity at 10-m height). We also consider calculated indices such as comparing the observed heat flux to the maximum sustainable heat flux of van de Wiel et al. (2012a). While microphysical properties, such as aerosol concentration and type are important for fog formation, the possibility of a microphysical predictive variable was not investigated due to the lack of appropriate observational data. For a complete list of the combinations assessed, see Table 2.4 in Appendix 1.

2.2.4 Assessment of Prediction Performance

Several indicators of prediction performance can be used, each with their own merits. We use the hit rate (*HR*), and false-alarm rate (*FA*), which were applied by Menut et al. (2014) and Román-Cascón et al. (2016a) as their primary indicators of prediction performance. Hit rate and false-alarm rate are based on the comparison of predictions and actual fog occurrence on a timestep-by-timestep basis. If (as per Table 2.2) the number of correct predictions is h (pre-fog diagnosed and occurs; hits) and the total number of missed predictions is m (fog occurs that is not diagnosed), then the hit rate (in percent) is simply the ratio of correct predictions to the total number of actual pre-fog occurrences (both those correctly diagnosed and those missed),

$$HR = 100\left(\frac{h}{h+m}\right). \tag{2.3}$$

	Pre-Fog Obs.	No Pre-Fog Obs.
Pre-Fog Pred.	Hit (h)	False Alarm (f)
No Pre-Fog Pred.	Miss (m)	Correct Clear (c)

Table 2.2: Forecast parameters for calculating *HR* (Eq. 2.3) and *FA* (Eq. 2.4).

Correspondingly, where the number of incorrect predictions is f (pre-fog diagnosed but not observed; false alarms), and the number of correct non-predictions is c (no pre-fog diagnosed and no fog in reality), the false-alarm rate is the number of false alarms divided by the total number of non-fog cases in reality ($f + c$),

$$FA = 100\left(\frac{f}{f+c}\right). \tag{2.4}$$

In practice, *HR* and *FA* values can be misleading, with the score dependent on the overall length of the time series. For example, if very few fog events are observed, then a single hit carries significant weight when assessing hit rate. Likewise, the false-alarm rate is very low if the time series is long due to the large denominator. As such, their values must always be taken into consideration with other factors such as the length of the time series.

2.2.5 Optimization for Desired Outcomes and Acceptable Risk

A perfect prediction with $HR = 100\%$ and $FA = 0$, while ideal, is far from realistic. As such, the performance of a forecast must be judged not only on the number of correct and incorrect predictions made, but also the needs of the user and stakeholders. Just as in numerical modelling where efficiency of calculation must be balanced with resolution demands, so too is there a trade-off between accurate foreasting and permissible levels of risk in a forecast.

It is conceivable that for some scenarios overprediction is desired (i.e., there can be little to no risk that an event be missed). Conversely, there may be some acceptable level of missed events when operations or needs are able to adjust. For example, this might occur at an airport where procedures are in place to adapt for inclement weather and the financial loss of altering schedules for an incorrect fog forecast could be greater than for delays caused by an occasional unforeseen fog event.

To this end, we tested different optimization schemes in order to demonstrate and evaluate the ability of the approach to be tuned for different needs. Using a simple evolutionary algorithm, the first three years of the dataset (2012—2014) are used to attain the desired performance by optimizing the thresholds of the different variables, and then the optimized thresholds are subsequently applied to the following two years (2015—2016). The optimization criteria are as follows:

1. **max*HR***:
   Thresholds are optimized to obtain the maximum hit rate possible.

2. **maxΔHR_{95}**:
   Some risk is tolerated, with thresholds optimized to first obtain $HR \geq 95\%$, after which the value of *FA* is minimized.

3. **maxΔ**:
   Thresholds are optimized to achieve the largest difference between the hit rate and false-alarm rate.

4. **maxΔFA^5**:
   Very little risk is tolerated, with thresholds optimized to achieve $FA \leq 5\%$, after which the value of *HR* is maximized.

Section 2.3.1 shows the impact the different optimization schemes have on the forecast scores when applied to the M14 method at Cabauw.

2.3 Performance of the M14 Method at Cabauw

In this section, the results of applying the M14 method at Cabauw for 2015—2016 are presented for lead times up to 1, 3, and 6 h. The performance of the optimized criteria is presented first for the original four variables proposed by Menut et al. (2014), followed by the results of using the different variable combinations described in Appendix 1.

2.3.1 Optimized Performance for Different Lead Times

We applied the M14 method as outlined in Sect. 2.2.3 using the newly optimized threshold values as described in Sect. 2.2.5. First, we optimized the thresholds using the data from 2012—2014, subsequently using these optimized thresholds to generate forecasts for 2015—2016. The results are presented for lead times of 1, 3, and 6 h (Fig. 2.4). The performance of the original thresholds from Menut et al. (2014) and Román-Cascón et al. (2016a) at a lead time of 6 h are presented for reference. The optimized threshold values for each of the four variables of RH, Q_n, $\Delta T^{3\ h}_{1.5}$, and u_{10} for the different schemes are in Table 2.3.

The maxΔHR_{95} and maxΔFA^5 criteria show similar performance to their RC16 counterparts, as expected since the optimization constraints are essentially the same. At 6 h, the other optimizations, max*HR* and maxΔ, do not perform well, with either a false-alarm rate that is far too high (70%) despite $HR = 100\%$, or an overall higher false-alarm rate (18%) for a relatively low hit rate (just under 70%). However, re-optimizing with decreasing lead time, there is a distinct score improvement over the equivalent 6-h predictions. In the case of the thresholds optimized to obtain a high hit rate (max*HR* and maxΔHR_{95}), the false-alarm rate decreases by 10% by shortening to a 3-h window, and up to 40% for the 1-h window. Likewise, the hit

rate increases significantly for the optimizations that favour a lower false-alarm rate (maxΔ and maxΔFA^5). Again, there is a roughly 10% improvement at 3 h, and between 25–35% for the 1-h window.

It should be noted that the improvement in scores is not simply due to a change in denominator in Eqs. 2.3 and 2.4 (e.g., larger denominator for *HR*—more pre-fog—and smaller denominator for *FA*—fewer non-pre-fog—at 6 h than at 1 h), as this changes the score between just 0.1–5%. With the shorter lead time, all optimizations result in either > 90% of all events being captured with the false-alarm rate between 13–30%. Or, conversely, very few events falsely forecasted, with the hit rate over 75%. Compared to the original RC16-H and RC16-F thresholds, and the newly optimized thresholds at 6 h, this is a significant improvement.

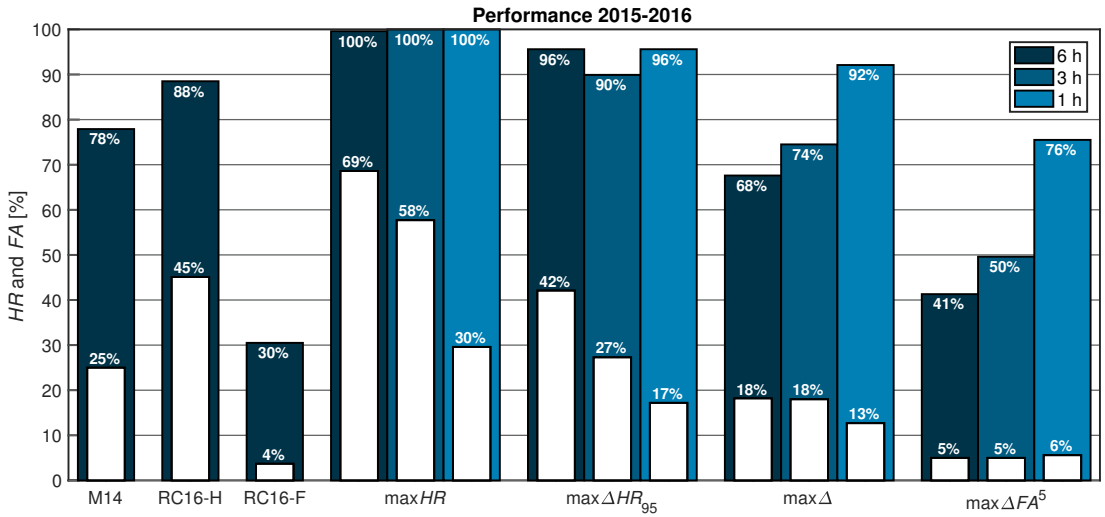

Figure 2.4: Hit rate (blue) and false-alarm rate (white) for pre-fog diagnosis between 2015–2016 using the original thresholds in Table 2.1, and thresholds optimized at 6-h, 3-h, and 1-h lead times according to the criteria described in Sect. 2.2.5. The optimized thresholds are in Table 2.3.

	Variable	Optimized Thresholds			
		maxHR	maxΔHR_{95}	maxΔ	maxΔFA^5
1 h	RH [%] $\geq$	89.4	93.1	94.1	96.6
	Q_n [W m^{-2}] $\leq$	6	-9	-19	-19
	u_{10} [m s^{-1}] $\leq$	2.2	2.0	2.0	1.4
	$\Delta T_{1.5}^{3h}$ [K] $\leq$	3.8	1.6	3.6	-1.1
3 h	RH [%] $\geq$	76.0	80.1	81.1	91.6
	Q_n [W m^{-2}] $\leq$	14	1	15	5
	u_{10} [m s^{-1}] $\leq$	3.4	2.0	1.9	1.3
	$\Delta T_{1.5}^{3h}$ [K] $\leq$	2.3	-0.5	-1.3	-2.3
6 h	RH [%] $\geq$	73.0	72.7	75.0	91.4
	Q_n [W m^{-2}] $\leq$	8	3	15	-25
	u_{10} [m s^{-1}] $\leq$	4.3	2.4	2.0	1.4
	$\Delta T_{1.5}^{3h}$ [K] $\leq$	7.1	2.9	-1.5	-2.1

Table 2.3: Optimized thresholds according to the different criteria in Sect. 2.2.5 for the three lead times tested.

Comparing the different optimization schemes for a given time window, it is apparent that *FA* values are initially more sensitive to stricter thresholds than *HR* values (by allowing for an incremental increase of risk, a larger increase in confidence is obtained; Fig. 2.5). In particular, accepting just a small drop in the hit rate (maxHR to maxΔHR_{95}), the false-alarm rate is immediately reduced by 10–30% (particularly for larger lead times). This suggests there are significantly more cases where it is marginally not fog than there are marginally fog. Interestingly, however, the maxΔFA^5 thresholds lead to roughly the same reduction in the hit rate as in the false-alarm rate from the maxHR optimization criterion (a drop of 20% at 1 h and 60% at 6 h).

The greatest compromise between a high hit rate and a low false-alarm rate is provided by the maxΔ optimization criterion at 1 h, providing $HR > 90\%$, and a false-alarm rate of just over 13%. It is, however, only marginally better than the maxΔHR_{95} optimization criterion, which is the best performer over all lead times. With a hit rate of 96% and false-alarm rate of 42%, it is the equivalent of RC16-H at 6 h. As the forecast window is reduced to 1 h, the hit rate is maintained while the false-alarm rate is reduced to just under 20%, which, while still far from ideal, is a reduction of over 50%.

Although significant improvements in predictive score can be achieved through employing shorter lead times and optimizing the thresholds to suit different needs, it is not possible to achieve a perfect score ($HR = 100\%$ and $FA = 0$). In the following sections, we investigate whether optimal performance can conceivably be achieved with the M14 method. First, alternative parameters are assessed (Sect. 2.3.2) in order to identify any potentially missing (local) factors in the methodology. The remaining reasons for false alarms are subsequently investigated in Sect. 2.4.

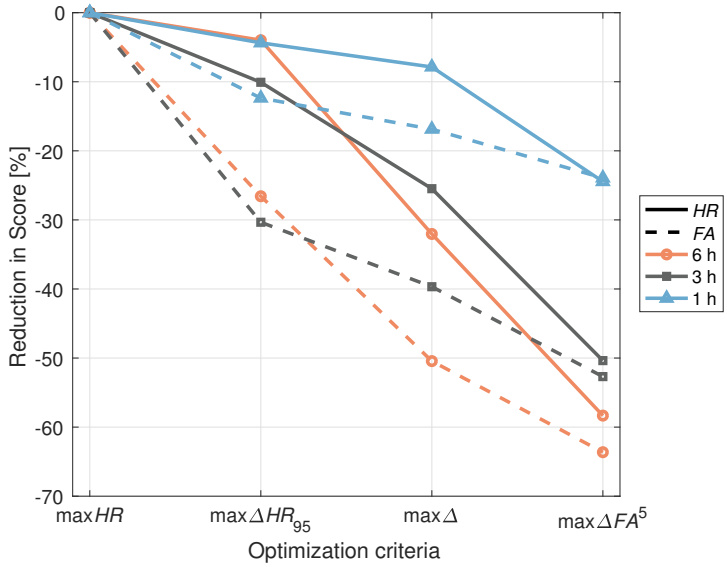

Figure 2.5: Reduction in hit rate (solid) and false-alarm rate (dashed) relative to the max*HR* criteria for increasing strictness of the thresholds (increased risk for increased confidence; left to right).

2.3.2 Other Variable Combinations

We tested a total of 31 variable combinations to determine whether additional or alternative parameters could be used to better diagnose radiation fog than the original four parameters of RH, Q_n, u_{10}, and $\Delta T_{1.5}^{3\ h}$ proposed by Menut et al. (2014). An overview of the different combinations is in Appendix 1.

Overall, none of the 31 other variable combinations resulted in a significant improvement in the scores; irrespective of the chosen variables, the optimization schemes result in nearly identical performance for most alternative combinations (Fig. 2.6). It is also not consistent for different optimizations and different lead times whether or not a combination leads to an improvement in the overall score.

For example, consider the inclusion of the modified fog stability index (FSI; see Table A1 #17 for the formula)—either in addition to the original variables, or in replacement of RH—at 10 and 200 m (FSI_{10} and FSI_{200}; 17-21 in Fig. 2.6). At best, the false-alarm rate is reduced by around 5%. While only a relatively small percentage, the 5% reduction is a significant decrease given the overall number of observations (a 5% reduction is equivalent to almost 2000 fewer false alarms). However, this is only the case for the max*HR* and maxΔHR_{95} criteria at 1 h, with no significant change at the other lead times or for the other optimization criteria.

Interestingly, dewpoint depression, which is a key component of the fog stability index, does not have a significant impact on prediction scores (8 and 9 in Fig. 2.6), nor does including other forms of vertical information, such as the temperature in-

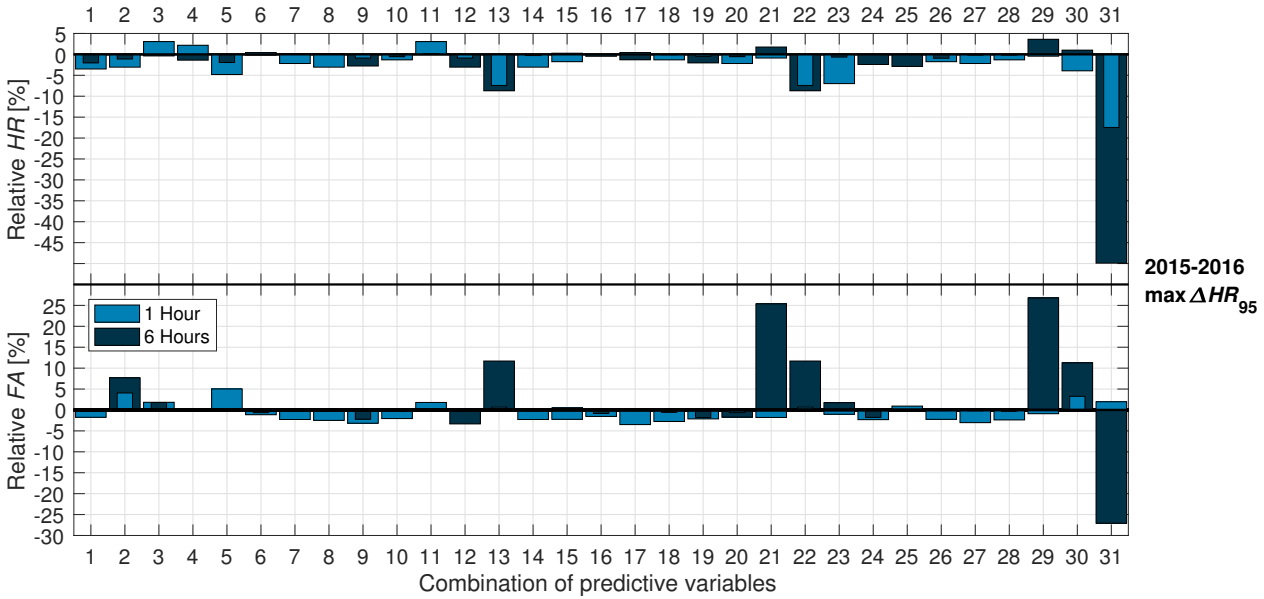

Figure 2.6: Relative hit rate (upper) and false-alarm rate (lower) for the maxΔHR_{95} pre-fog diagnosis between 2015–2016 at 1 h and 6 h for the different combinations of variables compared to the classical combination. The y-axis shows the difference between the scores with the alternative combination and the classical scores (i.e., relative $HR = HR_{alt.} - HR_{class.}$). The numbers on the x-axis correspond to the different combinations in Table A1.

version (14-16). Likewise, inclusion of further temporal information, such as the trend in relative humidity (24) makes no difference to the scores. The combinations proposed by Román-Cascón et al. (2016a) also do not lead to a significant change. In fact, they are slightly detrimental to the overall optimized scores at 1 h , with the prediction using u^* in replacement of u_{10} (2) leading to a drop in hit rate and increased false-alarm rate.

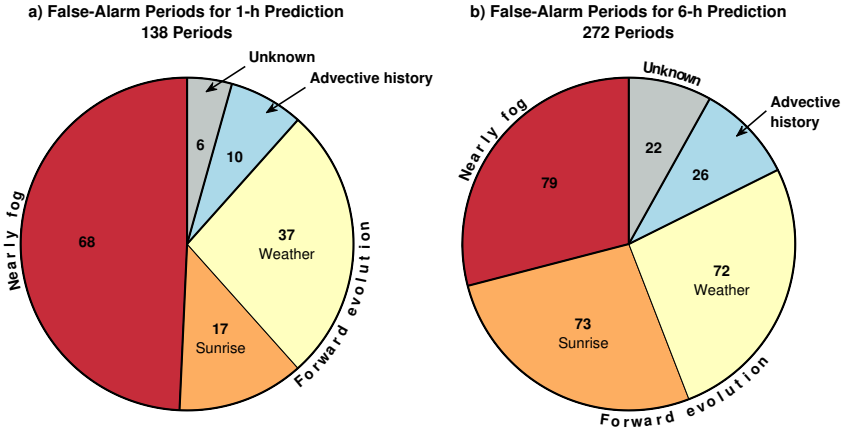

Figure 2.7: Total number of false-alarm periods manually classified according to the primary reason for the false alarm at both a) 1-h and b) 6-h prediction windows using the maxΔHR_{95}-optimized thresholds.

Some criteria sets are notably worse in performance than the classical prediction at 6 h . Sets 13 (adding RH_{10}), 21 (replacing u_{10} with FSI_{10}), 22 (including time to sunrise), and 29–31 (only predicting on FSI_{10}, FSI_{200}, or visibility) all result in either increased false-alarm rate or decreased hit rate at 6 h (between 10–50%). At 1 h, however, all but predicting on visibility alone (#31) result in similar scores compared to the original four-variable combination. Even still, visibility is not an entirely meaningless predictor at 1 h, with a hit rate as high as 80%.

2.4 Reasons for Remaining False Alarms

Even with optimization of the thresholds and reducing the lead time to 1 h, there is a maximum performance for the prediction methodology. A hit rate of 100% is possible, but at the cost of a false-alarm rate of roughly 20%, and even then, at only a 1-h lead time. Likewise, low false-alarm rates are attainable, but at significant cost to the hit rate. Here, we aim to identify the cause of the false alarms for the maxΔHR_{95}-optimized thresholds at 1-h and 6-h lead times.

Each false-alarm period was classified manually according to the observations during the period (Fig. 2.7). A false-alarm period is defined here as being continuously falsely diagnosed as pre-fog for at least 1 h in order to eliminate sporadic diagnoses. Periods where two or more variables are at the threshold level are also excluded from the analysis in order to avoid the influence of thresholds that are too relaxed. In total, there were 138 and 272 false alarm periods analyzed for the 1-h and 6-h prediction windows, respectively.

A large portion of the false-alarm periods (roughly 50% and 30% of the periods at 1 h and 6 h, respectively) are cases where the conditions are very close to being foggy, but are not quite foggy as observed at the 2-m level. These include cases where the

prediction is made too early (i.e. that fog does form, but after the prediction window) and situations where the visibility is below 1 km (or close to 1 km) for most of the false-alarm period, but never reaches the conditions required to be classified as a fog event. Note too that radiation fog may be very shallow. It is therefore possible that there is a shallow fog layer which does meet these conditions, but is not observed at 2-m height. Important to note is that the overall scores change little if a different, more relaxed definition is applied for the visibility (e.g., a threshold of 1.6 km as in Tardif and Rasmussen 2007).

The remaining false-alarm periods are divided according to three categories:

1. Forward Evolution of the System
   The M14 method is purely diagnostic based on recent observations (0-d in time), with no information about the future evolution of the system. This includes something as simple as the rising of the sun (more significant for the 6-h prediction) as well as a change in synoptic weather conditions. In total 54 out of 138 of the false-alarm periods for the 1-h prediction were due to changes to the system after the time the prediction was made, and 145 out of 272 of false-alarm periods for the 6-h prediction.

2. Advective History of the Airmass
   The method assumes that the local conditions are also representative of the upwind conditions (spatial influence), with the advection of an airmass with different properties (e.g., warmer or drier air of urban origin) making the conditions unfavourable for fog at a later time. 10 out of 138 false-alarm periods at 1 h, and 26 of the 272 periods at 6 h, were diagnosed as due to advection of unfavourable air properties (identified by changes in the termperature and/or humidity without a distinct change in wind speed, radiation, or turbulent mixing).

3. Unidentifiable from the Observations Alone
   Not all false alarms were obviously attributable to any cause based on the observations. These cases may include the exclusion of a key process in the prediction as well as the possibility of missed fog due to observational limitations (false false alarms; e.g., fog that is present, but too shallow to be captured at the lowest measurement level of 2-m height). This accounts for just 6 false-alarm periods for the 1-h lead time and 22 for the 6-h lead time.

An example of a false alarm caused by a change in the synoptic conditions is in Fig. 2.8, which shows visibility and u_{10} on the the nights of 9–10 and 10–11 April 2015. The two nights are neighbours in Fig. 2.2a with seasonal effects of temperature, solar radiation, and length of night (among other factors) roughly identical for the two days: both nights cooled around 15°C from sunset, with an initial dewpoint depression of around 10°C. The nocturnal evolution of the temperature inversion was approximately the same at the start of these “twin" nights, with low wind speeds (< 2 m s^{-1}), high relative humidity (increasing from 80% at sunset up to 100%), strong surface cooling ($\Delta T_{1.5}^{3\,h} < -4$ K), clear skies ($Q_n < -45$ W m^{-2}), and overall

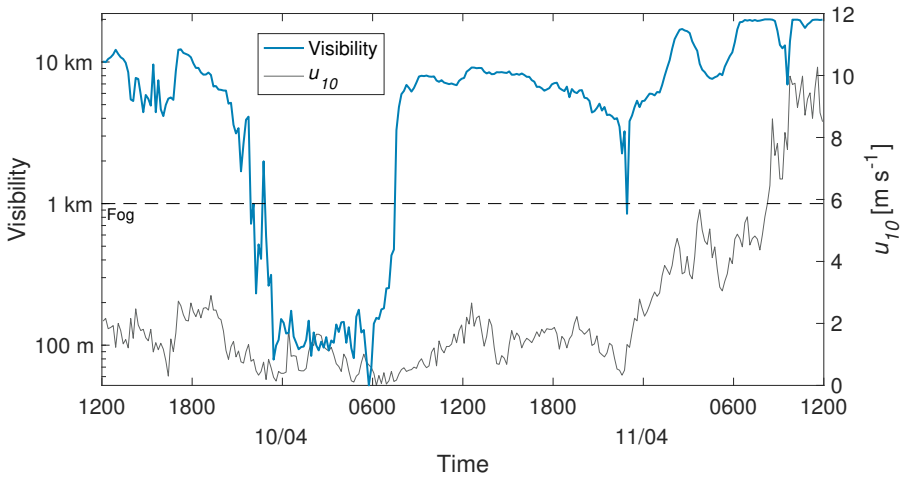

Figure 2.8: Visibility and wind speed for 48 h starting at 1200 UTC on 9 April 2015. Radiation fog formed on the first night, but not the second due to the increase in wind speed around 2300 UTC.

ideal conditions for radiation fog formation. Fog did indeed form on 9 April and last until sunrise on 10 April. However, just as fog was again about to form on 10 April, the wind speed increased as the result of a frontal system that passed through, making the conditions no longer favourable for fog formation. A diagnosis made up to 2300 UTC on both nights would, however, predict fog in the coming hours due to lack of information about the change in the system to come.

Including additional predictive variables that incorporate temporal information, however, does not lead to a reduction in the false-alarm rate. This was considered as part of the search for an additional predictive metric (Sect. 2.3.2), through including both the time before sunrise and the trend in atmospheric pressure, among others, with little change in the predictive scores.

The advection of warmer, drier air accounts for only a small fraction of the false-alarm periods assessed (10 and 26 periods for the 1-h and 6-h predictions, respectively), but is likely a contributing factor to the overall predictability and climatology of fog at Cabauw. The effect is most apparent when the nocturnal wind direction at Cabauw is considered (Fig. 2.9). The dominant (>50%) 10-m nocturnal wind at the CESAR facility is from the south to south-west and is the same for periods with high relative humidity (>90%) and low wind speed (<3 m s^{-1}). If there is no directional influence on the formation of fog at Cabauw, the distribution of winds preceeding fog events should be nearly identical. However, the distribution of winds for the subset of observations up to 6 h before a radiation-fog event is from predominantly the northward direction, with a correponding reduction in other directions, particularly from the south to south-west. In fact, situations where the flow originates from the north-west to north lead to fog almost twice as frequently as would be expected from the underlying distribution.

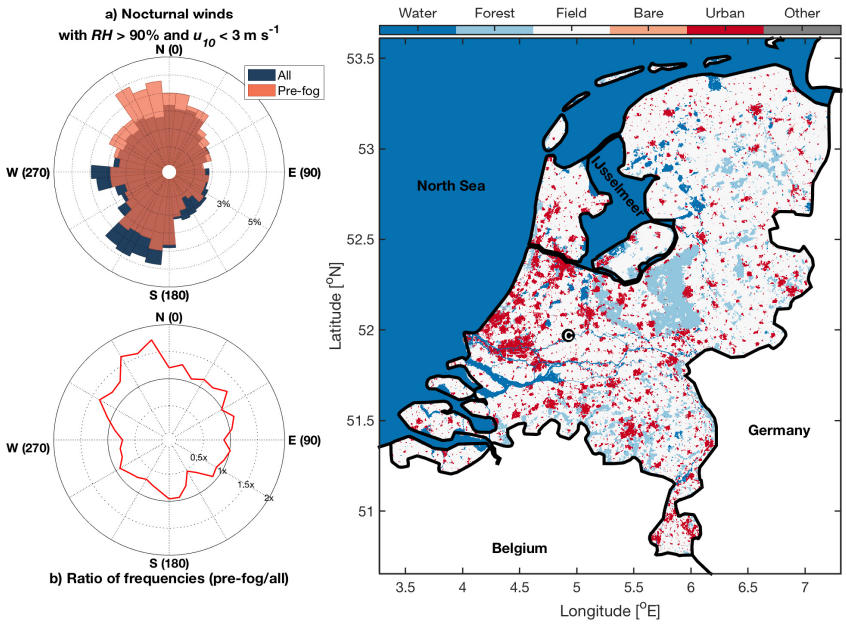

Figure 2.9: 300-m land use in the Netherlands in 2015 with a) the probability density function of observed nocturnal wind direction for conditions where $RH > 90\%$ and $u_{10} < 3$ m s^{-1}, as well as the subset that occurs up to 6 h before a radiation-fog event. b) The ratio of the probability density functions in a). The CESAR facility is marked on the map with the letter C in the black circle. Land use is from the ESA Climate Change Initiative (Hollmann et al. 2013) land cover dataset (accessible here: http://maps.elie.ucl.ac.be/CCI/viewer/index.php), broadly grouped into six categories.

While it is difficult to use point observations to assign a definitive reason for the reduction of the south to south-west peak in the distribution of observed winds that preceed radiation-fog events, we hypothesize that it is due to the history of an airmass prior to its arrival at Cabauw. When air travels from the north, it passes over predominantly flat agricultural land for several kilometres, in a region that is very similar to the Cabauw site, and with a lot of available moisture in the form of lakes and the North Sea and IJsselmeer. In contrast, the air that travels from the south to south-west must pass over more industrial regions (including the port city of Rotterdam) as well as over an embankment just south of the CESAR facility (leading to enhanced turbulent flow), and is also more likely continental air from the south.

This hypothesis is supported by the fact that the nights on which the wind is blowing from the south to south-west quadrant cool on average 2°C less than from the other directions. In many cases, this influence is excluded in the prediction with the threshold on $\Delta T_{1.5}^{3\ h}$, but not if a change in wind direction occurs throughout the night. It should be noted that this difference in distributions is not related to seasonal variability in the wind direction (even in autumn when fog is most common, the wind is predominantly from the south to south-west).

2.5 Discussion

2.5.1 Application of the M14 Method

We applied the M14 method at the CESAR facility to assess its predictive performance for the years 2015–2016 at both different lead times, and with different optimization schemes. In all, the methodology—comparing observations of specific variables to pre-determined thresholds—is straightforward to implement at the Cabauw site, with the results here showing the method provides valuable insight into whether or not a radiation-fog event is expected to occur.

Even at 6-h lead times, the two intermediate optimization schemes (maxΔ, and maxΔHR_{95}) lead to hit rates of approximately 70–95% and false-alarm rates of just 20–40% (Fig. 2.4). These optimizations favour a greater difference between hit rate and false-alarm rate, rather than necessarily attempting to maximize or minimize one of them, which would result in correspondingly high false-alarm rates (maxHR) or low hit rates (maxΔFA[5]) at 6 h. As the forecast window is decreased, however, the predictive capabilities of the M14 method are significantly enhanced for all optimizations. Optimizing to achieve the best hit rate (maxHR), for example, a hit rate of 100% is achieved with a 6-h prediction window, but with a false-alarm rate of 70%. With a reduced forecast lead time of 1 h, the false-alarm rate drops to just 30%. Overall, this significant improvement in the forecast score is encouraging and, depending on the needs of the user, may serve to offset the reduced lead time.

A similar effect is seen with stricter optimization constraints (Fig. 2.5). Whether a 6-h, 3-h, or 1-h lead time, accepting a small degree of risk in the form of a reduced hit rate immediately results in a significant increase in confidence of the prediction (i.e., reduced false-alarm rate). For example, the false-alarm rate is reduced by two to five times as much as the hit rate when comparing the results using the maxHR and the maxΔHR_{95} criteria. The relative reduction in FA and HR values is related to the parameter space of the observed variables for fog and non-fog events. Initially, as the thresholds become stricter, proportionally more non-fog events are excluded than fog events, resulting in the larger reduction in FA values than HR values. Eventually, the thresholds enter into the parameter space where most fog events occur, with further strictening of the thresholds leading to the exclusion of a large number of fog events and the subsequent reduction of the HR value.

It should be noted, however, that even with a reduction in the false-alarm rate, there is still a significant amount of false predictions. This is hidden in the calculation of FA values, with the total number of false alarms divided by the total number of observations which are not pre-fog (see Eq. 2.4). Although a false-alarm rate of 13% from the maxΔ optimization at 1 h, for example, appears reasonable, there are almost seven times as many non-fog obervations as there are pre-fog obervations, meaning that roughly 50% of all predictions of fog are false. This is an improvement on the 6-h prediction, but is still a concern when applying the methodology.

In an effort to reduce the false-alarm rate further, we tested 31 additional variable combinations as alternatives to the original combination of variables proposed

by Menut et al. (2014). None of the combinations, which include soil heat flux and vertical information, lead to any significant improvement in the prediction scores, or in fact any consistent change at different lead times or for different optimizations. This is most likely due to the interdependence of many of the variables (for example, dewpoint depression and relative humidity are essentially measuring the same thing), suggesting that any combination that measures the saturation, the atmospheric stability, and the cooling are sufficient for the methodology. This is a helpful insight when considering the application of the methodology at different sites. Although the original four variables chosen are commonly measured at meteorological stations, the fact that they can be interchanged with complementary observations means the method is even more portable.

The amount and type of aerosols present could not be considered in the analysis. Such data are limited in temporal coverage at Cabauw, and only at a height of 60 m, which does not correspond to the surface observations here. As such, direct analysis during the fog events considered here is not tractable. Aerosols are critical for fog formation, however, with hygroscopic particles acting as condensation nuclei for water droplets. Without them, much higher saturation relative humidities must be achieved. Boers et al. (2015) also indicated that decreasing hygroscopicity of aerosols in the Netherlands is correlated with a decrease in the occurrence of fog events at Cabauw. It may be that some false-alarm periods correspond with times of low aerosol content, or the presence of aerosols with reduced hygroscopicity. It would be enlightening to perform a dedicated observation campaign where particle counts and hygroscopicity can be measured in order to determine what impact they have on the prediction results.

Although the events are filtered such that they last for at least 2 h (and are therefore fully established as in Román-Cascón et al. 2016a), it should be noted that the method does not explicitly distinguish between the severity of different fog events (e.g., in terms of depth of the fog layer, or the minimum visibility). The hazard presented by a fog event is due to the reduction in visibility, with different modes of transportation able to better overcome this than others. Airplanes, for example, are higher off the ground when taxiing, and fly through low cloud at takeoff and landing, which is very different than a car driving down a highway. This means what is dangerous on highways is very different than what is dangerous at airports. Further study is needed to determine what results in thicker and deeper fog layers.

2.5.2 Reasons for False Alarms

One of our aims was to identify the reasons for false alarms when employing the M14 method. In Sect. 2.4, false-alarm periods lasting at least 1 h when using the $\max\Delta HR_{95}$ criteria were manually assessed in order to identify a reason for the lack of radiation-fog formation despite the threshold criteria being met. In total, 138 periods were identified for the 1-h, and 272 periods for the 6-h prediction windows (Fig. 2.7). Ultimately, it appears it is the lack of spatio–temporal information included in the method that limits its performance.

A large portion of the false-alarm periods are when the conditions are very close to—but not quite—fog events according to the definitions employed here (including predictions that are made too early, or when conditions are not sustained long enough to be classified as an event). The higher occurrence of “nearly fog" cases at the 1-h prediction window than the 6-h window is due to the conditions under which radiation fog occurs being much more definite at a shorter lead time (corresponding with the decrease in spatio–temporal false alarms). These borderline cases are less serious false alarms as they still represent periods of risky, reduced visibility conditions, in contrast to cases which are fully clear in spite of the pre-fog diagnosis. It would be interesting to explore such borderline situations further, where sensitivity to environmental parameters is likely high, but that is beyond the scope of this research.

While near-fog cases are mostly the result of the definition of fog events assessed, the remaining false-alarm periods are primarily due to the lack of temporal and spatial information encoded in the methodology. The M14 method is almost entirely zero-dimensional: a prediction is made at a single time and location based on the observations at that given time and location. As such, the method does not consider the possibility of the system evolving in time due to spatial and temporal influences. Three primary reasons for these non-local spatio-temporal causes for false alarms were addressed here: sunrise, synoptic weather/internal dynamics, and, related, the advective history of the airmass.

The so-called forward influences (in time) of sunrise and weather influences result in unfavourable local conditions after the prediction has been made (e.g., increased net radiation or wind speed as in Fig. 2.8). The influence of sunrise is particularly significant for the 6-h forecast window, where 6 h may be much longer than half the night. As such, there is a greater likelihood that the sun will rise before fog conditions are reached. Including time to sunrise as a predictive variable does not, however, lead to improved prediction scores (#22 in Fig. 2.6), instead resulting in increased *FA* values, and decreased *HR* values. At both the 1-h and 6-h prediction windows, the influence of weather (such as clouds and fronts) on the false alarms is approximately the same, indicative of the more random passage of such systems, as opposed to the very definite rising of the sun.

In addition to assuming a temporal stationarity, the method also inherently (and by necessity) assumes that the observations are representative of not only the current local conditions, but also the upwind conditions. However, if the upwind conditions are drastically different than the local conditions—say, for example that there is a city upwind where the air is warmer and relative humidity lower—then the predictions made at a given location may not be valid. Even though wind speeds are relatively low in the event of radiation-fog formation, an airmass propagating at a wind speed of just 3 m s^{-1} can travel approximately 10 km in the space of 1 h. That means any prediction made at a given time could potentially be on a parcel of air with entirely different properties than the upwind parcel that will be at the prediction location just a short time later.

Figure 2.9 shows that nocturnal winds with high relative humidity ($RH > 90\%$)

and low wind speed ($u_{10} < 3$ m s^{-1}) are more likely to lead to fog if they originate from the north-west to north than any other direction. This is in direct variation to the underlying distribution of winds, which are more common from the south to south-west. Including wind direction as a further predictive variable, however, would not lead to an improvement in prediction scores at the CESAR facility. As the radiation-fog events are not restricted to a single well-defined direction, but merely indicate a preference for a wind direction, to do so would result in a large number of missed pre-fog cases. While upwind influences do not result in a significant portion of false-alarm periods diagnosed here for Cabauw (Fig. 2.7), the analysis indicates that the broader land surface heterogeneity can play a role in the formation of localized fog events. This suggests that the localized picture of the factors influencing radiation fog is not entirely accurate. It is conceivable that in regions with larger variability than Cabauw, such as near cities or airports, such an effect may be further enhanced.

It is also possible that the relationship of wind direction is not entirely landscape-based, but related to overall circulation patterns. In particular, the sea-breeze transition described by Arrillaga et al. (2018) could be a compounding factor, with moist, aerosol-rich air coming from the sea leading to the enhancement of fog likelihood. A larger climatology of events would be needed to study such cases, however, as the number of events identified by Arrillaga et al. (2018) is small. Further analysis is beyond the scope of this work.

In some cases, a definitive reason for a false-alarm period could not be easily determined from the observations alone. However, we hypothesize two reasons for such cases which are related to observational restrictions. The first is that there is a critical variable which has not been considered. As shown in in Sect. 2.3.2, 31 variable combinations were tested in addition to the original four key variables proposed by Menut et al. (2014). These resulted in little change in overall optimized performance of the prediction method, but it is possible that some further factor is not considered. Aerosols—or the lack thereof—as discussed above, could prove important for marginal cases where conditions appear right for fog formation, but cannot form without appropriate condensation nuclei.

It is also possible that there is fog present, but it is too shallow, or too patchy, to be captured by the single-point observations at 2-m height. It is not uncommon, for example, to see shallow fog layers (see Fig. 2.10), or to drive along a road at night and suddenly encouter a patch of fog drifting across the road. Such conditions have also been demonstrated numerically, with high-resolution simulations of fog at the Charles de Gaulle Airport in Paris demonstrating the role heterogeneous land surfaces play in the resulting formation of heterogeneous fog (Philip et al. 2016). In this case, it is not necessarily a false alarm in the strict sense as there is still fog present, just not observed (a false false alarm). Of course, there is no way to investigate the full influence of such effects on the predictions made here with the available point observations, but it does pose interesting questions that should be considered in future observational campaigns and analysis, with high-resolution observations in this missed layer. While such events are perhaps not as hazardous as deep, thick fog cases, the presence even of shallow or sparse fog can be dangerous, particularly

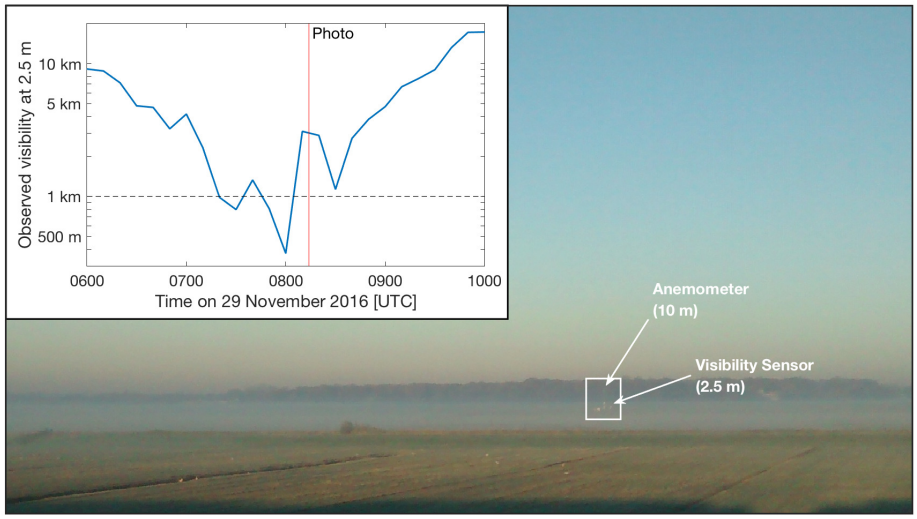

Figure 2.10: A dissipating shallow fog layer on the morning of 29 November 2016. A weather station can be seen (in the white rectangle), with the visibility sensor above the shallow fog layer and therefore not observing foggy conditions at the time of the photo (inset). The distance to the weather station is approximately 700 m, and 1.3 km to the tree line from the camera.

for automobile traffic. Likewise, understanding cases of shallow or patchy fogs, and whether or not they continue to develop into thicker, deeper fog layers is important for understanding the full lifecycle and evolution of fog events.

Although the false-alarm periods are presented as being due to the influence of one dominant factor, it should be noted that they are in reality the result of concurrent factors. For example, it will take longer for fog to form with reduced aerosol content and when air upwind is warmer, resulting in slower cooling locally. Given the extended period of time before sufficient cooling and condensation has occurred for fog to form, a frontal system or sunrise will have been more likely to break down the favourable conditions for formation. As such, the identification of these factors may be viewed as the final factor in leading to the false alarm (e.g., if there was no sunrise there could still be fog, just later in time), and seen as more of a qualitative assessment rather than robust quantitative analysis.

2.5.3 Practical Implications

Implications for Modelling

Our findings were not tested against numerical models, however, the results do present challenges for simulations of fog. For example, we show that models will need to not only capture the localized conditions (and accurately model the local surface characteristics), but also factors on a range of scales. For example, upwind

heterogeneity in surface properties may be important for the formation of local fog, but how much of this heterogeneity needs to be considered within a model? This is unclear and will likely depend on the regional variability of the simulation domain. At the same time, large-scale weather patterns have to be included. This conflict of scales, from highly localized to synoptic, may be best achieved through a nesting approach. Such an approach could, for example, be employed for specific regions of interest such as airports, where numerical studies have shown high horizontal and vertical resolution are needed to capture the influence of land surface heterogeneity induced by buildings and runways (Bergot et al. 2015; Philip et al. 2016). Yet, nesting remains a challenge. In fact, Steeneveld et al. (2015) have demonstrated nesting could potentially prove destructive to fog simulation, rather than constructive.

Both Menut et al. (2014) and Román-Cascón et al. (2016a) also assessed the performance of the M14 method using numerial output. In both cases, the model did not accurately capture the necessary conditions needed for fog to form, resulting in poor predictive capabilities. This is due to the difficulty in correctly capturing the local characteristics within the model (such as surface coupling, turbulent mixing, etc.), which is a common problem when performing fog simulations (e.g., Steeneveld et al. 2015) and a factor which has been shown important for the lifecycle of fog in sensitivity studies (Maronga and Bosveld 2017). It is possible that including more information on local land surface and improving horizontal resolution may improve results.

Vertical resolution of the models is also important. For example, Tardif (2007) and Maronga and Bosveld (2017) showed that sufficient resolution is needed to properly capture the evolution of fog. This is also important for capturing the initial growth phase of fog from the surface. The lack of near-surface observations, however, could make validation of such models difficult.

Operational Application of the M14 Method?

The M14 method is useful as a diagnostic tool, however, its limitations as discussed here must always be considered. As such, it is best viewed as a supplementary tool, rather than the sole tool for fog prediction.

Nevertheless, assessing the performance of different optimization schemes at different lead times provides insight into how the M14 method can be used in an operational setting. Depending on the needs of the user, a first prediction can be made at 6 h, which is useful for preparedness, but may not yet be critical. At this point where operations are not yet being adjusted, for example, overprediction may in fact be useful. With subsequently decreasing lead time, the confidence of the prediction—regardless of the optimization method—improves significantly.

An example of this application using the $\max\Delta HR_{95}$ threshold set is as follows. With a 6-h window, a diagnosis is made based on current observations that is expected to capture 96% of the events, though with a known over-prediction with $FA = 42\%$ (Fig. 2.4). Those in charge of adjusting operations or producing warnings are now aware that an event is possible, but may not need to react. A shorter

forecast window is then used to update the initial prediction, maintaining roughly the same hit rate, but now with increased confidence; the false-alarm rate is reduced by 15% at 3 h. By the 1-h prediction window, the prediction is over twice as certain as it was at 6 h, and operations can now be adjusted and warnings issued accordingly, in conjunction with other information received through the use of a numerical forecast and the forecasters' experience and knowledge.

2.6 Conclusions

Using observations from the CESAR facility in the Netherlands, we assessed the performance of the statistical method for diagnosing the onset of radiation-fog events developed by Menut et al. (2014). Our goals were: to determine the influence of different lead times on the forecast; to test the role of different optimization schemes and the potential for improved prediction through consideration of additional variables; and to identify reasons for false alarms.

Even at a lead time of up to 6 h, the M14 method is a useful diagnostic tool that can provide a hit rate of over 90% and a false-alarm rate under 40%. With decreasing lead time, we have shown that the method becomes increasingly more accurate for prediction, with the false-alarm rate being cut in half or the hit rate doubled. The significantly improved accuracy may help to offset the reduced benefit from shortened lead times depending on the needs of the user. In any case, the performance at reduced lead times encourages its use as a diagnostic now-casting and monitoring tool over short time periods.

We tested four different optimization schemes focused on different needs that balance confidence and acceptable risk, demonstrating the versatility of the M14 method to be tuned and applied for different applications. Accepting just a slight decrease in the hit rate (increased risk) leads to a significant reduction in the false alarm rate (increased confidence). This is an important and beneficial implication for implementation of the method in an operational setting.

In assessing the reasons for false alarms, 45–65% were attributed to either the forward temporal evolution of the system (changes in the weather conditions, for example), or the advection of warmer, drier air from upwind. Both spatio–temporal factors cannot be fully eliminated with the purely local method (in both space and time) and must be considered when employing the methodology. This also presents a potential challenge for numerical simulation of fog events, with a competing need to capture large scale influences (such as synoptic weather) and increasingly localized influences (e.g., land surface coupling and heterogeneity). In an effort to reduce the spatio–temporal false alarms using the M14 method, it would be interesting to assess the impact of supplementing the observations with numerical output from a synoptic weather model, or even a simple statistical regression model; both of which may help to provide an indication of the large-scale system evolution.

Further study should include seeking to understand the role of vertical growth of the fog layer both at the near-surface and toward deeper, thicker fogs; the influ-

ence of non-local heterogeneity on local fog formation; and the role aerosols play in determining whether or not fog events will occur. Further, the methodology should continue to be evaluated at different sites where local land use and climatology are different than at Cabauw. Finally, it would also be beneficial to explore similar diagnostic methodologies related to other fog types beyond radiation fog, which is the exclusive focus of the M14 methodology.

2.A Other Variable Combinations

In addition to the combination of four variables proposed by Menut et al. (2014)—here referred to as “Classic"—we tested a further 31 combinations where additional variables are either added to the set of predictors, or used in replacement of the original variables. They are summarized in Table 2.4 on the following pages.

Identifier	Description
Additional Near-Surface Information	
1. $+u^*$	Friction velocity must be low (no turbulence) for fog formation (as proposed by Román-Cascón et al. 2016a)
2. $-u_{10}+u^*$	Replace 10-m wind speed with the friction velocity (as proposed by Román-Cascón et al. 2016a).
3. $+G_0$	Soil heat flux. Should be low or negative.
4. $+\lvert H_0\rvert$	Absolute value of the sensible heat flux. Should be close to 0. (no turbulence).
5. $+[MSHF-H_0]$	Compare the *maximum sustainable heat flux* of van de Wiel et al. (2012a) to the sensible heat flux. Should be small positive, or negative.
6. $+\min u_{10}$	A minimum threshold on the wind speed (air should not be completely stagnant)
7. $+\min Q_n$	A minimum threshold on the net radiation. (Fig. 2.2d shows fog does not form when net radiation is too low, likely indicative of the available moisture)
8. $+[T-T_D]$	Dewpoint depression (difference between air and dewpoint temperatures at 1.5 m). Should be close to 0 or negative.
9. $-RH+[T-T_D]$	Replace relative humidity with the dewpoint depression.
10. $+[T_{1.5}-T_{0.1}]$	Difference in air temperature at 1.5 m and 0.1 m. Should not be too great or dew/frost formation may remove moisture and/or fog will be too shallow.
11. $+[T_{1.5}-T_{Soil}]$	Difference in air temperature at 1.5 m and soil temperature at -0.02 m.
12. $+P_{atm}$	Include atmospheric pressure at the surface. High pressure favourable.

Identifier	Description
Additional Vertical Information	
13. $+RH_{10}$	The 10-m relative humidity cannot be too low, otherwise entrainment of dry air from above could disrupt fog formation.
14. $+\Delta\Theta_{10}$ 15. $+\Delta\Theta_{200}$	Include the temperature inversion between 1.5–10 m and 1.5–200 m. A stronger inversion is favourable due to increased stability of the surface layer.
16. $-\Delta T_{1.5}^{3\ h} + \Delta\Theta_{200}$	Replace the temperature trend with the temperature inversion between 200 and 1.5 m.
17. $+FSI_{10}$ 18. $+FSI_{200}$	A modified *fog stability index* calculated at 10 and 200-m height (as opposed to 850 hPa; Holtslag et al. 2010): $FSI_z = 2(T - T_D) + 2(T - T_z) + u_z$. Low values ($\leq 31$) are favourable.
19. $-RH + FSI_{10}$ 20. $-RH + FSI_{200}$	Replace relative humidity with FSI_{10} and FSI_{200}.
21. $-u_{10} + FSI10$	Replace 10-m wind speed with modified FSI_{10}.
Additional Temporal Information	
22. $+[t_{sun} - t]$	Time to sunrise. Should not be too close to rising sun, otherwise conditions will no longer be fog-favourble (increased radiation, warming, decreased relative humidity).
23. Mean 1 h	Apply thresholds on the mean value of the classic variables over the past 1 h.
24. $+\Delta RH_{1.5}^{3\ h}$	Analogous to $\Delta T_{1.5}^{3\ h}$, the relative humidity at 1.5 m must not be decreasing significantly over the previous 3 h.
25. $+\Delta V_2^{1h}$	The visibility at 2 m must be decreasing over the previous 1 h (as proposed by Román-Cascón et al. 2016a)
26. $+\Delta P_{atm}^{3h}$	Change in atmospheric pressure over 3 h. Should not decrease significantly (worsening of synoptic conditions).
27. $+Precip_{24}$ 28. $+Precip_{48}$	Total precipitation in previous 24 h or 48 h. Indicator of soil moisture.
Single Variables	
29. Only FSI_{10} 30. Only FSI_{200}	Only predict on FSI_{10} or FSI_{200}, which include dew point depression and wind speed.
31. Only V_2	Only predict based on the visibility at 2 m

Table 2.4: The 31 other combinations of variables tested beyond the original four variables of Menut et al. (2014). + denotes an addition to the classical variables while − indicates one of the original variables is replaced (except when in [ ]).

Chapter 3

Missed Fog?

On the potential of obtaining observations at increased resolution during shallow fog events.

> . . . a thin streak of white mist . . . seemed to have a sentience and a vitality of its own.
>
> B. Stoker, *Dracula*

Summary

Conventional in situ observations of meteorological variables are restricted to a limited number of levels near the surface, with the lowest observation often made around 1-m height. This can result in missed observations of both shallow fog, and the initial growth stage of thicker fog layers. At the same time, numerical experiments have demonstrated the need for high vertical grid resolution in the near-surface layer to accurately simulate the onset of fog; this requires correspondingly high-resolution observational data for validation. A two-week field campaign was conducted in November 2017 at the Cabauw Experimental Site for Atmospheric Research (CESAR) in the Netherlands. The aim was to observe the growth of shallow fog layers and assess the possibility of obtaining very high-resolution observations near the surface during fog events. Temperature and relative humidity were measured at centimetre resolution in the lowest 7 m using distributed temperature sensing. Further, a novel approach was employed to estimate visibility in the lowest 2.5 m using a camera and an extended light source. These observations were supplemented by the existing conventional sensors at the site, including those along a 200-m tall tower.

This chapter has been published as:

Izett JG, Schilperoort B, Coenders-Gerrits M, Baas P, Bosveld FC, van de Wiel BJH (2019) Missed Fog? On the potential of obtaining observations at increased resolution during shallow fog events. Boundary-Layer Meteorol, doi:10.1007/s10546-019-00462-3

Comparison between the increased-resolution observations and their conventional counterparts show the errors to be small, giving confidence in the reliability of the techniques. The increased resolution of the observations subsequently allows for detailed investigations of fog growth and evolution. This includes the observation of large temperature inversions in the lowest metre (up to 5 K) and corresponding regions of (super)saturation where the fog formed. Throughout the two-week observation period, fog was observed twice at the conventional sensor height of 2.0 m. Two additional low-visibility events were observed in the lowest 0–0.5 m using the camera-based observations, but were missed by the conventional sensors. The camera observations also showed the growth of shallow radiation fog, forming in the lowest 0.5 m as early as two hours before it was observed at the conventional height of 2.0 m.

3.1 Introduction

Fog—defined as a surface cloud where visibility is less than 1 km (NOAA 2005)—presents a hazard for human navigation, affecting all modes of transport (e.g., Fu et al. 2010; Bartok et al. 2012; Huang and Chen 2016). Accurate monitoring and timely forecasts for low-visibility situations are therefore critical for ensuring the safety of travellers and continuity of commercial operations. Forecasts of fog, however, struggle to accurately predict the timing and severity of fog events (e.g, Steeneveld et al. 2015).

Previous studies (e.g., Tardif 2007; Maronga and Bosveld 2017) have shown that increased vertical grid resolution (as fine as sub-metre) near the surface is important for accurately capturing the onset and duration of fog events in numerical simulations, particularly in heterogeneous locations, such as at an airport (Bergot et al. 2015). Observations with similar sub-metre resolution are therefore necessary for validation of such efforts in this near-surface layer. However, typical observations, such as at the ParisFog site in France (Haeffelin et al. 2010) and the Cabauw Experimental Site for Atmospheric Research (CESAR) in the Netherlands (Monna and Bosveld 2013) are limited in their vertical resolution to point observations, with only one or two sensors in the lowest 10 m. Increased observational resolution would allow for both improved numerical validation, and a greater understanding of near-surface processes that need to be included in models.

Obtaining higher-resolution observations near the surface is particularly important for radiation fog, which is formed predominantly as the result of radiative cooling of the surface during weak-wind, clear-sky nights (e.g., Duynkerke 1991; Gultepe et al. 2007). Conventional visibility sensors located above 1-m height may miss shallow layers of fog, and the initial growth of radiation fog from the surface, such as in Fig. 3.1, where a growing radiation fog layer is missed by the conventional sensor located at a height of 2.0 m. Even more challenging to capture with traditional measurement techniques, Fig. 4 and the accompanying videos of Mahrt (2014) show the vertical and temporal heterogeneity in fog layers. When assessing the performance of forecasts, the possibility of missed fog also becomes important (e.g., Izett

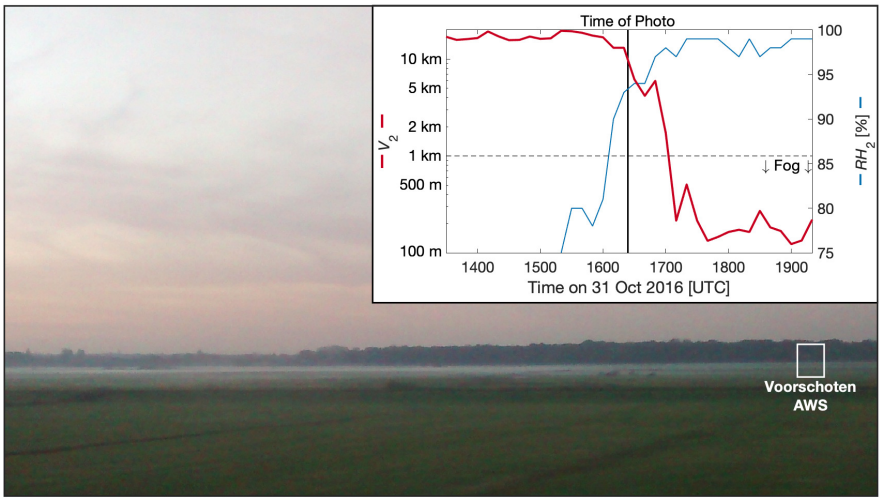

Figure 3.1: Shallow radiation fog forming at 1620 UTC on 31 October 2016 near Voorschoten, the Netherlands. Observations from an automatic weather station (AWS) of relative humidity (RH) and visibility (V) at 2.0-m height do not show the presence of the fog layer (visibility $<$ 1 km) until almost one hour after the photo was taken (inset). From the camera, the distances to the weather station and tree line are approximately 700 m, and 1.3 km, respectively.

et al. 2018c), with the potential for “false alarms" to be incorrectly diagnosed when shallow fog is present, but unobserved. At the same time, a better understanding of the conditions under which fog forms and deepens is needed, and the extent to which the near-surface plays a role is also unclear. Increased observational resolution that captures such shallow and growing events will lead to improved prediction and understanding of how these shallow fog layers form and grow from the ground upward. As it stands, conventional point observations of temperature and relative humidity are unable to fully resolve the large near-surface vertical gradients present under fog-forming conditions.

Two techniques are used in order to obtain observations in the near-surface layer at higher resolution than the conventional sensors. To measure temperature and relative humidity, we employ distributed temperature sensing (DTS; Sect. 3.2.2). Providing high spatial and temporal resolution, DTS has been successfully employed to determine surface temperature and soil heat fluxes (Bense et al. 2016), the radiative skin effect at the surface of water bodies (Solcerova et al. 2018), the Bowen ratio (Euser et al. 2014; Schilperoort et al. 2018), near-surface turbulent fluxes and dynamics under varying stability (e.g., Thomas et al. 2012), and wind speed (Sayde et al. 2015; van Ramshorst et al. 2019). It has even been combined with UAV technology to observe the morning boundary-layer transition from stable to unstable conditions (Higgins et al. 2018). Unlike conventional techniques, DTS is able to resolve steep gradients (e.g., Zeeman et al. 2015), making it particularly attractive for studies of the stable boundary layer. Using DTS, shallow cold pools have been

observed at high resolution (Thomas et al. 2012; Zeeman et al. 2015), which may be favourable for radiation fog formation. Hilgersom et al. (2016), however, found that the presence of fog can lead to elevated DTS temperatures of up to 0.7°C when compared to conventional temperature measurements. Likewise, whereas daytime measurements are prone to errors due to solar radiation (e.g., Schilperoort et al. 2018), under clear-sky, weak-wind conditions—as are favourable for radiation-fog formation—errors can also occur. For example, radiative cooling of the fibre and the influence of the support structures become more significant for DTS temperatures than when other energy sources are dominant (e.g., Hilgersom et al. 2016; Sigmund et al. 2017). The performance of the DTS technique needs to be further tested in order to ensure its reliability under stable, foggy conditions, with the present study serving to encourage future research.

High-resolution temperature and relative humidity measurements alone are not enough to observe the growth of shallow fog layers, which are identified by a reduction in visibility. To obtain higher spatial resolution than is offered by the conventional senors, methods have been previously developed to obtain visibility estimates from camera images using a range of image processing techniques (e.g., Bäumer et al. 2008; Pokhrel and Lee 2011; Kim 2015; Chaabani et al. 2017). Such methods allow for large spatial coverage by utilizing existing camera networks (such as are commonly found along highways and at airports) in a relatively efficient and inexpensive manner (e.g., Hautiere et al. 2008; Babari et al. 2012). Likewise, images are able to provide information on local heterogeneity, such as would accompany a shallow or patchy fog layer. However, the existing methods require ambient light, essentially restricting their applicability to daylight hours. Here, a simple methodology is presented for obtaining higher resolution estimates of visibility from cameras during the night using an artificial light source (see Sect. 3.2.3 and the Appendix).

An overview of the experimental set-up is presented in Sect. 3.2, with the results of the observations, including a validation of the increased resolution observations against their conventional counterparts, presented in Sect. 3.3. A discussion follows in Sect. 3.4, with future high-resolution studies encouraged.

3.2 Experimental Set-Up and Methods

3.2.1 Set-Up

The experiment was conducted at the CESAR facility (e.g., Monna and Bosveld 2013) located near Lopik in the province of Utrecht, the Netherlands (51.971 °N, 4.927 °E). The CESAR facility is operated by the Royal Netherlands Meteorological Institute (KNMI) and a consortium of research institutes and universities. It is surrounded by predominantly agricultural fields and small waterways. The primary feature at the CESAR facility is the 213-m tall instrument mast (referred to as the tower), which supports instruments that measure the vertical profiles of various meteorological variables. We use 10-min averaged values of air temperature (converted to potential temperature at the measurement height), relative humidity, wind speed,

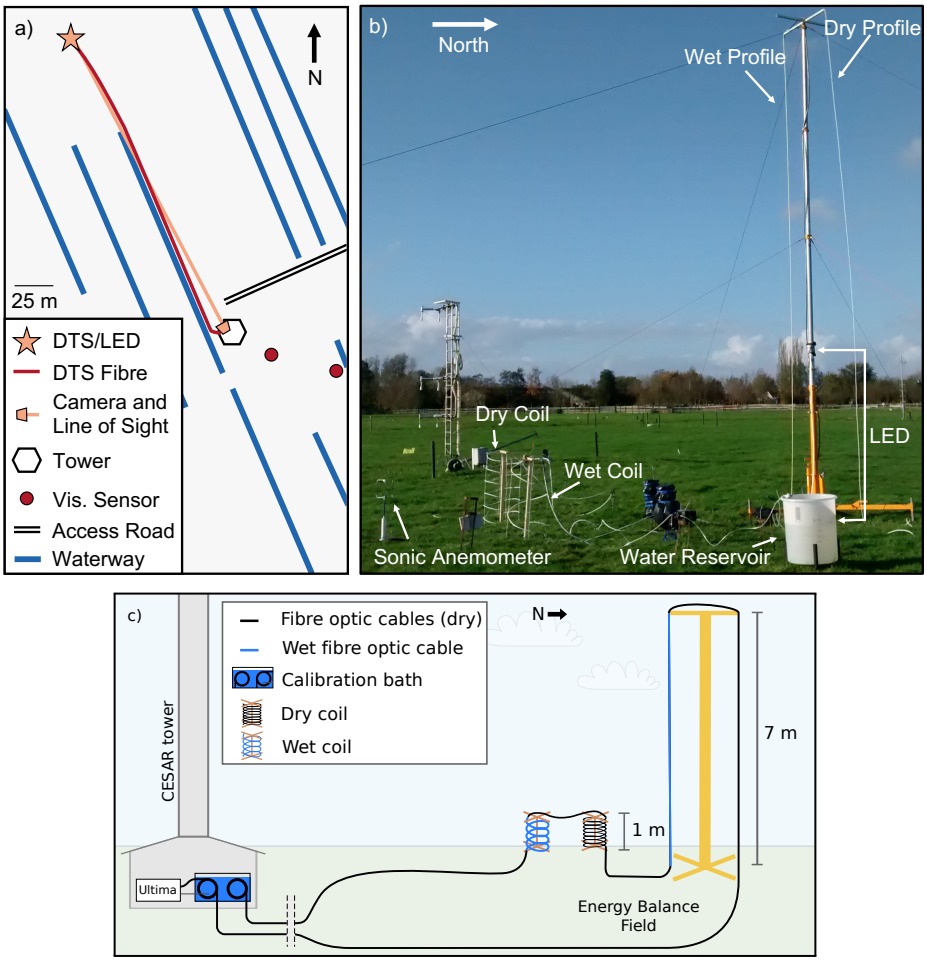

Figure 3.2: a) Map, b) photograph, and c) schematic of the experimental set-up.

and visibility. Air temperature is measured at eight heights: 0.1 m, 1.5 m, 10 m, 20 m, 40 m, 80 m, 140 m, and 200 m. Likewise, relative humidity is measured at the same heights 1.5 m and above, while wind speed is measured with cup anemometers at and above 10 m. There are two visibility sensors (Biral SWS-100; Fig. 3.2) located at 2.0-m height, followed by the six measurement heights above. Surface atmospheric pressure and components of the surface energy balance (e.g., shortwave and longwave radiation) are also available from the KNMI at the Cabauw site as 10-min averages. Data from the site are publicly and freely available through the KNMI data centre (https://data.knmi.nl/datasets?q=CESAR). For simplicity, we refer to the observational data from the existing instruments at the site as the “KNMI observations” throughout.

The experimental set-up was placed in what is known as the “energy-balance field", located approximately 200 m north of the tower (Fig. 3.2a). In this area, the

grass is maintained short (approximately 0.1 m at time of experiment, though with some variability in height and density), with surrounding waterways at least 50 m away from the set-up. Local time during the experiment was UTC+1 h, with all times reported here in UTC.

3.2.2 Distributed Temperature Sensing

Distributed temperature sensing measures temperature along fibre optic cables based on the back-scattered signal of a laser pulse (Selker et al. 2006). In the set-up employed here, a single 6-mm (diameter) reinforced fibre (with a white PVC coating) was used, connected to a Silixa Ultima-S DTS machine (2-km variant; Silixa Ltd 2018). The fibre itself had two multi-mode cores; however, the measurements were performed in a simple single-ended (non-duplexed) configuration.

The temperature was sampled every 0.125 m along the fibre, with the DTS signal having a spatial resolution of 0.35 m (such that the samples have overlapping regions of influence). The 30-s averaged temperatures were used, with no further spatial or temporal averaging except when comparing the DTS observations to the 10-min averaged KNMI observations, in which case the DTS observations were also averaged over 10 min. The fibre was run directly along the ground (i.e. resting on the surface with no support structures) from the DTS machine (which was housed in the tower building) through a calibration bath, to the energy-balance field, and back to the tower building where it was again passed through the calibration bath (Figs. 3.2a,c). The calibration bath was a water-filled styrofoam box at room temperature. A Pt100 temperature probe connected to the DTS machine was used to monitor the temperature, with an air bubbler used to ensure uniform temperature throughout the bath. The differential attenuation was calibrated by the Silixa software using temperature matching of the two calibration-bath segments. The internal reference temperature of the machine was used to correct for the temperature offset. This can result in a bias, but did not appear significant for our experiment.

At the measurement site in the energy-balance field, the fibre was mounted on a 7-m tall pneumatic mast with vertical temperature profiles sampled at 0.125-m resolution. One of the profiles (the descending portion) was maintained as the bare fibre, while the other (the ascending portion) was wrapped in a cotton gauze that was fed with a water pump in order to obtain wet-bulb temperature along the profile (as in Schilperoort et al. 2018). During periods where the air temperature was at or below 0°C, the wet-bulb temperatures were ignored.

In order to achieve even higher vertical resolution in the lowest metre, the fibre was wrapped in two helical structures approximately 0.5 m in diameter and 1-m tall. Again, one was wrapped in gauze and used to obtain the wet-bulb temperature. The dry coil was looped six times, giving an effective sampling resolution of 0.0145 m vertically. The wet coil was only wrapped twice to maintain a steeper slope along the fibre and facilitate the gravitational flow of water to keep the gauze wet. The effective vertical sampling resolution of the wet coil was 0.043 m.

During all periods where the air temperature was above freezing, relative hu-

midity (RH) was obtained from the DTS wet-bulb and dry-bulb temperatures (T_{wet} and T_{dry}, respectively) by relating the vapour pressure (e) to the saturation vapour pressure (e_s)

$$RH = 100\frac{e}{e_s\left(T_{dry}\right)}, \tag{3.1}$$

where, for a given temperature, T, in K, e_s (in Pa) is calculated as (Moene and van Dam 2014)

$$e_s\left(T\right) = 611.2\exp\left[\frac{17.62\left(T-273.15\right)}{T-30.03}\right], \tag{3.2}$$

and e is calculated from T_{wet} and T_{dry} as

$$e\left(T_{dry}, T_{wet}\right) = e_s\left(T_{wet}\right) - \gamma\left(T_{dry} - T_{wet}\right). \tag{3.3}$$

γ is the psychrometer constant (Moene and van Dam 2014)

$$\gamma = 1.61\frac{c_p}{L_v}P, \tag{3.4}$$

where c_p is the specific heat capacity of the air, L_v is the latent heat of vaporization, and P is the atmospheric pressure (in Pa). Corrections can be applied to c_p and L_v for moisture and temperature, respectively (see, for example, Moene and van Dam 2014), however within the observed range of conditions during our field experiment, the corrections are insignificant. As such, we use constant dry air values of $c_p = 1004$ J kg^{-1} K^{-1} and $L_v = 2.5 \times 10^6$ J kg^{-1}. Likewise, we assume P to be constant with height over the 7-m profile of the DTS. The 10-min averaged values of the KNMI-observed surface pressure were linearly interpolated to 30-s resolution in order to determine γ, and subsequently the relative humidity, at the same temporal resolution as the DTS measurements.

3.2.3 Visibility Estimates

We estimated nocturnal visibility using camera images of an artificial light source. A strip of light emitting diodes ("LED strip"; Groenovatie warm white, 2700–3000 K) was attached to the base of the pneumatic tower in a vertical orientation from the surface to 2.5-m height. The camera (GoPro Hero 4 Session) was mounted on the tower building (at a height of 2.5 m, and approximately 200 m from the LED strip) and set to take a photograph of the LED strip every 1 min. From the images, the pixel intensity as a function of height ($I(z)$, with values between zero and 1, indicating no light to saturation) was extracted and converted to a visibility estimate ($V_{est}(z)$) using a regression determined by comparing the pixel intensities at 2.0-m height to the observed visibility from the KNMI sensors at the same height

$$\log_{10}\left(V_{est}\left(z\right)\right) = a\log_{10}\left(1 - I(z)\right) + b. \tag{3.5}$$

The coefficients, and their 99% confidence intervals determined through linear minimum least squares regression, are: $a = -0.88 \pm 0.12$, and $b = 2.03 \pm 0.08$.

Further details on the method used to extract visibility estimates from the images can be found in the Appendix.

Visibility was estimated each night between 1700 and 0500 UTC in order to ensure minimum ambient daylight, which would otherwise pollute the recorded pixel intensities (i.e., the LED strip should be the only light source). Estimates were averaged over three layers: 0–0.5 m ($z = 0.25\ m$), 0.5–1.0 m (0.75 m), and 1.75–2.25 m (2.0 m), with a temporal resolution of 1 min. As with the DTS observations, further temporal averaging was only performed when comparing the camera–LED estimates to the 10-min averaged KNMI observations. A maximum value for the estimated visibility was set at 20 km. Using the camera, visibility estimates were obtained between 6–9 November, and 14–21 November, with storm conditions and obstructions to the line-of-sight excluding the other periods during the two weeks.

3.3 Results

This section presents the results of the two-week observation period. First, the higher-resolution temperature, relative humidity, and visibility observations are validated against the 10-min averaged KNMI observations from the CESAR facility in order to establish confidence in the data, and identify any potential methodological limitations (Sect. 3.3.1). Subsequently, individual nights are presented as case studies for more detailed analysis, and for the purpose of demonstrating the potential of the increased-resolution data (Sect. 3.3.2). During these nights, one radiative event, one advective event, and two cases of very shallow fog were observed.

3.3.1 Overview and Validation with Existing Data

Throughout the observation period, the majority of nights were weakly or near-neutrally stratified with respect to temperature, with significant cloud cover and wind speeds greater than 5 m s^{-1}. Three nights, however, had sustained periods of very stable conditions, with temperature inversions of a few degrees observed even within the lowest 1 m (in some cases, accounting for almost 50% of the total inversion over the 200-m tower) and wind speeds below 3 m s^{-1}.

Figure 3.3 shows that the 10-min averaged observations for temperature, relative humidity, and visibility using the higher-resolution techniques agree very well with the conventional KNMI observations. Specifically,

- At 0.1-m (1.5-m) height, the DTS-observed temperature has a bias of −0.22°C (−0.09°C) and root-mean-square error (*RMSE*) of 0.52°C (0.37°C), when compared with the KNMI-observed temperatures. Only under weak-wind, clear-sky conditions did the observations at 0.1-m height show any significant deviation (e.g., 6-7 November)
- The DTS relative humidity estimates (Eq. 3.1) result in an *RMSE* of 4% and a bias of 2%, compared to the KNMI observations, even under low-ventilation conditions

- For visibilities below 1 km, the camera–LED visibility estimates at 2.0 m result in an *RMSE* value of just 178 m with a bias of 74 m, with the method correctly able to distinguish between foggy conditions (visibility < 1 km) and no fog
- Two fog events were observed according to the KNMI observations of visibility at 2.0-m height (starting on 6 and 7 November, respectively), with the camera estimates also able to identify the onset and duration of these foggy periods correctly

Vertically, the increased-resolution of the DTS provides significant benefit to the conventional observations. Figure 3.4 shows the observed temperature profiles from the DTS and the reference observations on 6 November at 1800 and 1830 UTC. The sparse resolution of the conventional observations is unable to capture the near-surface curvature and large temperature inversion in the lowest 1 m of air. Generally, a logarithmic profile is assumed in the near-surface layer; however, such a profile is unable to capture the dynamic behaviour of the observed temperature profiles (such as the curvature at 1830 UTC between heights of 3–7 m).

The observed surface-temperature (from the fibre running along the ground between the tower and the energy-balance field) shows significant variability in space under weak-wind, clear-sky conditions (Fig. 3.5). Within approximately 40 m of the tower, temperatures were observed to be between 1–3°C higher than in the energy-balance field under stable conditions. The large slope on 6 November is a transient feature (likely due to the turbulent wake of the tower), with the surface profile nearly identical to that shown for 7 November at other times in the night. At the same time, there are co-located peaks in the surface temperature profiles on the different nights, likely caused by small-scale topographic features (e.g., due to small changes in the surface or changes in height and density of the grass). In contrast, during times of weakly stable/unstable vertical temperature stratification and higher wind speeds, the variability in surface temperature was negligible. The observed surface-temperature profiles were identical for both the outbound and inbound segments of the fibre, ruling out calibration error as the source of the temperature variability.

The overall error in the visibility estimates is dominated by observations during periods of increased visibility ($>$ 2–3 km) when the camera pixels are saturated by the light from the LED strip. For example, the KNMI observations recorded visibility of between 3–4 km on the nights of 8–9 and 9–10 November. The camera-estimated visibilities, however, are at the 20 km threshold, with the camera pixels saturated. Conversely, the visibility on 18–19 November and 21–22 November is estimated much lower (approximately 1 km) using the camera than observed by the KNMI sensors ($>$ 10 km). These nights also experienced very heavy rain (droplets of which temporarily obscured the camera image on 18 November), which led to reduced visibility estimates due to the scattering and absorption of light by the rain droplets.

The 1-min camera observations (Fig. 3.6) show the visibility and depth of the fog

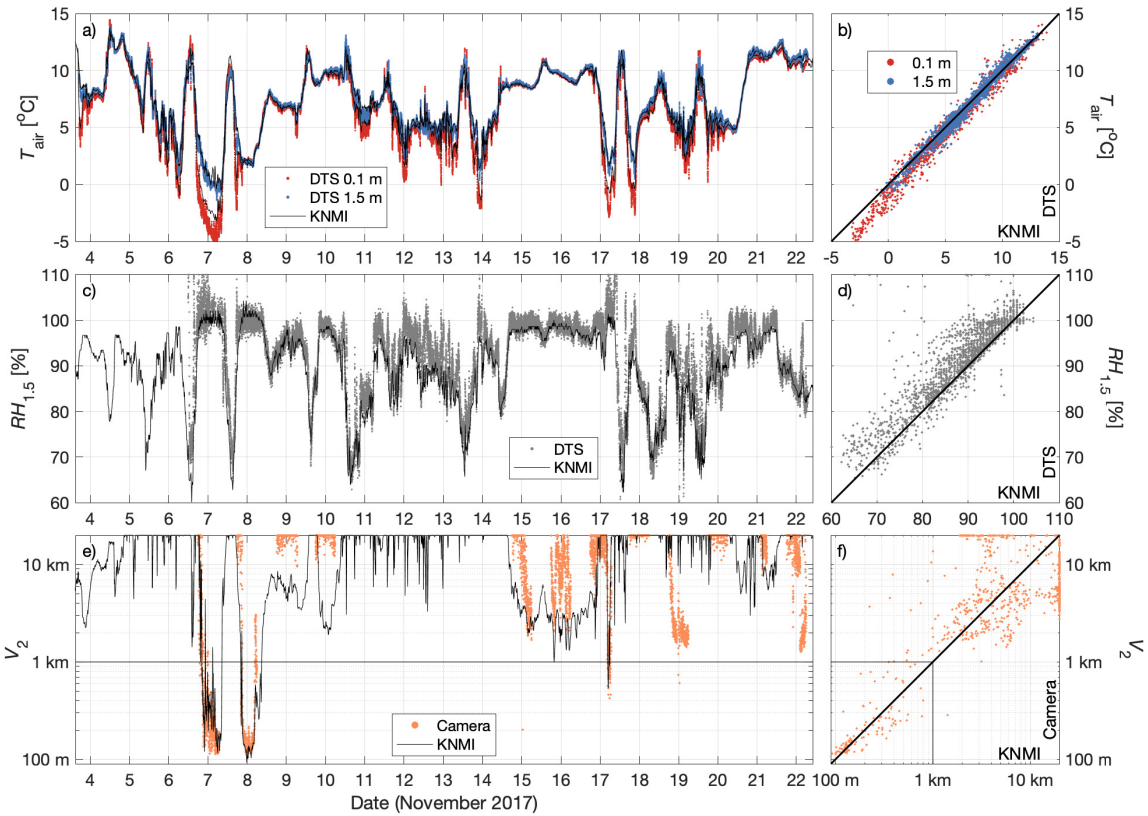

Figure 3.3: Comparison of the increased-resolution data with the corresponding conventional KNMI observations. a) Time series and b) 10-min averaged values compared to 1:1 line for the 0.1 m and 1.5 m temperature. c) Time series and d) 1:1 comparison of relative humidity at 1.5-m height. e) Time series and f) 1:1 comparison of visibility at 2.0-m height.

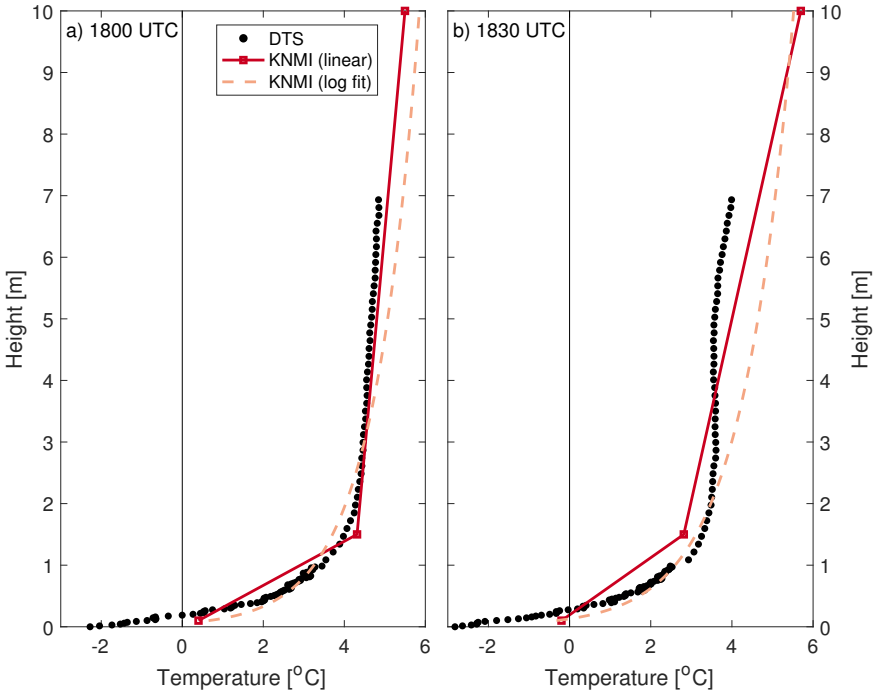

Figure 3.4: 10-min averaged temperature profiles from the DTS and KNMI sensors on 6 November 2017 at a) 1800, and b) 1830 UTC. The KNMI data are plotted with both a linear interpolation, and logarithmic fit.

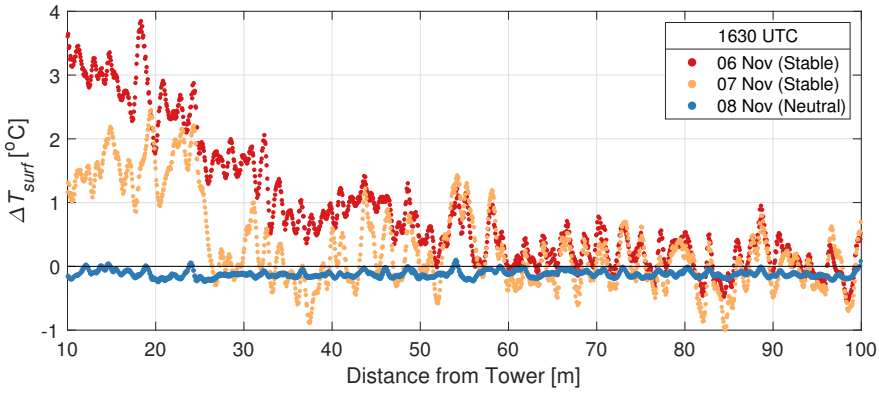

Figure 3.5: Difference in DTS-observed surface temperature as a function of distance from the Cabauw tower on three consecutive nights with different static stability. ΔT_{surf} is the local surface temperature measured along the fibre, referenced to the surface temperature measured in the energy-balance field $\left(T_{surf}(x) - T_{surf,EB}(x = 200\ m)\right)$. Profiles are instantaneous from 1630 UTC on all three nights.

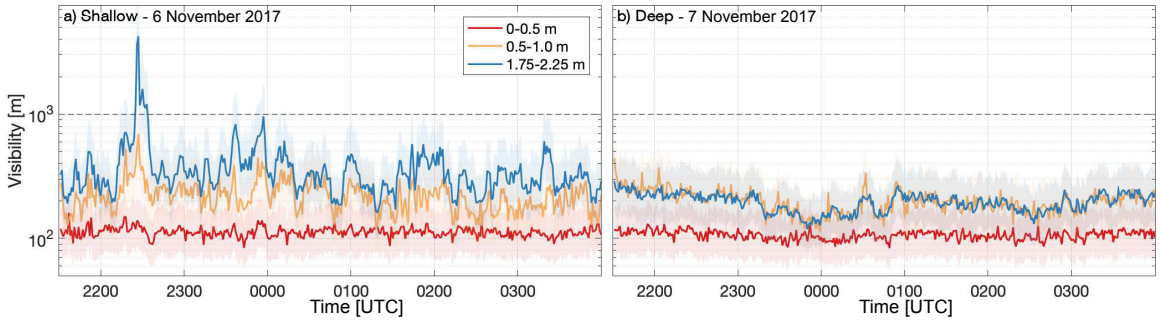

Figure 3.6: Comparison of 1-min near-surface visibility observed with the camera at three heights during a) shallow (between 2–10 m deep) radiation fog on 6 November 2017 and b) deep (up to 80 m) advection fog on 7 November 2017, showing the contrast in variability of the observed visibility

layer (see also the images in Izett et al. 2018a) to be highly variable under shallow-fog conditions as observed on 6 November (Fig. 3.6a). This is particularly true at aheight of 2 m, as the observations are made near the top of the fog layer (see also the vertical heterogeneity in the movie accompanying Mahrt 2014). In contrast, during the deep advection-fog event on 7 November the near-surface visibility observations are much more uniform in time (Fig. 3.6b) due to the fact that the fog layer was much deeper than the observation heights and the overall temperature and humidity profiles were vertically well-mixed.

3.3.2 Analysis of Individual Nights

With confidence in the accuracy of the measurements established in Sect. 3.3.1, the following subsections present analyses of individual nights where fog was observed; either both in the KNMI observations and the camera estimates, or when there was shallow fog and/or a low-visibility event that was missed by the KNMI observations at 2-m height, but observed in the lowest 0.5 m by the camera–LED set-up.

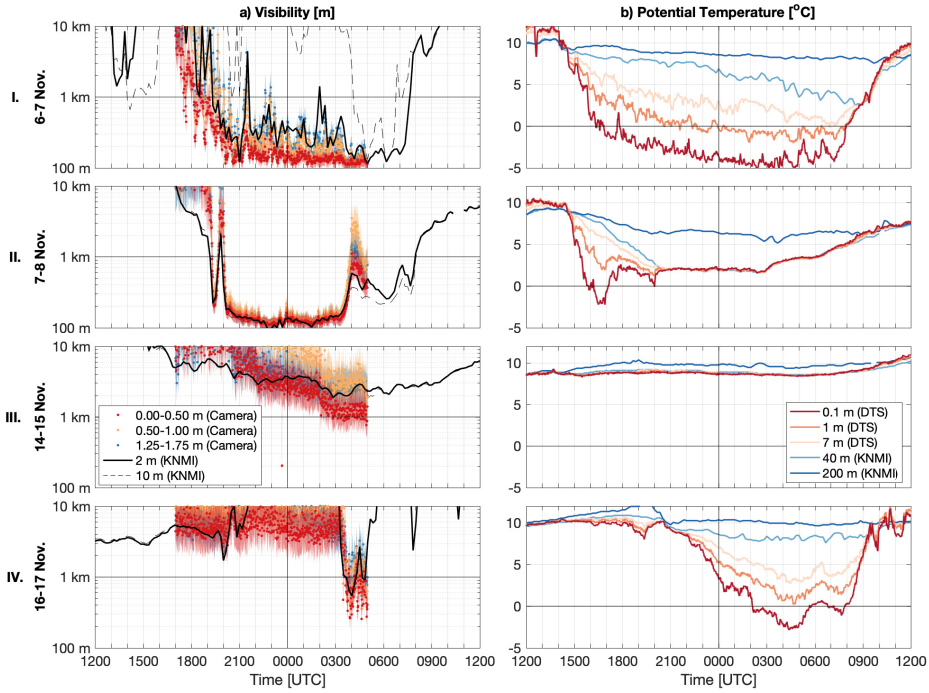

Figure 3.7: Visibility and potential temperature for four nights. The rows correspond to different nights: I. 6–7 November, II. 7–8 November, III. 14–15 November, and IV. 16–17 November. The columns indicate a) 1-min camera-estimated visibility (coloured dots) with uncertainty (shading), and the 10-min averaged KNMI visibility observations at 2.0 m and 10-m height (black lines); and b) potential temperature from the DTS at 0.1 m, 1.0 m, and 7.0-m height (red/orange), with KNMI observations at 40 m and 200-m height (blue).

Radiation Fog

Low wind speeds and clear skies were observed on the night of 6–7 November due to the presence of a high pressure system, resulting in subsequently strong surface cooling. The day preceding was also warm, providing moisture to the air through evaporation. Overall, the conditions were extremely favourable for the formation of radiation fog. For an animation of the observations during the night of 6–7 November (including the GoPro images, temperature profiles, and estimated visibility), the reader is directed to Izett et al. (2018a).

Patches of very shallow mist were already seen forming at the surface as early as 1600 UTC on 6 November. According to the KNMI visibility observations, fog formed around 1920 UTC at the 2.0-m level and persisted throughout the night, ultimately reaching a depth between 10–20 m (Fig. 3.7I.a). The camera estimates at 2.0-m height agree well with the KNMI-observed visibility, with conditions estimated to be foggy around 1930 UTC. However, the camera observations indicate an established fog layer was present in the lowest 0–0.5 m as early as 1730–1800 UTC. As such,

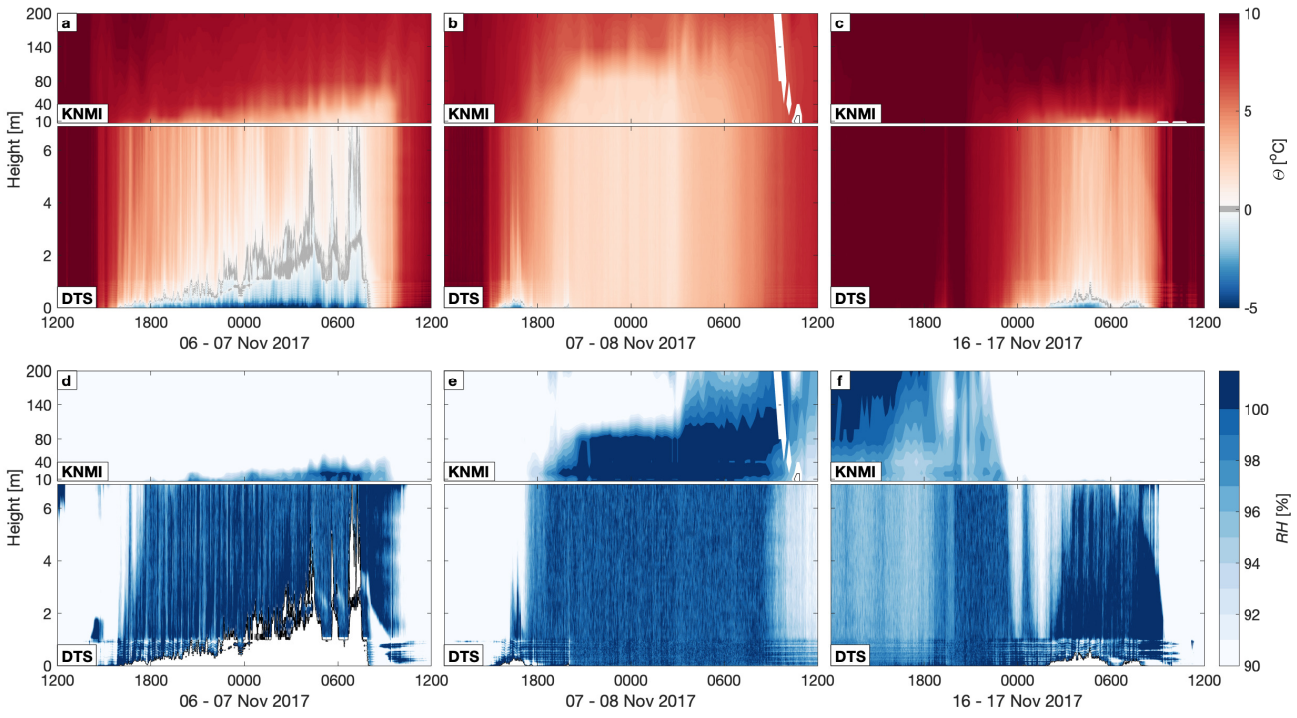

Figure 3.8: Potential temperature (θ; a-c) and relative humidity (RH; d-f) for the three fog events observed during the field campaign. a and d) the radiative event on 6–7 November, b and e) the advection-fog event on 7–8 November, and c and f) the potentially missed fog on 16–17 November. The lower panels show the DTS estimates from 0–7-m height, while the upper panels plot the interpolated tower observations up to 200-m height. Relative humidity is not included where T_{air} is below 0°C (white outlined in black).

shallow fog was observed almost two hours before conditions became foggy at 2.0 m.

One of the most interesting features of the fog growth was its temporal—and not only vertical—heterogeneity. Reminiscent of the videos from Mahrt (2014), the camera images clearly show large variations from one image to the next in both fog thickness and depth as the layer grows irregularly from the surface upwards. This can be seen in Fig. 3.7I.a, as well as in the video of the observations during the event (Izett et al. 2018a).

Preceding the reduction in visibility, the surface cooled strongly under the clear-sky, weak-wind conditions (Fig. 3.7I.b, Fig. 3.8a), resulting in freezing temperatures near the surface, and a temperature inversion of almost 5°C in the lowest 1 m of air. This inversion accounted for almost 50% of the total inversion over the 200-m tower. The depth of the freezing layer grew throughout the night, eventually reaching 7 m by sunrise. Throughout the night, wind was low ($<$ 2 m s^{-1} at 10-m height), and net radiation was strongly negative ($\leq$ –40 W m^{-2}).

The very shallow inversion corresponded directly with a very shallow region of saturation (Fig. 3.8d) which is already visible in advance of the freezing conditions at the surface. With limited mixing from above, the cold, moist air was maintained at saturation, allowing both fog and frost formation. As the depth of the saturated layer grew, so did the fog layer, with the depth of the fog layer directly related to fluctuations in the relative humidity profile initiated by temperature fluctuations. Only after the rising of the sun and the warming of the surface did this shallow saturated layer break down, and the fog dissipate.

Advection Fog

The night of 7–8 November began much the same as the previous night when radiation fog formed (Fig. 3.7II). Again, a large inversion of roughly 5°C developed in the lowest metre of air (Fig. 3.7II.b), with shallow patches of mist forming along the ground and in the small waterways. However, warming of the near-surface at 1700 UTC resulted in a weakening of the temperature stratification and a reduction in relative humidity, despite the continuation of clear skies. Over this time, visibility dropped steadily (Fig. 3.7II.a) until around 1930 UTC when visibility decreased almost simultaneously at all levels up to 80-m height on the tower. After a brief recovery, foggy conditions were fully established at around 2000 UTC and remained for the duration of the night. The net radiation also became less negative at this time (from $<$ $-$60 W m^{-2} to $-$15 W m^{-2}), with an optically thick, well-mixed fog layer that radiated from its top, rather than from the surface.

In spite of the low wind speeds ($<$ 3 m s^{-1}), the increased surface temperature and sudden onset of fog indicate this was an advective event with well-mixed, moist air blown over the measurement site from the east. This is also seen in Fig. 3.8e where a “wall” of saturated air was observed around 1800UTC. Further, observations of visibility from upwind weather stations show fog first formed in the east and propagated westward (not shown).

Missed Fog

On the nights of 14–15 and 16–17 November, visibility was observed by the existing sensors at 2.0-m height to be above foggy conditions for most of the night (between 3–10 km). The exception to this being the final hour of the night on 17 November when visibility dropped below 1 km, but was not sustained long enough to be classified as an “event" as defined here. From the camera estimates, however, the visibility drops below 1 km in lowest 0.5 m on both nights (Fig. 3.7III.a and IV.a), and is sustained for more than one hour in both cases.

On 15 November, this is the culmination of a steady decline in visibility throughout the night that is associated with rain showers. Unlike the other events, the surface layer remained neutrally stratified (Fig. 3.7III.b), with the relative humidity near saturation throughout the entire 200-m column. Visibility between 0–0.5-m height dropped to around 1 km just after 0300 UTC and remained around 1 km for the rest of the night (Fig. 3.7III.a), most likely due to rainfall.

More interesting is the night of 16 November. Initially the sky was cloudy and the entire profile was near saturation, with a uniform vertical temperature profile. However, following rain (between roughly 2100–0000 UTC) the sky cleared of clouds and the air aloft became much drier (Fig. 3.8f). With the clearing sky (and corresponding decrease in incoming longwave radiation), a strong near-surface temperature inversion grew in the lowest metre of air (Fig. 3.7IV.b), as on 6 November (Fig. 3.7I.b), and a shallow saturated layer formed (Fig. 3.8f). Within this layer, fog began to form around 0330 UTC (Fig. 3.7IV.a). Before the fog layer reached a depth of 2 m, the near-surface warmed and the fog dissipated. In the lowest 0.5 m, however, the fog remained until at least 0500 UTC when visibility could no longer be estimated accurately from the camera images due to the rising of the sun.

3.4 Discussion

Temperature, relative humidity, and visibility at increased resolutions were observed over two weeks in November 2017 using DTS and a novel approach of estimating visibility from the intensity of pixels in camera images of an extended (LED) source.

The DTS-observed temperature agreed well with the KNMI-observed temperatures throughout the two weeks (e.g., Fig. 3.3). However, during weak-wind, clear-sky, nocturnal conditions, the error in DTS-observed temperature can be large due to radiation of the fibre itself (Sigmund et al. 2017), particularly for larger fibres, as was the case here. Indeed, while the errors in temperature are small at 1.5-m height (Fig. 3.3), the DTS-observed temperatures at 0.1-m height under the very stable conditions of 6 November were approximately 1-3°C lower than the KNMI observations at the same height. A large part of this discrepancy may be due to the radiative error. The observed temperature difference is on the same order as the 0.7-K elevated temperatures found by Hilgersom et al. (2016) during fog; however, here the observed temperatures were lower than expected, rather than higher.

We further hypothesize that the observed temperature difference is due to two

additional factors, 1) small-scale topographic features (such as a slight slope of the ground surface between the tower and the energy-balance field), and 2) slight differences in land properties between the region near the tower where the KNMI observations are made, and the energy-balance field, including grass density and uneven ground. This is also supported by the findings of Pfister et al. (2017) who found surface characteristics and micro-topography can significantly impact the observed near-surface temperature. In addition to small-scale variability along the path, Fig. 3.5 shows the surface temperature near the tower (where the KNMI temperature measurements are made) to be between 1–3°C higher than in the energy-balance field, which would account for the observed discrepancy between the DTS and the KNMI observations. This variability also draws into question the common assumption of "homogeneity" at the Cabauw site and suggests small-scale heterogeneity at the site—including the influence of the small waterways—would be an interesting feature to study with future DTS campaigns.

The DTS relative humidity estimates were also accurate when compared to the KNMI observations, however, challenges remain when considering its use in future stable-boundary-layer research. In determining the wet-bulb temperature (and subsequently the relative humidity), for example, freezing conditions limit when observations can be reliably made (as on the nights of 6 and 7 November). Likewise, the limited ventilation of the wet fibre during the nights with low wind speed will influence the observed temperature and relative humidity. This is likely what leads to the slight positive bias in the DTS-estimated relative humidity when compared to the KNMI observations, with the wet-bulb temperature higher than it should be (not enough evaporative cooling with low wind speeds). That being said, the error is still small, and the method's ability to provide even an approximate profile of relative humidity is a significant benefit when compared to the resolution of conventional sensors.

While DTS is an established measurement technique, using the camera to obtain visibility estimates was far more speculative at the outset of this research, initially intended to simply provide an approximate indication of whether or not fog was present. However, the quality of the estimates far exceeded expectations. Most encouraging is the ability of the methodology to easily distinguish between clear and reduced-visibility conditions, while at the same time providing high-precision estimates of visibility when it falls below a few kilometres (errors of just a few tens to hundreds of metres compared to the conventional KNMI observations). While the magnitude of the error is large during periods with increased visibility, errors during higher visibility periods are less significant (e.g., estimating 5 km vs 15 km) when compared to errors during reduced-visibility conditions (e.g., 500 m vs. 1.5 km) as such periods are still clear from the perspective of human vision.

That being said, while the method proved reliable in this experiment and provided increased resolution beyond the conventional sensors, it is still limited. For example, the method is inherently an integrated measure of visibility both vertically and horizontally. While an integrated measure is representative of human vision, it limits the ability to observe heterogeneity in fog, particularly in the case of hori-

zontally patchy fog (vertical heterogeneity can be inferred to some degree based on the vertical pattern of pixel intensity). In order to observe some of the horizontal heterogeneity, it may be possible to use multiple light sources at different distances, angles, and heights relative to the camera, providing a more distributed view of the fog (rather than just a single vertical segment as employed here). Multiple light sources would also help to calibrate the relationship and determine visibility with greater accuracy.

With regard to calibration, the camera and light source(s) used, as well as the distance between the camera and light source(s) (approximately 200 m here) will influence the sensitivity to different visibility ranges. The use of the method also relies on the relative heights of the camera and light source(s) as it influences the optical path to the camera. Our camera was approximately level with the top of the LED strip, though with some possible elevation differences along the path. As such, the relationship between recorded pixel intensity and visibility (Eq. 3.5) needs to be determined for each unique set-up using a co-located conventional sensor (after which the set-up could be re-located, provided the geometry is carefully maintained).

3.4.1 Missed Fog: Is High Resolution Necessary?

The data presented here provide an unprecedented look at the formation of radiation fog as a “ground–up" process. However, it is reasonable to question whether the increased resolution of the techniques employed is truly necessary when compared to the conventional observations.

The region between the ground and the lowest observation level was identified in Izett et al. (2018c) as a potential source of “false false alarms" in the diagnosis of fog events from observations. Overall, just two fog events would have been diagnosed from the conventional observations at 2-m height (6 and 7 November). However, supporting the assertion in Izett et al. (2018c), a further fog event was diagnosed from the camera observations made in the lowest half metre (16–17 November), with low-visibility also observed in the lowest 0.5 m on 14 November due to precipitation. At the same time, the shallow fog on 6–7 November, formed within the lowest 0.5 m up to two hours before it reached the conventional sensor height, growing along with a deepening layer of saturated air. The detection of this otherwise “missed fog” is scientifically significant as the near-surface growth can be studied.

Even in the absence of fog formation, the strong temperature inversions in the lowest 1 m of air observed with the DTS measurements would be impossible to observe with conventional set-ups (e.g., Fig. 3.4). While assumptions can be made (such as the use of a logarithmic fit), only through the increased resolution offered by techniques such as DTS can the near-surface profiles be properly resolved, thereby reducing the error that would be made through incorrect, but otherwise necessary, assumptions.

Inability to resolve the near-surface has also been shown significant in numerical simulations of fog. Maronga and Bosveld (2017), for example, found that a vertical grid spacing of 1 m or less was required to accurately simulate the onset and duration

of a radiation-fog event (due to the need to capture the strong near-surface gradients, similar to those presented here). Given that the majority of operational weather models are run with considerably larger vertical grid spacing than 1 m (for example, the ECMWF L137 grid which has its lowest level at 10 m; ECMWF 2018), the formation of shallow fog is an entirely subgrid-scale process. Future observational campaigns with increased resolution near the surface could help to guide the development of a subgrid-scale parametrization of fog growth, either directly, or through providing the requisite high-resolution data for validation of high-resolution models.

The above relates primarily to shallow fog, such as was observed on 6 and 17 November. However, fog events (and other dynamics) controlled by large-scale processes (such as the advection-fog event on 7–8 November) do not require the use of higher-resolution techniques near the surface, as the processes involved in the fog formation are less dependent on local surface properties. As shown in Figs. 3.8b,e, the boundary layer is typically more homogeneous in the shallow layers where the increased-resolution is otherwise desirable.

3.4.2 A Note on Practical Implications: Visibility Monitoring

The delay between fog formation and detection with height; the possibility of a very shallow, undetected fog layer; and the temporal variability of the fog observed in this campaign raise questions about how fog is formally defined and reported. While the 10-min averaged KNMI observations show a fairly stable decline in visibility, the 1-min camera observations (Fig. 3.6a) show the fog layer to be much more variable in thickness and depth. This suggests that, whereas the mean visibility is often used, the minimum visibility over a given observation/prediction period would be a more appropriate measure of fog for monitoring and reporting purposes. In this case, erring on the side of caution would result in safer conditions. Further, while the observation resolution need not be on the order of 0.5 m as employed here, even adding a single conventional sensor below 1-m height would lead to increased detection of shallow fog events. Such an approach would also provide a physical “early warning” of fog, with a shallower layer detected earlier than at 2.0-m height.

The camera–LED methodology presented could conceivably be incorporated into larger monitoring networks, with only minor modifications and using existing infrastructure. Take, for example, visibility observations along a highway. Highways are often monitored with a network of cameras to assess congestion and current weather conditions. Some methods already seek to exploit such infrastructure for visibility monitoring (e.g., Hautiere et al. 2008); however, they are only possible during daytime conditions. Yet, as with cameras, streetlights are also abundant and provide artificial light sources for estimates to be made in a similar fashion as presented here. Before the methodology could be employed extensively, however, some practical concerns would need to be addressed (such as calibration, light pollution from headlights, and the volume of data). That is beyond the scope of this work.

3.5 Conclusions

We presented the results of a two-week field campaign with the aim of assessing the performance and value of increased-resolution temperature, relative humidity, and visibility observations for fog research, particularly in regard to observing the growth and presence of very shallow fog layers that are otherwise missed by current sensors, which are conventionally located above 1-m height.

Using a novel camera–LED method for obtaining visibility estimates, we show that shallow fog (< 0.5-m deep) formed up to two hours before it was observed at the 2-m height of the conventional sensor. At the same time, at least one further shallow fog event was observed that never deepened to reach the conventional 2-m observation height and would otherwise have been unobserved. This "missed fog" is important from a scientific perspective in order to understand the growth of radiation fog layers from the ground upward, as well as from a monitoring and human safety perspective. While an additional sensor could be placed below 1-m height to capture such events, the camera methodology is further able to observe the growth of the fog layer in a near-continuous manner. The methodology not only allows for further high-resolution studies of fog, but could also be applied as part of large-scale monitoring networks using existing camera infrastructure, such as along motorways, which would also result in an excellent source of observational data for studies of two-dimensional patterns of fog. This fills a gap in existing camera monitoring techniques which are only applicable for daylight hours.

We supplemented the camera–LED observations with DTS observations of high-resolution temperature and relative humidity, showing the presence of large, shallow temperature inversions and saturated layers preceding the formation of the shallow fog. Similar observations in future campaigns will allow for deeper understanding of the conditions under which fog forms and grows. Further, we found significant horizontal heterogeneity in surface temperature, highlighting the need to better understand heterogeneity in the near-surface and its role in the development of the stable, nocturnal boundary layer, and fog formation.

This small experiment should serve as a guide for future observational research into the near-surface micrometeorological processes that control the formation and evolution of fog. Further three-dimensional studies with more complex orientations of the DTS fibre, such as used by Thomas et al. (2012) for turbulence measurements, would be especially enlightening, as would a large-scale campaign in the style of the recent Local and Non-local Fog EXperiment (LANFEX; Price et al. 2018) where multiple techniques were combined. Such efforts would provide further insights into near-surface fog formation and growth, as well as provide valuable input and validation data for the requisite sub-metre resolution needed by numerical models.

Of course, future study is not restricted to fog, but the broader near-surface (stable) boundary layer. The ability of DTS to capture steep gradients in both temperature and relative humidity should lead to better physical understanding of such processes as the collapse of turbulence at the onset of the stable boundary layer, intermittent turbulence within the stable boundary layer, and the transition between

different boundary-layer regimes.

3.A Estimating Visibility from Camera Images

The basic steps to estimate visibility from camera images are presented below for the case of an extended source (as employed here) giving an estimate of spatial—in this case vertical—heterogeneity in observed visibility. However, the methodology is also equally valid for a more localized source (such as a street light) or as an average value over a range (see step 4 below). The primary assumption in determining visibility from the camera images is that a reduction in pixel intensity in the image of the LED strip is directly caused by the reduction in visibility (similar to the principle behind a transmissometer).

To estimate visibility (Fig. 3.9):

1. The true-colour images are converted to a greyscale intensity image, with pixel intensities ranging from zero (no light) to 1 (pixel is saturated).

2. The shape of the light source on the camera is mapped by taking a known clear image and identifying the region where the pixels are saturated (in this case, an intensity value of ≥ 0.94 was used to create the map).

3. The mask is applied to each image, with the intensity of the individual pixels within the mask determined.

4. The pixel intensities are averaged according to the desired spatial resolution. If an extended source, they can be binned according to select heights or horizontal locations. If a localized source, or a bulk measurement, then a simple average over all relevant pixels is calculated.

5. Visibility is estimated from the averaged intensities using an empirical function and dependent on the light source/camera combination (determined here through relation with the KNMI observations at 2.0-m height; Fig. 3.10.)

The pixel intensities were normalized by the clear-image intensity, with a new clear image defined every few days to account for slight shifts in the camera due to wind. In order to ensure minimal contamination of the pixel intensities by ambient daylight, only images between 1700 and 0500 UTC were used to estimate visibility.

If multiple light sources and/or an extended light source are used, careful mapping of the LED image on the camera is required in order to ensure the pixels are properly aligned and spatial information can be obtained. The camera must also be stable and remain in a fixed position as any change in alignment alters the position of the light source within the camera images. Given that the path length for the light is on the order of one hundred metres, any slight change in camera position will lead to a large change in which pixels are illuminated. For this reason, a new reference image was selected as frequently as clear conditions allowed.

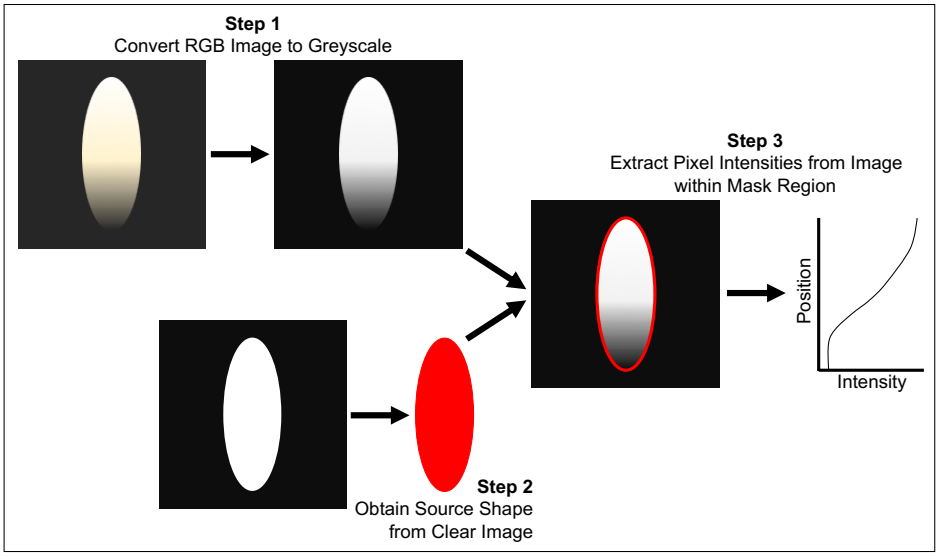

Figure 3.9: Schematic representing steps 1–3 for determining the intensity of pixel images. See the video of the event on 6–7 November (Izett et al. 2018a) for examples of real camera images.

In a practical implementation, the choice of empirical function to determine visibility will depend on the specific characteristics of the light source and camera available, and will need to be calibrated with a co-located visibility sensor. Here, the visibility at a certain pixel location (V_P) is assumed to be a direct function of the intensity in that pixel (I_P).

$$V_P = f(I_P). \tag{3.6}$$

This assumes that the pixel location is representative of the optical path over which the light travels (e.g., that the height of the pixel is the same over the majority of the optical path). In essence, this is an oversimplification, with the pixel signal the integrated effect over the entire optical path; however, it is sufficient for our purposes.

By comparing the pixel intensity averaged over 1.75–2.25-m height to the observed visibility at 2.0-m height from the two existing sensors, a linear regression was obtained whereby the logarithm of the visibility (V_{est}) is a function of the logarithm of the pixel saturation (1-I) as in Fig. 3.10.

$$\log_{10}(V_{est}) = a \log_{10}(1-I) + b \tag{3.7}$$

To avoid saturation effects, only data with pixel intensities below 0.99, and visibility observations less than 10 km were considered in the regression. Using a linear-least-squares regression, the coefficients in Eq. 3.7 and their corresponding 99% confidence intervals are: $a = -0.88 \pm 0.12$ and $b = 2.03 \pm 0.08$. The fit is very good with an r^2 value of 0.85 and a p-value of 0 indicating the fit is significant. Errors

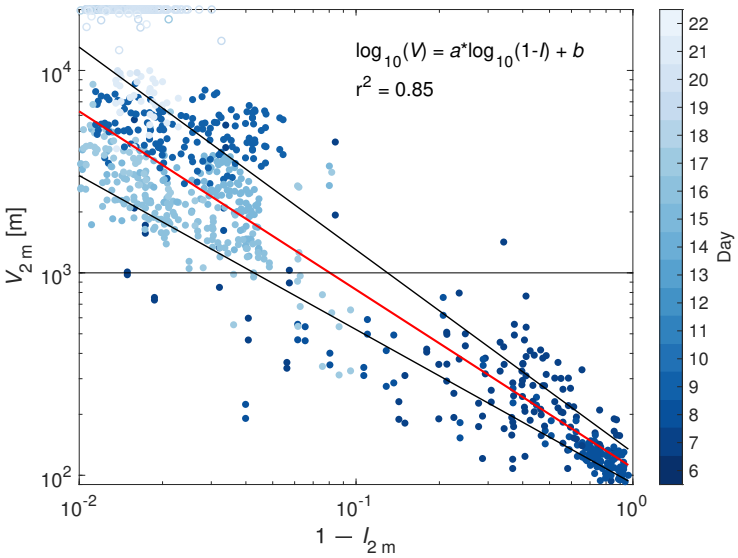

Figure 3.10: Regression relating the saturation of the camera pixels (1 minus pixel intensity) at 2.0-m height to the observed visibility measured on both KNMI visibility sensors. The red line is the linear regression of Eq. 3.7 and the black lines are the 99% confidence intervals. The empty circles indicate data that were excluded from the regression.

are dominated by the spread in visibility observations at high pixel intensities (near saturation).

Variables V_P and I_P can be calculated from any combination of pixels, ranging from individual pixels to get the highest spatial resolution (but also greatest noise) up to an average of all pixels. Here, the pixel values are averaged within different height bins such that $I_P = I(z)$, giving intensity (and therefore the visibility estimates) as a function of height. However, an overall average pixel intensity can just as easily be used (e.g., in the case of a street lamp).

Chapter 4

Dutch Fog

On the observed spatio-temporal variability of fog in the Netherlands.

> Jip wordt wakker. En hij kijkt uit het raam. En het is zo gek. Hij ziet niets buiten.
> ...Wat is het gek. Met die mist.
>
> A. M. G. Schmidt, *Jip en Janneke, Mist*

Summary

The Netherlands is characterized by highly variable land use within a small area, and a strong influence of the North Sea on national climate. Devoid of significant topography, it is an excellent location for assessing the relative influence of various factors on fog occurrence in the absence of terrain effects. 45 years of observations from a dense network of weather stations is used to assess the Dutch fog climate. On a national scale, inter-annual variability is linked to changes in synoptic pressure-gradient forcing. Within the country, a comprehensive in-depth analysis of regional differences between fog occurrence is made, together with an assessment of local physical factors that could bias fog formation in one location over another. Regional variability is shown to be strongly related to the mesoscale influences of urbanization and the North Sea. In fact, some locations experience over twice as much fog as others. From this finding, a simple index is presented, which combines the water and urban fraction surrounding a station. This "Regionally Weighted Index" (*RWI*) is able to accurately sort the stations according to their relative fogginess. Its practical use is encouraged for assessing a given site's climatological favourability, even when in situ meteorological observations are unavailable.

This chapter, including a supplement, has been published as:

Izett JG, van de Wiel BJH, Baas P, van Hooft JA, Schulte RB (2019) Dutch Fog: On the observed spatio–temporal variability of fog in the Netherlands. Q J Royal Met Soc, doi:10.1002/qj.3597

4.1 Introduction

Fog is a hazard that impacts all modes of transport. Yet, it remains challenging to predict its occurrence using numerical models. In part, this is because of the need to capture both the large-scale processes, e.g. the evolution of synoptic weather systems, as well as to accurately describe the local, small-scale processes, such as surface fluxes and microphysics (Gultepe et al. 2007; Steeneveld et al. 2015). In this paper we seek to better understand the influence of various factors on the spatio-temporal variability of fog by analyzing climatolgies of fog observations from a dense network of weather stations spread throughout the Netherlands. Two data sets are used, one long-term data set spanning 45 years, and a short-term data set that is 6 years long (see Sect. 4.2.1 for more detail). While the Netherlands is a relatively small, flat country, land use and population density vary significantly. Combined with the influence of the North Sea, the varied landscape can lead to significantly different localized weather conditions. This is particularly apparent in the absence of other external forcing, such as during clear-sky nights with weak-wind conditions, when the near-surface temperature can vary by several degrees, even over short distances (e.g., see Fig. 4.1a). Related, the frequency and type of fog events are expected to be highly variable throughout the country as well. We seek to identify factors on a range of spatial scales—from mesoscale to synoptic—that influence Dutch fog occurrence regionally and on inter-annual timescales. The aim of this work is twofold: 1) to report on the observed spatio-temporal variability of fog in the Netherlands, and 2) to relate the observed variability to external influencing factors that can be used to better identify when and where fog is most likely to occur.

Previous observational studies of fog have focused primarily on single-site observations. For example, Dutch fog has been studied extensively through observations at the Cabauw site (e.g., Duynkerke 1991, 1999; Izett et al. 2018c, 2019a) located in the centre of the Netherlands. Likewise, observational campaigns such as at the ParisFog site in France, (e.g., Haeffelin et al. 2010), at the CIBA site in Spain (e.g., Román-Cascón et al. 2016a), and the FRAM project in Canada (Gultepe and Milbrandt 2007) look primarily at local fog occurrence at independent locations. Often, the measurement sites are at or near airports due to the need for accurate real-time information about current visibility conditions. While from a practical standpoint this is important, the local setting of an airport—with buildings, runways, and often near major urban centres—is not a representative landscape; a regional study with multiple diverse measurement locations is therefore desirable.

Regional studies are, however, much less common. This is likely due to the difficulty in obtaining dense, compatible observations across large areas. In this regard, the contribution from Tardif and Rasmussen (2007) provides an excellent example in the literature of an investigation of regional fog variability. They analyze 20 years of fog observations in and around the New York City region on the northeastern coast of the United States. With 17 stations in an area approximately half the size of the Netherlands, their study region features complex terrain, with deep river valleys (such as the Hudson valley) and dense urban centres (including Manhattan).

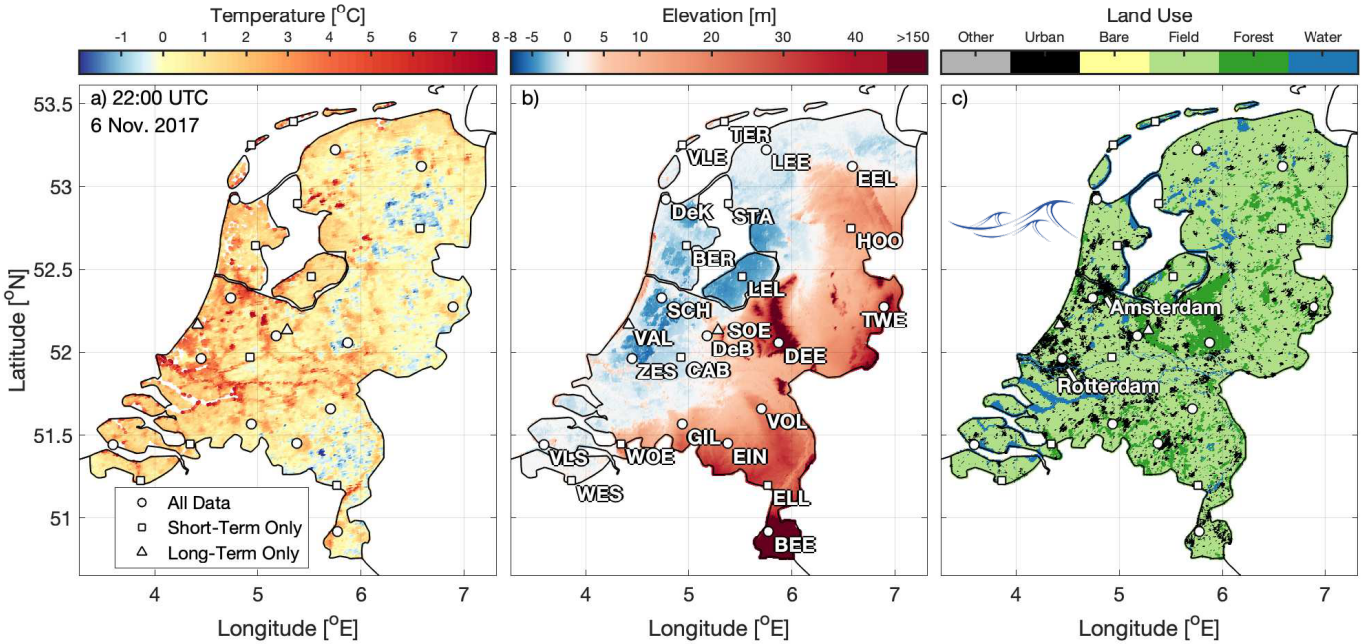

Figure 4.1: Heterogeneity in the Netherlands. a) MODIS-observed nocturnal land surface temperature under clear sky-conditions on 6 November, 2017 (Wan et al. 2015); b) AHN2 surface elevation, and c) ESA-CCI land use (Hollmann et al. 2013). Note the North Sea lies to the north-west, while IJsselmeer is the enclosed lake north-east of Amsterdam. The weather stations used in this work are indicated by white scatter points. Details of the stations can be found in Sect. 4.2.1 as well as Table 4.1, with a browsable map at https://jonathan-izett-research.weebly.com/dutch-fog.html

Overall, they conclude that fog occurs most frequently at coastal, rural and suburban stations, with the least fog in urban settings. However, topographic effects, while significant in determining a local fog climatology, potentially obscure other underlying influences related to such properties as land use.

Further regional studies include work by Bendix (2002) who investigated the regional occurrence of fog and low stratus in Germany (and surrounding areas). Using 10 years of satellite imagery, Bendix finds significant variability throughout the region, both in terms of fog occurrence, as well as fog type. However, the study is limited to observations during high-cloud-free satellite overpasses, and is unable to distinguish between fog and low cloud. More recently, Egli et al. (2017, 2019) present an analysis of satellite-derived fog occurrence over Europe, focusing on the continental-scale patterns of fog distribution, which are heavily influenced by topography. In a much smaller area, Cereceda et al. (2002) study the occurrence of fog at a handful of sites in the Atacama desert in Chile, showing the coastal influence on fog type. Finally, Price et al. (2018) conducted a series of observations and simulations in England during the 18-month Local and Non-Local Fog Experiment (LANFEX). Within the LANFEX regions of interest, small-scale topographic features were important in determining local fog occurrence (particularly the deepening of fog layers) through their influence on the turbulent properties of the stable boundary layer. The relatively small areal extent of the region, and similarly short-term extent of the observations, however, make it difficult to assess the wider regional and climatic influence of other factors. All studies are heavily influenced by topography.

In contrast to the other study regions, and many regions around the world, the Netherlands provides a unique setting to study regional influences on fog in what is a largely topographically uniform country. Figure 4.1b shows the surface elevation from the second Actueel Hoogtebestand Nederland data set (AHN2; "Current Height of the Netherlands") which can be accessed at ahn.nl. Except in the southeast, much of the Netherlands is flat, low-lying terrain. As a result, the influence of various factors can be investigated without the additional complexity, and potential obscuration, of topographic effects. At the same time, the small scale of the country (a land area of less than 35 000 km^2), large variability in land use (Fig 4.1c from the European Space Agency's Climate Change Initiative database, ESA-CCI; Hollmann et al. 2013), and extensive network of observations allow for a highly detailed look at different influences in a range of settings.

Not only is regional variability important to investigate, but temporal variability as well. Boers et al. (2015) noted that, on average, the occurrence of fog in the Netherlands has decreased significantly since the mid-1950s. They largely attribute the underlying long-term trend to a combination of decreased aerosol concentrations, offset by increased aerosol hygroscopicity. However, their study used the average observations of five stations spread throughout the country—as opposed to the individual trends at each station—which hides any potential regional variability. Likewise, they do not investigate inter-annual variability of the signal, which is not monotonic in time. Similarly, while Tardif and Rasmussen (2007) use 20 years of observational data, they do not investigate the inter-annual and long term trends in the

data. Here we will therefore assess the long-term trend and inter-annual variability in fog occurrence in order to gain a better understanding of climatic variability.

Several factors are expected to influence the overall Dutch fog climate on regional and national scales. For example, the Dutch landscape is characterized by large agricultural regions, interspersed with dense cities (Fig. 4.1c). The Randstad area, for instance, is the densely populated region in the west of the country containing the cities of Amsterdam, The Hague, Utrecht, and Rotterdam. Nestled within the Randstad region is the "Groene Hart" (Green Heart) of the Netherlands, an agricultural region dominated by the classical polder landscape. Urban environments typically experience higher nocturnal temperatures due to the heat island effect, which has been shown to impact the local fog climate at various sites (e.g., Bendix 1994; Sachweh and Koepke 1995, 1997; Steeneveld et al. 2011). At the same time, the possibility of a "wind island effect" (Droste et al. 2018) and the enhanced roughness of cities has implications for the downwind turbulent characteristics, potentially impacting a site's favourability for fog formation. However, the presence of urban features may not be entirely detrimental to the formation of fog, with increased aerosols and moisture as the result of anthropogenic emissions (Hage 1972). Similarly, the presence of the North Sea and the IJsselmeer (the large freshwater lake in the north of the country) have a significant impact on local weather conditions, through such effects as sea-breeze circulation, which can alter aerosol concentration (Arrillaga et al. 2018) and local temperatures, as well as the modulation of diurnal and seasonal temperature cycles through the increased heat capacity of the water. At the same time, the North Sea also brings with it a thermal memory in the form of the Gulf Stream circulation, making the coastal waters warmer than they would otherwise be without the trans-Atlantic transport of heat from the tropical and Equatorial regions (Palter 2015). Further, its location in northwestern Europe means that the Netherlands is influenced by large-scale teleconnections, such as the North Atlantic Osciallation (NAO), and possibly even the El Niño–Southern Oscillation (ENSO) in the tropical Pacific, which can have significant impact on northern European weather (e.g., Toniazzo and Scaife 2006; Hirschi and Sinha 2007; Riaz et al. 2017; King et al. 2018). However, the extent to which these factors influence the occurrence of fog on inter-annual and spatial scales remains unclear.

Section 4.2 describes the data used in this work as well as the methods of analysis. Following in Sect. 4.3, the fog climatologies are presented, along with investigations into the observed spatio-temporal variability of fog, including the development of an index to describe mesoscale variability in fog occurrence. A discussion of the results follows in Sect. 4.4, with recommendations for practical application of the results.

4.2 Observational Data and Methods

4.2.1 Meteorological Data

The meteorological data used in this study are from the land-based weather station network maintained by the Royal Netherlands Meteorological Institute (KNMI). All

stations conform to World Meteorological Organization standards (e.g., over grass; WMO 2014). Table 4.1 provides an overview of the stations and their data coverage, while the weather station locations can be seen in Fig. 4.1, as well as in an interactive Google map[†].

On average, the stations are separated from their nearest neighbour by 30 km. The smallest separation between neighbouring stations is 7 km, and the maximum separation 50 km. Weather station coverage is densest in the Randstad region. The majority of the weather stations are located in grass/cropland settings, with many of the stations at (former) airfields. Two main exceptions to this are the Vlissingen station (VLS; located within an urban setting on a peninsula) and Vlieland (VLE; on one of the Wadden Sea islands where the weather station is in a dune environment). Likewise, most of the stations are located in fairly flat terrain within a few metres of sea level, and with negligible slopes. The Beek station (BEE; located at the Maastricht airport in the southeast of the country) is the only major exception to this, being over 100 m above sea level, with more complex terrain surrounding the station. Other stations with local elevation elements (though on a much smaller scale) are, for example, Twente (TWE) and Deelen (DEE).

Two observational records are used; one long-term data set, and one short term. The bulk of the analysis was conducted using the long-term data set of hourly observations dating back to 1955[‡]. Hourly observations of visibility, temperature, relative humidity, atmospheric pressure, cloud cover, and wind speed/direction are used. Other variables are available, but not considered in this analysis. All stations operated continuously throughout the day, with no consistent observational gaps that would be associated with infrequent sampling. A range of observational methods were employed to determine visibility, including the use of dedicated observers and later transmissometers. While the observation method changed, there are no obvious discontinuities in the data before the year 2000, with variability also similar between different stations. After the year 2000 there appear to be some inconsistencies in the records as the instruments were again changed in the early 2000's. As a result, we only perform the long-term analysis up to, and including, the year 2000. At the same time, we restrict our analysis to stations that have complete records ($\geq$ 90% of data in a given year) for at least 40 years. Overall, the long-term data set comprises of 15 stations with complete records.

We also use data from a short-term data set of 10-minute averaged observations from 27 automatic weather stations (AWS) for the years 2012-2017 in order to assess the occurrence of individual fog events. 13 of the 15 long-term stations are also in the short-term data set. The AWS record meteorological optical range (MOR), which is an objective measure of the visibility (WMO 2014). While the absolute measurements may differ from the "historical" observations of visibility, our results are not influenced as we avoid making any direct comparisons between the two data sets. For simplicity, we also use the term "visibility" throughout the rest of the manuscript to refer to both the long-term visibility observations and MOR.

[†] embedded at https://jonathan-izett-research.weebly.com/dutch-fog.html

[‡]also used by Boers et al. 2015; available at http://projects.knmi.nl/klimatologie/metadata

Station			Lon. (°)	Lat. (°)	Elev. (m a.s.l.)	D_o (km)	Long-Term Data	Short-Term Data	Setting
1.	ASS	Assendelft	4.73	52.48	-2.0	9.2	–	2012–2018	Polder/Agricultural
2.	BEE	Beek	5.77	50.92	112.7	173.7	1955–2000	2012–2018	Rolling terrain; forest nearby
3.	BER	Berkhout	4.98	52.64	-2.4	23.8	-	2012–2018	Flat polder; grassland/arable
4.	CAB	Cabauw	4.93	51.97	-0.7	44.6	-	2012–2018	Grass polder
5.	DEE	Deelen	5.87	52.06	45.2	98.7	1955–2000	2012–2018	Slightly sloped; shrub/forest
6.	DeB	De Bilt	5.18	52.10	1.9	53.5	1955–2000	2012–2018	Half open grass/arable with buildings
7.	DeK	De Kooy	4.78	52.92	0.6	3.9	1955–2000	2012–2018	Coastal polder
8.	EEL	Eelde	6.58	53.12	3.2	35.3	1955–2000	2012–2018	Flat/open grassland
9.	EIN	Eindhoven	5.38	51.45	20.7	107.3	1955–2000	2012–2018	Half open mixed vegetation
10.	ELL	Ell	5.76	51.20	30.0	146.2	-	2012–2018	Grass
11.	GIL	Gilze-Rijen	4.94	51.57	11.9	75.6	1955–2000	2012–2018	Half open grass/arable
12.	HOO	Hoogeveen	6.57	52.75	15.8	75.8	-	2012–2018	Open arable
13.	LEE	Leeuwarden	5.75	53.22	0.3	12.3	1955–2000	2012–2018	Flat polder; mainly grass
14.	LEL	Lelystad	5.52	52.46	-4.4	62.4	-	2012–2018	Grass polder
15.	MUI	Muiden	5.09	52.34	-5.6	37.9	–	2012–2018	Polder/Agricultural
16.	NWK	Nieuwkoop	4.76	52.15	-1.2	26.0	–	2012–2018	Polder/Agricultural
17.	NWV	Nieuw Vennep	4.65	52.25	-4.9	13.6	–	2012–2018	Polder/Agricultural
18.	SCH	Schiphol	4.74	52.33	-4.2	15.5	1955–2000	2012–2018	Mixed polder
19.	SOE	Soesterberg	5.28	52.13	14.0	58.2	1955–2000	–	Forest
20.	STA	Stavoren	5.38	52.90	-1.3	18.1	-	2012–2018	Open grassland
21.	TER	Hoorn Terschelling	5.35	53.39	0.7	2.9	-	2012–2018	Grass polder
22.	TWE	Twente	6.89	52.27	33.0	145.5	1955–2000	2012–2018	Slightly sloped/rolling; mixed surface
23.	VAL	Valkenburg	4.42	52.16	-0.2	3.9	1955–2000	–	Flat/open grassland
24.	VLE	Vlieland	4.94	53.25	1.7	0.5	-	2012–2018	Dune
25.	VLS	Vlissingen	3.60	51.44	8.0	<0.1	1955–2000	2012–2018	Urban/coastal
26.	VOL	Volkel	5.71	51.66	19.9	109.3	1955–2000	2012–2018	Half open mixed grass/arable and forest
27.	WES	Westdorpe	3.86	51.22	1.7	31.3	-	2012–2018	Open polder; grass/arable
28.	WOE	Woensdrecht	4.34	51.45	15.0	44.9	-	2012–2018	Forested
29.	ZES	Zestienhoven	4.45	51.96	-5.1	19.1	1956–2000	2012–2018	Grass polder

Table 4.1: Overview of stations in the analysis, including elevation, distance to the ocean (D_o), data coverage, and physical setting of the stations. Locations can be seen in Fig. 4.1. More information is contained in the interactive map at https://jonathan-izett-research.weebly.com/dutch-fog.html

4.2.2 Assessing Fog Occurrence

Fog is defined as conditions where the observed visibility is less than 1 km (NOAA 2005). We compare the occurrence of fog at different stations by first assessing the total count of observed fog, n_{fog} (i.e., the number of observations where the visibility is at or below 1 km) in a given month or year. To account for variations in month length, observational record, and the possibility of missing data, the total count is converted to a fog fraction, F_{fog}, which is n_{fog}, divided by the number of valid observations over the comparison period, n_{obs}.

$$F_{\text{fog}} = \frac{n_{\text{fog}}}{n_{\text{obs}}} \tag{4.1}$$

Whether calculating the monthly or annual value, we restrict ourselves to periods where at least 90% of the observations are valid to avoid gaps in the record influencing our results. We define the mean of F_{fog} over all stations as the "Dutch mean". In order to remove general temporal trends (e.g., long-term decreases, or inter-annual variability), we divide F_{fog} at each station by the Dutch Mean. Taking the mean of this relative value over the entire data record gives a station's "relative fogginess", *RF*, over the long-term period.

The number of fog events are also diagnosed for the short-term data. As in Tardif and Rasmussen (2007), a fog event is identified when conditions are foggy (here using the visibility threshold of ≤ 1 km) for at least 50 minutes out of one hour (at least 5 out of 6 consecutive 10-minute observations). Two events are then deemed independent when separated by at least two hours as in Román-Cascón et al. (2016a). While there are several types of fog (each defined by their formation process), we restrict the bulk of our analysis to the occurrence of fog *in general*, regardless of the type of fog. The exception being that we investigate the relative occurrence of radiation fog—formed on weak-wind, clear-sky nights under strong nocturnal cooling due to the net imbalance of longwave radiation—and other fog types. This is because the formation of radiation fog, as opposed to, for example, advection fog, is primarily dependent on local cooling processes indicative of the underlying substrate and immediate surroundings. Such properties vary on regional scales, which should lead to regional variability in the occurrence of radiation fog. For the 21 out of 27 short-term stations with cloud data available, a simplified version of the Tardif and Rasmussen (2007) algorithm is used to classify fog events as radiation fog based on the conditions before onset. An event is classified as radiation fog if, in the hour prior to onset, cloud cover is less than 10%, 10-m wind speed is below 2.5 m s^{-1}, and the air temperature decreased. No precipitation or ceiling data are available, so they are ignored. If the above criteria are not met, then an event is classified as "other". The use of such simple criteria can—and likely does—result in some mis-classification of events, including missing some radiation events, or classifying "other" events incorrectly as radiation fog. It also neglects the possibility of combination types, such as advection-radiation fog, which is likely represented in both categories of "radiation" and "other" used here. However, we assume that the mis-classification works in both directions, while at the same time primarily assessing fog in general. As such,

the possibility of mis-classification does not significantly affect the results presented herein.

4.3 Results

4.3.1 Underlying Meteorological Conditions at the AWS

Before assessing the occurrence of fog at the weather stations, we first present the observed underlying meteorological conditions at the stations in order to highlight synoptic similarity and regional variability.

Overall, daytime and nocturnal air temperatures follow fairly uniform seasonal cycles at the weather stations (Fig. 4.2a). Day and night are determined according to local sunrise/sunset times, excluding the hour on either side of sunrise/sunset. Peak temperatures are observed in July and August, although coastal stations have a delayed peak (September), coinciding with the North Sea surface temperature (see Fig. S1a in the supplement). The probability density function (PDF) of temperatures is also fairly consistent between stations. However, the differences in observed temperature between stations are magnified when the mean diurnal cycle (daytime maximum temperature minus night time minimum temperature) is assessed (Fig. 4.2b). The stations at Vlissingen (VLS) and De Kooy (DeK), shown with dashed lines, exhibit much smaller diurnal temperature ranges, with a mean day-night difference of only 5°C. Both stations are located on peninsulas within 1 km of the North Sea (Vlissingen) or the IJsselmeer (De Kooy). Conversely, some stations have diurnal cycles of 10°C throughout the year. All stations have a fairly uniform diurnal cycle throughout the spring to autumn, with the weakest diurnal variability in winter.

Related to temperature, the seasonal cycle of daytime relative humidity is pronounced for all stations (Fig. 4.2c), with mean daytime relative humidity around 85% in winter, and as low as 70% in spring and summer. In general, nocturnal relative humidity is more uniform throughout the year, with slightly elevated relative humidity in autumn and winter. The lowest nocturnal relative humidity values, and highest daytime values, are observed at the coastal stations (reduced diurnal variability). While the ocean provides abundant moisture, it appears the reduced cooling near the coasts means the nocturnal relative humidity does not reach the same high values typically observed at the inland stations.

Seasonally, mean wind speeds at all stations vary by approximately 3–5 m s^{-1}, with stronger mean winds in winter than in summer (Fig. 4.2d). However, there is a large spread in observed wind speeds between stations, with inland stations experiencing much weaker winds overall. Vlissingen (VLS) has the highest wind speed observations, with mean seasonal values above 6 m s^{-1} throughout the year.

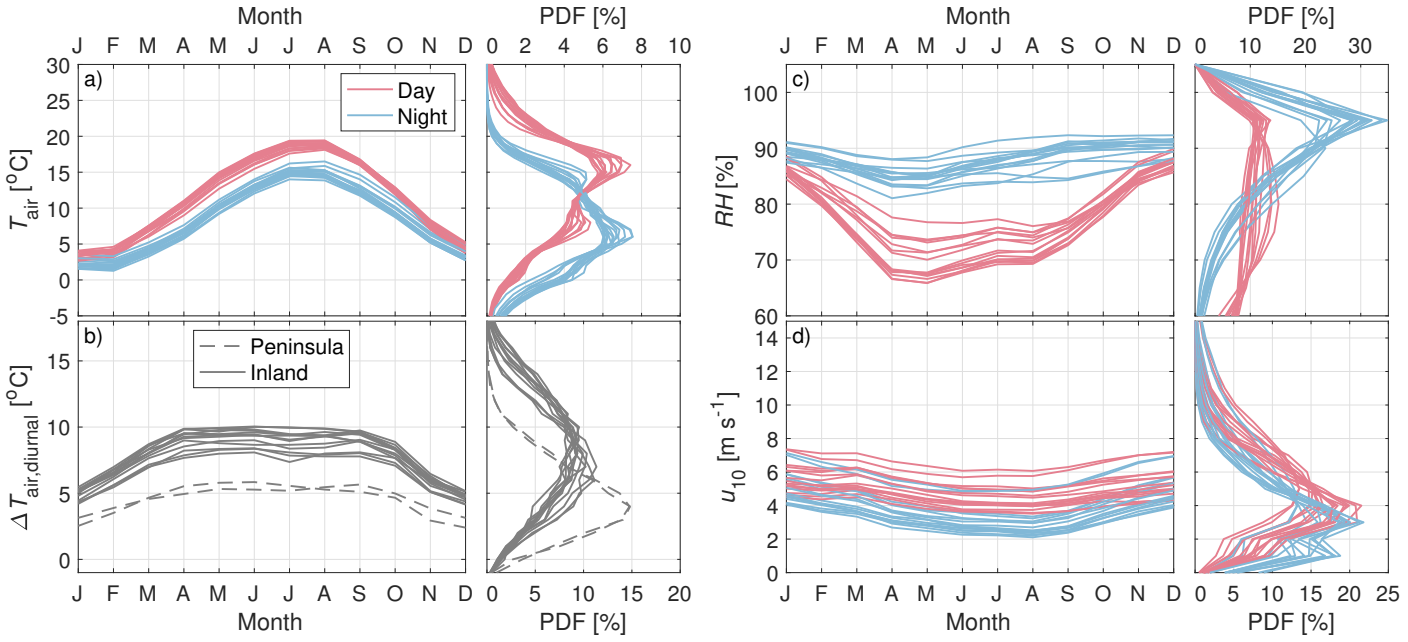

Figure 4.2: Monthly distributions of mean values and probability density functions of observed meteorological variables at the long-term stations. a) Daytime/nocturnal air temperature , b) diurnal temperature difference (day time maximum − night time minimum) with the peninsular stations of Vlissingen (VLS) and De Kooy (DeK) shown in dashed lines, c) daytime/nocturnal relative humidity, and d) daytime/nocturnal wind speed.

4.3.2 Observed Fog Climatology

Here we assess the overall fog climatology at each station. Compared to the Dutch mean, relative fogginess at the long-term stations ranges from 0.75 to 1.4 (Fig. 4.3; see Sect. 4.2.2 for definitions). In an absolute sense, the factor of two difference corresponds to over 200 hourly observations of fog per year. It should be noted that similar inter-station variability is observed when different metrics are used to assess fog occurrence, such as the total number of days on which fog is observed, or the number of non-consecutive fog observations.

Overall, stations in the centre and northeast of the country exhibit higher fog occurrence than stations in the south and west, particularly along the coast of the North Sea. The fewest observations of fog were recorded at the Vlissingen station (VLS), which is located in an urban setting on a peninsula. Low fog occurrence is also observed at the Beek station (BEE; located in the most complex terrain of all stations in the southeast of the country) and, notably, Schiphol International airport (SCH). Deelen (DEE)—located within a forest clearing next to the largest national park in the Netherlands—was observed to experience the most fog. On this, we note that analysis of the short-term data set agrees with the long-term analysis: similar spatial patterns are observed , with less fog near the coast. Vlissingen, Beek, and Schiphol again have the lowest observed fog occurrence.

Interesting to note is the difference in fog occurrence, even over short distances. For example, the De Bilt (DeB) and Soesterberg (SOE) stations are located within 7 km of each other. However, Soesterberg is, most years, 10% foggier than De Bilt in the long-term record. This is likely due to the more urbanized setting of the De Bilt station, which is located at the KNMI headquarters just outside the city of Utrecht, whereas Soesterberg is a more rural location that was a military air base until 2008.

Greater than 50% of all of the observed fog events (in the short-term dataset) were classified as radiation fog events. This, however, varies according to station (see Fig. S2 in the supplement). For example, coastal stations experience only 10% radiation fog events, with the inland rural station at Ell having the greatest proportion of radiation fog events (82%). Overall, the frequency of radiation fog events increases inland. However, while the number and type of events varies, the character of events (i.e., onset time, event duration, mean visibility) are similar across all stations (Fig. S3 in the supplement). When a fog event is observed at one station, an event is generally also observed at one or more other stations within a few hours ($>$ 90% of all events; not shown). However, fog events at Beek (BEE; hilly station in the south, located furthest from any other station) occur more often in isolation from events at the other stations (20% of all events at Beek occur in isolation).

Seasonally, fog occurs, on average, most frequently in the autumn and winter months, accounting for 75% of the total annual fog (Fig. 4.4a). All stations exhibit a nearly identical annual distribution to the Dutch mean, with the most fog occurring in late autumn and winter, and the least fog in summer (see Fig. S1b in the supplement). That being said, the peninsular stations of De Kooy (DeK) and Vlissingen (VLS) exhibit the largest seasonal amplitudes, with less than 2% of the annual fog occurring

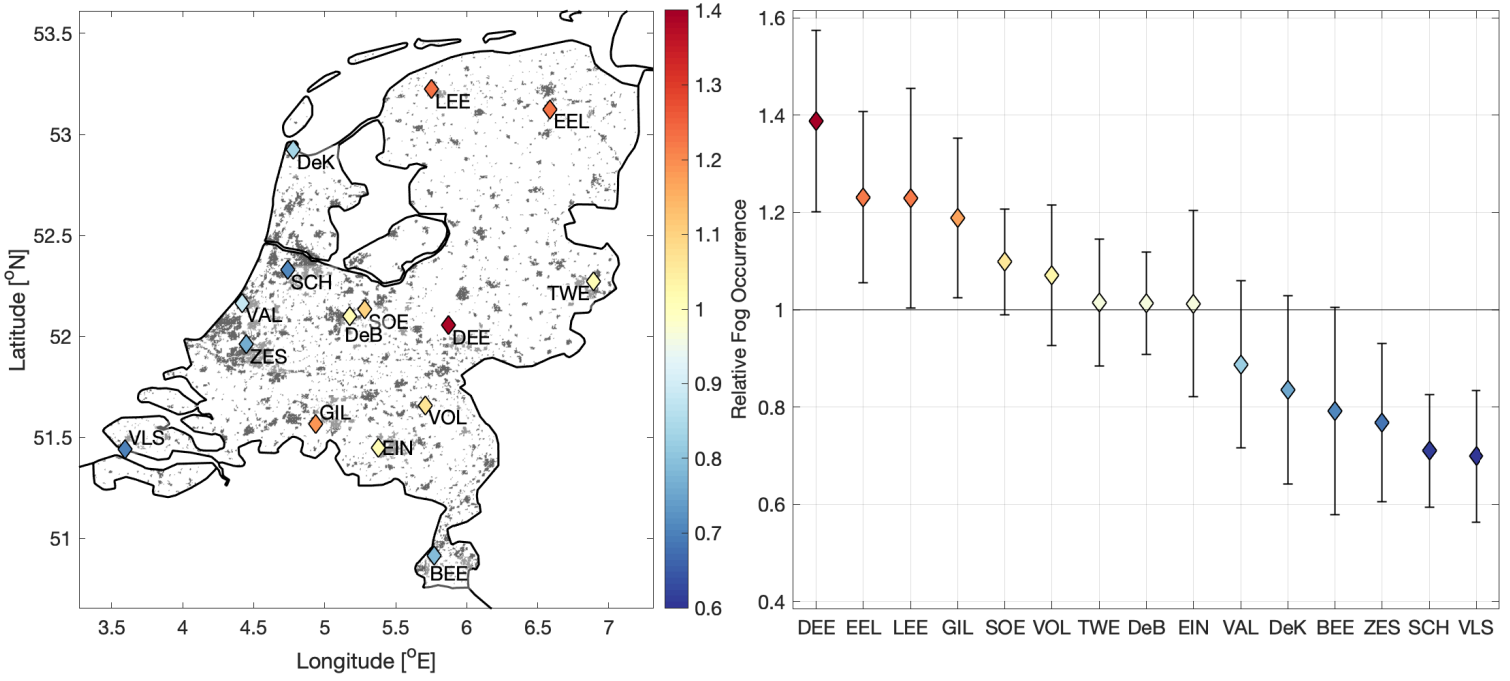

Figure 4.3: Relative occurrence of fog (compared to the Dutch mean) at each station between 1955 and 2000. The errorbars indicate one standard deviation.

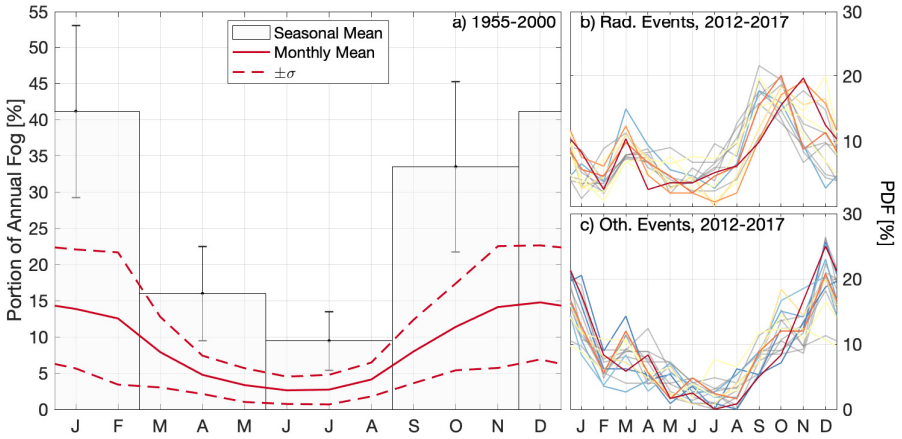

Figure 4.4: Mean fog occurrence throughout the year. a) Seasonal and monthly fog occurrence between 1955 and 2000, averaged for all stations in the Netherlands. Monthly occurrence of b) radiative, and c) non-radiative fog events between 2012–2017. The colours are the same as in Fig. 4.3.

in July and August, and greater than 17% of the annual fog in each of the winter months.

Their seasonal signals also lag the mean signal by one month, corresponding to the seasonal sea surface temperature of the North Sea, which reaches its maximum in September. Conversely, the stations with the most fog overall have the most uniform seasonal distribution, with the summer months having at least 10% of the annual fog. This points to local favourability of the sites as they are able to form fog in otherwise less favourable conditions (i.e., shorter nights). Likewise, the general seasonal pattern is also observed in the short-term data, with radiative events occurring most frequently in autumn, and uniformly throughout the rest of the year (Fig. 4.4b). The other fog types, including advection fog, occur almost exclusively in winter (Fig. 4.4c) when the land is considerably cooler than the ocean. This is what drives the strong seasonal cycle at the coastal stations where “other” fog is more common.

Boers et al. (2015) showed that the occurrence of fog in the Netherlands has decreased significantly since the 1950s. However, they looked at the trend based on the mean annual occurrence of five stations. Figure 4.5 shows that the long-term trend dating back to 1955 is significantly different at different stations. Fitting a linear regression to the long-term annual fog occurrence between 1955 and 2000, the mean trend (with 95% confidence interval) of all stations is -0.07 ± 0.02% per year (Fig. 4.5b). While this is negligible on an annual timescale, over five decades this amounts to a total reduction of 3.3 ± 1.0% (roughly half of the 1955 value; Fig. 4.5c). The station with the most rapid decline in fog occurrence between 1955 and 2000 is the Eindhoven station (EIN) with a slope of −0.11 ± 0.03% per year,

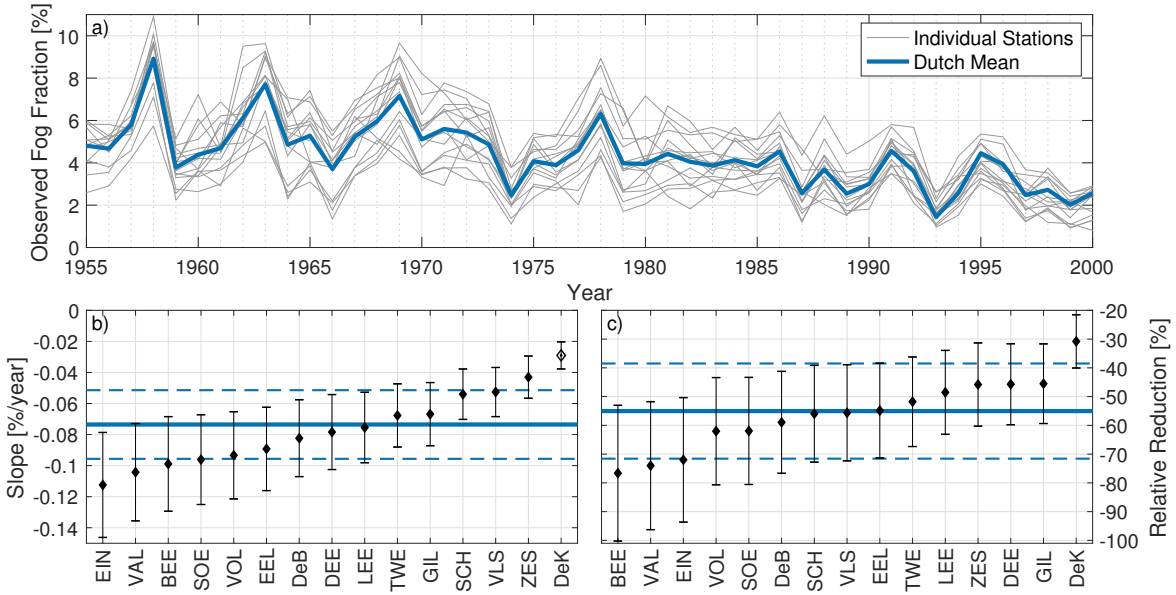

Figure 4.5: Annual occurrence of fog from 1955 to 2000 at each station, and the mean of all stations. a) Observed fog fraction (F_{fog}). b) Long-term trend in fog fraction (slope) obtained through linear regression. c) The relative reduction in fog over 40 years, compared to the 1955 value. Note, the trend at De Kooy is not statistically different from 0.

amounting to a total reduction between 1955 and 2000 of 72% of the original 1955 value! Conversely, the trend at De kooy (DeK) is statistically insignificant.

4.3.3 Factors Influencing the Inter-Annual Variability of Fog Occurrence

The observed fog occurrence in the Netherlands over the past several decades is punctuated by large inter-annual variability (Fig. 4.5a). In many cases, the inter-annual variability is far greater than the inter-station variability, and long-term decline in fog occurrence. Given that all stations exhibit similar variability (i.e., the timing and magnitude of peaks/troughs in fog occurrence is roughly the same), we focus on the Dutch mean signal, rather than attempting to discern temporal variability at individual stations.

Overall, the inter-annual variability is characterized by a multi-year oscillatory signal with a period of approximately 4-6 years (Fig. 4.5). Within each cycle, the observed occurrence of fog can be more than doubled; e.g., in 1958 roughly 9% of the observations were foggy, compared to 1959, when just 4% were. Much of this inter-annual variability is due to variability in the winter months of December, January, and February. In fact, the wintertime fog anomaly accounts for over 90% of the total annual anomaly (not shown).

In general, positive annual fog anomalies occur in years with winters that have weaker winds, while negative fog anomalies occur in years with winters that experience stronger winds (Fig. 4.6d). Likewise, the frequency of northeasterly winds is higher than average in years with more fog, and lower than average in years with less fog (not shown). This points to the significance of synoptic pressure forcing. We look specifically at years that are either anomalously foggy (foggy years) or anomalously clear (clear years) by more than 1 standard deviation (1σ). In total, there are seven such foggy years, and seven clear years between 1955 and 2000. To assess the synoptic pressure forcing in these years, we make use of the monthly mean sea level pressure (*SLP*) from the CERA-20C re-analysis (Laloyaux et al. 2018, retrieved at a horizontal resolution of 0.1°). Comparing the mean wintertime (December, January, February) *SLP* anomaly in the foggy years to the mean *SLP* anomaly in the clear years, there is a significant difference in the overall field in the northern hemisphere (Fig. 4.6a and b). On average, the mean sea level pressure over Northern Europe is higher in foggy years (a positive anomaly), and lower in clear years (negative anomaly). Important to note is that the increased pressure is not necessarily pointing to high pressure conditions, but rather a weakening of persistent low-pressure conditions. This is due primarily to the strength and position of the Icelandic low. In foggy years, the 1000 hPa contour level is shifted further west toward Newfoundland, and reduced in extent, while in clear years, the low-pressure region covers a much larger area, with lower pressures over Europe.

The change in the pressure field over northern Europe in winter leads to changes in the magnitude of the pressure gradient, $|\nabla P|$, over the Netherlands. Looking at the wintertime anomalies, there is a negative correlation between the pressure-gradient

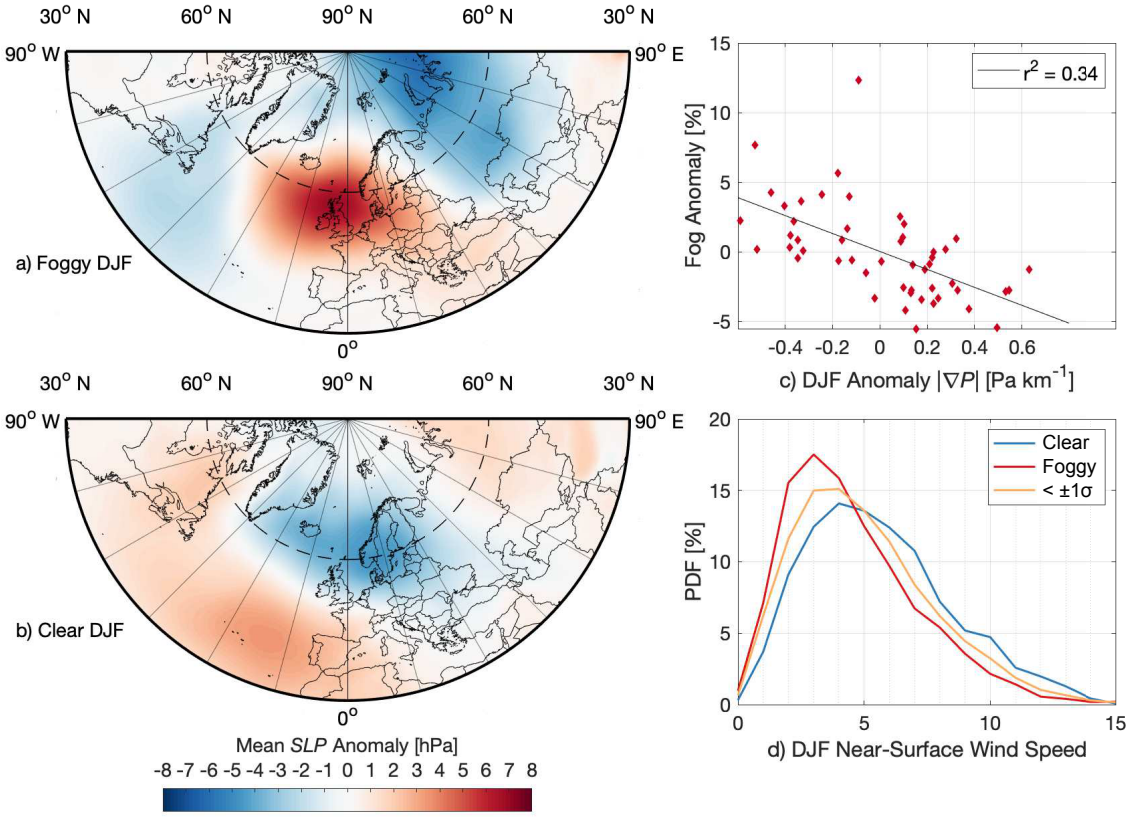

Figure 4.6: Average winter conditions 1955-2000. a) and b) Mean SLP from the CERA-20C reanalysis (Laloyaux et al. 2018) during years with $> 1\sigma$ fog (or clear) anomaly; c) seasonal fog anomaly as a function of mean wintertime $|\nabla P|$; and d) PDF of near-surface wind speeds in foggy and clear winters.

forcing and the occurrence of fog (with an r^2 value of 0.34; Fig. 4.6c), with winters that experience weaker forcing (negative anomaly in $|\nabla P|$) observed to have more fog. Ultimately, the weakened pressure-gradient forcing is what results in the observed weaker near-surface wind speeds during foggy years (van der Linden et al. 2017; Fig. 4.6d), which are favourable for fog formation.

Beyond the anomaly in $|\nabla P|$, factors including anomalies in sea surface temperature, the strength of the North Atlantic Oscillation (NAO), the position of the Icelandic Low, and the absolute SLP anomaly over Europe were all investigated in an effort to identify a single index that could describe the inter-annual variability in fog occurrence. However, other than the potential link to $|\nabla P|$, no stronger, direct correlation could be found linking anomalously foggy/clear years to the other conventional indices. This is not necessarily an indication that there are other synoptic influences at play, but rather that one single index cannot fully describe the relationship between synoptic pressure and fog variability the Netherlands.

4.3.4 Influences on Regional Fog Occurrence

In this section we look to describe the regional variability of fog in relation to other factors, ideally in terms of non-meteorological variables. Given the lack of significant topography at most of the stations, elevation is not included. We focus instead on two main factors: the influence of the North Sea, and the role of urbanization.

The Dutch climate is strongly influenced by the North Sea. With increasing distance from the coast (i.e., distance from a station location to North Sea, here excluding the IJsselmeer), the magnitude of the clear-sky diurnal cycle (daytime maximum minus night-time minimum temperature) increases (Fig. 4.7a). This is due to the high heat capacity of the water, and its modulating effect on local diurnal variability, as well as the fact that wind speeds are, on average, stronger at the coastal stations than inland (Fig. 4.7b). The combination of stronger cooling and weaker winds inland is favourable for fog formation. With distance from the coast, the fraction of fog events that are radiative increases (see Fig. S2 in the supplement). However, relative fog occurrence is not directly related to distance from the ocean. While the occurrence of fog is indeed lowest at the coast, it is not a monotonic increase inland, with decreased relative fog occurrence further inland (Fig. 4.7d). This non-linear relation indicates there is more involved than simply an ocean influence.

The coastal region between Rotterdam and Amsterdam is, however, also more urbanized with the presence of the Randstad region. We therefore use the European Space Agency's Climate Change Initiative (ESA-CCI) land use database (Hollmann et al. 2013) to compare the urban fraction; i.e., the fraction of the area surrounding a station (in this case within a radius of 5 km) that is classified as urban, against distance from the ocean (Fig. 4.7c). Indeed, the most urbanized stations are within approximately 50 km of the North Sea, after which they are predominantly rural until Eindhoven (EIN) and Beek (BEE), which are again more urbanized. The general pattern is nearly the inverse of the pattern seen in fog occurrence.

The influence of urban surroundings on fog occurrence is most apparent when

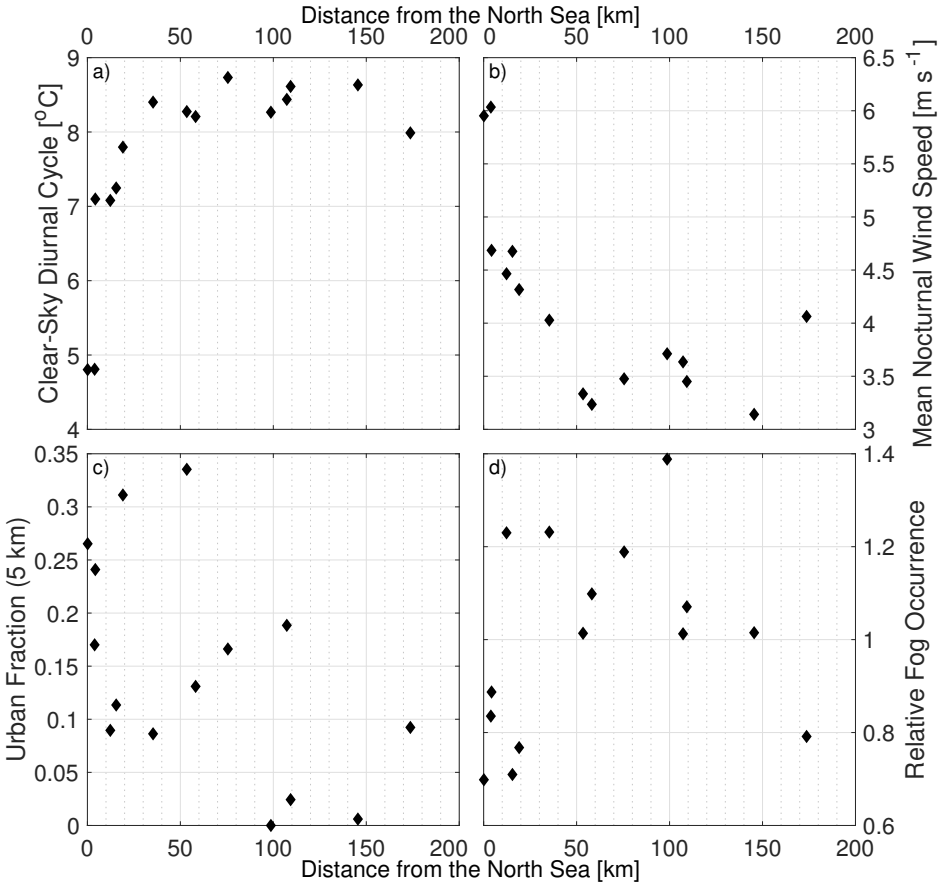

Figure 4.7: Local properties at the weather stations (1955-2000) as a function of distance from the North Sea. a) mean diurnal temperature difference, b) mean nocturnal wind speed, c) urban fraction within 5 km, and d) relative fogginess.

looking at the occurrence of fog events at the Zestienhoven weather station (ZES), which is notable for its setting. Located at the Rotterdam–The Hague airport, the city of Rotterdam lies directly to the south, while to the north are predominantly agricultural fields stretching for more than 10 km (Fig. 4.8a). The land use contrast can be seen when assessing the wind directions from which radiation fog ultimately forms (Fig 4.8b). To focus primarily on radiation fog, the observations were filtered according to nocturnal conditions with wind speeds below 5 m s^{-1}, relative humidity above 90%, and clear skies. In such cases, the mean wind direction is clearly from the south/southwest (the direction of Rotterdam) and the northeast. If the upwind land-surface heterogeneity would play no role in influencing the fog climatology, then the distribution of wind direction just before fog events would be expected to have the exact same distribution as the winds in general. However, radiation fog forms almost exclusively when wind is blowing from the north, with a significantly reduced contribution from the south. In other words, radiation fog forms less than half

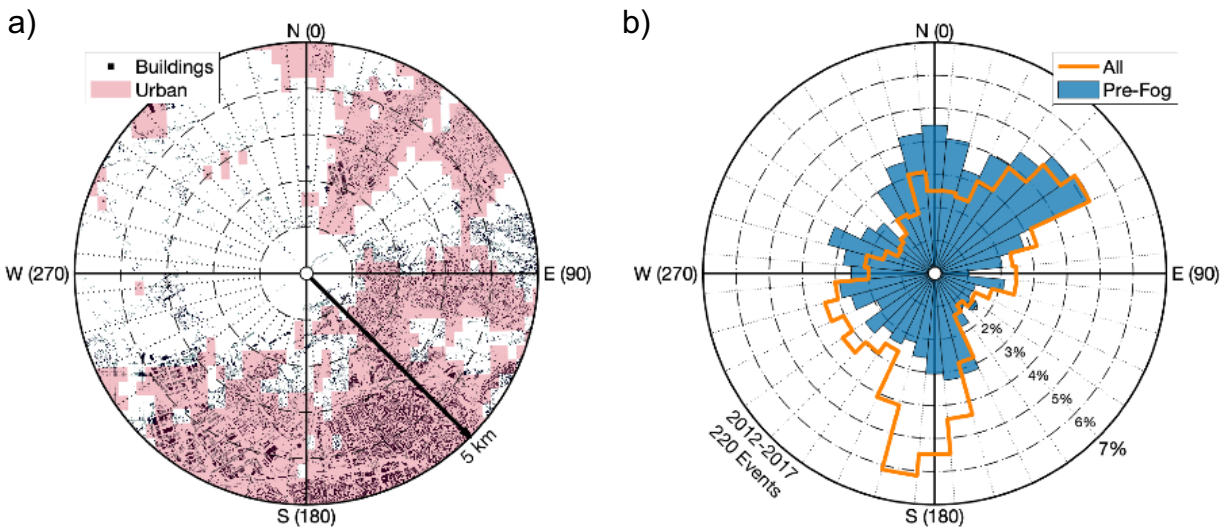

Figure 4.8: Influence of urbanization on the occurrence of fog at Zestienhoven (ZES). a) Land use within a 5-km radius of the station with black indicating buildings in the AHN2 elevation data set, and pink the 300-m grid cells that are classified as urban in the ESA-CCI land use database. b) Probability density function of observed wind directions (i.e., percentage as a function of direction; not a wind rose) for all weak winds with high relative humidity, and the subset that are up to 3 hours before the onset of a radiation fog event.

as frequently as would be expected when the wind is blowing from the city of Rotterdam. It should be noted that this distribution does not vary seasonally. While the Zestienhoven station provides the most extreme example of a directional preference for fog formation, directionality is observed at other stations as well (see Fig. S4 in the supplement), including Schiphol airport (SCH; also a preference for northerlies, with terminal buildings to the southeast), Cabauw (CAB), and Beek (BEE; with increase in fog from the north due to upslope, topographic effects). On the other hand, rural stations, such as Eelde (EEL),

show little to no directional preference. It should be noted that wind direction is poorly defined under weak-wind conditions; however, we assume erroneous observations are normally distributed (i.e., they do not lead to peaks in the distribution).

The Regionally Weighted Index, *RWI*

Based on the apparent ocean and urban influences on Dutch climate and fog occurrence, we identify a simple index combining the two influences of ocean and land use, which we call the "Regionally Weighted Index" (*RWI*). Within a given radius, *R*, the fraction of a given angular bin (i.e., wedge) that is classified as either urban or ocean (f_{uo}) is determined (here, from the ESA-CCI land-use database; Hollmann et al. 2013). This "urban or ocean fraction" is calculated as simply the number of grid points within a wedge that are classified as either urban or ocean, divided by the total number of gridpoints within that wedge. The weighted mean of all angular bins (where a refers to the bin index) is then taken

$$RWI(R) = \sum_{a} w(a) f_{uo}(a,R). \tag{4.2}$$

The weights, $w(a)$, are calculated from the underlying wind distribution (e.g., PDF in Fig. 4.8b). This allows more weight to be given to the region from which the wind predominantly blows. In the case where the wind PDF is not known, the *equally weighted RWI* is simply the mean value of $f_{uo}(a,R)$ (i.e., $w(a)$ is equal to $1/n_{\text{bins}}$, where n_{bins} is the number of wedges). It should be noted that the use of the index to compare the relative likelihood of fog at two different locations requires that they are in similar settings (for example, that the synoptic climatology is the same, as well as aerosol quantity and composition).

As a simple example, assume a region divided into four quadrants. In each of the four angular bins, f_{uo} is 0.75,0.5,0.25, and 0, respectively. The equally weighted value of *RWI* is the mean: 0.375. If the wind blows 70% of the time from quadrant 1, and equally from the others (10%), then w is 0.7,0.1,0.1, and 0.1, respectively, and the wind-weighted *RWI* is equal to 0.6. On the other hand, if the wind blows 70% of the time from quadrant 4, and equally from the others (10%), then $w = 0.1, 0.1, 0.1$, and 0.7, respectively, and *RWI* is just 0.15.

Here we calculate *RWI* at each station in the long-term data set using 36 angular bins (centred every 10°) and a radius of 5 km. 5 km was chosen in order to allow for sufficient data points (e.g., 1 km would only include a limited number of land-use cells given the 300-m resolution of the database), while at the same time ensuring that the index is still regional (a radius of 10 km would include locations too far away from the observation site to be relevant). The calculated values range from as low as 0.05 at the rural station of Deelen (DEE), up to 0.65 at the coastal-urban station of Vlissingen (VLS). Figure 4.9 shows the comparison between relative fogginess and *RWI* at all stations, weighted according to the underlying wind PDF at each station (as in, e.g., Fig. 4.8). An analogous figure showing the relationship between *RF* and the equally weighted *RWI* is presented in the supplement (Fig. S5). While

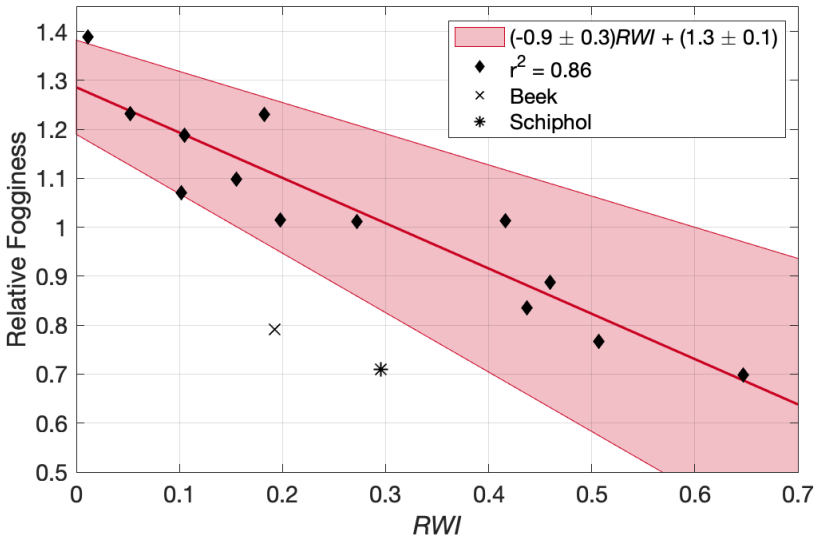

Figure 4.9: Relative fogginess as a function of *RWI* (Equation 4.2) calculated using 36 angular bins and a radius of 5 km. The linear regression excluding Beek (BEE) and Schiphol (SCH) is shown with 95% confidence intervals indicated by the shading (Equation 4.3).

not perfect, the agreement between the two variables is striking, with correlations of 0.56 and 0.62 for the equally-weighted and weighted indices, respectively. Only two stations deviate significantly from the others, Beek (BEE) and Schiphol (SCH). This is not surprising. Beek, as above, is in the most complex terrain of all stations, and is meteorologically isolated from the other stations, with few fog events occurring at the same time as at other stations. Being located at a major international airport, the Schiphol station is surrounded by far more concrete and urban construction than is resolved in the land-use data set (i.e., should be further to the right on the x-axis). Further, the constant flight activities of the airport can have a significant impact on the localized meteorology (see the Appendix). The two stations are also statistical outliers according to the Generalized Extreme Studentized Deviate test (GESD; Rosner 1983). Removing the two stations from the regression for the physical reasons mentioned above, the strength of the correlation increases significantly, up to 0.82 and 0.86 for the equally weighted and weighted calculations, respectively, with *RWI* providing a strong indicator of whether or not one location may be regionally favourable for fog occurrence compared to another.

With Beek and Schiphol excluded, the regression (and 95% confidence intervals) relating relative fogginess, *RF*, to *RWI* is

$$RF = (-0.93 \pm 0.29)\,RWI + (1.3 \pm 0.1) \tag{4.3}$$

If using the *equally weighted RWI*, the slope and intercept are -0.85 ± 0.27 and -1.3 ± 0.1, respectively.

4.4 Discussion

Fog occurrence in the Netherlands over the past half century was assessed using observations from a dense network of stations. In spite of the relatively small extent, and generally uniform topography of the Netherlands, the overall occurrence of fog was shown to vary significantly, even within a few kilometers. In general, stations in the centre and northeast of the country exhibit greater fog occurrence than those in the south, and particularly those near the coast (Fig. 4.3).

Since the mid-1950s, fog occurrence has decreased—on average—throughout the country (Fig. 4.5). Boers et al. (2015) attribute much of this decline to the changing quantity and composition of aerosols. However, the trend is not uniform throughout the country, with the largest decrease occurring at the Eindhoven station (EIN); a 50-year reduction of over 70% of the original value (-0.11% per year). On the other hand, the De Kooy station (DeK) showed comparatively little change in observed fog occurrence over the same period. We do not investigate the causes for this in great detail; however, it is likely related—at least in part—to the relative changes in urbanization over the past few decades. Eindhoven experienced a technology boom in the second half of the 20th century, with the founding of its Technical University, and the expansion of the Phillips electronic company, with significant population growth over the same period (Ekamper et al. 2003). Of course, linking the socio-economic expansion of a region to fog occurrence is tenuous, but not unreasonable.

While the general trend in fog occurrence is negative throughout the past half century, the inter-annual variability of fog occurrence is much greater, accounting for over a factor of 2 difference from one year to the next (Fig. 4.5). No strong quantitative relationship could be found to relate the fog anomaly to synoptic indices (e.g., the NAO); however, there is a clear signal in the large-scale pressure-gradient forcing over Europe in years with significantly more or less fog (Fig. 4.6). Particularly in anomalously foggy years, the winter-time sea level pressure was higher, on average, over northwestern Europe, corresponding with a westward shift of the Icelandic Low toward Newfoundland, and a general weakening of low-pressure conditions over northern Europe. The result of the *SLP* anomaly is primarily manifest as a change in wind speed, due to a change in pressure-gradient forcing. van der Linden et al. (2017) showed that different boundary layer stability regimes can be classified according to the pressure-gradient forcing, with weaker forcing corresponding to more stable nocturnal boundary layer conditions. As such, one can infer from the weaker pressure gradient that the nocturnal conditions are more often (very) stable in the foggy years. Given that stable conditions are favourable for the formation of radiation fog, and that radiation fog is the most common type of fog in the Netherlands, this is significant.

Fog as far away from the North Atlantic as the Indo-Gangetic plains has been linked to northern hemisphere teleconnections (Hingmire et al. 2018). However, while we could find no such direct link to a single teleconnection, the link between large-scale pressure forcing and Dutch fog that we find is not surprising given the established relationship between synoptic pressure fields, including the state of tele-

connections, and weather in Northwestern Europe. For example, previous studies have shown links between inter-annual variability in Northwestern European temperature and wind speed—particularly in winter—to such synoptic influences as the North Atlantic Oscillation, and even the El Niño–Southern Oscillation (Toniazzo and Scaife 2006; Hirschi and Sinha 2007; Riaz et al. 2017; King et al. 2018; KNMI 2019). It should be further noted that while we only claim weak correlation between the pressure-gradient forcing and the fog anomaly, the other studies also only found relatively weak correlations ($\sim$0.4) between the synoptic indices and their relevant variables of interest. In terms of predictability, it is conceivable that the large-scale pressure gradient might be used to forecast in advance whether a given winter may be more or less foggy than usual, even though a direct quantitative relationship is difficult to define. However, the exact the pressure field, including the state of such teleconnections as the NAO—particularly the onset of anomalous events—are difficult to forecast beyond a few days to weeks (e.g., Jung et al. 2011; Domeisen et al. 2018). As such, the the utility of such forecasts for statistical fog prediction (i.e., being able to say whether a given winter will be more or less foggy than average) is limited.

Regionally, we relate the relative occurrence of fog to the mesoscale surroundings of a station. Specifically, stations that are in a more urban or ocean-influenced environment are observed to have less fog on average than those in more rural, inland settings (e.g., Fig. 4.3). This is due to the thermal and climatic influence of the surfaces, through, for example, the influence of the urban heat island effect (e.g., Bendix 1994; Sachweh and Koepke 1995, 1997) and the increased thermal capacity of the water. A striking example of the role surrounding conditions play in the relative occurrence of fog is the Zestienhoven station where, in direct contrast to the underlying wind distribution, fog rarely forms when wind is blowing from the city of Rotterdam (Fig. 4.8). The results are similar to those found by Tardif and Rasmussen (2007), with urbanization significantly reducing the overall fog occurrence. However, they also found increased fog occurrence at coastal stations, whereas the most fog was observed in the centre of the Netherlands. This could be due to the difference in landscape (more complex terrain in the New York City study region), or climatological differences in, for example, offshore water temperatures and prevailing wind direction.

Our analysis does not look directly at where the observed fog is formed. However, it is possible that fog may form in one location, and then be advected elsewhere (for example, inland fog advected to the coast, or sea fog advected inland, by the land-sea circulation). That being said, systematic advection of fog is still a regional effect that would naturally be included in the analysis. At the same time, if it is not occurring systematically, but randomly, then it will also not affect our climatological analysis as random events will be masked by more dominant patterns.

One factor we did not—and could not—consider in detail is the role of aerosols in determining the relative occurrence of fog. This was primarily due to the complexity of assessing the role aerosols play in terms of both hygroscopicity and overall number concentrations, as well as the limited availability of coincident observational data.

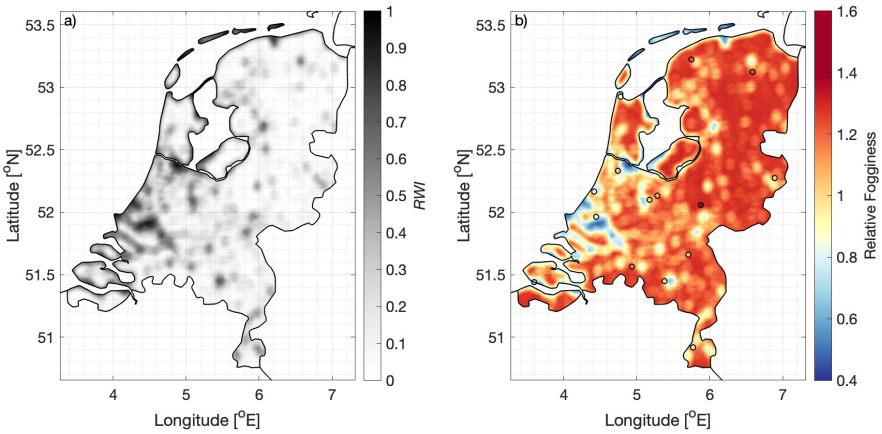

Figure 4.10: Map of the Netherlands showing the a) equally weighted *RWI* calculated from the ESA-CCI Land Use database, and b) the relative fogginess (from Equation 4.3) expected throughout the country. The observed relative fogginess at the weather stations is shown in the colour of the scatter points, allowing for comparison to the estimated value.

One would expect, however, that aerosol composition is highly variable throughout the country, influenced by such factors as upwind urbanization or agriculture. At the same time, the ocean influence extends to the aerosols, with sea salt (a hygroscopic cloud condensation nucleus; CCN) most abundant near the coast and decreasing in concentration with distance from the ocean. Manders et al. (2009) show that the decrease is nearly linear from the ocean toward the southeast, with the lowest aerosol concentrations in the country found near the Beek station (BEE). This may, in part, be an explanation for the low occurrence of fog at Beek. However, a full aerosol study would be required to assess the overall impact on fog throughout the country.

4.4.1 Applying *RWI*

The concept of the Regionally Weighted Index (*RWI*, Equation 4.2) demonstrates that knowing the surrounding land use leads to the ability to determine—on the mesoscale—whether one location will have more fog than another (assuming the stations are in similar settings; e.g., the synoptic conditions are the same, as well as the aerosol content). Figure 4.10, for example, shows the equally weighted *RWI* (i.e., without observations of wind directon) in the Netherlands converted to a relative fogginess map. Coastal and urban influences are immediately apparent. While for a vastly different region, the hypothetical map is similar in character to the image in Lee (1987), with urban "pockets" clearly discernible. *RWI* can, as a result, potentially be used with a view toward practical applications. Unlike existing indices, such as the fog potential index of Perry and Symons (2002), *RWI* is straightforward to define, relying on quantitative measures, without subjective attribution of a value to a given variable (e.g., the "general expression of any environmental factors").

Unfortunately, the stations investigated here are still not as diverse as would be desired. While the mesoscale variability is large, in situ characteristics of the stations are largely similar. For instance, given that all stations assessed conform to WMO standards, they are all locally above grass. This means that highly localized features, such as the immediate land cover or soil type can not be easily assessed, in spite of their impact on near-surface temperature inversions (van de Wiel et al. 2017). Likewise, while the flat terrain of the Netherlands allows for simpler analysis of other factors, regions with more complex topography will need to be considered, perhaps including an additional scaling term that measures the variability of topography, such as the variance, or even the divergence ($-\nabla^2$) which could give an indication of where cold air would be likely to pool. Further testing of *RWI* in a range of settings—through further observational and numerical study—is therefore required, and an additional scaling may need to be incorporated. It should also be noted that the value of *RWI* changes with R (the radius of interest), and the land-use dataset from which the urban/ocean fraction, f_{uo}, is calculated. While a radius of 5 km was chosen in order to balance representativity with sufficient land-use data, the "correct" value for R is difficult to define objectively. Perhaps a weighted distance can be included to give more weight to closer cells, making the choice of R insignificant. As it stands, the "correct" value for R is difficult to define objectively.

The two outliers in the relationship between relative fogginess and *RWI*—Beek (BEE) and Schiphol (SCH)—are obvious outliers in terms of the stations' physical characteristics. Beek, located in the south of the country, is completely isolated from the other stations with an independent fog climatology, and surrounded by complex topography. It may also have lower CCN concentrations in the form of sea salt aerosols (Manders et al. 2009). This violates the assumption that the stations be in a similar synoptic setting. Likewise, the Schiphol station is located in the highly urbanized setting of one of Europe's busiest airports. The buildings and runways are not resolved in the wider land use analysis, nor can airport operations be accounted for, such as the movement of airplanes which can increase surface temperatures significantly (see the Appendix), pointing to a "built-in" fog dispersal system.

4.5 Conclusions

The Netherlands provides an excellent setting for studying the influences on fog occurrence in the absence of significant topography. Through the long-term analysis of visibility observations throughout the country, fog is shown to be highly variable in both time and space. Inter-annual variability in the observed signal is shown to be related to changes in the synoptic pressure field over the northern hemisphere, with increased wintertime sea level pressure over Scandinavia and northwestern Europe leading to increased fog occurrence; likely related to the increased stability of the near-surface boundary layer. This inter-annual variability is considerably larger than the observed long-term decrease in fog.

Inter-station variability is similarly large throughout the Netherlands. Over the past 45 years, fog was observed up to twice as frequently in rural locations as semi-

urban and coastal locations. Combining this, a simple index was identified to describe the mescoscale influences of water bodies and urbanization, providing an indication of whether one location will have (relatively) more fog than another. This has very practical applications, with the potential to assist, for example, in infrastructure planning and or risk assessments (even without the need for long-term meteorological observations when using the equally weighted *RWI* as in Fig. 4.9). However, it will first need to undergo further extensive testing in a range of settings, such as over different land surfaces.

We suggest *RWI* also be used in other locations beyond the Netherlands, testing its limitations and potential. Provided the separation between locations is not too large—and therefore synoptic setting is similar—it should be able to provide a consistent estimate of the relative fogginess between two locations. While complex topography will affect the comparison, it may be possible to add another weighted term describing topographic variability in the case where two locations are not the same; for example, the elevation variance, or the relative elevation of the location to its surroundings. In order to facilitate the analysis, satellite-derived climatologies, such as presented by Egli et al. (2019) would be extremely useful.

The observational results presented here also have wider implications for the simulation of fog. They further highlight the importance of the various range of scales on which fog is influenced. The climatology of fog is driven by wider mesoscale and synoptic forcing conditions. Particular attention should therefore be paid to ensuring the accuracy of synoptic forcing and mesoscale land surface characteristics. That being said, individual fog events, as opposed to the climatology, will be highly sensitive to localized conditions. This reinforces the need to have accurate models on a range of scales, which has been identified in several previous works (e.g., Gultepe et al. 2007; Steeneveld et al. 2015).

4.A Weather Modification by Airplanes?

Fog occurrence is shown to be considerably lower than would be expected at Amsterdam's Schiphol International Airport (weather station SCH here) when compared to other stations in the Netherlands. This is likely related to the unique environment around Schiphol, and indeed most major airports.

According to the ESA-CCI land use database, the majority of the area surrounding Schiphol is agricultural. However, it is locally highly urbanized, with the expansive terminal buildings and large areas of cement making up the many taxiways and runways (Fig. 4.11). Bergot et al. (2015) show that heterogeneous surfaces and airport structures can have a large impact on localized fog formation. At the same time, the airport is spread over a large area (close to 3000 hectares; Schiphol 2019), with the most remote Polderbaan runway (18R/36L) located more than 4 km from the main terminal buildings. Observations show that there is a significant difference in fog occurrence measured around the airport, with the Polderbaan far more susceptible to fog and low-visibility conditions (Kattenberg et al. 2013).

There is also a further highly localized feature at Schiphol (in both space and time) that affects the observed weather: airplanes. Schiphol is one of Europe's busiest airports, with almost 500 000 airplane movements (take-off/landing) per year (Schiphol 2019). First shown in Schulte (2017), the take-off of airplanes can lead to temporarily elevated near-surface wind speeds, and subsequent near-surface warming.

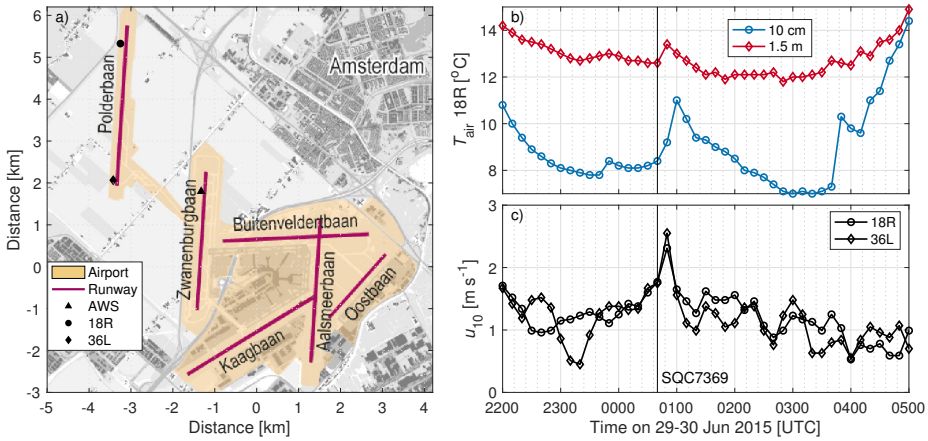

Figure 4.11: a) Map of Schiphol airport and surroundings (modified from: CLO 2017). 10-minute averaged observations of b) 10-cm and 1.5-m temperature next to runway 18R, and c) 10-m wind speed measured next to 36L and 18R, with the northbound take-off time of flight SQC7369 indicated—the only large aircraft to take off during the night—just after 0040 UTC.

Figures 4.11b and c show 10-minute averaged temperature and wind speed measurements made at stations located along the Polderbaan and Zwanenburgbaan (18C; the AWS used in this study) runways on the night of 29–30 June 2015. Skies remained cloud free throughout the night, which, combined with weak wind conditions, led to very stable temperature stratification near the surface (a maximum difference of 4.5°C between 10 cm and 1.5 m). A few double-engine aircraft (e.g., Airbus 321) took off on runway 36L (northbound take-off on the Polderbaan runway) during the night, but only one very large aircraft, a Boeing 747 with four engines (Singapore Airlines Cargo flight 7369). The observations show a spike in wind speed, followed by near-surface warming at the same time as the flight's northbound departure on the Polderbaan runway. At 10-cm height, the increase in temperature is around 3°C! This is most likely due to both the downward heat transport from the engine wake (through enhanced turbulent mixing and vertical transport), and the input of energy to the system from engine exhaust. After take-off, it took an hour for temperature to recover to pre-take-off conditions. This is one of the most extreme examples in the data set, but it is not the only example.

The near-surface warming brought on by jet engines has implications for fog at airports. Appleman and Coons (1970) showed that the wake of a stationary jet can dissipate fog in a matter of minutes, in a fashion similar to the Fog Investigation

Dispersal Operation (FIDO) system developed during the Second World War, which used flames on either side of the runway to mix and evaporate thick fog so that airplanes could land (Science 1945). Combined with the thermal influence of the urbanized surfaces at airports, the increased turbulent mixing (including downward mixing of drier air aloft) and reduced cooling/periods of sudden warming due to aircraft operations, will make the sites unfavourable for fog, particularly radiation fog. That is likely why Schiphol appears to have less fog than would be expected when compared to other Dutch stations (Fig. 4.9).

Overall, the highly local influence of airport urbanization and airplane movements may result in a surprising benefit. While fog can have a large impact on airport operations, they ultimately have "built-in" fog mitigation. The benefit grows with the size of the airport. The larger and busier the airport (e.g., Heathrow, and Paris–Charles de Gaulle), the more damaging a fog event can be, but the greater potential for disruption of fog formation due to air traffic. While analysis is naturally limited here, the "airport effect" on nocturnal weather would be extremely interesting for future study, both observationally and numerically; particularly the impact of aircraft on fog formation/dissipation.

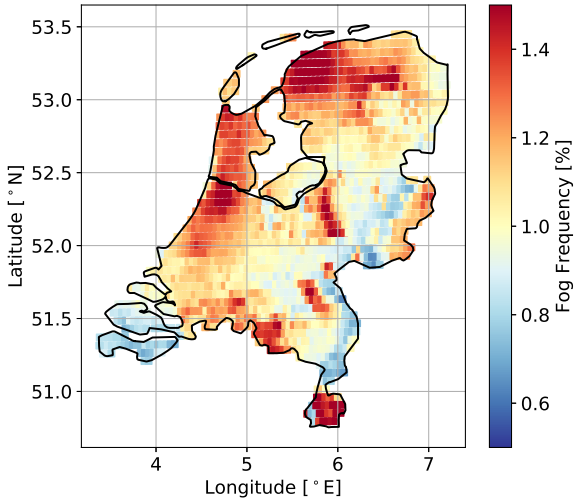

Figure 4.12: Satellite-based estimate of fog occurrence in the Netherlands for 2006–2015 (Egli et al. 2019). Each square is one grid point in the analysis. Note, although the axis limits are the same as Fig. 4.10b), the variable plotted here is the fog frequency, and not the relative fogginess.

4.B Comparison with Satellite Observations

Around the time the research in Chapter 4 was completed (early 2019), Sebastian Egli published a satellite-based climatology of fog occurrence over Europe (Egli et al. 2019), using a novel machine-learning retrieval system (Egli et al. 2018) that deter-

mines cloud base altitude, and compares it against local topography. His data are openly available online, accessible at Egli (2018).

Comparing the Egli et al. (2019) climatology with the results presented in Fig. 4.10b, there is significant qualitative agreement, with, for example, the Veluwe and Friesland regions having more fog than other parts of the country. Notable differences, however, are seen in the Randstad region where the fog occurrence is relatively high in the satellite climatology compared to the rest of the country, but the weather stations show much lower relative fog occurrence (Fig. 4.3). However, the actual *quantitative* values are much lower in the Egli et al. climatology than in the analysis of ground-based observations presented here, with the actual fog frequency lower by a factor almost 4. It may be that the relatively uniform, low-lying topography of the Netherlands means the presence of fog cannot be as easily determined using the cloud base altitude estimates. One notices, for example, that the Veluwe and Maastricht regions have the highest fog occurrence and are also the most distinct topographic regions in the country. Further, while the Egli et al. (2018) methodology does incorporate weather station data, it only does so from the 10 METOP stations (located in and around airfields). Finally, differences in averaging and determination of the fog frequency likely also contribute to the discrepancies between the two products.

Fog At Schiphol Airport

Fog occurrence in the Netherlands varies significantly, even on scales of just a few kilometres (Chap. 4). This can be attributed, in part, to varying levels of urbanization. On an even more localized scale, the occurrence of fog at and around Schiphol International Airport also shows significant variability.

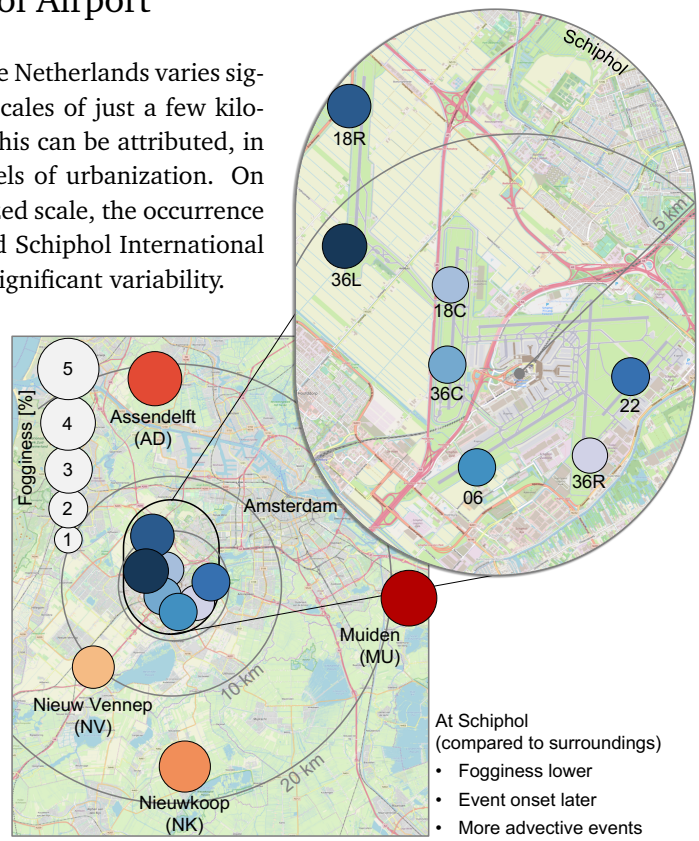

Fog is observed less frequently near the terminal buildings, with the distant "Polderbaan" runway (18R/36L) the foggiest location within the Schiphol complex. All runway observations indicate much lower fog than the surroundings.

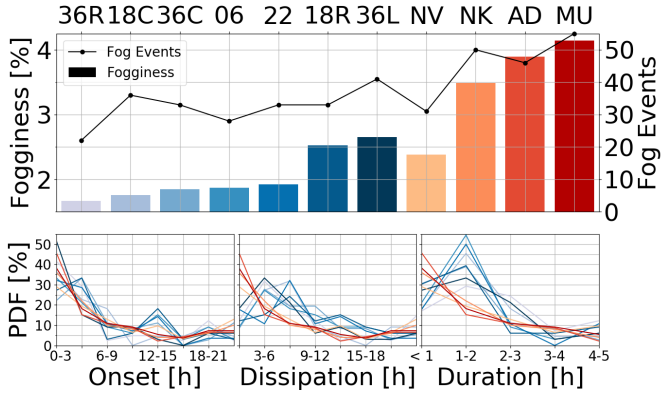

This work was presented as part of a poster at EMS 2019 in Copenhagen

Chapter 5

The Sensitivity of Saturation in the Context of Fog

> A strong breeze had stirred up the soupy fog,
> revealing a patch of bare ground.
>
> C. Gray, *Master and Apprentice*

Summary

The onset of fog is challenging to forecast and simulate accurately. Recent numerical studies have shown considerable sensitivity to a range of factors, including model resolution, and surface properties. Here we analytically assess the contribution of different local variables to the error in estimating the relative humidity. Through linear uncertainty propagation, we show that relative humidity is most sensitive to temperature, with any error in temperature leading to a roughly 20 times greater error in relative humidity. Conversely, uncertainties in the specific humidity and atmospheric pressure only contribute with roughly equal magnitude to the uncertainty in estimated relative humidity. However, errors in specific humidity are generally much larger than those in temperature and pressure, meaning that the final contribution may be equal to that of temperature. Ultimately, the results help in understanding and identifying errors and uncertainty in the determination of saturation, aiding to guide efforts to improve the representation of fog in simulation. They also serve as a reminder that significant effort should continue to be directed toward ensuring accurate representation of the (dry) thermodynamic properties of the (stable) atmospheric boundary layer within numerical models, and that initial conditions need to be accurate and precise.

5.1 Introduction

To mitigate the hazard that fog presents to human activities, accurate simulation—in order to understand the relevant processes—and forecasting are paramount. To this end, efforts have utilized a range of models, including numerical weather pre-

diction (NWP; e.g., Tardif 2007; Zhou et al. 2012; Steeneveld and de Bode 2018), large-eddy simulation (LES; e.g., Nakanishi 2000; Maronga and Bosveld 2017; Mazoyer et al. 2017), and analytical/conceptual models (e.g., Derbyshire 2019). While the type and philosophy of model varies, general conclusions are the same: fog is very difficult to simulate with accuracy, and its formation is sensitive to many different factors. It is largely due to the complex interplay between processes and scales that fog is challenging to predict both observationally and numerically (e.g.Menut et al. 2014; Steeneveld et al. 2015; Izett et al. 2018c). Radiation fog—formed under clear-sky, weak-wind, nocturnal conditions due to radiative cooling at the surface—is particularly challenging to represent, in part due to the challenges associated with accurate simulation of the steep gradients of (in particular) near-surface temperature within the (very) stable boundary layer (e.g., Mahrt 2014; Steeneveld 2014).

In an effort to improve the forecasting and simulation of fog, efforts have focused on understanding model sensitivities in order to identify where challenges lie, and improvements can be made. For example, several studies have shown the importance of high vertical resolution, particularly near the surface (e.g., Tardif 2007; Maronga and Bosveld 2017). Further, Maronga and Bosveld (2017) showed the importance of, e.g., turbulent mixing and near-surface soil temperature in correctly simulating the timing of fog onset. A large focus has also been on the importance of microphysical properties (e.g., Mazoyer et al. 2019; Poku et al. 2019) in the evolution of a fog event. Ongoing is the Global Energy and Water Exchanges (GEWEX) Global Atmospheric System Studies (GASS) intercomparison project titled, "Demistify" (Boutle et al. 2018a). In the spirit of the previous GEWEX Atmospheric Boundary Layer Study (GABLS) intercomparisons (now in its fourth installment, e.g., Holtslag et al. 2013; Bosveld et al. 2014b), Demistify aims to further understand the challenges faced by LES and NWP models in the forecasting of fog, and to determine where future model development should be focused. Making the analysis more complicated, the errors in different parameters may offset each other (e.g., Steeneveld and de Bode 2018), potentially resulting in simulations being "right for the wrong reasons", or masking underlying sensitivities.

In identifying sensitivity of fog to specific processes, a general understanding of why these processes are significant may be lost. In essence, the condensation of water vapour, and the subsequent onset of fog is a process determined by the underlying thermodynamic state. As a result, it is errors in temperature and specific humidity—which are the direct consequences of specific processes—that ultimately determine the error and uncertainty in saturation. We therefore seek to identify the sensitivity and tolerance when estimating saturation by conducting a simple "back-of-the-envelope" analytical analysis of uncertainty/error in the equations of relative humidity (RH) and liquid water specific humidity (q_l). We take the position of looking at the onset of fog through the reaching of saturated conditions *before fog forms*, and the initial formation of liquid water, as opposed to investigating the full development and lifecycle of a fog layer. We do this not only to simplify the analysis, but also because without first achieving accurate saturation, any subsequent evolution is incorrect. Following the analytical analysis, we look at what typical errors might

be in the observed and simulated parameters. While microphysical effects are important in determining saturation and condensation, they are not considered here as they only become relevant from a numerical perspective *after* a given saturation threshold is reached. This note is also not intended as a rigorous assessment of (specific) model capabilities, but rather as an indicator of where focus could be placed to improve future modelling efforts, as well as a foundation for understanding the contribution of different error sources.

Section 5.2 provides an overview of linear uncertainty propagation, along with the equations needed to determine the moist properties of the boundary layer. Subsequently, Section 5.3 presents the results of the uncertainty analysis for relative humidity and the (initial) formation of liquid water, along with an assessment of typical errors. A discussion of the results follows in Section 5.4.

5.2 Propagation of Errors

We make use of the linear error propagation formula (e.g., Bevington and Robinson 2003) in order to provide an estimate of the sensitivity of moist parameters to other meteorological values. For any dependent variable, y, with n independent variables, x_1, x_2, up to x_n, the error (or uncertainty) in y (s_y) depends on the squared sum of the errors/uncertainties in x_n (s_n), multiplied by the derivatives of y with respect to x_n

$$s_y^2 = s_{x_1}^2 \left(\frac{\partial y}{\partial x_1}\right)^2 + s_{x_2}^2 \left(\frac{\partial y}{\partial x_2}\right)^2 + \ldots + s_{x_n}^2 \left(\frac{\partial y}{\partial x_n}\right)^2 + 2s_{x_1,x_2} \frac{\partial y}{\partial x_1} \frac{\partial y}{\partial x_2} + \ldots 2s_{x_i,x_j} \frac{\partial y}{\partial x_i} \frac{\partial y}{\partial x_j} \quad (5.1)$$

Here the cross terms account for any correlation between the errors in the independent variables x_n, with $s_{x_i,x_j} = \rho_{x_{i,j}} s_{x_i} s_{x_j}$, and ρ_{x_i,x_j} the correlation between the errors for all $i \neq j$ in n. Note, from here we use the term "error" throughout the manuscript to refer to both true errors (e.g., incorrect measurement) as well as "uncertainty" (e.g., due to observational precision). While not technically interchangeable, it simplifies matters for the purpose of this note and readability.

When we consider the moist atmosphere and the onset of fog, we are particularly interested in estimating relative humidity, *RH*, and the liquid water specific humidity, q_l (amount of liquid water in a given amount of air). *RH* can be expressed (in decimal form) by comparing the specific humidity of water vapour, q, to the saturation specific humidity, q_{sat}

$$RH = \frac{q}{q_{sat}}, \quad (5.2)$$

where q_{sat} is estimated from the saturation vapour pressure, e_{sat}

$$q_{sat} = \frac{R_d}{R_v} \frac{e_{sat}}{p + e_{sat}\left(\frac{R_d}{R_v} - 1\right)}. \quad (5.3)$$

R_d and R_v are the dry and wet gas constants, respectively, and p is the atmospheric pressure. e_{sat} is then

$$e_{sat} = e_{sat,0}\exp\left[\frac{A(T-273.15)}{T-B}\right], \tag{5.4}$$

with T the (absolute) air temperature and $e_{sat,0} = 610.87$ Pa. A and B are constants, with $A = 17.62$ and $B = 30.03$ K when $T \geq 273.15$ K, and $A = 22.46$ and $B = 0.53$ K when $T < 273.15$ K. The above equations can be found in the majority of meteorological textbooks, including Moene and van Dam (2014). While the equations are, of course, approximations and simplifications of the natural system, their analytical tractability (as compared to other formulations) and general application to the atmosphere serve the purpose of this note, and provide an approximate order of magnitude estimate of the errors involved.

We focus on the use of analytical analysis through Eq. 5.1 in order to give a mathematical expression for the error; however, the following results also hold by directly calculating perturbed RH values by inserting perturbed T, q, and p values into Eqs. 5.2–5.4.

5.3 Results

5.3.1 Error Propagation

The initial onset of fog in simulation is due to first reaching saturation (or a given saturation threshold); the primary requirement being that relative humidity (RH) must be estimated accurately. As such, we first look at the sensitivity of RH as a function of assumed error in temperature (T), total water specific humidity (q), and atmospheric pressure (p).

For the sake of brevity, the full derivation is not shown; however, the partial derivatives of RH (needed for the error formula, Eq. 5.1) can be written from Eq. 5.2–5.4 as

$$\frac{\partial RH}{\partial q} = \frac{RH}{q}, \tag{5.5}$$

$$\frac{\partial RH}{\partial p} = \frac{RH}{p + e_{sat}\left(\frac{R_d}{R_v} - 1\right)} \approx \frac{RH}{p}, \tag{5.6}$$

$$\begin{aligned}\frac{\partial RH}{\partial T} &= -\frac{RH}{T}\left(1 - q_{sat}\left(\frac{R_d}{R_v} - 1\right)\right)\left[\frac{A \cdot T\,(273.15 - B)}{(T-B)^2}\right] \\ &\approx -\frac{RH}{T}\left[\frac{A \cdot T\,(273.15 - B)}{(T-B)^2}\right].\end{aligned} \tag{5.7}$$

The additional temperature-scaling in Eq. 5.7 comes from the derivative of e_{sat} with respect to T. Note, we also multiply the temperature derivative by T/T in order to maintain a consistent formulation with the other derivatives, and to allow for

expressing the error as a fraction (i.e., s_T/T), rather than an absolute value. Further, because $p >> e_{sat}$ and $q_{sat} << 1$ for the temperature and pressure considered here (assuming near-surface values), we only take the approximate forms of the T- and p-derivatives in order to simplify the expressions (the difference is negligible).

Inserting Eqs. 5.5-5.7 into Eq. 5.1, and dividing both sides by RH, we see that the error fraction (i.e., s_{RH}/RH) is directly proportional to the error fractions of q and p, with the error in T being scaled by the additional temperature-dependent factor

$$\left(\frac{s_{RH}}{RH}\right)^2 \approx \left(\frac{s_T}{T}\right)^2 \left[\frac{A \cdot T\,(273.15-B)}{(T-B)^2}\right]^2 + \left(\frac{s_q}{q}\right)^2 + \left(\frac{s_p}{p}\right)^2 - 2\rho_{T,q}\left(\frac{s_T}{T}\right)\left(\frac{s_q}{q}\right)\left[\frac{A \cdot T\,(273.15-B)}{(T-B)^2}\right] \quad (5.8)$$

We assume that only errors in T and q are correlated (as T and q have similar physical transport mechanisms in the atmosphere), but that they are not correlated with errors in p. This, of course, does not include observational or methodological errors, which would not necessarily be expected to be correlated.

For errors of equal magnitude, RH is much more sensitive to s_T/T; a factor of ∼17–23 times (with a temperature range of 263–300 K). Therefore, in order to achieve an error in RH of below 1%, the error in T must be less than 0.05% (on the order of 0.12-0.15 K). The scaling is highlighted when the temperature-dependent factor in Eq. 5.8 is simplified further, noting that the numerator and denominator are both on the order of T^2,

$$\left(\frac{s_{RH}}{RH}\right)^2 \sim A^2\left(\frac{s_T}{T}\right)^2 + \left(\frac{s_q}{q}\right)^2 + \left(\frac{s_p}{p}\right)^2 - 2A\rho_{T,q}\left(\frac{s_T}{T}\right)\left(\frac{s_q}{q}\right). \quad (5.9)$$

Thus, the error scales roughly with A, with only a minor contribution from additional T-scaling.

In a similar fashion, we can also look at the calculation of liquid water specific humidity (q_l) just after saturation, assuming that the initial condensation will be directly related to the amount of super saturation.

$$q_l = q - q_{sat}, \qquad \text{where } q \geq q_{sat}. \quad (5.10)$$

It is interesting to note that the resulting error is nearly equivalent to that of RH, with just an additional dependence on q (cf. Eq. 5.9)

$$\left(\frac{s_{q_l}}{q}\right)^2 \sim A^2\left(\frac{s_T}{T}\right)^2 + \left(\frac{s_q}{q}\right)^2 + \left(\frac{s_p}{p}\right)^2 - 2A\rho_{T,q}\left(\frac{s_T}{T}\right)\left(\frac{s_q}{q}\right). \quad (5.11)$$

5.3.2 Possible Values of Error and Uncertainty

The previous section presents the analytical analysis of the sensitivity of RH to errors and uncertainty in T, q, and p. While RH is shown to be most sensitive to T, estimates

	$\frac{s_T}{T}$ (%)	$\frac{s_q}{q}$ (%)	$\frac{s_p}{p}$ (%)	$\frac{s_q/q}{s_T/T}$ (-)
Instrument	0.04	0.5	0.009	12.5
Std. Dev.	0.04	0.9	0.004	22.5
SCM	1.6	20	–	12.5

Table 5.1: Typical values of s_X/X for the CESAR facility based on instrument accuracy (Bosveld 2019), standard deviation of hourly observations, and SCM output from the GABLS3 intercomparison (Bosveld et al. 2014a).

of the magnitude of errors—in observation and simulation—is assessed here in order to identify the resulting contribution of different parameters to estimating saturation. A summary of the values is in Table 5.1.

Observations

Observational error and uncertainty can primarily result from two sources: instrument accuracy and precision, and errors associated with the (lack of) spatio-temporal representation of point observations (as opposed to sampling a 3D field continuously). We quantify these errors based on the instruments and data at the Cabauw Experimental Site for Atmospheric Research (CESAR) in the Netherlands (Monna and Bosveld 2013).

At the CESAR facility, air and dew point temperature are measured with both accuracy and resolution of 0.1 K (see Bosveld 2019 for an overview of the instruments and their specifications). At 280 K, this corresponds to an error/uncertainty of $s_T/T = \pm 0.04\%$. Specific humidity is subsequently estimated from the dew point observations, resulting in $s_q/q = 0.5\%$ for moderate air temperatures ranging from ∼273–290 K (12.5 times that of the error in T). Note, this methodology inherits some of the errors highlighted in the previous section, with q dependent on T_d. The instrument error in estimating p is much smaller, at just 0.1 hPa (∼0.01%).

In order to quantify the sampling error, we look at the hourly standard deviation of the (detrended) 10-minute observations of T, q, and p at the CESAR facility. As with the instrument error, q is (relatively) the most variable quantity of the three, with a mean (relative) standard deviation over the entire period spanning 2001–2020 of roughly 22.5 times that of both temperature and pressure.

Ultimately, this means that observation error in both T and q contribute with roughly equal significance to the resulting error in RH. The errors in q contributing 1:1, and the smaller errors in T scaled by a factor of 17-23, demonstrated in, e.g., Eq. 5.9.

Simulation

To gain an idea of possible errors in simulation, we look to the results of the GABLS3 single-column model (SCM) intercomparison (Bosveld et al. 2014a), the case setup of which was based on observations at the CESAR facility, including stable boundary-layer conditions. We look to the spread in simulated T and q at 2-m height, as illustrated in Fig. 3 of Bosveld et al. (2014a), and define s_X/X as the spread in values

at midnight, divided by 2 (the amplitude), and subsequently divided by the median of the spread.

The SCM show a total spread of roughly 6 K in T, and 0.003 kg kg^{-1} in q, with median values around 291 K and 0.011 kg kg^{-1}, respectively. As a result, $s_T/T \approx 1\%$, and $s_q/q \approx 14\%$; s_q/q is again much greater than s_T/T, meaning that errors in T and q contribute with roughly equal magnitude to the resulting error in *RH*.

Unfortunately, it is not as straightforward to identify the errors that might arise from incorrect representation of features (e.g., landscape heterogeneity) on discretized grids; however, they are likely in line with the observational variability above.

5.4 Discussion

The analysis presented herein indicates that the simulation/estimation of saturation and the initial formation of a fog layer is most sensitive to temperature, with a relative error in T leading to an error that is roughly 20 times greater in *RH* (Eq. 5.8). However, while *RH* is less sensitive to specific humidity, the typical scale of errors in both observation and simulation are (relatively) much larger for q than T (Sect. 5.3.2), meaning that the two contribute with nearly equal significance to the overall error in *RH*.

While it is understood that NWP, in particular, is constrained by operational and resource requirements, and that parametrizations and errors are unavoidable, the results presented should help to guide assessment of errors in fog studies, particularly those using research models such as LES. In particular, it is hoped that the sensitivity analysis presented here can assist in assigning priorities for improvements that could be made in reducing errors of thermodynamic variables. On one hand, a reduction in temperature errors will lead to a much more rapid reduction in *RH* errors due to the additional scaling. Comparatively, reducing errors in the value of q will only lead to an equivalent error reduction in *RH* (1:1 dependence). Yet, with the larger errors in q, there may be more potential for reduction of these errors. Ultimately, the exact model used to estimate saturation will determine where maximum benefit can be achieved through the reduction of errors in T and/or q. Such errors can result from many sources, including observational error leading to incorrect initial/boundary conditions, or parametrization error. Further, the specific type of fog will determine the relative scale of errors involved. For example, errors under stable conditions (favourable for radiation fog) may be larger than those preceding advection fog. Through the framework presented here of the analytical analysis, one can guide the search for identifying model errors that result in fog errors, and assign priority to addressing different sources of error.

Our focus was on the conditions preceding saturation and the initial production of liquid water; however, there is obviously much more to consider when simulating a fog layer. Microphysical parametrizations (e.g., Mazoyer et al. 2019; Poku et al. 2019), for example, determine the partitioning of liquid water among droplets of different sizes, as well as the growth rates and sedimentation of these particles. The

further interaction of a model's radiation scheme with the properties of the water vapour/droplets/particles is also of key importance. Incorrect representation here will again influence the temperature, which, in turn, will alter the relative humidity in the same magnitude as presented here. In reality, microphysical properties also determine the point at which condensation can occur, including in under-saturated conditions. Such an effect can also be on the order of a few percent in *RH*.

It should also be remembered that the analysis presents the *maximum* error and uncertainty that can be expected in estimation of relative humidity and liquid water specific humidity. In reality, opposing errors in properties such as temperature and total specific humidity could counteract such that the simulated saturation parameters are still correct, for example, in the case of both T and q being too high (e.g., as with the competing processes shown by Steeneveld and de Bode 2018). However, as can be inferred from Eq. 5.8, it would take a contrasting error in q of 17–23 times that in T to obtain correct saturation levels. While it is unavoidable in numerical settings—and indeed, may be the case as shown in Sect. 5.3.2—this is still a significant error.

5.5 Conclusions

The estimation of relative humidity is shown to be most sensitive to temperature. However, typical errors in specific humidity are generally much larger (in a relative sense) than for temperature, meaning the two contribute approximately equally to overall errors in *RH*. The exact means of achieving smaller errors in *RH* will therefore depend on the method and model in question. On one hand, reducing errors in T will lead to a larger reduction in *RH* errors, while q will only lead to a 1:1 reduction. Yet, given already low values of temperature errors, particularly for observations, the reduction of errors in q may prove to be a more quickly achieved goal in specific cases.

Chapter 6

Why Does Fog Deepen?

An Analytical Perspective

> The fog had now buried all heaven. As the last rays of daylight dwindled and disappeared, absolute blackness settled down.
>
> R. L. Stevenson, *Treasure Island*

Summary

The overall depth of a fog layer one of the important factors in determining the severity of a fog event. With discrete observations and often coarse numerical grids, however, fog depth cannot always be accurately determined. Understanding, and predicting, the deepening of a fog layer is therefore an important step in improving the prediction of, and preparedness for, fog events. To this end, we derive a simple analytical relation that describes the change in depth of a fog interface with time, which depends on the tendencies and vertical gradients of temperature and moisture. We also present an estimate for the maximum depth that a fog layer could reach, assuming a mixing of the vertical profiles of temperature and moisture. The analytical description is subsequently tested using observations, and the results of large-eddy simulations. Overall, the analytical expression for fog growth does a very good job of accurately estimating the growth rate of both the observed and simulated fog layers, even over several hours, and when coarse observational resolution is used. With such a description, sub-grid, or inter-observation fog depth can be accurately estimated. This enables the possibility of a sub-grid parametrization of fog depth and growth rate for numerical weather models, as well as observation networks.

This chapter has been published as:

Izett JG, van de Wiel BJH (2020). Why Does Fog Deepen? An Analytical Perspective. Atmosphere 11(8), doi:10.3390/atmos11080865

6.1 Introduction

This chapter presents an analytical description of fog growth and evolution. We do this with two goals: 1) to provide a simple framework for understanding the evolution of fog layers, and 2) to allow for continuous estimation of fog depth and growth rate in otherwise discrete settings.

Fog is a hazard to human activities, especially transportation. As a result, accurate monitoring and forecasting of fog events is essential. In addition to knowing the timing of events, it is important to know the severity of the event, including the depth of the fog layer. For example, the hazard that a shallow fog layer presents to airport operations is much less than that of a deeper fog layer. The dynamics and lifecycle of fog, particularly radiation fog, are also dependent on the depth that the fog layer achieves (e.g., (Smith et al., 2018)). Shallow fog, for example, is optically thin, allowing longwave radiation to pass through without significant absorption, while deeper fog layers (on the order of a few tens of metres) can be optically thick to longwave radiation, resulting in a well-mixed, convective fog layer. Understanding how, at what rate, and why a shallow fog layer transitions to a deep layer is therefore essential. It has been shown that very shallow (<1 m) fog layers can exist long before the evolution, and even in the absence of, a deeper fog layer Izett et al. (2019a). The need to identify when—and why—these fog layers ultimately deepen was highlighted as an important follow-up.

Unfortunately, accurately characterizing fog depth—observationally or through simulation—is not always straightforward. Continuous resolution is unattainable due to the discretization of observational and numerical systems. Standard observational sites are limited to only a few discrete sensor heights; while fog can be observed at the discrete heights, providing a range of possible depths, the rate of progress between two observational levels cannot be characterized. Higher resolution observations can, of course, be made; however, it becomes impractical in many settings. In an attempt to overcome observational limitations, near-surface micrometeorological observations have been previously employed to estimate fog depth, including Román-Cascón et al. (2016b) and Ju et al. (2020), and references therein. Such methods rely on statistical relations between primarily surface parameters and resulting fog depth. Ju et al. (2020) investigate the effectiveness of such methods, and find that they provide a good estimate of the mean height of fog layers. However, the statistical relationships are site-dependent, only provide an idea of the expected depth, and do not allow for a simple means of estimating a rate of deepening or erosion of the fog top. We therefore seek a general description of the fog-top evolution through means of simple analytical analysis of the fog interface.

Where high-resolution numerical models and diagnostic methods can provide estimates of fog depth and evolution, a conceptual approach also allows for understanding the natural evolution of a fog layer. For example, through an analytical framework, it becomes easier to understand why fog in one stage of its lifecycle is more vulnerable to dissipation than in other stages. Or to understand why the growth of radiation fog tends to accelerate in time, while optically thick fog typically

slows down its own growth, and with higher vulnerability to base-lifting as time proceeds. Previous efforts to understand fog-top evolution have focused on specific processes, such as turbulent mixing and surface characteristics (e.g., Maronga and Bosveld 2017; Smith et al. 2018; Price 2019) and their ultimate influence on the overall depth of the fog layer. In contrast, we aim at a simple formula that takes the effect (e.g., interfacial cooling) of the process into account, but without explicit consideration of specific processes. This enables a general understanding of the lifecycle that can be applied in a range of settings.

In Sect. 6.2, we derive an analytical description for the rate of deepening or erosion of the fog interface from a Lagrangian perspective. We then compare this with observational data (Sect. 6.3) from the campaign of Izett et al. (2019a), as well as idealized large-eddy simulation (LES; Sect. 6.4) output based on the case described in Maronga and Bosveld (2017), in order to test the accuracy of the description. With the results presented herein, it becomes possible to provide insight into the immediate evolution of a fog layer as well as quickly and easily diagnose fog depth between standard observation levels. We elaborate further upon these two aspects in the discussion in Sect. 6.5.

6.2 An Analytical Description for the Interface of a Saturated Layer

In this section, an analytical description for the growth (or erosion) rate of the fog interface is presented, providing a means of diagnosing the location and evolution of the interface, even when observational and simulation resolution my be insufficient. In order to maintain generality and simplicity, we approach from the view that cooling and mixing are taking place at the interface, but do not consider specific processes leading to the evolution; the exact processes and their influence will depend on the specific conditions under which the fog has evolved. Our analysis is performed from a localized perspective, focused primarily at the fog interface itself.

We also present a further metric, the “Maximum Attainable Mixed Depth” (MAMD), a lengthscale measure indicating the depth to which a fog layer could extend if the profiles of temperature and moisture were redistributed as well-mixed profiles. A fog layer that is closer to this depth with be more sensitive to drying and mixing influences, than one in otherwise similar conditions that is further from MAMD.

6.2.1 Derivation of Interfacial Evolution

At the saturation interface of a fog layer (I_z in m), the total specific humidity (q in kg kg^{-1}) is, by definition equal to the saturation specific humidity (q_s[†])

$$q = q_s \tag{6.1}$$

where q_s is estimated from the saturation vapour pressure, e_s

$$q_s = \frac{R_d}{R_v} \frac{e_s}{p + e_s\left(\frac{R_d}{R_v} - 1\right)}. \tag{6.2}$$

R_d and R_v are the dry and wet gas constants, respectively, and p is the atmospheric pressure in Pa. e_s is then

$$e_s = e_{s,0} \exp\left[\frac{A(T - 273.15)}{T - B}\right], \tag{6.3}$$

with T the (absolute) air temperature and $e_{s,0} = 610.87$ Pa. A and B are constants, with $A = 17.62$ and $B = 30.03$ K when $T \geq 273.15$ K, and $A = 22.46$ and $B = 0.53$ K when $T < 273.15$ K. The above equations can be found in the majority of meteorological textbooks, including Moene and van Dam (2014).

Because the air below the interface is saturated, and unsaturated above, it must be true that, at the interface itself,

$$\frac{\partial q_s}{\partial z} > \frac{\partial q}{\partial z}. \tag{6.4}$$

If the values were equal, then the saturated layer would be deeper than the assumed interface. At the same time, a reversal of the inequality represents the *lower* interface of a cloud above clear air. In the case of fog, this is the surface; or, the lower interface (B_z) of a lifted fog layer (e.g., at sunrise).

Figure 6.1a) illustrates this. Given a hypothetical profile for q_s at the interface, Eq 6.4 must be true at the interface itself (but not necessarily at a distance), and fog can exist if q is in the shaded regions. However, if these assumptions are not met, then fog is not present. For example, if $q \geq q_s$ up to a height that is greater than I_z, then either a deeper fog layer is present (i.e., not assessing at the interface), or a lifted cloud is present.

We can assess the change in interfacial values of q and q_s from a Lagrangian

[†]For simplicity, we assume this to be the point of 100% relative humidity; however, it could, e.g., be adjusted for microphysical effects, or the threshold at which sufficient liquid water has condensed to reduce visibility to foggy conditions.

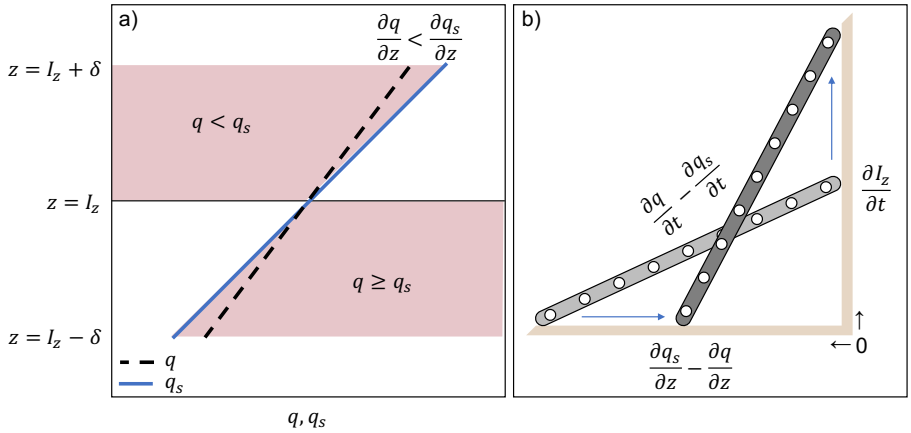

Figure 6.1: a) Sketch of the conditions in which fog exists, following Eq 6.4. Given the hypothetical profile of q_s near the interface, the profile of q must exist within the shaded regions, represented by the dashed line. b) Eq 6.7 illustrated as a ladder against a wall. The shallower (steeper) the ladder, the lesser (greater) the distance that can be travelled vertically.

perspective, by taking the *total* derivatives of q and q_s at $z = I_z$,

$$\begin{aligned} \left.\frac{\mathrm{d}q}{\mathrm{d}t}\right|_{I_z} &= \frac{\partial q}{\partial t} + \frac{\partial q}{\partial z}\frac{\partial I_z}{\partial t} \\ \left.\frac{\mathrm{d}q_s}{\mathrm{d}t}\right|_{I_z} &= \frac{\partial q_s}{\partial t} + \frac{\partial q_s}{\partial z}\frac{\partial I_z}{\partial t}. \end{aligned} \tag{6.5}$$

We assume that the profiles are in a quasi-steady state such that (relative) moistening is the same on either side of the interface.

For Eqs. 6.1 and 6.4 to be satisfied at $t = t_0 + \Delta t$ and a height of I_z, then it must be true for the total derivatives that $\left.\frac{\mathrm{d}q}{\mathrm{d}t}\right|_{I_z} = \left.\frac{\mathrm{d}q_s}{\mathrm{d}t}\right|_{I_z}$, such that

$$\frac{\partial q}{\partial t} + \frac{\partial q}{\partial z}\frac{\partial I_z}{\partial t} = \frac{\partial q_s}{\partial t} + \frac{\partial q_s}{\partial z}\frac{\partial I_z}{\partial t} \tag{6.6}$$

Rearranging, the interfacial growth/erosion can be written as,

$$\frac{\partial I_z}{\partial t} = \left(\frac{\partial q}{\partial t} - \frac{\partial q_s}{\partial t}\right)\left(\frac{\partial q_s}{\partial z} - \frac{\partial q}{\partial z}\right)^{-1}. \tag{6.7}$$

The definition provided in Equation 6.4 means the denominator will always be positive in the case of a fog layer. Therefore, the growth, maintenance, or erosion of

the fog top depends on the interfacial values of $\partial q_s/\partial t$ and $\partial q/\partial t$:

$$\frac{\partial q}{\partial t} - \frac{\partial q_s}{\partial t} \begin{cases} > 0 : \text{Growth} \\ = 0 : \text{Maintenance} \\ < 0 : \text{Erosion} \end{cases} . \tag{6.8}$$

The exact values of the moistening will depend on the specific processes involved, and can be diagnosed either through observations, or through a more detailed budget analysis of the interface. It is important to note that, while the approach is different, this result does not contradict the mixing analysis of Price (2019); the resulting saturation of the fog layer must be maintained or enhanced for fog to grow. Further, the greater the relative moistening, the more rapidly the growth can occur.

Two further conclusions can be drawn regarding the denominator. First, $\frac{\partial q_s}{\partial z} \neq \frac{\partial q}{\partial z}$ at the interface. Otherwise, there would be infinite growth or erosion. Similarly, the difference between $\frac{\partial q_s}{\partial z}$ and $\frac{\partial q}{\partial z}$ modulates the growth of the fog layer, with a greater difference leading to a slower rate of change. The concept can be thought of as similar to moving up and down a ladder placed against a wall (Fig. 6.1b). The length travelled along the ladder is the numerator, the horizontal base is the denominator, and the vertical axis is $\partial I_z/\partial t$. If placed at a shallow angle against a wall (large denominator), it takes many more steps to climb to the same height as if the ladder were more steeply angled (small denominator).

Important to note is that the relationship does not only hold for the case of a fog layer, but the interface of any saturated region. In the case of a lifted cloud, both the upper and lower interfaces can be described with Eq 6.7. The only difference is that the sign of the denominator will be negative at the lower interface, as the inequality in Eq. 6.4 is reversed. This, by extension, means that subsidence and lifting of the cloud base, B_z, correspond to situations where the numerator is positive and negative, respectively (cf. Eq. 6.8).

In the following we present idealized examples of Eq. 6.7. First, the case of constant moisture, followed by an illustration of a stably stratified log-linear temperature profile.

Equation 6.7 in the Case of Constant Moisture

To demonstrate the principles of Equation 6.7, we present a simple illustration of the special case where where $\partial q/\partial t = \partial q/\partial z = 0$ (i.e., the total specific humidity is constant in height and time), and the air cools at a constant rate. Equation 6.7 then simply becomes

$$\frac{\partial I_z}{\partial t} = -\frac{\partial q_s}{\partial t}\left(\frac{\partial q_s}{\partial z}\right)^{-1} = -\frac{\partial T}{\partial t}\left(\frac{\partial T}{\partial z}\right)^{-1}, \tag{6.9}$$

since q_s depends only on z and t through the temperature. Then, trivially, $I_z(t) = -t \cdot \frac{\partial T}{\partial t}\left(\frac{\partial T}{\partial z}\right)^{-1} + I_{z,0}$.

We obtain, then, the intuitive case that the rate of growth or erosion depends

on whether or not cooling is occurring at the interface, and the steepness of the temperature gradient is responsible for modulating the overall growth of the fog layer. A steeper gradient means slower growth or erosion than a shallower gradient, which can evolve much more rapidly for for the same cooling rate (Fig. 6.1b).

Equation 6.7 in a Stable Boundary Layer

One can further assume a stable temperature profile, as might occur during a radiation fog event. We take a simple log-linear profile of temperature in the nocturnal boundary layer, such as would arise from the Businger-Dyer relationship (e.g., (Dyer, 1974)), for which the vertical gradient of temperature is given by

$$\frac{\partial T}{\partial z} = \frac{\theta_*}{\kappa z}\left(1 + \frac{z\alpha}{L}\right) \tag{6.10}$$

where θ_* is the temperature scale, κ the von Kármán constant, α the linear slope parameter (~ 5 under stable conditions), and L the Obukhov length scale. Assuming a quasi-steady state, with $\partial T/\partial t$ constant over the boundary layer, the growth rate at $z = I_z$ can be expressed, following Eq. 6.9, as

$$\frac{\partial I_z}{\partial t} = -\frac{\partial T}{\partial t}\frac{\kappa I_z L}{\theta_*(L + I_z\alpha)} \tag{6.11}$$

Figure 6.2 illustrates the (non-dimensional) growth rate as a function of (non-dimensional) fog depth (Eq 6.11). Two things are apparent. First, the growth rate accelerates with fog depth (due to the shallower vertical gradient in T), meaning that the second derivative of I_z is positive. Second, there is a maximum attainable growth rate for such a profile, which becomes asymptotically linear at large z. We can diagnose this maximum growth rate by taking the limit as $I_z \to \infty$

$$\max\left(\frac{\partial I_z}{\partial t}\right) = -\frac{\partial T}{\partial t}\frac{\kappa L}{\theta_*\alpha} \tag{6.12}$$

If we assume that $\partial T/\partial t = -1$ K h^{-1}, $L = 10$ m, and that $\theta_* = 0.1$ K, then the fog layer would deepen at rates of 1.6 m h^{-1} and 6.7 m h^{-1} at depths of 0.5 m and 10 m, respectively. The maximum growth rate would be 8 m h^{-1}.

6.2.2 The Maximum Attainable Mixed Depth

Here we coin an additional metric to describe a fog layer, the “Maximum Attainable Mixed Depth" (MAMD), or, M_z. One can imagine taking a shallow, non-well-mixed fog layer, and identifying the depth to which an equivalent well-mixed fog layer would reach (i.e., redistribute the profiles of q and T equally such that the saturated layer is deeper). This is akin to determining the depth to which a sudden mixing event, or transition from optically thin to optically thick fog might obtain. MAMD is not a true depth of the fog layer, but rather a thermodynamic lengthscale that describes the amount of moisture available in a vertical profile. As such, the

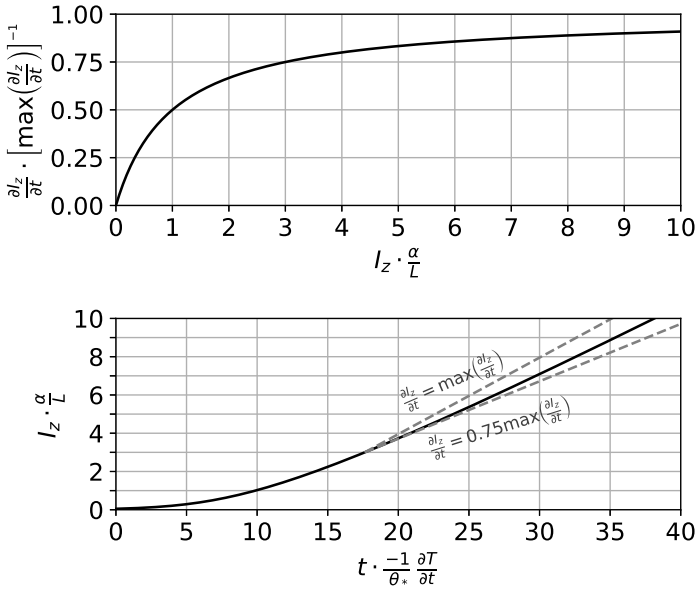

Figure 6.2: Fog growth in a quasi-steady stable boundary layer. a) The rate of growth as in Eq. 6.11. b) The value of I_z in time. The dashed lines indicate the linear growth rate at $I_z = 3L/\alpha$ and the maximum growth rate.

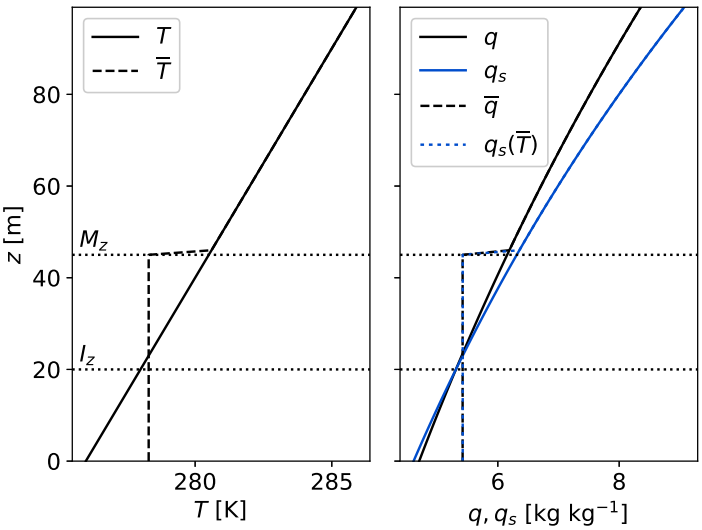

Figure 6.3: Illustration of M_z using linear temperature and relative humidity profiles. M_z is deeper than I_z due to the super saturation within the fog layer. In stable conditions, $M_z \sim 2I_z$ (Sect. 6.2.2).

MAMD provides both a hypothetical upper limit of fog depth, as well as an indication of the depth over which mixing can occur and a fog layer still be sustained. Mixing over a deeper layer than M_z will result in dissipation of the fog as there is insufficient moisture to maintain saturation. Likewise, if the layer were to dry through, e.g., advection or warming, then MAMD would decrease below the fog depth, and dissipation would need to occur.

M_z is determined through conservation of thermal energy and total specific humidity

$$\begin{aligned} \int_0^{M_z} \rho T dz &= \overline{\rho}\,\overline{T} M_z \\ \int_0^{M_z} q dz &= \overline{q} M_z \end{aligned} \quad , \tag{6.13}$$

where the overline represents the well-mixed properties, which are the mean values in the layer

$$\begin{aligned} \overline{T} &= \frac{\int_0^{M_z} \rho T dz}{\overline{\rho} M_z} \\ \overline{q} &= \frac{\int_0^{M_z} q dz}{M_z} \end{aligned} \quad . \tag{6.14}$$

The well-mixed profile must also be (super)saturated throughout the layer, adhering to the conditions of Eq. 6.1 and Eq 6.4, with $\overline{q} \geq q_s\left(\overline{T}\right)$ over the entire M_z. Note, we assume complete mixing over the entire M_z, with the fog layer being mixed into the air above, such that M_z will only be deeper than I_z by as much as the supersaturation within the fog layer allows.

Unfortunately, it is not possible to solve for M_z for a general atmosphere. Instead, we present an idealized case in the following subsection. An iterative approach is also sufficient to estimate the MAMD from a given (observed or simulated) profile. Starting from the current fog depth, one can simply determine the maximum depth that satisfies the conditions for a fog layer. A simple example is shown in Fig. 6.3, with linear profiles for temperature and relative humidity.

M_z in an Idealized Atmosphere with Linear Temperature Profile

An explicit, *a priori* expression for Mz cannot be given for general T and q profiles, where M_z must instead be found iteratively. However, below we present a canonical example, that of a linearly stratified profile, that does allow such explicit expression (at least approximately). This case shows that, as a rule-of-thumb, $M_z \sim 2I_z$ for a stable temperature profile.

As in Sect. 6.2.1, we assume a constant value of q throughout the domain, along

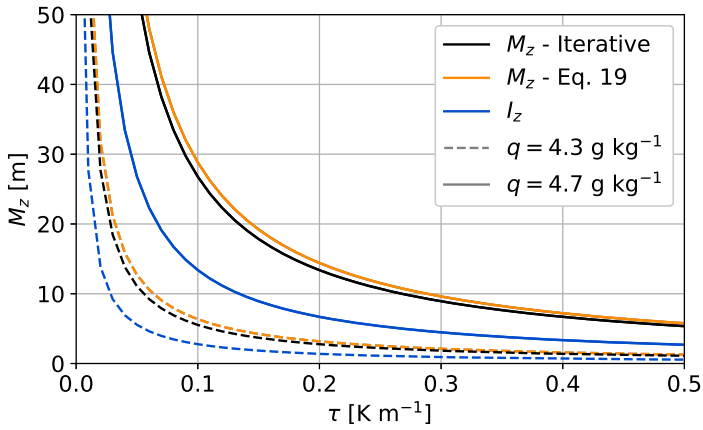

Figure 6.4: M_z and I_z as a function of slope for a linear temperature profile with $T_0 = 275$ K and two values of $\overline{q}$, corresponding to relative humidities at the surface of 102%, and 110%, respectively. M_z is determined iteratively as well as using the approximate solution in Eq 6.19. Note that in both cases, $M_z \sim 2I_z$.

with constant density, and a linear temperature profile with $T = T_0 + \tau z$. Assuming further that the density, ρ, is constant, $\overline{T} = T_0 + \frac{1}{2}\tau M_z$. The saturation vapour pressure can be expressed using a linear approximation as per Penman (1948)

$$e_s\left(\overline{T}\right) \approx e_s\left(T_0\right) + s\left(T_0\right)\left(\overline{T} - T_0\right), \tag{6.15}$$

with $s\left(T\right)$ the derivative of e_s with respect to T,

$$s\left(T_0\right) = e_s\left(T_0\right)\left[\frac{A(B + 273.15)}{\left(T_0 + B\right)^2}\right]. \tag{6.16}$$

Assuming that $e_s \ll p$,

$$\begin{aligned}\overline{q} &= \frac{R_d}{R_v p}\left[e_s\left(T_0\right) + s\left(T_0\right)\left(\overline{T} - T_0\right)\right] \\ &= \frac{R_d}{R_v p}\left[e_s\left(T_0\right) + s\left(T_0\right)\frac{\tau M_z}{2}\right],\end{aligned} \tag{6.17}$$

we obtain,

$$I_z = \frac{1}{s\left(T_0\right)\tau}\left[\frac{\overline{q} p R_v}{R_d} - e_s\left(T_0\right)\right], \tag{6.18}$$

and

$$\begin{aligned}M_z &= \frac{2}{s\left(T_0\right)\tau}\left[\frac{\overline{q} p R_v}{R_d} - e_s\left(T_0\right)\right] \\ &= 2I_z.\end{aligned} \tag{6.19}$$

Figure 6.4 plots the approximate value of M_z in Eq 6.19 as well as the iterative value of M_z as a function of the slope in temperature, with $T_0 = 275$ K and two values of $\overline{q}$, corresponding to relative humidities at the surface of 102%, and 110%, respectively. While Eq. 6.19, does overestimate the iterative value of M_z, it is still a reasonable estimate. From Eq. 6.19, we see that the steeper the gradient (larger τ), the shallower the fog layer possible within the mixed layer. Further, it is apparent that the value of M_z is always greater than I_z through redistribution of the supersaturation over a deeper region.

6.3 Comparison with Observational Data

We now test the accuracy of the analytical description of fog growth by comparing it with two observational datasets collected on 6–7 November 2017 at the CESAR facility in the Netherlands. We do this in order to establish confidence in the description.

6.3.1 Description of the Observational Data and Methods

The data used in this section were collected as part of the field campaign described in Izett et al. (2019a) that took place at the CESAR facility (e.g., Monna and Bosveld 2013) during November 2017. During the campaign, high-resolution observations ($\leq$12.5 cm spatially, and 30 s in time) of wet- and dry-bulb temperature were obtained within the lowest 7 m using distributed temperature sensing (DTS), which determines temperature based on the backscattered laser pulse within a fibre-optic cable (e.g., (Selker et al., 2006)). Complementing the temperature observations, a camera-LED setup was used to image the shallow fog layer up to a depth of 2.5 m, with an effective resolution of 0.5 m. The high-resolution campaign was conducted in tandem with routine observations made by the Royal Netherlands Meteorological Institute (KNMI) along the 200-m tall tower at the site, with visibility measured at 1.5 m, 10 m, 20 m, 40 m, 80 m, 140 m, and 200 m. Temperature and humidity are also recorded at the same heights. Further details of the data collection are not discussed here, with the reader instead referred to Izett et al. (2019a) and Monna and Bosveld (2013). The data are openly available, with the DTS data stored on the 4TU data repository (Izett et al., 2018b) and the KNMI-observed variables available from the KNMI data centre (https://data.knmi.nl/datasets?q=CESAR).

We focus on the night of 6–7 November in this analysis. Following sunset, a strong near-surface temperature gradient (5 K in 1 m) and very stable conditions resulted in the formation of a shallow radiation fog layer. The layer was observed to grow slowly throughout the night, ultimately reaching a height of between 20 and 40 m before dissipation just after sunrise.

At each time step (corresponding to the respective observation), Equation 6.7 is calculated, with $I_z(t)$ estimated through forward time integration using the gradients

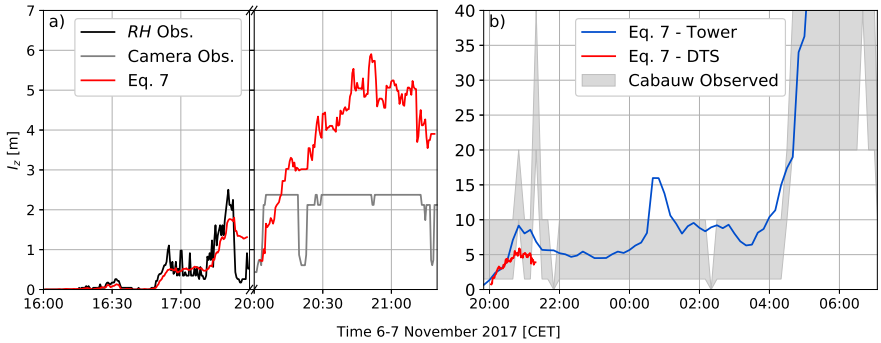

Figure 6.5: Observed fog height compared with the height estimated by forward integration of Equation 6.7. a) High-resolution comparison using DTS-estimated saturation (i.e., $RH = 99\%$ as the interface (left) and the camera-derived observations of fog depth. b) Comparison against the fog depth observed along the Cabauw tower. Note, the camera is limited to a depth of 2.25 m, and the tower is restricted to discrete heights such that the observed fog depth is between the maximum height of observed fog, and the level above.

diagnosed from the observations

$$I_z(t) = I_z(t - \Delta t) + \Delta t \frac{\partial}{\partial t}\left[I_z(t - \Delta t)\right]. \tag{6.20}$$

The vertical gradients are determined as the discrete difference between the two observation depths that immediately bound the estimated interface, $q_{(s),2} - q_{(s),1}/(z_2 - z_1)$. Similarly, the time derivatives are estimated from the discrete observations as the average value of $q_{(s),2} - q_{(s),1}/(t_2 - t_1)$ at z_1 and z_2.

6.3.2 Comparison with High-Resolution Observations

We estimate q_s and q as a function of height from the wet and dry-bulb temperatures. These were then used to calculate Eq 6.7 and estimate the fog depth as a function of time.

We first look at the so-called "saturation interface", and not the fog interface itself. Due to microphysical effects these are not necessarily the same. We define the saturation interface as the point at which the DTS observations indicate an *RH* value of $\geq 99\%$ (rather than 100%). Figure 6.5a, left, shows the observed interface depth (back line) and the projected depth (red) of the interface determined with Eq 6.20, starting at 16.00 local time and calculated every 30 s, as consistent with the observational resolution. We stop the comparison at 17.30, after which freezing of the wet-bulb fibre meant that reliable *RH* estimates could no longer be calculated. Note that no filtering of either the observed or estimated interfacial depths was performed. The agreement between the observed saturation interface depth and the projected interface is striking. The initial growth of the saturated layer is captured accurately, as are periods of the saturated layer shrinking.

Due to freezing conditions, the value of q cannot be accurately estimated until

after the fog layer has deepened above the freezing layer (roughly 20.00 local time). After this point, we diagnose the fog interface from the one-minute camera images. Again, the forward-integrated fog depth (red line, Figure 6.5a, right) agrees well with the observed depth of the fog layer (grey line), capturing an initial steep growth before eventually exceeding the maximum observable height of the camera (2.5 m). Unfortunately, the accuracy above this height cannot be directly confirmed.

6.3.3 Comparison with Tower Observations

We also estimate the growth rate of the fog layer using the coarser-resolution tower observations (Fig. 6.5b). Due to the observational resolution of the tower, we can only say that the fog interface exists between the highest level at which visibility is ≤ 1 km. For example, if visibility is 500 m at 1.5-m height, and 3 km at 10-m height, then the fog interface exists between 1.5–10-m height. This is the shaded region in Fig. 6.5b. The vertical gradients needed for Equation 6.7 are computed as the bulk slope between the two boundary heights of the fog depth (i.e., the difference in values, divided by the spatial separation at two heights).

The estimated fog depth (blue line) fits extremely well within the constraining envelope, deepening steadily throughout the night, and, other than a temporary deepening event estimated around 01:00, reaching the 10-m and 20-m levels at the correct time. This is particularly encouraging as any errors in the projected fog depth would accumulate over the long period of integration (roughly 10 hours). The DTS-estimated fog depth from Fig. 6.5a is also plotted in Fig 6.5b (red line), showing good agreement between the two estimated depths, in spite of the difference in spatio-temporal resolution of the DTS and tower.

This is, of course, only one event. We did, however, also look at the agreement between observed and estimated fog depths for a further 238 shallow (<40 m) radiation fog events that occurred at the CESAR facility between April 2011 and September 2020 (Fig. 6.6). We compute the deviation of the estimated I_z from the observed range. If the estimated depth falls within the envelope, then the deviation is 0. Otherwise, the difference is calculated between the estimated fog depth and the nearest range boundary. While there are some instances of very large differences between the observed and estimated I_z, the majority agree. In particular, I_z falls within the correct range more than 80% of the time within the first 3 hours of fog onset, and, except for 5 h and 10 h, is accurate more than 60% of the time.

6.4 Comparison with Large-Eddy Simulation Output

Due to observational—primarily vertical resolution—constraints, we are unable to accurately observe a deep (optically thick) fog layer; above 40-m height on the tower, Δz becomes $> 40\ m$, which does not allow for reliable derivatives to be estimated. Therefore, we also run a series of simple large-eddy simulations (LES) to test whether Equation 6.7 might also hold for deeper (and simulated) fog layers. We use the Dutch Atmospheric Large Eddy Simulation (DALES; Heus et al. 2010) for our simulations.

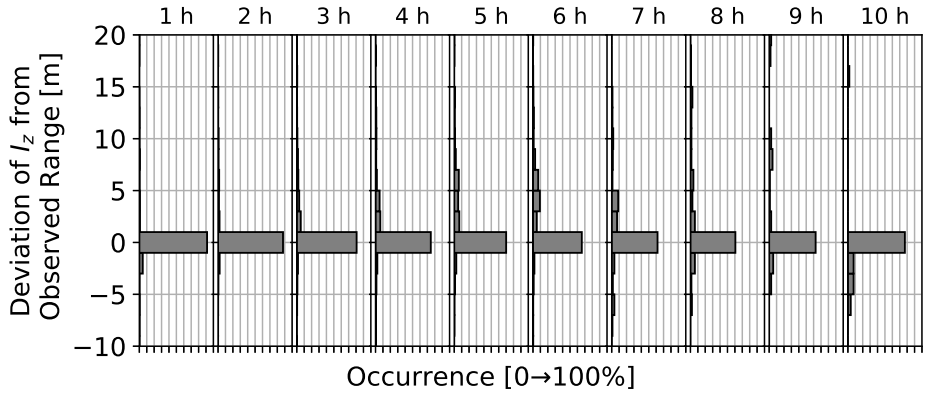

Figure 6.6: Deviation of estimated I_z from the observed range for 238 shallow radiation fog events observed at the CESAR facility between April 2011 and September 2020. The PDFs show the difference in 2-m bins, over each hour after fog onset.

DALES is an open-source atmospheric model written to simulate a range of processes, including stratocumulus clouds as well as convective and stable boundary layers. It was also previously used to simulate the dissipation of fog (Wærsted et al. 2019). DALES is available at https://github.com/dalesteam/dales. For the purposes of this work, the specific formulation of DALES is not discussed. Instead, the interested reader is directed to Heus et al. (2010) for further detail.

It is important to note that in this section we are are not so much concerned with the accuracy of the simulation as we are with illustrating and testing the qualitative principles behind Eq. 6.7

6.4.1 Case Setup

The simulated case is based on a fog event observed on 23 March 2011 at the CESAR facility, which was previously described (Boers et al. 2013) and simulated (Maronga and Bosveld 2017) in the literature. In total, we performed seven simulations (see Tables 6.1 and 6.2), each with a three-letter identifier. The baseline setup (BAS) most closely resembles the reference set-up in Maronga and Bosveld (2017).

The simulations are initialized at midnight with idealized profiles as in Maronga and Bosveld (2017) (Fig. 6.10). Piece-wise linear profiles with a boundary-layer depth of 50 m are defined for the liquid-water potential temperature (θ_l) and relative humidity (RH), which are then used to determine the initial profile of q_t according to the DALES formulations. We use a small computational domain, measuring just 50 m × 50 m in the horizontal (representing the same area as the energy-balance field in which the DTS observations in Sect. 6.3 were made), and 384 m in the vertical. We recognize that the horizontal extent of the domain is small compared to the ultimate depth of the fog layer. However, the early stages of fog development within the stable boundary layer will be represented accurately. Further, initial tests

on domain size showed little difference in the overall fog evolution, with the small domain therefore selected as providing a balance between computational efficiency and accuracy. Again, we note that we are also not concerned with producing a 100% accurate simulation of the case as we are with testing the qualitative principles behind the equations presented.

In the lowest 100 m of the domain, a grid cell resolution of 1 m^{-3} ($\Delta x = \Delta y = \Delta z = 1$ m) was used. Above 100-m height, the vertical grid was stretched linearly with a slope of 1.25 m per grid cell (maintaining a 1-m horizontal resolution). Periodic boundary conditions were used in the horizontal direction. The simulation output was averaged and saved every minute (of simulated time). Further detail on the case set up and simulation specifications can be found in the Appendix.

We performed six additional simulations with modified parameters compared to BAS (Tab. 6.2). Aerosols were increased (AEI) from $N_c = 150$ cm^{-3} to $N_c = 200$ cm^{-3}, such that there is a greater number of smaller droplets. Enhanced near-surface mixing (EMI) was achieved through increasing the values of z_0 for momentum and heat by 10%. To modify the amount of mixing due to vertical shear, we perform simulations with a reduced wind speed (RWI) of $U_{geo} = 3$ m s^{-1}, and an increased wind speed (IWI), with $U_{geo} = 5$ m s^{-1} (from 4 m s^{-1} in the BAS case). Finally, to test the influence of the vertical gradients on growth, the slopes of temperature in the residual layer (IRS) and depth of the boundary layer (IBL) were increased, maintaining the same temperature and *RH* values at the surface and top of the BL.

We attempted to perform additional simulations beyond the six included here (e.g., modifying the surface conductivity, decreasing the depth of the boundary layer, or with larger changes in the variables); however, due to the sensitivity of the conditions, these additional simulations either produced no fog, or were computationally unstable within the simulation environment. As it stands, the only simulation included here that produced no liquid water is IWI; however, it is included for completeness and to provide one example of fog-free conditions.

We determine the simulated saturation interface from profiles of the liquid water specific humidity, q_l, at the horizontal centre of the domain. We use a threshold value of $q_l \geq 0.01$ g m^{-3} (same as in Maronga and Bosveld 2017) to identify the foggy/saturated layer. I_z is only determined when the saturated layer is in contact with the surface (i.e., before lifting after sunrise). We then determine $\partial I_z / \partial t$ as the discrete derivative of the simulated I_z in time. As with the observational comparison in Section 6.3, we also estimate the gradients at the interface and use them to project the growth rate forward in time from $t = 0$ to estimate I_z (Eq. 6.20). Given the numerical setting, we are also able to determine the position of the lower interface after lifting (B_z), and estimate its position and lifting rate according to the same process as I_z. We further estimate the value of M_z using an iterative approach as described in Sect 6.2.2, and assuming a liquid water content of 0.15 g m^{-3} for a fog layer (Pilie et al. 1972). Where a mixed value of 0.15 g m^{-3} or greater cannot be achieved, even for the existing saturated layer, M_z is set to the value of I_z.

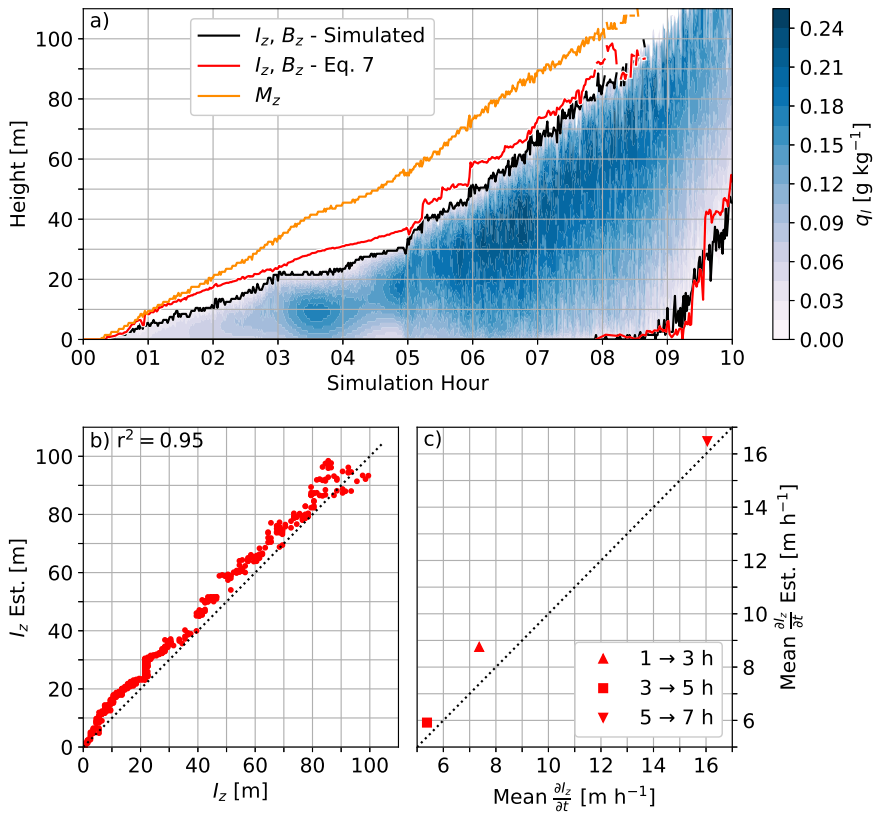

Figure 6.7: BAS simulation. a) Liquid water specific humidity with lines indicating the simulated and estimated (according to Eq 6.20) I_z, B_z, and M_z. b) 1:1 comparison of estimated fog depth to simulated fog depth. c) Comparison of mean estimated growth rate (Eq 6.7) with simulated growth rate over two-hour segments.

6.4.2 Simulation Results

We present the results of the BAS simulation in Fig. 6.7. One-minute profiles of q_l are shown in Fig. 6.7a, along with the diagnosed and projected upper and lower interfaces, I_z and B_z, as well as the estimated MAMD, M_z. Figs 6.7b and c show the direct comparison between the estimated and simulated I_z, and mean growth rates, respectively. We determined the mean rates as the average over the two hour periods indicated. Overall, the estimated interface agrees very well ($r^2 = 0.95$) with the simulated interface, even over the roughly nine hours of estimation. I_z is slightly overestimated, but that is primarily due to just a few points where the growth rate is too high. Notably, the average growth rates during the 2-hour periods are very similar.

The estimated and simulated interface heights of the other simulations from Tab. 6.2 are shown in Fig. 6.11. As with BAS, I_z is well-estimated using the analytical expression in Eq 6.7, and projected forward in time as in Eq 6.20. Although

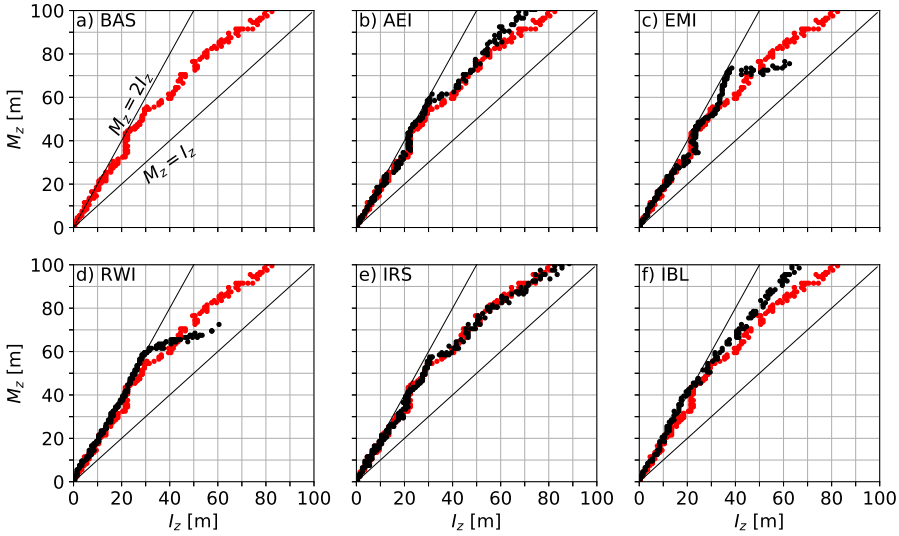

Figure 6.8: M_z vs I_z for the simulations, with $M_z = 2I_z$ and $M_z = 2I_z$ for comparison. a) BAS simulation. b–d) Labelled simulation (black) on top of BAS simulation (red).

the depth is different than the BAS case, the simulated and estimated interfaces agree well ($r^2 = 0.78$–0.94) . As with the BAS simulation, the value of I_z approaches M_z toward the end of the simulation.

In Fig. 6.8, M_z is plotted as a function of the simulated I_z for all fog-forming simulations. M_z remains around $2I_z$ for all simulations while up to $I_z \sim 25$ m (roughly 2–5 hours into the simulations). This identifies the transition from an optically thin, stably stratified fog layer to an optically thick, well-mixed fog layer. As the level of mixing increases, M_z and I_z converge. During the transition period, M_z continues to deepen while I_z remains nearly constant. This is because the fog layer continues to cool, with the restricted vertical growth leading to a build-up of excess moisture in the fog layer.

Figures 6.7 and 6.9 also plot the simulated and estimated values of the lower interface, B_z, after the fog lifts from the ground, becoming a shallow stratocumulus cloud. As with the upper interface, the lifting of the cloud base is also well described by Eq 6.7. The agreement between simulated and estimated B_z is particularly good for BAS, AEI, EMI, and IRS ($r^2 = 0.85$–0.96), even with large variations in the lifting rate between the simulations. Overall, B_z is underestimated for the RWI and IBL simulations, though still qualitatively similar. Due to the lack of liquid water simulated in IWI, B_z is irrelevant.

The IBL and IRS cases (Fig. 6.11g and i) demonstrate the importance of the vertical gradients in determining the growth rate. With the deeper BL (IBL), the slope in temperature is correspondingly shallower in order to maintain the same temperature at BL-top. As a result—due to the reduced stability near the surface and the smaller denominator in Eq. 6.7—the fog layer grows much more rapidly.

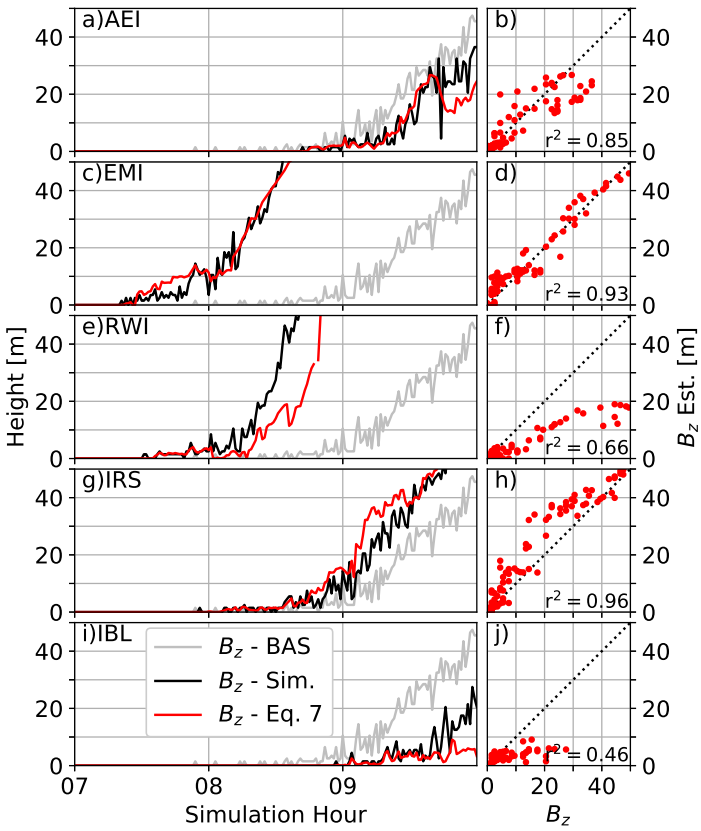

Figure 6.9: The simulated and estimated locations of the lower interface, B_z, for each of the six simulations in Tab 6.2. The panels correspond to those in Fig 6.11.

M_z is also much deeper for the IBL simulation as the profile is such that more of the layer is near saturation (reduced slope). At the same time, the "stalling" seen in other simulations does not occur. Instead the fog layer is able to grow continuously throughout its evolution. Conversely, the increased slope in the residual layer (IRS), though only a difference of 10%, is enough to slow the growth rate slightly compared to the BAS simulation.

The analysis in Sect. 6.2.1 (Eq. 6.11), suggests that the growth rate of radiation fog increases in time, due to the fact that the strongest inversion occurs close to the surface (convex temperature profiles). Interestingly, this appears to be a general feature of the fog growth in our simulations (e.g., Fig. 6.7c), due to the smaller vertical gradient above the BL. One also sees that the growth temporarily slows during transition from optically thin to optically thick fog (roughly between 3-5 hours), though this may also be related to the boundary-layer height of the simulation. During this time, there is an over-estimation of I_z, which is primarily due to an initial over-estimation at the time of the vertical profiles becoming well-mixed (top-down

convection). After this initial overestimation in the interface depth ($\partial I_z/\partial t$ too large as the denominator is close to 0), the mean estimated and simulated growth rates are approximately equal (e.g. Fig 6.7c).

6.5 Summary and Discussion

We begin by first summarizing the previous sections, followed by a discussion of the use and significance of the results presented herein.

In Sect. 6.2 we derive an analytical expression to describe the rate of deepening/erosion of a fog interface. Given the conditions under which fog exists, the relative moistening or drying at the interface determines whether the fog layer will deepen or erode, while the gradients in specific and saturation-specific humidities modulate the rate of growth. We also present a lengthscale estimate of the maximum depth that a fog layer can achieve, the "maximum attainable mixed depth" (MAMD), as might occur if there was a sudden mixing event that equalizes the vertical profiles of temperature and humidity. This MAMD also gives an indication of the robustness of a fog layer to a given level of mixing; any mixing deeper than MAMD, or a reduction in MAMD below the existing fog depth, will lead to dissipation.

We subsequently validate the analytical formulation in Eq. 6.7. We utilized both a high-resolution and a coarse-resolution data set for the observational comparison (Sect. 6.3). In both cases, the analytical expression results in an estimated fog depth that agrees very well with the observed fog interface, lending confidence to its accuracy. Even with the coarser data from the CESAR tower, the timing of deepening is remarkable, especially considering the length of the night over which the estimated interface is determined. This is not only true for the highlighted case, but also for 238 events assessed between April 2011 and September 2020. Unfortunately, though, the observational data are insufficient for a truly direct comparison. First, the coarse resolution (especially from the tower data) means that only an approximate agreement can be determined. Second, observations of deeper fog layers are needed to ensure the relationship holds for optically thick fog layers; the resolution above 40-m height (at least at the CESAR facility) is too coarse to determine reliable vertical gradients.

As a surrogate, we performed several numerical simulations of an idealized radiation fog layer that grew to become optically thick over the course of roughly nine hours (based on the case in Maronga and Bosveld 2017; Sect. 6.4). The estimated interface depths again agree very well with the simulated depths; both for the baseline (BAS) case, and the perturbed cases (see Tab 6.2). Problems mainly arise when the denominator of Eq. 6.7 is close to zero (very shallow vertical gradients), in which case very large values of $\partial I_z/\partial t$ are estimated. This means that either shorter integration times need to be used, or such spikes must be removed or averaged in order to obtain accurate estimates of I_z.

In addition to the estimated interface depth, we also determine M_z for the simulations, assuming a well-mixed fog layer. Throughout the first few hours, M_z remains at the predicted $2I_z$ for all simulations (Fig. 6.8), with the two values approaching

each other after the transition. The more rapid deepening of M_z than I_z in the middle of the simulations is likely due to the restriction of vertical mixing as the top of the boundary layer is reached, and the time of transition from optically thin to optically thick fog. During this time, I_z is mechanically constrained, while the super saturation continues to increase significantly due to the continued cooling within the shallow layer.

Of the seven simulations that we performed, only the one with increased geostrophic wind speed (IWI) resulted in no simulated fog (Fig. 6.11k), with dew point only briefly achieved at the surface near the beginning of the simulation. However, applying Eq. 6.7 would still lead to an estimated fog layer that is 30 m deep. This highlights the need to ensure that Eq. 6.7 be applied to estimate the growth of an existing fog layer, rather than to forecast a fog layer that has not yet appeared. Otherwise, the assumptions and the conditions in Sect. 6.2 are not met, and the relationship is invalid.

6.5.1 Equation 6.7 to Interpret the Evolution of Typical Fog Layer

We now highlight how Eq. 6.7 can be used to interpret and understand the evolution of a fog layer. The observations in Sect. 6.3.2 and simulations in Sect. 6.4 indicate that such a fog layer will initially grow slowly, with accelerating growth before slowing toward the transition to well-mixed fog. Eventually, top-down erosion of the fog interface, or lifting of the cloud at the surface will take place.

We begin by assuming a very shallow radiation fog forming within a quasi-steady, stable boundary layer. The fog will grow according to the rate of quasi-steady cooling (Eq. 6.9). Due to the decreasing vertical gradients (smaller denominator) with height, the rate of growth increases with fog depth (Eq. 6.11). The acceleration means that there is a sort of "early warning" in the system (such as highlighted in Izett et al. 2019a). At the same time, Eq. 6.7 also implies that there is a maximum growth rate possible for a given temperature profile (Eq. 6.12).

As the fog layer undergoes the transition to a well-mixed fog layer, the gradients in temperature and moisture become smaller below the interface, and larger above the interface. According to the analysis here, this results in a slowing of the fog growth (e.g., Fig. 6.11), with competing profiles above and below the interface; the more uniform profile just below the interface favours erosion of the fog layer. A similar "upside-down" interface exists when the fog lifts from the surface, becoming a shallow stratocumulus cloud. As with the fog top, this lower interface is also seen to be well-described by the analytical expression that we derive in Sect. 6.2, as evidenced through the numerical comparison in Figs. 6.7 and 6.9. The well-mixed profile means that just a small amount of warming or drying is needed in order to reduce the relative humidity at the surface.

Under stable conditions, M_z is shown to be roughly equal to $2I_z$ (Sect 6.2.2). This means, intuitively, that deeper fog layers are more robust to increases in turbulent mixing, whereas shallow fog layers can be rapidly dissipated. This is evidenced in the "twin nights" presented in Fig. 8 of Izett et al. (2018c) where an increased wind speed

on the second night prevents a fog layer from forming, in spite of otherwise identical conditions. Significant deviation from the 2:1 ratio indicates that mixing has taken place (Fig. 6.8). The closer I_z is to M_z, the more mixing has occurred, but also the closer the fog layer is to its maximum sustainable depth. Beyond a height of M_z, the fog layer cannot be sustained unless significant moisture advection occurs. This leads to the fog-top erosion, or cloud-base lifting seen toward the end of a fog's lifecycle, which, as above, can be understood through the small denominator of Eq. 6.7.

6.5.2 Equation 6.7 as a Diagnostic Tool

Beyond simply understanding, our analytical expression enables precise estimation of fog depth, particularly in settings where discrete observational levels are insufficient for continuous tracking of fog depth. Equation 6.7 provides this, with the time and space derivatives able to be determined from previous observations, and used to project the evolution forward in time (e.g., Eq. 6.20). This can be used as both an *a priori* estimate of fog evolution in the coming minutes or hour, as well as an *a posteriori* tool for tracking the evolution of a fog layer, and relating it to the processes involved. It may also be that the methodology is useful in a numerical setting, providing a sub-grid indication of fog depth.

Equation 6.7 also provides a means of determining the sensitivity of fog layer to calculation errors, as well as to changes in physical processes. In particular, when the denominator of Eq. 6.7—which modulates the growth rate—is small, the fog layer will be extremely sensitive to any changes in moisture, e.g., through advection or changes in turbulent mixing. This carries over into the computational domain, where numerical experiments will become increasingly sensitive to slight computation or input errors.

M_z, which is derived from thermodynamic conservation principles (Eq. 6.13), provides an indication of the amount of mixing that can be tolerated before fog dissipation. If the mixing lengthscale is larger than M_z, mixing will dry out the air such that the fog will dissipate. It also provides an upper limit estimate of the depth to which a fog layer could reach under the current conditions, were a mixing event—such as the transition to well-mixed fog and/or increased turbulent mixing—to take place.

All of this assumes that the gradients and time derivatives can be accurately determined. Within the near-saturated SBL, errors in determining temperature and humidity can be large. One can assume, though it is not guaranteed, that the error will be similar at all heights, meaning that the relative values used to estimate derivatives will still be reasonably accurate. At the same time, the results presented here do still suggest the method is reliable, even under challenging conditions. Equation 7 also provides us with a means of understanding the sensitivity of our observations/predictions to errors. By including approximate errors into the framework, we see how sensitive results may be. For example, if the error means that the sign of Eq. 7 changes, then the conditions are extremely sensitive to miscalculation. On the other hand, it may be that the overall magnitude of the terms is sufficiently large

that the errors only affect the magnitude, but not the actual growth/erosion.

6.5.3 Specific Processes at the Interface

Price and Stokkereit (2020) have shown through the use of infra-red imagery that several processes can influence the evolution of a fog layer. It is beyond the scope of this research to explicitly consider the specific processes that modify the terms in Eq. 6.7, however, one could utilize the conceptual framework here in addition to leveraging multiple sources of information in order to interpret the evolution. For example, the moisture budgets could be determined through consideration of relevant boundary-layer processes, rather than observational diagnosis alone. Ultimately, they can be broadly grouped into three categories: radiative, advective, and turbulent processses. While the exact role of any process will depend on the specific conditions, we briefly discuss them here.

Radiative cooling will serve to modify the saturation specific humidity through means of altering the temperature in both time and space. As the fog layer becomes optically thick, the cooling interface will change, sharpening vertical temperature gradients near fog top (slowing the growth of fog), while at the same time, continuing to cool the interface (leading to fog deepening). In the absence of other processes, the growth rate will remain positive, but gradually decrease in time.

Advection of cooler and or more moist air will lead to a deepening of the fog layer; often a rapid deepening as the vertical gradients are reduced. Conversely, warmer, drier air will lead to evaporation and dissipation of the fog. The ultimate state of saturation will depend on the amount of mixing that takes place, and the original state of the air masses in question (Taylor, 1917; Price, 2019).

It has been shown that turbulence acts to limit the formation of radiation fog, with weak to no wind required (e.g., Roach et al. 1976). At the same time, others have found that at least some turbulence is necessary for fog formation in order to mix the air vertically and lead to saturation over a deeper region (e.g., Duynkerke 1999). In Price (2019), a threshold is defined for the level of turbulence (w'^2 must be less than 0.002–0.005 $m^2\ s^{-2}$) for radiation fog to form, provided the air is sufficiently close to saturation; above this threshold, the air will dry out, rather than lead to a saturated mixture. We can further reconcile the role of turbulence through contemplation of Eq. 6.7 as follows. Turbulent mixing will serve to reduce the vertical gradients of temperature and humidity, such that the denominator becomes smaller, increasing sensitivity of the fog top to changes in moisture. At the same time, however, turbulent transport will also (under stable conditions) bring warmer, (relatively) drier air from aloft, and reduce the relative moistening at the interface. If the turbulent mixing is too great, then erosion will take place. In the case of weak to no turbulence, a quasi-steady boundary layer will form, where the gradients remain approximately constant. This means that any growth will be driven by the relative moistening through cooling by radiative processes alone; a much slower process. We see this reflected even in our simple simulations. The fog layer grows deeper and more rapidly in our BAS simulation than either of the reduced or increased wind

cases (RWI and IWI). In the case of the former, this may be due to the reduced vertical mixing, while in the latter no fog forms due to the too-large drying influence.

6.6 Conclusions

We derive an analytical expression that describes the rate of fog deepening or erosion as the ratio of the time derivatives of moisture to the vertical gradients (Eq. 6.7)

$$\frac{\partial I_z}{\partial t} = \left(\frac{\partial q}{\partial t} - \frac{\partial q_s}{\partial t}\right)\left(\frac{\partial q_s}{\partial z} - \frac{\partial q}{\partial z}\right)^{-1},$$

The denominator is always positive in the case of fog top, and the sign of the numerator governs whether the fog layer will deepen or erode. Observations and simple simulations of idealized fog layers show that the relationship does a good job of explaining the fog evolution.

We also present a lengthscale estimate of a fog layer: the maximum attainable mixed depth (MAMD). This is both an indication of the depth a fog layer could potentially reach due to a sudden mixing event, as well as the maximum depth over which mixing can occur before a fog layer will dissipate due to insufficient moisture content. Under stable conditions, we show this to be roughly $2I_z$; significant deviation from this ratio indicates that mixing has occurred, and that the fog layer may be closer to dissipation.

The analytical description can be applied diagnostically. It is particularly useful for identifying the growth rate and interface depth in an observational setting. Where observations are limited to discrete heights, Eq. 6.7 can be used to identify the position of the fog interface between levels. This can then be related back to observed processes, and possibly used to improve the output of numerical models by providing a more precise location of fog height, rather than simply an observed range of possible depths. Further, it may prove useful as a subgrid component of numerical models, though that is not directly investigated here.

The analytical framework also provides a formalized means of understanding why fog evolves the way it does. Through consideration of the equation and the contributing processes, one can identify the role that different factors play in the growth and dissipation of a fog layer. Among other things, we show that acceleration of fog growth with height, the temporary pause in growth during the transition to well-mixed fog, and the ultimate dissipation and/or lifting can all be explained through Eq. 6.7 and the concept of the MAMD.

We recognize that the present analysis is very much of local nature, and primarily applicable to radiation fog. It would be interesting to extend the present rationale to advective tendencies as well in order to obtain a more general description of fog growth and erosion. It would also be enlightening to assess the full budget equations for the upper interface—including turbulent mixing processes, radiative cooling, and advective tendencies—in order to quantify the gradients and tendencies in Eq. 6.7. This would be particularly interesting in conjunction with the use of a range of data

sources, including traditional sensors and emerging techniques such as infra-red photography. Finally, we welcome further testing of the presented metrics in a range of settings, including, other observational sites, as well as numerical weather prediction.

6.A Additional Information Regarding the Large-Eddy Simulations

In this appendix, we present additional information, including tables and figures, in support of Sect. 6.4. Tables 6.1 and 6.2 present an overview of the parameters used in the BAS and modified simulations, respectively.

Symbol	Parameter	Value
λ	Surface conductivity	$4\,\mathrm{W\,K^{-1}\,m^{-2}}$
N_c	Droplet number concentration	$150\,\mathrm{cm^{-3}}$
$s_{T,BL}$	Slope of temperature in the BL	$0.08\,\mathrm{K\,m^{-1}}$
$s_{T,RL}$	Slope of temperature in the RL	$0.01\,\mathrm{K\,m^{-1}}$
RH_0	Surface relative humidity	98%
RH_{BL}	Relative humidity at BL top	90%
RH_{TOP}	Relative humidity at top of domain	85%
T_0	Surface temperature	276 K
T_S	Soil temperature	279 K
U_{geo}	Geostrophic wind speed	$4\,\mathrm{m\,s^{-1}}$
z_{max}	Maximum height of domain	384 m
z_{BL}	Depth of the initial boundary layer	50 m
$z_{0,m}$	Roughness length for momentum	0.15 m
$z_{0,h}$	Roughness length for heat	0.235×10^{-4} m

Table 6.1: Overview of the main parameters used to initialize the BAS simulation. Parameters modified for the other simulations are listed in Table 6.2.

Simulation		Changed Parameters
AEI	Aerosols increased	$N_c = 200\ \mathrm{cm^{-3}}$
EMI	Enhanced mixing	$z_{0,m} = 0.165$ m, $z_{0,h} = 0.259 \times 10^{-4}$ m
RWI	Reduced geostrophic wind speed	$U_{geo} = 3\ \mathrm{m\ s^{-1}}$
IWI	Increased geostrophic wind speed	$U_{geo} = 5\ \mathrm{m\ s^{-1}}$
IRS	Increased residual slope	$s_{T,RL} = 0.011\ \mathrm{K\ m^{-1}}$
IBL	BL-depth increased	$s_{T,BL} = 0.04\ \mathrm{K\ m^{-1}}$, $z_{BL} = 100$ m

Table 6.2: Overview of the six additional simulations performed, with the the remaining parameters the same as in the BAS setup (Table 6.1).

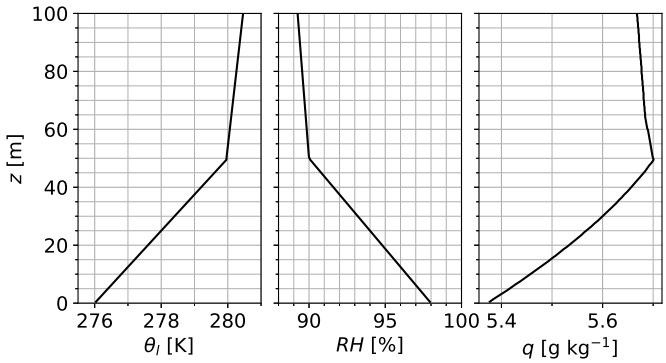

Figure 6.10: Initial profiles, as described in Maronga and Bosveld (2017) of a) temperature, b) relative humidity, and c) specific humidity (calculated from T and RH) for the BAS simulation.

Figure 6.10 shows the initial profiles of θ_l, RH, and q used to initialize the BAS simulation. Within a boundary layer of 50-m depth, θ_l increases linearly from 276 K with a slope of 0.08 K m^{-1}, while RH decreases from 98% in the lowest grid cell to 95% at the top of the boundary layer (BL). Above the BL, θ_l increases more slowly at 0.01 K m^{-1}, and RH goes from 90% to 85% at the top of the domain.

Within the model, radiative transfer is calculated via the rapid radiative transfer model developed for general circulation models (RRTM-G, Mlawer et al. 1997), as well as the bulk microphysical scheme of Seifert and Beheng (2001, 2006), with droplet settling enabled. Note that initial tests showed little dependence on the microphysical scheme employed. The surface is described by an interactive scheme with four soil layers (of uniform temperature).

Figure 6.11 plots the comparison for the additional simulations presented in (Tab. 6.2). In the left-hand column, we show simulated I_z, along with the estimated value of I_z using Eq. 6.7, and M_z. For comparison, I_z from the BAS simulation is shown in grey. On the right, the estimated I_z is compared directly with the simulated I_z. Except for the IWI simulation where no fog formed, I_z is very well estimated with Eq. 6.7.

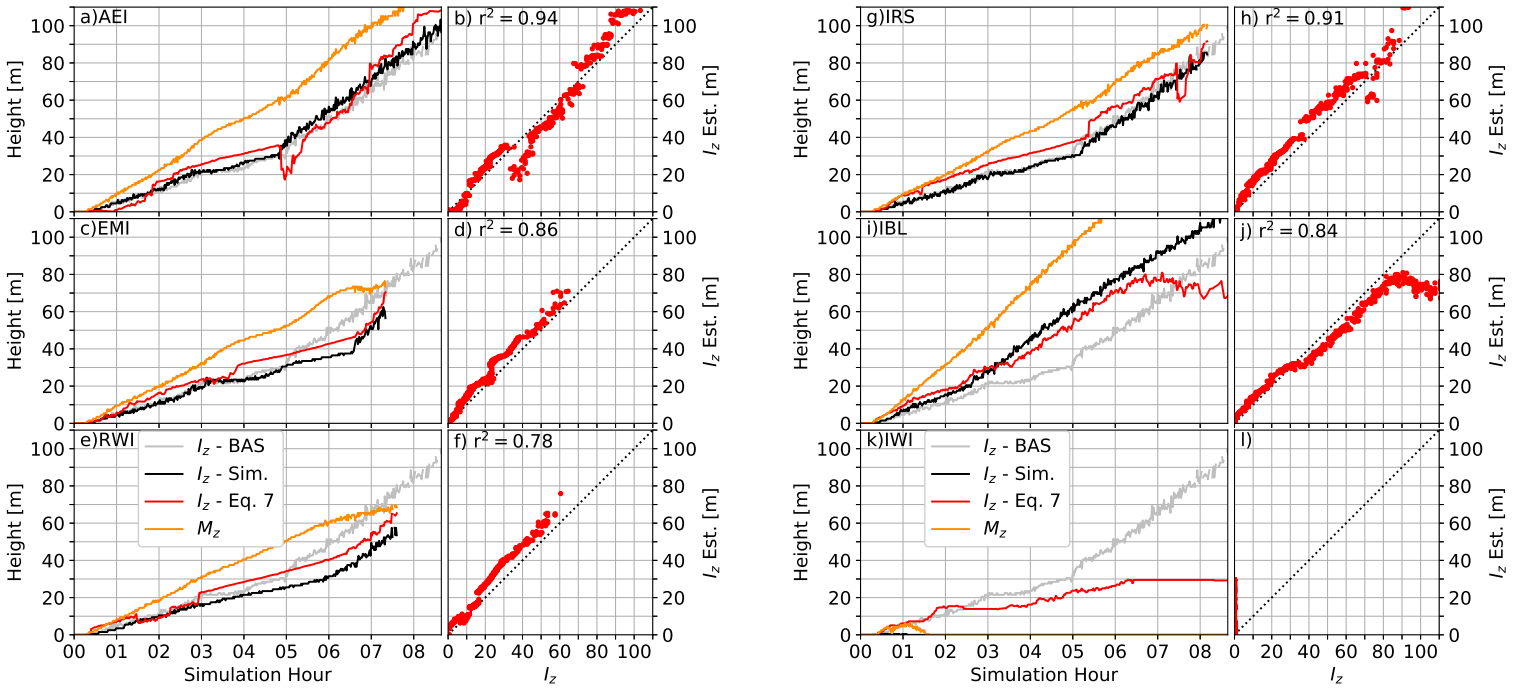

Figure 6.11: Estimated and simulated interface heights for the additional simulations (see Tab. 6.2). a, c, e, g, i, k) Timeseries of estimated and simulated fog depth, including the simulated depth from the BAS simulation (as in Fig 6.7a). b, d, f, h, j, l) 1:1 comparison of estimated fog depth to simulated fog depth (as in Fig 6.7b)

Chapter 7

The Evolution of Radiation Fog

Foundations of a Conceptual Model

> Above, a pink sky was slowly filling with fog.
>
> J. le Carré,
> *Tinker, Tailor, Soldier, Spy*

Summary

This chapter presents initial work on developing a conceptual framework for understanding and modelling the evolution of a radiation fog layer, building upon the results of the previous chapters. Radiation fog forms under (very) stable atmospheric conditions. However, if the fog layer becomes deep enough, the fog layer becomes optically thick to longwave radiation, and a transition to a neutrally stratified fog layer occurs. We describe this transition conceptually based on the principles of boundary-layer theory, assuming a quasi-steady boundary layer that cools uniformly in height. From this starting point, we are able to analytically define the growth rate of the fog layer, the time and depth of the transition to well-mixed fog, and the mean properties of the fog layer.

7.1 Introduction

The hazard that fog presents to human activities depends on both the minimum visibility, as well as the depth to which the low visibility extends. It is therefore important to know how a fog layer might evolve throughout the course of its lifetime, and at what stage the hazard of the fog layer is increased. Typical approaches, such as the use of numerical models, can be computationally expensive, and, in the case of radiation fog, unable to capture the onset and evolution with accuracy (e.g., Steeneveld

This chapter represents ongoing research that is still in the exploratory stage.

et al. 2015). For this reason, we turn to a simple analytical approach in order to estimate and understand the timing and evolution of key stages in the lifecycle of a radiation fog layer.

Radiation fog typically forms under stably stratified conditions when a large negative imbalance in the surface longwave radiation leads to rapid cooling. As the surface cools, saturation (the dew point) is reached. Subsequent cooling, in the absence of other processes, then leads to deepening of the fog layer. Eventually the fog layer reaches sufficient depth that it becomes *optically thick* to longwave radiation. In other words, there is so much liquid water between the surface and the top of the fog layer, that the longwave radiation is completely absorbed by the fog itself, and the net surface radiation tends toward zero. At this point, a transition occurs in the fog, whereby the stable stratification is overcome, and the temperature and moisture profiles become well mixed (e.g., Román-Cascón et al. 2016b; Smith et al. 2018; Boutle et al. 2018b; Price 2019).

Previous efforts to describe the initial stages of fog onset and growth include the work by Menut et al. (2014) (and subsequently followed by Román-Cascón et al. 2016a; Izett et al. 2018c), where a diagnostic method is used to predict the onset of a fog layer at the surface. While accurate upwards of 80% of the time, their diagnostic methodology does not look at the later evolution of the fog layer. Derbyshire (2019) presents a simple, "toy model" describing the evolution of a fog layer that cools at a constant rate in time, with a prescribed turbulent profile within the boundary layer. His toy model, however, does not include the internal feedback of radiation on the evolution of the fog layer.

Price (2011) presents detailed analysis of the evolution of radiation fog using roughly two and a half years of data from Cardington in England. Of the 38 events considered, roughly half transitioned to well-mixed fog. While the exact mechanisms for the transition were not identified, Price highlights that the transition will most likely take place as a result of the optical thickness becoming too great for surface cooling to persist, and the migration of the cooling interface from the surface to the fog top. As a result, the surface warms, and fog top cools, equalizing the temperature profile. He further states that, if the depth at which fog becomes optically thick can be identified "then it would likely be a useful indicator as to whether a fog will undergo temperature convergence".

Boutle et al. (2018b) subsequently investigated the role of aerosols in the transition to well-mixed fog. Through observations and large-eddy simulations, they demonstrate three key factors in determining the transition to radiation fog, namely, 1) the amount of time fog has to develop, 2) the rate with which the fog can deepen, and 3) the amount and type of aerosols present. The first two relate to the fact that the optical thickness of a fog layer is dependent on its physical depth. As explained in Izett and van de Wiel (2020), fog growth is slow under strong stratification, so that it takes more time to reach an optically thick state. Simply put, if the fog deepens at a slow rate (e.g., under strong stratification as demonstrated in Izett and van de Wiel 2020), then it will need more time to develop. If, however, the environmental setting changes, such as with sunrise, then the fog may never reach a sufficient

depth to achieve a well-mixed profile. The third point made by Boutle et al. (2018b) relates to the optical properties of the cloud droplets. The more activated aerosols (i.e., those that become condensation nuclei for water droplets), greater the effect on blocking the longwave radiation, and the shallower the fog layer needed in order to realize an optically thick cloud.

In this research, we present a simple conceptual model of radiation fog growth and evolution. We build upon the work by Izett and van de Wiel (2020), where a simple description of the growth of a fog layer is presented, in which the growth is ultimately shown to be proportional to the ratio of cooling at the fog top, and the vertical gradient of temperature. We specifically aim to identify the initial deepening of the shallow, stably stratified fog layer, and the point at which it transitions to a deep, well-mixed fog layer. The goal is to provide a simple conceptual description, as well as *a priori* estimates of fog depth, surface (longwave) radiation, and the transition to well-mixed fog conditions.

We first present a brief overview of observed transitions from stably stratified to well-mixed radiation fog events from the Cabauw Experimental Site for Atmospheric Research (CESAR; e.g., Monna and Bosveld 2013) in the Netherlands (Sect. 7.2). We then describe our conceptual framework, including our guiding assumptions, followed by a presentation of analytical solutions to the equations (Sect. 7.3). In Sect. 7.4, we compare our analytical description to the observations from the CESAR facility.

7.2 Observations

We begin by first presenting observations of radiation fog events from the CESAR facility in the Netherlands. Our analysis period is from April 2011 to September 2019, inclusive, when relevant surface radiation and visibility data are regularly available. The CESAR facility is located in relatively flat terrain, with only a ∼7-m tall embankment roughly 1 km to the southeast providing any significant topographic influence. This makes the site ideal for studying the transition of radiation fog to well-mixed fog in the absence of the topographic effects that were noted during the LANFEX study (Price et al. 2018).

We first identify radiation fog events according to the algorithm of Tardif and Rasmussen (2007), and only look at "independent events" separated by at least two hours, as per Román-Cascón et al. (2016a). Based on this classification, a total of 501 fog events occurred over the 8.5 years in question, with roughly 60% being radiation fog events (Fig. 7.1a). Of these radiation fog events, just 15% transitioned from stable temperature stratification to well-mixed, neutrally stratified fog layers. The transition was identified subjectively according to visual homogenization of the temperature profiles.

The observed transitions occurred at a range of fog depths, though most commonly between 40–80 m (Fig. 7.1b). We note that, while the time it takes for the fog layer transition varies, the transition itself can be very rapid, even occurring over

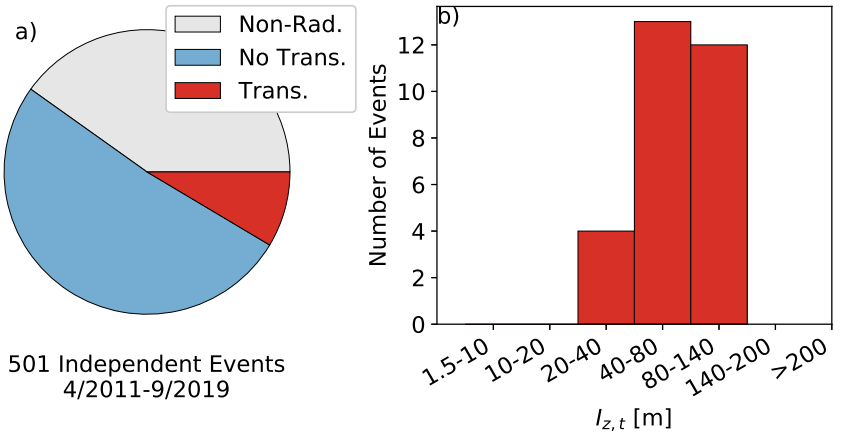

Figure 7.1: Overview of observations of transitions in radiation fog at the CESAR facility between April 2011 and September 2019. a) Statistics of fog event types, and b) depth of the fog layer when the transition occurs.

just a few observations.

Many of the observed transitions occurred at sunrise. While not the mechanism sought in this research, it does suggest that the surface energy balance plays a role in triggering the transition. As the sun rises, the relative heating of the surface compared to the air aloft leads to an unstable temperature profile and convective mixing. Analogously, we note that nocturnal transitions occur in almost all cases when the observed energy balance at the surface approaches zero; i.e., the long wave radiative cooling is less than the heating from the soil and sensible heat fluxes. We therefore use this as our condition for the analytical model, such that the transition occurs when $Q_n = H + G_0$. This is similar to the condition identified by Price (2011), namely, that surface cooling effectively ceases.

Figure 7.2 shows observations of a radiation fog event that took place on 7 April 2015. Fog (visibility ≤ 1 km) was first observed at 21.30 (CET), and persisted over ten hours. The fog layer deepened within a shallow, quasi-steady, very stable boundary layer with a large temperature gradient near the surface (Fig 7.2a). After roughly 2.5 hours, however, the depth and liquid water content (determined according to the visibility relationship of Kunkel 1984) of the fog layer (Fig. 7.2c) were sufficient to significantly reduce the surface longwave imbalance below the compensating soil heat flux (Fig. 7.2c). At this time, the temperature profile becomes convex near the surface, indicating that the surface is warming relative to the air above, and the transition to an optically thick fog layer takes place.

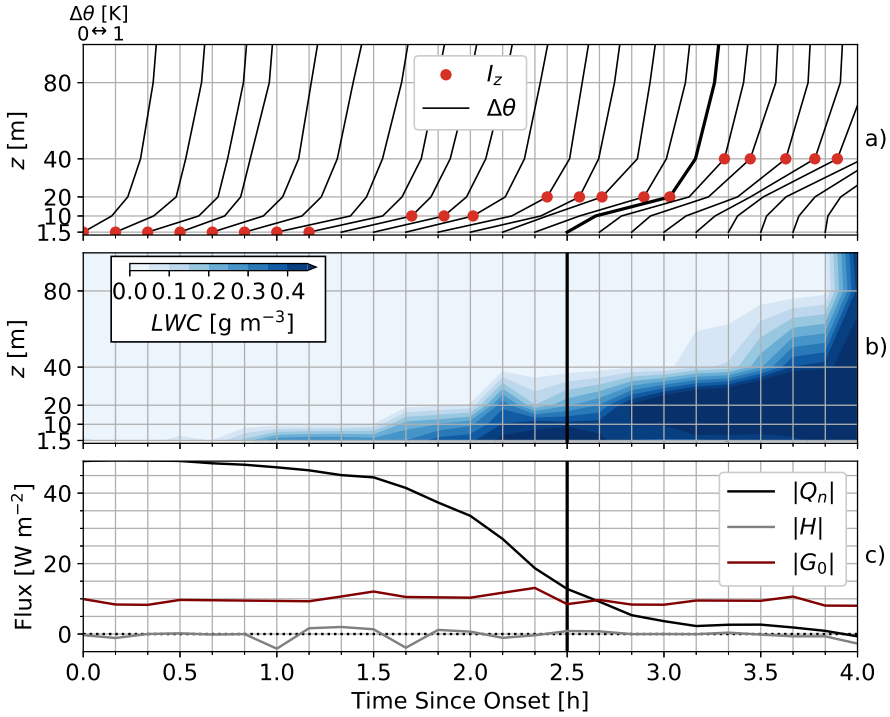

Figure 7.2: Observations during a radiation fog event on 7 April 2015. The thick black lines indicate the transition. a) Temperature profiles (plotted as $\theta - \theta_{1.5}$), with the zero point corresponding to the time of the observation, with the vertical lines corresponding to the 10-minute observation period, and $\Delta\theta = 6$ K. Fog depth is indicated on the profile with the red dots. b) Liquid water content determined from visibility observations according to the parametrization of Kunkel (1984). c) Surface fluxes.

7.3 Conceptual Description

In this section, we outline the conceptual framework that describes the fog layer. We begin by explaining our assumptions, followed by describing the fog layer before and after the transition to a well-mixed, adiabatic fog layer.

In order to construct our model, we make use of the following assumptions:

1. We only consider nocturnal conditions
2. The dew point temperature*, θ_D, and the specific humidity, q, are constant in time, and vertically homogeneous
3. There is no advection of heat or moisture

We acknowledge that the second assumption is not accurate for real fog layers, which typically show height variation of the specific humidity profile. However, this vari-

*Note: we use temperature and potential temperature as roughly interchangeable. While this is far from accurate, it simplifies the analysis considerably.

ability is often much smaller under (very) stable conditions than that of the saturation specific humidity, q_s, which depends on temperature. Therefore, q can be assumed constant compared to q_s. The second and third assumptions are also employed by Derbyshire (2019). Further, pre-transition:

1. The temperature profile can be described as the surface value, plus some additional height-dependent scaling, $f(z)$, such that $\theta(t,z) = \theta_s(t) + f(z)$
2. The fog layer is in a quasi-steady state such that the entire profile cools at the same rate as the surface—that is, $-\lambda$ [K s^{-1}]— maintaining the $f(z)$ shape

and, post-transition:

1. The temperature is well-mixed throughout the fog layer ($\overline{\theta}$), with the profile above the fog layer equal to $\theta_D + g(z)$
2. The fog layer can be treated with a box model approach, such that energy extracted for fog growth is equal to the net (integrated) flux over the entire fog layer

We describe the net longwave radiation according to the simple parametrization of Bretherton et al. (1999). The net radiation is constant at the top of the fog layer, ΔF_0, and decays according to the liquid water path

$$F(z) = \Delta F_0 \exp(-a_0 \cdot W), \tag{7.1}$$

where a_0 is the mass absorptivity of the liquid water (130 m^2 g^{-1}). The liquid water path, W [kg m^2], is the total amount of liquid water between the evaluation height, and the top of the fog layer, I_z,

$$W = \int_z^{I_z} \rho \cdot q_l dz, \tag{7.2}$$

where ρ is the density, q_l the liquid water specific humidity (positive values of $q - q_s$). $\rho \cdot q_l$ is the liquid water content, *LWC*. The value of the net radiation at the surface is then,

$$F_s = \Delta F \exp(-a_0 \overline{LWC} \cdot I_z), \tag{7.3}$$

where $\overline{LWC}$ is the mean liquid water content over the entire fog layer.

Figure 7.3 shows a schematic of temperature profiles before and after the transition, as well as some of the relevant terms in the model.

7.3.1 Evolution at Different Stages

We now present several expressions to describe the evolution of fog in time. All of these expressions can be estimated *a priori* through the assumptions we employ.

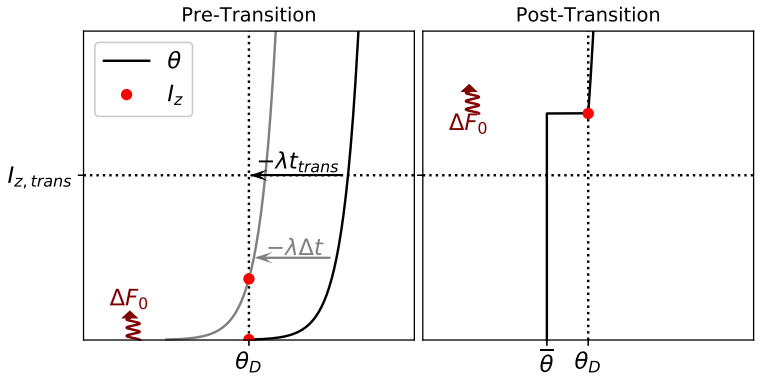

Figure 7.3: Temperature profiles before and after the transition to well-mixed fog. Prior to the transition, radiative cooling primarily occurs at the surface, with the profile assumed to cool at a constant rate, $-\lambda$. After the transition occurs (at time t_trans), then the fog is well-mixed, with a mean temperature throughout the fog layer, and radiative cooling at the top.

Pre-Transition: Initial Growth

As demonstrated in Izett and van de Wiel (2020), a radiation fog layer evolving under the assumptions listed above will deepen as the ratio of the cooling, divided by the vertical gradient of the temperature profile at the fog top, such that

$$\frac{\partial I_z}{\partial t} = \lambda \left(\frac{\partial f(z)}{\partial z}\bigg|_{z=I_z} \right)^{-1}. \tag{7.4}$$

The mean temperature of the fog layer over time is, simply,

$$\begin{aligned} \overline{\theta}(t) &= \frac{1}{I_z}\int_0^{I_z} \theta(t,z)\,dz \\ &= \theta_s(t) + \frac{1}{I_z}\int_0^{I_z} f(z)\,dz \end{aligned} \tag{7.5}$$

We can linearize q_s as in Penman (1948) such that $q_s \approx q_{s,0} + s_{q_l}(T)\,dT$, with $q_{s,0}$ and s_q the values of q_s and $\partial q_s/\partial T$ at the surface, respectively. The mean liquid water content—necessary for Eq. 7.3—then takes on a similar form.

$$\begin{aligned} \overline{LWC} &= \frac{1}{I_z}\int_0^{I_z} \rho(q - q_s)\,dz \\ &\approx \rho q_{l,0} - \frac{s_{q_l}}{I_z}\int_0^{I_z} f(z)\,dz \end{aligned} \tag{7.6}$$

In many cases, the mean liquid water content can be well estimated as half of the

surface *LWC* (as in the simplest case of a linear profile of *LWC* decreasing from $q_{l,0}$ toward zero at fog top. $q_{l,0}$ is known as a function of time through the assumption of constant cooling.

The Transition

Based on the assessment of the observed transitions, we define the transition point as when the surface energy budget is balanced

$$|F_s| = |H| + |G_0| \tag{7.7}$$

There exists, therefore, a critical liquid water path at which the transition will take place. Inserting Eq. 7.3 into Eq. 7.7

$$W_C = \frac{1}{a_0} \ln\left(\frac{\Delta F_0}{H + G_0}\right) \tag{7.8}$$

Assuming a mean liquid water content throughout the fog layer, the "transition depth" of the fog is simply

$$I_{z,trans} = \frac{1}{a_0 \overline{LWC}} \ln\left(\frac{\Delta F_0}{H + G_0}\right) \tag{7.9}$$

$\overline{LWC}$ can either be assumed, determined according to Eq. 7.6, or, determined as $LWC\left(\overline{\theta}\right)$; the liquid water content of the well-mixed fog layer. With this, the transition depth can be estimated *a priori* knowing only the surface fluxes and approximate shape of the temperature profile. The time to transition is then simply the time it will take for the transition depth to be achieved

$$t_{trans} = \frac{1}{\lambda}\left[f\left(I_{z,trans}\right) + \left(T_{s,0} - T_D\right)\right] \tag{7.10}$$

where $T_{s,0}$ is the initial surface temperature. Note, this will be earlier than the actual observed transition (in the absence of external forcing, such as through advection), as the rate of surface-cooling will decrease in time due to the reduced longwave deficit as the fog layer deepens. The transition depth and time to transition can also be updated iteratively as $\overline{LWC}$ evolves in time.

Post-Transition: Well-Mixed Fog

Following the transition, the temperature is well-mixed within the fog layer, such that $\theta(z) = \overline{\theta}$ throughout. As such, we can now think of the post-transition fog layer in terms of a box model, with any surplus or deficit in the energy budget of the entire fog layer resulting in a change in fog depth. The integrated longwave radiative cooling (in units of K s^{-1}) is

$$\mathscr{F} = \frac{F_0 - F_s}{\rho c_p I_z} \tag{7.11}$$

As the depth increases, the radiative imbalance is the same, but the volume over which is acts is increased. Therefore, the cooling over the entire fog layer decreases with time.

Radiation alone is likely insufficient to model the well-mixed fog layer. Another process that may be important to consider is that of latent heat release due to the condensation of water vapour. Under our assumption of instant mixing, any deepening of the fog layer means that the previously above-fog air will have to cool toward $\overline{\theta}$, leading to significant latent heat release. As a result, the radiative cooling is offset by latent heat release, which, because we assume a constant q, is

$$\begin{aligned}\mathscr{L} &= \frac{L_v}{\rho c_p I_z}\frac{\partial W}{\partial t} \\ &= \frac{L_v}{\rho c_p I_z}\frac{\partial}{\partial t}\left(\overline{LWC}\cdot I_z\right) \\ &= \frac{L_v}{\rho c_p I_z}\left(I_z\frac{\partial \overline{LWC}}{\partial t} + \overline{LWC}\frac{\partial I_z}{\partial t}\right)\end{aligned} \tag{7.12}$$

where L_v is the latent heat of evaporation/condensation (2.26×10^6 J kg^{-1}).We now have a equation to describe the evolution of the well-mixed fog layer, such that

$$\begin{aligned}\frac{\partial I_z}{\partial t} &= \frac{F_0 - F_s}{\rho c_p I_z} - \frac{L_v}{\rho c_p I_z}\frac{\partial}{\partial t}\left(\overline{LWC} I_z\right) \\ &= \left(\frac{F_0 - F_s}{\rho c_p I_z \frac{\partial\theta}{\partial z}} - \frac{L_v}{\rho c_p}\frac{\partial \overline{LWC}}{\partial t}\right)\left[1 + \frac{L_v}{\rho c_p I_z \frac{\partial\theta}{\partial z}}\overline{LWC}\right]^{-1}\end{aligned} \tag{7.13}$$

If latent heat is not important, then we can ignore the additional terms.

7.3.2 A Log-Linear SBL

We now present the above equations assuming a logarithmic temperature profile with $f(z) = m\ln(z/z_0)$. z_0 is the roughness length, and m a slope parameter. As the height increases, we also make use of the fact that the logarithmic profile can be assumed near-linear, such that above the transition depth, $g(z) = a(z - I_z) + \theta_D$. With these assumptions, the above equations simplify considerably.

Before the transition, the growth of the fog layer deepens according to Eq. 7.4

$$\frac{\partial I_z}{\partial t} = \lambda\frac{I_z}{m} \tag{7.14}$$

where I_z can also be analytically determined

$$I_z = z_0\exp\left(\frac{\theta_D - \theta_S}{m}\right). \tag{7.15}$$

Throughout the fog layer, the mean potential temperature (i.e., the value that

will be assumed in a well-mixed layer) is,

$$\overline{\theta} = \theta_D - m\left(1 - \frac{z_0}{I_z}\right), \tag{7.16}$$

which approaches a constant value of $\theta_D - m$ for large I_z. Before the transition, $\overline{LWC}$ increases with time. After the transition, however, *LWC* is a function of the constant $\overline{\theta}$ at large I_z (Eq. 7.16), and not time. Therefore, we use the constant value of $\overline{\theta}$ in order to determine $\overline{LWC}$ needed to estimate the transition depth. Note, this is distinct from the value computed with Eq. 7.6, which will be larger.

Following the transition, the fog layer deepens at the rate determined by the radiative cooling and latent heating of the fog layer, with a constant $\overline{LWC}$ throughout (Eq. 7.13)

$$\frac{\partial I_z}{\partial t} = \frac{F_0 - F_s}{\rho c_p a I_z}\left[1 + \frac{L_v}{\rho c_p a I_z}\overline{LWC}\right]^{-1} \tag{7.17}$$

such that we can solve for I_z, with

$$I_z = \sqrt{\left(I_{z,trans} + \frac{L_v\overline{LWC}}{\rho c_p a}\right)^2 + 2\frac{F_0 - F_s}{\rho c_p a}(t - t_{trans})} - \frac{L_v\overline{LWC}}{\rho c_p a} \tag{7.18}$$

with the negative square root rejected for being un-physical. Important to note in this description is that fog growth slows with time. As above, simply removing the LWC terms gives the solution without latent heat effects.

With our log-linear description, we can therefore predict the evolution of the fog layer in time, including its depth and the point at which it will transition to a well-mixed fog layer, from *a priori* analysis and estimates/observations of surface-based initial conditions. Non-dimensionalized illustrations of the evolution of such a fog layer are presented in Fig. 7.4. Note in Fig. 7.4a) that the post-transition evolution is shown with and without the latent-heat correction.

Doubling Time

In addition to the time to transition, another important timescale would be the doubling time of the fog layer. The time (Δt_χ) to a χ-times increase in depth from the current depth is

$$\Delta t_\chi^{\text{thin}} = \frac{m}{\lambda}\ln(\chi) \tag{7.19}$$

for our logarithmic, shallow fog layer, and

$$\Delta t_\chi^{\text{thick}} = \frac{\rho c_p a I_z}{2(F_0 - F_s)}\left[\left(\chi^2 - 1\right)I_z + 2(\chi - 1)\right] \tag{7.20}$$

for a well-mixed layer. Notice that the optically thin fog will multiply at a constant rate, while the well-mixed fog will take longer to multiply with increasing depth (due to the nature of the exponential and square-root forms of the equations).

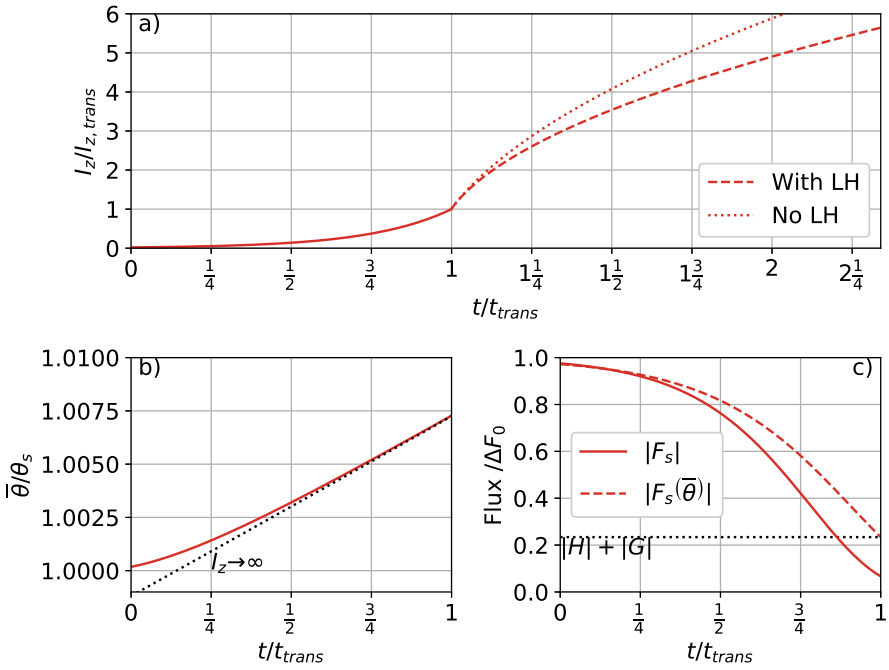

Figure 7.4: *A priori* evolution of a log-linear fog layer. a) I_z (Eq. 7.14) divided by the transition depth (Eq. 7.9). Two two dashed lines illustrate the evolution with and without taking latent heating into account. b) $\overline{\theta}$ divided by θ_s as determined from Eq 7.16 for all I_z, and for large I_z. c) Surface net radiation relative to the clear-sky value. F_s is calculated using both the modelled evolution of $\overline{LWC}$, and by assuming a constant value of $\overline{\theta}$

7.4 Validation of the Analytical Formulae

Here, we compare the estimates of fog evolution from the analytical model with the observed evolution of a radiation fog event. We compare our analytical solutions to the event observed on 7 April 2016 presented in Fig. 7.2. The observed event was selected for adhering most closely to the assumptions outlined in Sect. 7.3.

We begin by making analytical fits through the observed mean temperature profile in the hour preceding fog onset (Fig. 7.5). We fit both a logarithmic profile, as well as a linear fit above 40 m. $\overline{\theta}_D$ is similarly estimated as the mean value of the observations in the pre-fog hour (278.5 K), as is the rate of cooling, $\lambda = 0.96\ \mathrm{K\,h^{-1}}$.

The evolution of the pre- and pos-transition temperature profile is shown in Fig. 7.2. Figure 7.7a) shows the comparison between the observed and *a priori* estmiates of fog depth over seven hours. The initial growth of the fog layer is very well represented by Eq. 7.14. The transition is reached roughly 15 minutes earlier than observed, however, the close timing is quite remarkable given the simplicity of the model. The difference likely arises because the rate of cooling is assumed constant, while in reality it will decrease as the transition approaches due to the weakening

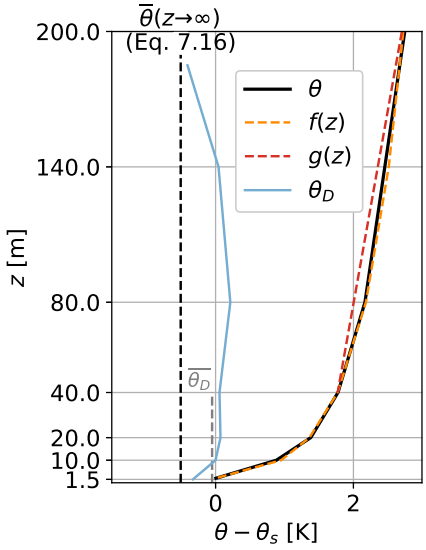

Figure 7.5: Mean temperature and dew point temperature profiles in the hour prior to fog onset, with the logarithmic ($f(z)$) and linear ($g(x)$ above 40 m) fits shown, along with the value of $\overline{\theta}$ estimated from Eq. 7.16.

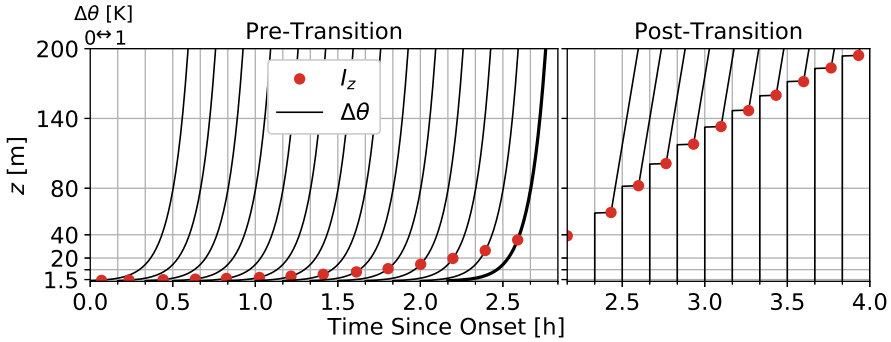

Figure 7.6: Evolution of temperature as modelled with the conceptual model. cf, Fig. 7.2a.

radiative imbalance at the surface. Post-transition, the latent-heat curve accurately predicts the growth to 140 m, though predicting 200-m depth too soon (by roughly 1 h). This may be related to the decrease in fog depth seen around 4.5 h into the event, perhaps indicative of external forcing, or a significant deviation from the assumptions, such as that the specific humidity remain constant. Overall, the qualitative behaviour of the fog evolution is well represented. For example, we see the accelerating growth within the stable boundary layer, followed by the decelerating growth after the transition.

The evolution of the longwave radiation at the surface is shown in Fig. 7.7b). In addition to the observed longwave defecit, we also show Eq. 7.3 calculated using the observed liquid water content. While not identical, it is close enough to the observed radiation that we can have confidence in the parametrization. The analytical surface radiation is then calculated using the mean liquid water content given the modelled

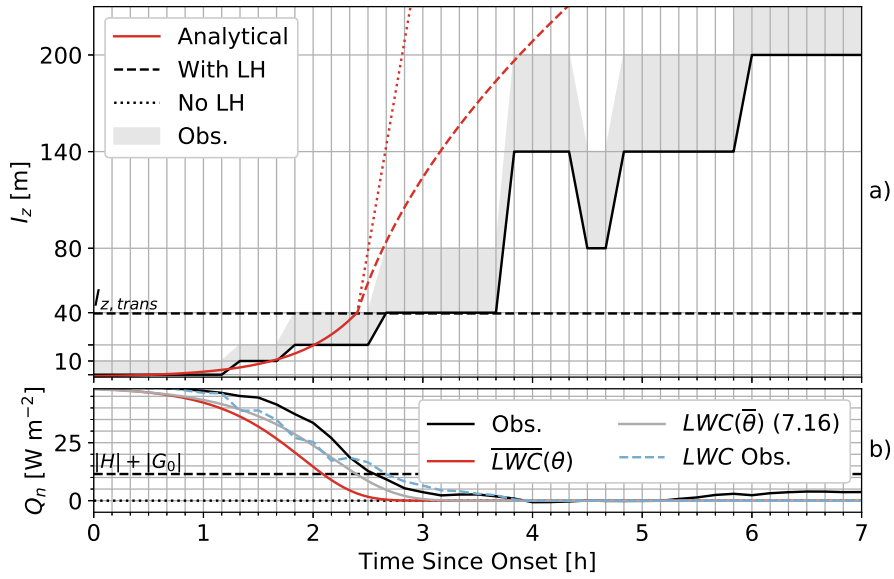

Figure 7.7: Comparison between analytical estimates and observed fog properties on 7 April 2016. a) Fog depth. After the transition, the depth is estimated with and without the consideration of latent heat fluxes at fog top. b) Net longwave radiation at the surface as observed, and determined with Eq. 7.3. The grey line determines F_s through assuming a constant $\overline{\theta}$ (Eq. 7.16) within the fog, while the red line calculates $\overline{LWC}$ using the modelled temperature profile. For comparison, the blue dashed line shows the estimated F_s with the observed LWC profile.

temperature profile, and the liquid water content assuming a well-mixed temperature profile (Eq. 7.16) as would occur in a deep fog layer. Both underestimate the imbalance. This is related to the overestimation of fog depth due to the assumption of constant cooling.

7.5 Summary and Discussion

In this chapter, we present an overview of ongoing work to describe the evolution of a fog layer within a conceptual framework. Observations at the CESAR facility in the Netherlands show that radiation fog makes up roughly two thirds of all fog events at the site, of which 15% of the radiative events transition to deep, well-mixed fog. This is a much lower fraction than observed by Price (2011) at a site in England, although there are far more radiation fog events considered here. The majority of transitions occur when there is a change in the surface energy balance that results in convection through surface heating; either the sun rises, or the fog becomes so optically thick that the longwave cooling ceases at the surface. It is the latter in which we are most interested.

By assuming quasi-steady evolution of the stable boundary layer, we are able

to express fog growth as a function of the rate of cooling and vertical temperature profile. In doing so, we are able to present simple formulae that describe the depth of fog in time (as well as the growth rate, as per Izett and van de Wiel 2020), and identify the point at which the fog will undergo transition to a well-mixed fog layer. By assuming different temperature profiles, analytical solutions to these formulae are possible, allowing *a priori* estimates of fog evolution. In general, the transition point is estimated sooner than the observed transition. This is primarily due to the fact that our framework does not account for a slowing of cooling as the fog layer deepens and the longwave deficit is reduced.

As a simplification, we assume that moisture is constant in time and space. While this is not the case in the majority of situations, changes in temperature generally play a larger role in the in situ development of fog through modification of the saturation humidity. Of course, advective processes, such as transport of moisture, can be significant, but that is not considered here.

Note: the transition at the point of surface energy balance is significant. While it is likely not the "true" switch for the transition, it provides a reasonable estimate. More likely, the cooling at fog top will need to exceed that of the surface, such that an elevated inversion is formed in the profile. This is, however, difficult to diagnose without more detailed observations. The surface energy balance has the added benefit of also being easily observable and/or diagnosed.

We assess in-situ, locally driven fog evolution. Conversely, the LANFEX campaign identified small-scale topographic features (such as hills) as contributing to the growth of fog (Price et al. 2018). They observed rapid deepening due to the formation of fog on top of hills, which was subsequently advected over top of underlying fog in valleys (for an overview, including fantastic video footage, see Price and Stokkereit 2020). The CESAR facility, however, is famed for its relatively uniform topography, the greatest feature of which is a levee just south of the site. Unlike the hills in Bedfordshire and Shropshire, the levee is only a very small feature, and while it may contribute to additional turbulent mixing to the CESAR facility, it is not sufficiently large for fog to form and blow on top of existing fog as seen in LANFEX.

One effect not considered here is the role of aerosols, which Boutle et al. (2018b) note to be significant. In effect, the mass absorptivity parameter, a_0 represents the effective absorption of the fog layer, which we assume to be uniform. In reality, this will vary according to the type and amount of aerosols present, as well as their vertical distribution. One sees that the value of a_0 is important in determining the transition depth, with the greater the absorptivity (larger impact on the radiation), the lower the transition depth (radiation is extinguished more rapidly).

We also do not explicitly consider the role of the gradients above and below the well-mixed fog layer, including their role in turbulent transport. As noted in Izett and van de Wiel (2020), the well-mixed layer has a vertical temperature gradient near zero, while above the fog layer there exists a finite slope. The two will counteract each other, which may contribute to slowing down seen after the transition. In fact, it may be that this effect, and not only that of latent heating, is also responsible for the less rapid growth seen in observations. More work is required to investigate this.

7.5.1 Why is the Transition so Rapid?

In Sect. 7.2, we note that the transition to deep fog can occur quite rapidly (within a few tens of minutes). There will exist, therefore, some positive feedback. Here we briefly discuss the role that radiation and turbulence play.

As outlined above, radiation fog first forms in the highly stratified, low-turbulence regime. The location of maximum radiative cooling subsequently moves from the surface toward fog top as the fog layer deepens and approaches optically thick conditions. At this point, the fog top cools relative to the surface, reducing the temperature stratification, and allowing for greater mechanical mixing. This, then, results in increased turbulent heat flux, which in turn leads to reduced stratification, etc. If sufficient degradation of the stratification occurs, then the regime change occurs. This is related to the concept of the "maximum sustainable heat flux" (MSHF) of van de Wiel et al. (2012b), with the stratification reduced through the radiation-turbulence feedback until sustained turbulent mixing is possible.

7.6 Conclusions and Next Steps

In this chapter, the development of radiation fog development is outlined using conceptual analysis. Analytical formulae are presented that describe the growth rate of fog as a function of cooling and vertical profiles, to predict the transition point of the fog layer from stable to well-mixed fog, and to identify the time until the transition. These can be used diagnostically to estimate the evolution through *a priori* observations alone. Through the conceptual analysis, we also understand the role of, e.g., turbulent heat flux in the transition, with the buoyancy constraints of the initial stable profile rapidly overcome by the equalization of the temperature profile.

Moving forward, several next steps present themselves. First, the transition is treated as an instantaneous, and completely homogenizing, event. It is likely, however, that a mixing timescale is needed in order to accurately describe the change from stable to well-mixed profiles. Further, how actual mixing takes place at the interface will influence the evolution significantly. As the research continues, it will also be necessary to parametrize turbulent mixing in a conceptual model (such as in Derbyshire 2019), that also includes the effects of longwave radiation. The entire lifecycle can then be modelled, including the effects of turbulent mixing and slowing of the radiative growth, which are not explicitly included here. Finally, only one event is presented here as a point of comparison. How accurate the analytical formulae are for other events, whether they transition or not, must also be confirmed.

Chapter 8

Concluding Remarks

> "Men who venture into the mist lose their souls", a woman whispered. Her words raised a question. . . . What, then, had happened to his soul?
>
> B. Sanderson, *The Final Empire*

In this chapter, the extent to which the research objectives as presented in Chapter 1 have been reached are discussed in the context of the previous chapters. Recommendations on how this work can be extended are also discussed.

8.1 Conclusions

The main goal of this thesis was, broadly, to improve understanding of the conditions under which fog forms and deepens. To address this, several methods were applied, including statistical (Chapters 2 and 4), observational (Chapters 2–4), analytical (Chapters 5–7), and, to an extent, numerical (Chapter 6). The range of methods was necessary to investigate different aspects of fog formation, in order to best understand its nature.

In Chapter 2, a simple observational/statistical prediction method was utilised to investigate when fog forms, and the likelihood of fog formation given seemingly favourable conditions. It was shown that any combination of variables that measure saturation, turbulent mixing, and radiative cooling can be used to predict the onset of fog. However, while the methodology could accurately identify over 95% of fog events, an unacceptably high "false alarm rate" indicates that while conditions such as high humidity and low wind speeds are necessary for the formation of radiation fog, they are far from sufficient. In many cases, the prediction failed due to the transient nature of the atmosphere. While conditions may be favourable for fog formation at a given time of observation, they are prone to change in the coming hours. Further, the methodology relies on observations made at a given time and place. As Chapters 3 and 4 show, the spatio-temporal variability of fog can be large.

Chapter 3 followed directly from the research presented in Chapter 2, where it

was identified that many shallow fog layers could be missed by conventional sensors that are typically placed at least one metre above the surface, resulting in false false alarms. As an initial study of such (very) shallow layers, a field experiment was conducted, making use of distributed temperature sensing (providing high-resolution observations in both time and space) and a continuous visibility measurement through analysis of timelapse camera images of the developing fog layer. As expected, the conventional point observations were shown to miss the development of shallow fog; by up to 2 hours in some cases. This reinforces the need for increased resolution near the surface; not only observationally, but numerically as well.

Increased horizontal resolution is also beneficial. In Chapter 4, observations from the land-based Dutch weather station network were analyzed to identify long-term trends (over the past 45 years) and spatial patterns in fog occurrence throughout the Netherlands. Previous research had shown that fog occurrence in the Netherlands is decreasing due to a reduction in the amount of aerosols in the Dutch atmosphere (Boers et al. 2015). However, the decrease in fog occurrence is not monotonic, but rather shows inter-annual peaks and troughs that are of much larger magnitude than the long-term trend. This inter-annual variability is shown here to be linked to changes in the wintertime pressure-gradient forcing over the Netherlands, with weaker pressure gradients leading to more frequent stable boundary layer conditions that are favourable for fog. Further, analysis of the weather station network showed that the overall trend varies significantly throughout the country, with larger, expanding cities seeing a more rapid decline in fog occurrence than more rural locations. A reversed pattern was noted when assessing the overall annual occurrence of fog, with more rural locations—particularly those inland—observing up to twice as much fog as urban and coastal stations. This was attributed to the thermal influences of urban centres and the North sea, resulting in the distillation of a simple "regional weighting index" to describe mesoscale fog variability.

With a clearer understanding of observed fog, the focus turned toward more analytical/conceptual understanding. Where previous work has looked at performing sensitivity studies with numerical models, in Chapter 5, the mathematical equations describing airmass saturation were investigated in order to determine the sensitivity of saturation to underlying thermomdynaic properties. Through uncertainty/error propagation, it was shown that relative humidity is most sensitive to temperature. Unlike specific humidity which has a direct contribution to any error in *RH*, errors in temperature result in errors in *RH* that are roughly 20 times larger. However, errors in specific humidity are generally larger that those of temperature (roughly 10–20 times), meaning they can have equal significance in the determination of saturation. It is imperative that temperature and specific humidity be therefore accurately determined. The analysis provides a means of identifying where such observational and numerical improvements can (most efficiently) be achieved, through assessing the relative errors of different properties and their impact on the resulting saturation estimate.

Chapter 6 built upon the observational work of Chapter 3, seeking to understand and describe the growth of a fog layer. An analytical expression was derived to esti-

mate the rate of growth (or erosion) based on the moisture tendencies and profiles at fog-top. The expression was shown to be able to accurately estimate the interfacial depth when compared against: the high-resolution observations described in Chapter 3, the coarser tower observations at the CESAR facility, and numerical output from LES. With such an analytical expression, the depth of a fog layer can now be estimated, even when it is a "sub-grid" feature of either a model or observation network. Perhaps more significantly, the analytical perspective also enables greater understanding of the conditions under which fog forms and grows.

Finally, the analytical description for fog growth is expanded to a conceptual model of an evolving fog layer in Chapter 7. Through assuming simple evolution of a quasi-steady stable boundary layer, the growth and evolution of a shallow fog layer into a deep, well-mixed fog layer can be expressed. This allows for *a priori* estimates of fog evolution to be made with only simple diagnostic (observational) inputs. This research remains a work in progress.

8.2 Directions for Further Research

While progress has been made in this thesis toward improving understanding of fog formation and evolution, there are many challenges that remain to be addressed. The following presents a discussion of a range of topics and how, in the context of this thesis, they might be approached.

Observational Challenges

Current observational techniques are unable to properly capture the initial formation stages of fog, particularly very shallow fog (Chapter 3). The spatial patterns shown in Chapter 4 indicate the need for continuous—or at least network—observations to be made across wider regions. **Spatially continuous visibility measurements, such as from images produced by (either bespoke or existing) camera networks, are paramount for ensuring accurate detection of fog layers**. This is particularly important from a monitoring and warning perspective where human safety is concerned; the earlier a detection can be made, the safer it will be. **Future efforts should also be directed toward continued leverage of emerging techniques**, such as DTS and infra-red imagery, which have been shown here (Ch. 3) and elsewhere (e.g., Price and Stokkereit 2020) to provide reliable, high-resolution observations. The development of satellite methods for the detection of fog (such as in Egli 2018) must also continue to be improved with the relatively low vertical resolution of such observations and the difficulty in distinguishing fog from upper-level clouds a current limitation in their widespread use.

At the small scale, dew (and droplet settling) are notable sinks of liquid water from fog. However, **it is unclear how the processes of fog and dew formation interact**. For example, under which conditions does dew form, without the onset of fog? Or, perhaps there is always fog, just a very shallow layer such as those seen in this thesis? Does the formation of dew in the initial stages of fog lead to a delay

in the onset of a fog layer? What is the rate of dew formation during different fog events? Many of these questions can be inferred from analytical and conceptual thinking, as well as from assessing imbalances in the surface energy budget (e.g., de Roode et al. 2010). However, **it would be beneficial to install simple lysimeters at more observation sites** (such as used by Jacobs et al. 2006; Price et al. 2018; Riedl et al. 2019), including Cabauw, in order to quantify dew deposition. Combined with additional information from, e.g., DTS, a more complete picture of the fog lifecycle can be realized. The installation of such a lysimeter could conceivably form part of a future PhD project, or even an MSc graduation project (including the design, installation, and validation of the device).

As with the camera-LED setup in Chapter 3, **other less conventional means of acquiring data should also be investigated**. For example, vehicle speed data, as is often collected and communicated via GPS systems, combined with knowledge of meteorological conditions, could be linked with adverse visibility and weather (i.e., slower traffic than usual, when not due to an accident, would indicate drivers are slowing for another reason). Or, perhaps a sensor could be developed to measure the headlight reflection and scattering in foggy conditions? Another option still: the attenuation of (high-frequency) sound, or cellular signals—as already done with heavy rainfall—could perhaps be used to identify foggy regions. With a an ever-increasing connectivity of devices and sensors, the possibilities are seemingly limitless. The biggest challenge then would be to make use of all of the data available, likely requiring artificial intelligence and machine learning approaches.

Numerical Challenges

In all numerical models, fog is an entirely parametrized/diagnosed feature, determined through relationships to other variables. These variables, such as temperature, are also often dependent on sub-grid parametrizations, including mixing schemes, with moist processes determined by microphysical schemes. While success has been achieved in improving fog simulation through increased vertical resolution, this comes with the need for higher computer resources. One aid in this is the development of adaptive grids (e.g., van Hooft et al. 2018), which allow for computer resources to be directed only where they are needed. **The use of adaptive grids may prove invaluable in future high-resolution simulations of fog**. However, grid resolution alone is insufficient. **In addition to continued improvement of (observed) input variables, fog-related parametrizations must continue to be improved**. One such parametrization would be to describe the growth rate of fog on sub-grid scales. To this end, the analytical description of fog growth presented in Chapter 6 could prove useful. This would allow for more detailed descriptions of the simulated fog layer, and even help in the issuing of warnings and forecasts of fog hazards.

To improve understanding of fog events, recent sensitivity studies (e.g., Maronga and Bosveld 2017; Wærsted et al. 2019) have sought to identify the role of different processes in determining the characteristics of a fog layer. Often, the approach in such a study is to perturb a parameter (e.g., soil heat flux, pressure-gradient forcing)

within the simulation environment, and see how the resulting simulation compares to a reference case. However, such perturbations are made at the beginning of a simulation, and the end result is then compared. While this is important for understanding the overall lifecycle effects, it does not help to elucidate the relative significance of different processes at different stages. For example, Maronga and Bosveld (2017) showed that the soil heat flux is important in determining the timing of fog onset. However, one can imagine that a established, deep fog layer will be less influenced by surface properties, and perhaps be more significantly influenced by the radiation or microphysical schemes. As such, **it would be extremely interesting to perform a series of simulations with perturbations at different stages of the fog lifecycle**. Beginning from a reference simulation, parameters could be modified at the start, middle, and end of the simulation (restarting the simulation as appropriate). With that, one could identify whether or not processes contribute equally at all stages.

Fog is also a very sensitive phenomenon. There are fundamentally only two distinct states for the system, "clear", and "foggy"; however, while certain conditions can be taken to represent one state versus the other with a high degree of certainty (e.g., $RH << 100\%$ is almost guaranteed to be fog-free), there is a "grey zone" where a given set of conditions could perhaps be equally likely to be foggy, or clear. With this, **can a (pseudo) stochastic/probabilistic model be developed to describe/predict fog transitions?** Similar, perhaps, to the Markov Chains used by Monahan et al. (2015) and Abraham et al. (2019), it may be possible to define the probability of being in one state or the other given current conditions, as well as the probability of transition to another state at a given time in the future. (This would also build on Chapter 2). One could imagine that it begins with a simple observational analysis of the definitely clear and foggy states, identifying the extent of the "grey zone" that exists between the two.

Stable Boundary Layer Issues

Chapter 5 in particular highlights the need for accurate representation of the stable boundary layer within numerical simulations. However, it is also shown in Chapter 3 that the small spatial scales and steep gradients of the stable boundary layer can only be accurately observed with high-resolution techniques such as DTS. **Further developments must therefore be made in the understanding, observation, and simulation of the *dry* stable boundary layer in order for the improved understanding, observation, and simulation of the *moist* SBL.**

Related to the observational and numerical challenges discussed above, an important question to be answered is: **at what scale does surface heterogeneity matter to the vertical properties of the SBL?** Chapters 3 and 4 both demonstrate the challenge that surface heterogeneity presents; however, it is manifest on different scales. Yet, the degree to which these scales—micro to mesoscale—are relevant for fog (and other boundary layer processes) is unclear. One can imagine, however, that it depends on the ratio of the horizontal scale to the vertical position of observation (e.g., an observation at 1-m height will likely depend more on the surface properties

directly below the sensor than at, say, 100-m height, which may be better described by the mean footprint over a wider area). To determine the scales of relevance for fog (and indeed, atmospheric boundary layer research in general), would require a combination of careful experimentation using the high-resolution techniques mentioned above, as well as idealized simulations. Only through highly idealized simulations can the factors be sufficiently controlled to be able to determine approximate scaling.

Consistency

One of the greatest obstacles facing fog research is one that has not been discussed widely throughout this thesis, but has rather been noted throughout the course of research. Fog research is, in general, too fractured and focused—as is also the case in this thesis—on just one fog "type". In reality, however, nature knows no such distinction, with all fog the result of condensation near the surface, and often several different processes responsible for creating the conditions under which the fog forms. **A unified description of fog formation and analysis should therefore be the goal**, rather than identifying conditions and caveats for different (artificially defined) types. A simple process-based framework may be suitable. One could imagine analyzing the T–q phase space to determine the influence of different processes. For example, radiative cooling would manifest only along the T-axis, while evaporation/condensation would only manifest along the q-axis. Processes, such as the mixing or advection of airmasses, would appear in both dimensions.

8.3 The Last Word

Fog is—and will remain—a challenge to understand and predict, even for modern computational and forecasting systems. Until we can understand the precise conditions required for its formation, there will remain an element of uncertainty in its appearance. With emerging technologies, such as high-resolution observational methods, or new computational techniques, there is great potential for advancement. Such progress will also by necessity come in tandem with continued development in other areas, such as stable boundary layer research.

While less pressing, perhaps, than other scientific—and certainly socio-political—challenges of this new decade, the study of fog is even more important now than ever before.

Figure 8.1: Caspar David Friedrich's "Wanderer über dem Nebelmeer" (Wanderer Above the Sea of Fog). Held by the Hamburger Kunsthalle.
(https://online-sammlung.hamburger-kunsthalle.de/de/objekt/HK-5161)

As highlighted throughout this thesis, fog is a hazard to human activity, and as human activity continues to increase—more cars on the road, more planes in the sky—the hazard will grow in tandem. It is therefore essential that efforts continue to be directed toward improving our understanding and ability to forecast fog events.

On reaching the end of this thesis, I feel rather like Friedrich's wanderer (Figure 8.1). Over the past four years, I too have climbed through the sea of fog, and gained a new perspective—if only briefly—of its beauty and complexity.

Appendix

Some More Photographs of Fog

Throughout the past four years, often to the chagrin of my wife, I have taken several photographs of fog (including those presented earlier, such as Figure 1.1). Several friends and colleagues have also contributed to my collection. Rather than consign these photos solely to a folder on my computer, I have included some of my favourites here (with permission of the photographer as appropriate).

Figure A.1: Me taking a photo of fog. (Liverpool, England; taken by Maaike van Kooten)

Figure A.2: The photo I was taking in A.1. A relatively shallow fog layer sat above the river Mersey, though still deep enough that all but the very top of the ship was obscured; can you spot it? (Liverpool, England)

Figure A.3: This thesis largely focuses on radiation fog, but here we see a beautiful image of steam fog on a lovely stable-boundary layer night. (Kejimkujik National Park, Canada; taken by Christoph Renkl)

Figure A.4: Morning radiation fog. (Near Utrecht, The Netherlands; taken by Steven van der Linden)

Figure A.5: Very shallow morning fog. Note the stationary wind turbines in the background, indicative of stable conditions. (Leiden, The Netherlands)

Bibliography

Abraham C, Holdsworth AM, Monahan AH (2019) A prototype stochastic parameterization of regime behaviour in the stably stratified atmospheric boundary layer. Nonlin Processes Geophys 26(4):401–427, doi:10.5194/npg-26-401-2019

Alpert JC, Feit DM (1990) An operational marine fog prediction model. NOAA Office Note 371

Andrews E (2019) The Sinking of Andrea Doria. https://www.history.com/news/the-sinking-of-andrea-doria

Appleman HS, Coons FG Jr (1970) The use of jet aircraft engines to dissipate warm fog. J Appl Meteorol 9:464–467, doi:Fog, Airport

Arrillaga JA, Villà-Guerau de Arellano J, Bosveld FC, Klein Baltink H, Yagüe C, Sastre M, Román-Cascón C (2018) Impacts of afternoon and evening sea-breeze fronts on local turbulence and CO_2 and ^{222}Rn transport. Q J R Meteorol Soc doi:10.1002/qj.3252

Babari R, Hautiere N, Dumont E, Paparoditis N, Misener J (2012) Visibility monitoring using conventional roadside cameras - emerging applications. Transportation Research Part C 22:17–28, doi:10.1016/j.trc.2011.11.012

Bartok J, Bott A, Gera M (2012) Fog prediction for road traffic safety in a coastal desert region. Boundary-Layer Meteorol 145:485–506, doi:10.1007/s10546-012-9750-5

Bäumer D, Versick S, Vogel B (2008) Determination of the visibility using a digital panorama camera. Atmospheric Environment 42:2593–2602

Bendix J (1994) Fog climatology of the Po valley. Riv Meteor Aeronaut 54(3-4):25–36

Bendix J (2002) A satellite-based climatology of fog and low-level stratus in Germany and adjacent areas. Atmos Res 64:3–18

Bense VF, Read T, Verhoef A (2016) Using distributed temperature sensing to monitor field scale dynamics of ground surface temperature and related substrate heat flux. Agricultural and Forest Meteorology 220:207–215, doi:http://dx.doi.org/10.1016/j.agrformet.2016.01.138

Bergot T, Escobar J, Masson V (2015) Effect of small-scale surface heterogeneities and buildings on radiation fog: Large-eddy simulation study at Paris–Charles de Gaulle airport. Q J R Meteorol Soc 141:285–298, doi:10.1002/qj.2358

Bevington PR, Robinson DK (2003) Data Reduction and Error Analysis for the Physical Sciences, 3rd edn. McGraw-Hill, Boston

Boers R, Klein Baltink H, Hemmink HJ, Bosveld FC, Moerman M (2013) Ground-based observations and modeling of the visibility and radar reflectivity in a radiation fog layer. J Atmos Ocean Technol 30:288–300, doi:10.1175/JTECH-D-12-00081.1

Boers R, van Weele M, Meijgaard E, Savenije M, Siebesma AP, Bosveld F, Stammes P (2015) Observations and projections of visibility and aerosol optical thickness (1956-2100) in the Netherlands: Impacts of time-varying aerosol composition and hygroscopicity. Environ Res Lett 10, doi:10.1088/1748-9326/10/1/015003

Boneh T, Weymouth GT, Newham P, Potts R, Bally J, Nicholson AE, Korb KB (2015) Fog forecasting for Melbourne Airport using a Bayesian decision network. Weather Forecast 30:1218–1233, doi:10.1175/WAF-D-15-0005.1

Bosveld FC (2019) Cabauw In-situ Observational Program 2000 – Now: Instruments, Calibrations and Set-up. http://projects.knmi.nl/cabauw/insitu/observations/documentation

Bosveld FC, Baas P, Steeneveld GJ, Holtslag AAM, Angevine WM, Bazile E, de Bruijn EIF, Deacu D, Edwards JM, Ek M, Larson VE, Pleim JE, Raschendorfer M, Svensson G (2014a) The Third GABLS Intercompari-

son Case for Evaluation Studies of Boundary-Layer Models. Part B: Results and Process Understanding. Boundary-Layer Meteorol 152(2):157–187, doi:10.1007/s10546-014-9919-1

Bosveld FC, Baas P, van Meijgaard E, de Bruijn EIF, Steeneveld GJ, Holtslag AAM (2014b) The Third GABLS Intercomparison Case for Evaluation Studies of Boundary-Layer Models. Part A: Case Selection and Set-Up. Boundary-Layer Meteorol 152(2):133–156, doi:10.1007/s10546-014-9917-3

Boutle I, Hill A, Romakkaniemi S, Bergot T, Lac C, Maronga B, Steeneveld GJ (2018a) Demisity: An LES & NWP fog modelling intercomparison. GASS White Paper

Boutle I, Price J, Kudzotsa I, Kokkola H, Romakkaniemi S (2018b) Aerosol–fog interaction and the transition to well-mixed radiation fog. Atmos Chem Phys 18(11):7827–7840, doi:10.5194/acp-18-7827-2018

Bretherton CS, Macvean MK, Bechtold P, Chlond A, Cotton WR, Cuxart J, Cuijpers H, Mhairoutdinov M, Kosovic B, Lewellen D, Moeng CH, Siebesma P, Stevens B, Stevens DE, Sykes I, Wyant MC (1999) An intercomparison of radiatively driven entrainment and turbulence in a smoke cloud, as simulated by different numerical models. QJ Royal Met Soc 125(554):391–423, doi:10.1002/qj.49712555402

CBS (2019) Aanbod en verbruik van elektriciteit, 1995-2017. https://www.clo.nl/indicatoren/nl0020-aanbod-en-verbruik-van-elektriciteit?ond=20881

Cereceda P, Osses P, Larrain H, Farías M, Lagos M, Pinto R, Schemenauer RS (2002) Advective, orographic and radiation fog in the Tarapacá region, Chile. Atmos Res 64:261–271

Chaabani H, Kamoun F, Bargaoui H, Outay F, Yasar AUH (2017) A Neural network approach to visibility range estimation under foggy weather conditions. Procedia Computer Science 113:466–471, doi:10.1016/j.procs.2017.08.304

CLO (2017) Externe veiligheid rond Schiphol , 2000-2014. https://www.clo.nl/indicatoren/nl0305-externe-veiligheid-rondom-schiphol

Cook AJ, Tanner G (2015) The Cost of Passenger Delay to Airlines in Europe - Consulation Document. Tech rep

de Roode SR, Bosveld FC, Kroon PS (2010) Dew Formation, Eddy-Correlation Latent Heat Fluxes, and the Surface Energy Imbalance at Cabauw During Stable Conditions. Boundary-Layer Meteorol 135(3):369–383, doi:10.1007/s10546-010-9476-1

Derbyshire SH (2019) Stable boundary-layer relative humidity profiles and the conditions for onset of radiation fog over land. QJR Meteorol Soc 145(722):2292–2307, doi:10.1002/qj.3558

Domeisen DIV, Badin G, Koszalka IM (2018) How predictable are the arctic and north atlantic oscillations? Exploring the variability and predictability of the northern hemisphere. Journal of Climate 31:997–1014, doi:10.1175/JCLI-D-17-0226.1

Droste AM, Steeneveld GJ, Holtslag AAM (2018) Introducing the urban wind island effect. Environ Res Lett 13, doi:10.1088/1748-9326/aad8ef

Dupuy L (2019) Dode en negentien gewonden bij kettingbotsing A32 door mist. NRC

Duynkerke PG (1991) Radiation fog: A comparison of model simulation with detailed observations. Mon Weather Rev 119:324–341

Duynkerke PG (1999) Turbulence, radiation, and fog in dutch stable boundary layers. Boundary-Layer Meteorol 90:447–477

Dyer AJ (1974) A review of flux-profile relationships. Boundary-Layer Meteorol 7(3):363–372, doi:10.1007/BF00240838

ECMWF (2018) L137 model level definitions. https://www.ecmwf.int/en/forecasts/documentation-and-support/137-model-levels

Egli S (2018) Fog frequencies in Europe (monthly means). Dataset doi:10.5678/LCRS/DAT.311

Egli S, Thies B, Drönner J, Cermak J, Bendix J (2017) A 10 year fog and low stratus climatology for Europe based on *Meteosat* Second Generation data. Q J R Meteorol Soc 143:530–541, doi:10.1002/qj.2941

Egli S, Boris Thies, Jörg Bendix (2018) A Hybrid Approach for Fog Retrieval Based on a Combination of Satellite and Ground Truth Data. Remote Sensing 10(4):628, doi:10.3390/rs10040628

Egli S, Thies B, Bendix J (2019) A spatially explicity and temporally highly resolved analysis of variations in fog occurrence over Europe. Q J R Meteorol Soc doi:10.1002/qj.3522

Ekamper P, van der Erf R, van der Gaag N, Henkens K, van Imhoff E, van Poppel F (eds) (2003) Bevolk-

ingsatlas van Nederland: Demografische Ontwikkelingen van 1850 Tot Heden. Nederlands Interdisciplinair Demografisch Instituut

Euser T, Luxemburg WMJ, Everson CS, Mengistu MG, Clulow AD, Bastiaanssen WGM (2014) A new method to measure Bowen ratios using high-resolution vertical dry and wet bulb temperature profiles. Hyrdol Earth Syst Sci 18:2021–2032, doi:10.5194/hess-18-2021-2014

Fabbian D, de Dear R, Lellyett S (2007) Application of artificial neural network forecasts to predict fog at Canberra International Airport. Weather Forecast 22(2):372–381

Fu G, Li P, Crompton JG, Guo J, Gao S, Zhang S (2010) An observational and modeling study of a sea fog event over the Yellow Sea on 1 August 2003. Meteorol Atmos Phys 107:149–159, doi:10.1007/s00703-010-0073-0

Gultepe I, Milbrandt JA (2007) Microphysical observations and mesoscale model simulation of a warm fog case during FRAM project. Pure Appl Geophys 164:1161–1178, doi:10.1007/s00024-007-0212-9

Gultepe I, Müller MD, Boybeyi Z (2006) A new visibility parameterization for warm-fog applications in numerical weather prediction models. J Appl Meteorol Climatol 45, doi:10.1175/JAM2423.1

Gultepe I, Tardif R, Michaelides SC, Cermak J, Bott A, Bendix J, Müller MD, Pagowski M, Hansen B, Ellrod G, Jacobs W, Toth G, Cober SG (2007) Fog research: A review of past achievements and future perspectives. Pure Appl Geophys 164:1121–1159, doi:10.1007/s00024-007-0211-x

Haeffelin M, Bergot T, Elias T, Tardif R, Carrer D, Chazette P, Colomb M, Drobinski P, Dupont E, Dupont JC, Gomes L, Musson-Genon L, Pietras C, Plana-Fattori A, Protat A, Rangognio J, Raut JC, Rémy S, Richard D, Sciare J, Zhang X (2010) ParisFog: Shedding new light on fog physical processes. Bull Am Meteorol Soc pp 767–783, doi:10.1175/2009BAMS2671.1

Hage KD (1972) Urban growth effects on low-temperature fog in edmonton. Boundary-Layer Meteorol 2:334–347

Hautiere N, Bigorgne E, Bossu J, Aubert D (2008) Meteorological conditions processing for vision-based traffic monitoring. Proceedings of the Eighth International Workshop on Visual Surveillance - VS2008

Heus T, van Heerwaarden CC, Jonker HJJ, Siebesma AP, Axelsen S, van den Dries K, Geoffroy O, Moene AF, Pino D, de Roode SR, de Arellano" JVG (2010) Formulation of the Dutch Atmospheric Large-Eddy Simulation (DALES) and overview of its applications. Geosci Model Dev 3:415–444, doi:doi:10.5194/gmd-3-415-2010

Higgins CW, Wing MG, Kelley J, Sayde C, Burnett J, Holmes HA (2018) A high resolution measurement of the morning ABL transition using distributed temperature sensing and an unmanned aircraft system. Environ Fluid Mech doi:10.1007/s10652-017-9569-1

Hilgersom K, van Emmerink T, Solcerova A, Berghuis W, Selker J, de Giesen" Nv (2016) Practical considerations for enhanced-resolution coil-wrapped distributed temperature sensing. Geosci Instrum Method Data Syst 5:151–162, doi:10.5194/gi-5-151-2016

Hingmire D, Vellore RK, Krishnan R, Ashtikar NV, Singh BB, Sabade S, Madhura RK (2018) Widespread fog over the Indo-Gangetic Plains and possible links to boreal winter teleconnections. Climate Dynamics doi:10.1007/s00382-018-4458-y

Hirschi JJM, Sinha B (2007) Negative NAO and Cold Eurasian Winters: How exceptional was the winter of 1962/1963? Weather 62(2):43–48

Hollingsworth A, Viterbo P, Simmons AJ (2003) The Relevance of Numerical Weather Prediction for Forecasting Natural hazards and for Monitoring the Global Environment. In: Johnson RH, Houze Jr RA (eds) A Half Century of Progress in Meteorology: A Tribute to Richard Reed, p Chapter 8

Hollmann R, Merchant CJ, Saunders R, Downy C, Buchwitz M, Cazenave A, Chuvieco E, Defourny P, de Leeuw G, Forsberg R, Holzer-Popp T, Paul F, Sandven S, Santhyendranath S, van Roozendael M, Wagner W (2013) The ESA Climate Change Initiative: Satellite data records for essential climate variables. Bull Am Meteorol Soc 94(10):1541–1552, doi:10.1175/BAMS-D-11-00254.1

Holtslag AAM, Svensson G, Baas P, Basu S, Beare B, Beljaars ACM, Bosveld FC, Cuxart J, Lindvall J, Steeneveld GJ, Tjernström M, van de Wiel BJH (2013) Stable atmospheric boundary layers and diurnal cycles: Challenges for weather and climate models. Bull Am Meteorol Soc pp 1691–1706, doi:10.1175/BAM S-D-11-00187.1

Holtslag MC, Steeneveld GJ, Holtslag AAM (2010) Fog forecasting: “old fashioned” semi-empirical methods from radio sounding observations versus “modern" numerical models. 5th International Conference

on Fog, Fog Collection, and Dew, 25 - 30 July 2010, Münster, Germany

Huang H, Chen C (2016) Climatological aspects of dense fog at Urumqi Diwopu International Airport and its impacts on flight on-time performance. Nat Hazards 81:1091–1106, doi:10.1007/s11069-015-2121-z

Huang JC (2019) Seasonal variation of water inputs for epiphytic plants at a subtropical rainforest, Fu-Shan in northern Taiwan

Izett JG (2016) Estimating the efficiency of cross-shelf transport of terrestrially derived materials in river plumes. Master's Thesis, Dalhousie University

Izett JG (2017) What does a river deliver? Current Tides

Izett JG, Fennel K (2018a) Estimating the Cross-Shelf Export of Riverine Materials: Part 1. General Relationships from an Idealized Numerical Model. Glob Biogeochem Cycle 32(2), doi:10.1002/2017GB005667

Izett JG, Fennel K (2018b) Estimating the Cross-Shelf Export of Riverine Materials: Part 2. Estimates of Global Freshwater and Nutrient Export. Glob Biogeochem Cycle 32(2), doi:10.1002/2017GB005668

Izett JG, van de Wiel BJH (2020) Why does fog deepen? An analytical perspective. Under Revision

Izett JG, Schilperoort B, Coenders-Gerrits M, Baas P, Bosveld FC, van de Wiel BJH (2018a) High-Resolution Temperature and Visibility Observations During a Radiation Fog Event on 6 November, 2017. doi:10.5446/36212

Izett JG, Schilperoort B, Coenders-Gerrits M, van de Wiel BJH (2018b) High-Resolution DTS Temperature Measurements During Fog at Cabauw. Dataset doi:10.4121/uuid:e780eb4a-b53f-4482-a946-63994a41ef34

Izett JG, van de Wiel BJH, Baas P, Bosveld FC (2018c) Understanding and reducing false alarms in observational fog prediction. Boundary-Layer Meteorol 169(2):347–372, doi:10.1007/s10546-018-0374-2

Izett JG, Schilperoort B, Coenders-Gerrits M, Baas P, Bosveld FC, van de Wiel BJH (2019a) Missed Fog? On the potential of obtaining observations at increased resolution during shallow fog events. Boundary-Layer Meteorol doi:10.1007/s10546-019-00462-3

Izett JG, van de Wiel BJH, Baas P, van Hooft JA, Schulte RB (2019b) Dutch fog: On the observed spatio–temporal variability of fog in the Netherlands. Q J Royal Met Soc doi:10.1002/qj.3597

Jacobs AFG, Heusinkveld BG, Wichink Kruit RJ, Berkowicz SM (2006) Contribution of dew to the water budget of a grassland area in the Netherlands. Water Resour Res 42(3), doi:10.1029/2005WR004055

Ju T, Wu B, Zhang H, Liu J (2020) Parameterization of Radiation Fog-Top Height and Methods Evaluation in Tianjin. Atmosphere 11(5):480, doi:10.3390/atmos11050480

Jung T, Ferranti FVaL, Morcrette JJ (2011) Origin and predicatbility of the extreme negative NAO winter of 2009/10. Geophys Res Lett 38:L07,701, doi:10.1029/2011GL046786

Kattenberg A, Verver G, Homan CD, Jilderda R, Leander R, Wijnant IL, Stepek A (2013) Klimaatbestendig schiphol: Syntheserapport HSMS02. Royal Dutch Meteorological Insitute (KNMI), Tech rep

Kim KW (2015) Estimation of visibility using a visual image. Environ Monit Assess 187:66, doi:10.1007/s10661-015-4297-9

King MP, Herceg-Bulić I, Bladé I, García-Serrano J, Keenlyside N, Li FKC, Sobolowski S (2018) Importance of late fall ENSO teleconnection in the Euro-Atlantic sector. Bull Am Meteorol Soc 99(7):1337–1343, doi:10.1175/BAMS-D-17-0020.1

KNMI (2019) Barre winter van 1963. https://www.knmi.nl/kennis-en-datacentrum/uitleg/barre-winter-van-1963

Köhler H (1936) The nucleus in and the growth of hygroscopic droplets. Transactions of the Faraday Society 32:1152–1161, doi:10.1039/TF9363201152

Kunkel BA (1984) Parametrization of Droplet Terminal Velocity and Extinction COefficient in Fog Models. J Clim Appl Meteorol 23(1):34–41

Laloyaux P, de Boisseson E, Balmaseda M, Bidlot JR, Broennimann S, Buizza R, Dalhgren P, Dee D, Haimberger L, Hersbach H, Kosaka Y, Martin M, Poli P, Rayner N, Rustemeier E, Schepers D (2018) CERA-20C: A coupled reanalysis of the twentieth century. Journal of Advances in Modeling Earth Systems 10(5):1172–1195, doi:10.1029/2018MS001273

Lee TF (1987) Urban clear islands in california central valley fog. Mon Weather Rev 115:1794–1796

Li Y (2016) Detection, Imaging and Characterisation of Fog Fields by Radar. PhD thesis, TU Delft

MacGillivray A, McPherson C, McPherson G, Izett JG, Gosselin J, Li Z, Hannay D (2014) Modelling Underwater Shipping Noise in the Great Barrier Reef Marine Park Using AIS Vessel Track Data. In: InterNoise, Melbourne, Autralia

Mahrt L (2014) Stably stratified atmospheric boundary layers. Annu Rev Fluid Mech 46:23–45

Manders AMM, Schaap M, Jozwicka M, van Arkel F, Weijers EP, Matthijsen J (2009) The Contribution of Sea Salt to PM_{10} and $PM_{2.5}$ in the Netherlands. Netherlands Environmental Assessment Agency, BOP report

Maronga B, Bosveld FC (2017) Key parameters for the life cycle of nocturnal radiation fog: A comprehensive large-eddy simulation study. Q J R Meteorol Soc 143:2463–2480, doi:10.1002/qj.3100

Maronga B, Gryschka M, Heinze R, Hoffmann F, Kanani-Sühring F, Keck M, Ketelsen K, Letzel MO, Sühring M, Raasch S (2015) The Parallelized Large-Eddy Simulation Model (PALM) version 4.0 for atmospheric and oceanic flows: Model formulation, recent developments, and future perspectives. Geosci Model Dev 8:2515–2551, doi:10.5194/gmd-8-2515-2015

Martinez J (2019) Great Smog of London. Encyclop\aedia Brittanica

Mazoyer M, Lac C, Thouron O, Bergot T, Masson V, Musson-Genon L (2017) Large eddy simulation of radiation fog: Impact of dynamics on the fog life cycle. Atmos Chem Phys 17:1307–13,035, doi:10.5194/acp-17-13017-2017

Mazoyer M, Burnet F, Denjean C, Roberts GC, Haeffelin M, Dupont JC, Elias T (2019) Experimental study of the aerosol impact on fog microphysics. Atmos Chem Phys 19(7):4323–4344, doi:10.5194/acp-19-4323-2019

Menut L, Mailler S, Dupont JC, Haeffelin M, Elias T (2014) Predictability of the meteorological conditions favourable to radiative fog formation during the 2011 ParisFog campaign. Boundary-Layer Meteorol 150:277–297, doi:10.1007/s10546-013-9875-1

Ministeria de Transportes y Communicaciones (1978) {Colision Aeronaves Boeing 747 PH-BUF DE K.L.M. y Boeing 747 N 737 PA de Panam en Los Rodeos (Tenerife) el 27 de marzo de 1.977}. Joint Report

Mlawer EJ, Taubman SJ, Brown PD, Iacono MJ, Clough SA (1997) Radiative transfer for inhomogeneous atmospheres: RRTM, a validated correlated-k model for the longwave. J Geophys Res 102(D14):16,663–16,682, doi:10.1029/97JD00237

Moene AF, van Dam JC (2014) Transport in the Atmosphere-Vegetation-Soil Continuum. Cambridge University Press

Monahan AH, Rees T, He Y, McFarlane N (2015) Multiple regimes of wind, stratification, and turbulence in the stable boundary layer. J Atmos Sci 72:3178–3198, doi:10.1175/JAS-D-14-0311.1

Monna W, Bosveld F (2013) In higher spheres: 40 years of observations at the Cabauw site. Tech Rep Royal Netherlands Meteorological Institute, KNMI-Publications 232 232

Nakanishi M (2000) Large-eddy simulation of radiation fog. Boundary-Layer Meteorol 94:461–493

NOAA (2005) Federal Meteorological Handbook No. 1, Surface Weather Observations and Reports. US Department of Commerce/NOAA, Tech. Rep. FCM-H1-2005

Palter JB (2015) The role of the gulf stream in european climate. Annu Rev Mar Sci 7:113–37, doi:10.1146/annurev-marine-010814-015656

Penman HL (1948) Natural Evaporation from Open Water, Bare Soil and Grass. P Roy Soc Lond A Mat 193(1032):120–145

Pérez-Díaz J, Ivanov O, Peshev Z, Álvarez-Valenzuela M, Valiente-Blanco I, Evgenieva T, Dreischuh T, Gueorguiev O, Todorov P, Vaseashta A (2017) Fogs: Physical Basis, Characteristic Properties, and Impacts on the Environment and Human Health. Water 9(10):807, doi:10.3390/w9100807

Perry AH, Symons LJ (2002) Highway meteorology. CRC Press, chap 6, pp 120–122

Pfister L, Sigmund A, Olsech J, Thomas CK (2017) Nocturnal near-surface temperature, but not flow dynamics, can be predicted by microtopography in a mid-range mountain valley. Boundary-Layer Meteorol 165:333–348, doi:DOI 10.1007/s10546-017-0281-y

Philip A, Bergot T, Bouteloup Y, Bouyssel F (2016) The impact of vertical resolution on fog forecasting in the kilometric-scale model AROME: A case study and statistics. Weather Forecast 31:1655–1671, doi:10.1175/WAF-D-16-0074.1

Pilie R, Eadie W, Mack E, Rogers C, Kochmond W (1972) Project Fog Drops Part I: Investigations of Warm Fog Properties. National Aeronautics and Space Administration (NASA), Contractor Report CR-2078

Pokhrel R, Lee H (2011) Algorithm development of a visibility monitoring technique using digital image analysis. Asian Journal of Atmospheric Environment 5-1:8–20, doi:10.5572/ajae.2011.5.1.008

Poku C, Ross AN, Blyth AM, Hill AA, Price JD (2019) How important are aerosol–fog interactions for the successful modelling of nocturnal radiation fog? Weather doi:10.1002/wea.3503

Price J (2011) Radiation Fog. Part I: Observations of Stability and Drop Size Distributions. Boundary-Layer Meteorol 139(2):167–191, doi:10.1007/s10546-010-9580-2

Price J, Stokkereit K (2020) The Use of Thermal Infra-Red Imagery to Elucidate the Dynamics and Processes Occurring in Fog. Atmosphere 11(3):240, doi:10.3390/atmos11030240

Price JD (2019) On the Formation and Development of Radiation Fog: An Observational Study. Boundary-Layer Meteorol 172(2):167–197, doi:10.1007/s10546-019-00444-5

Price JD, Lane S, Boutle IA, Smith DKE, Bergot T, Lac C, Duconge L, McGregor J, Kerr-Munslow A, Pickering M, Clark R (2018) LANFEX: A field and modeling study to improve our understanding and forecasting of radiation fog. Bull Am Meteorol Soc doi:10.1175/BAMS-D-16-0299.1

Raux PS, Gravelle S, Dumais J (2020) Design of a unidirectional water valve in Tillandsia. Nat Commun 11(1):396, doi:10.1038/s41467-019-14236-5

Riaz SMF, Iqbal MJ, Hameed S (2017) Impact of the North Atlantic Oscillation on winter climate of Germany. Tellus A: Dynamic Meteorology and Oceanography 69(1):1406,263, doi:10.1080/16000870.2017.1406263

Riedl A, Li Y, Eugster W (2019) Quantification of Dew and Fog Water Inputs for Swiss Grasslands

Roach WT, Brown R, Caughey SJ, Garland JA, Readings CJ (1976) The physics of radiation fog: I - a field study. Q J R Meteorol Soc 102:313–333

Román-Cascón C, Steeneveld GJ, Yagüe C, Sastre M, Arrillaga JA, Maqueda G (2016a) Forecasting radiation fog at climatologically contrasting sites: Evaluation of statistical methods and WRF. Q J R Meteorol Soc 142:1048–1063, doi:10.1002/qj.2708

Román-Cascón C, Yagüe C, Steeneveld GJ, Sastre M, Arrillaga JA, Maqueda G (2016b) Estimating fog-top height through near-surface micrometeorological measurements. Atmos Res 170:76–86, doi:10.1016/j.atmosres.2015.11.016

Rosner B (1983) Percentage points for a Generalized ESD many-outlier procedure. Technometrics 25(2):165–172, doi:10.2307/1268549

Sachweh M, Koepke P (1995) Radiation fog and urban climate. Geophys Res Lett 22:1073–1076

Sachweh M, Koepke P (1997) Fog dynamics in an urbanized area. Appl Climatol 58:87–93

Sayde C, Thomas CK, Wagner J, Selker J (2015) High-resolution wind speed measurements using actively heated fiber optics. Geophys Res Lett 42:10,064–10,073, doi:10.1002/2015GL066729

Schemenauer RS (1988) Fog Water to Quench a Desert's Thirst. WMO Bulletin 37(4):281–286

Schilperoort B, Coenders-Gerrits M, Luxemburg W, Jiménez Rodríguez C, Cisneros Vaca C, Savenije H (2018) Technical note: Using distributed temperature sensing for Bowen ratio evaporation measurements. Hyrdol Earth Syst Sci 22:819–830, doi:10.5194/hess-22-819-2018

Schiphol (2019) Amsterdam airport schiphol airport facts. https://www.schiphol.nl/en/route-development/page/amsterdam-airport-schiphol-airport-facts/

Schulte RB (2017) Observed scales of short-lived nocturnal turbulent structures. PhD thesis, TU Delft, doi:http://resolver.tudelft.nl/uuid:d50ced04-26c8-4126-b9d7-526d1e8e5408

Science P (1945) How FIDO licked Airfield fog

Seifert A, Beheng KD (2001) A double-moment parameterization for simulating autoconversion, accretion and selfcollection. Atmospheric Research 59-60:265–281, doi:10.1016/S0169-8095(01)00126-0

Seifert A, Beheng KD (2006) A two-moment cloud microphysics parameterization for mixed-phase clouds. Part 1: Model description. Meteorol Atmos Phys 92(1-2):45–66, doi:10.1007/s00703-005-0112-4

Selker JS, Thévanez L, Huwald H, Mallet A, Luxemburg W, de Giesen" Nv, Stejskal M, Zeman J, Westhoff M, Parlange MB (2006) Distributed fiber-optic temperature sensing for hydrologic systems. Water Resources Research 42:W12,202, doi:10.1029/2006WR005326

Sigmund A, Pfister L, Sayde C, Thomas K (2017) Quantitative analysis of the radiation error for aerial

coiled-fiber-optic distributed temperature sensing deployments using reinforcing fabric as support structure. Atmos Meas Tech 10:2149–2162, doi:10.5194/amt-10-2149-2017

Silixa Ltd (2018) Distributed temperature sensing with ULTIMA DTS. http://silixa.com/%20technology/ultima-dts/

Smith DKE, Renfrew IA, Price JD, Dorling SR (2018) Numerical modelling of the evolution of the boundary layer during a radiation fog event. Weather 73(10):310–316, doi:10.1002/wea.3305

Solcerova A, van Emmerink T, de Ven" Fv, Selker J, de Giesen" Nv (2018) Skin effect of fresh water measured using distributed temperature sensing. Water 10(2):214, doi:10.3390/w10020214

Steeneveld GJ (2014) Current challenges in understanding and forecasting stable boundary layers over land and ice. Front Environ Sci 2:1–6, doi:10.3389/fenvs.2014.00041

Steeneveld GJ, de Bode M (2018) Unravelling the relative roles of physical processes in modelling the life cycle of a warm radiation fog. Q J R Meteorol Soc 144(714):1539–1554, doi:10.1002/qj.3300

Steeneveld GJ, Koopmans S, Heusinkveld BG, van Hove LWA, Holtslag AAM (2011) Quantifying urban heat island effects and human comfort for cities of variable size and urban morphology in the Netherlands. J Geophys Res 116:D20,129, doi:doi:10.1029/2011JD015988

Steeneveld GJ, Ronda RJ, Holtslag AAM (2015) The challenge of forecasting the onset and development of radiation fog using mesocale atmospheric models. Boundary-Layer Meteorol 154:265–289, doi:10.1007/s10546-014-9973-8

Stolaki S, Pytharoulis I, Karacostas T (2012) A study of fog characteristics using a coupled WRF-COBEL model over Thessaloniki Aitport, Greece. Pure Appl Geophys 169:961–981, doi:10.1007/s00024-011-0393-0

Tardif R (2007) The impact of vertical resolution in the explicit numerical forecasting of radiation fog: A case study. Pure Appl Geophys 164(1221-1240), doi:10.1007/s00024-007-0216-5

Tardif R, Rasmussen RM (2007) Event-based climatology and typology of fog in the New York City region. J Appl Meteorol Climatol 46:1141–1168, doi:10.1175/JAM2516.1

Taylor GI (1917) The formation of fog and mist. Q J R Meteorol Soc 43(183):241–268

Thomas CK, Kennedy AM, Selker JS, Moretti A, Schroth MH, Smoot AR, Tufillaro NB, Zeeman MJ (2012) High-resolution fibre-optic temperature sensing: A new tool to study the two-dimensional structure of atmospheric surface-layer flow. Boundary-Layer Meteorol 142:177–192, doi:10.1007/s10546-011-9672-7

Toniazzo T, Scaife AA (2006) The influence of ENSO on winter North Atlantic climate. Geophys Res Lett 33:L24,704, doi:10.1029/2006GL027881

Valdez J (2000) National Weather Service—A high impact agency . . . we make a difference: Reinvention goals for 2000. National Weather Service

van de Wiel BJH, Moene AF, Jonker HJJ (2012a) The cessation of continuous turbulence as precursor of the very stable nocturnal boundary layer. J Atmos Sci 69:3097–3115, doi:10.1175/JAS-D-12-064.1

van de Wiel BJH, Moene AF, Jonker HJJ, Baas P, Basu S, Donda JMM, Sun J, Holtslag AAM (2012b) The minimum wind speed for sustainable turbulence in the nocturnal boundary layer. J Atmos Sci 69:3116–3127, doi:10.1175/JAS-D-12-0107.1

van de Wiel BJH, Vignon E, Baas P, van Hooijdonk IGS, van der Linden SJA, van Hooft JA, Bosveld FC, de Roode SR, Moene AF, Genthon C (2017) Regime transitions in near-surface temperature inversions: A conceptual model. J Atmos Sci 74:1057–1073, doi:10.1175/JAS-D-16-0180.1

van der Linden SJA, Baas P, van Hooft JA, van Hooijdonk IGS, Bosveld FC, de Wiel" BJHv (2017) Local characteristics of the nocturnal boundary layer in response to external pressure forcing. J Appl Meteorol Climatol 56:3035–3047, doi:10.1175/JAMC-D-17-0011.1

van Hooft JA, Popinet S, van Heerwaarden CC, van der Linden SJA, de Roode SR, van de Wiel BJH (2018) Towards Adaptive Grids for Atmospheric Boundary-Layer Simulations. Boundary-Layer Meteorol 167(3):421–443, doi:10.1007/s10546-018-0335-9

van Ramshorst JGV, Coenders-Gerrits M, Schilperoort B, van de Wiel BJH, Izett JG, Selker JS, Higgins CW, Savenije HHG, van de Giesen NC (2019) Wind speed measurements using distributed fiber optics: A windtunnel study. Atmos Meas Tech Discuss pp 1–21, doi:10.5194/amt-2019-63

Wærsted EG, Haeffelin M, Steeneveld GJ, Dupont JC (2019) Understanding the dissipation of continen-

tal fog by analysing the LWP budget using idealized LES and *in situ* observations. QJR Meteorol Soc 145(719):784–804, doi:10.1002/qj.3465

Wan Z, Hook S, Hulley G (2015) MOD11_L2 MODIS/Terra land surface Temperature/Emissivity 5-Min L2 swath 1km V006 [dataset]. NASA EOSDIS LP DAAC doi:doi: 10.5067/MODIS/MOD11_L2.006

WMO (2014) Guide to Meteorological Instruments and Methods of Observation. World Meteorological Organization

Zeeman MJ, Selker JS, Thomas CK (2015) Near-surface motion in the nocturnal, stable boundary layer observed with fibre-optic distributed temperature sensing. Boundary-Layer Meteorol 154:189–205, doi:10.1007/s10546-014-9972-9

Zhou B, Du J, Gultepe I, Dimego G (2012) Forecast of low visibility and fog from NCEP: Current status and efforts. Pure Appl Geophys 169:895–909, doi:10.1007/s00024-011-0327-x

List of Publications and Presentations

Publications

First Author, Peer Reviewed:

Izett JG, van de Wiel BJH (2020). Why Does Fog Deepen? An Analytical Perspective. Atmosphere 11(8), doi:10.3390/atmos11080865

Izett JG, van de Wiel BJH, Baas P, van Hooft JA, Schulte RB (2019b) Dutch fog: On the observed spatio–temporal variability of fog in the Netherlands. Q J Royal Met Soc doi:10.1002/qj.3597

Izett JG, Schilperoort B, Coenders-Gerrits M, Baas P, Bosveld FC, van de Wiel BJH (2019a) Missed Fog? On the potential of obtaining observations at increased resolution during shallow fog events. Boundary-Layer Meteorol doi:10.1007/s10546-019-00462-3

Izett JG, van de Wiel BJH, Baas P, Bosveld FC (2018c) Understanding and reducing false alarms in observational fog prediction. Boundary-Layer Meteorol 169(2):347–372, doi:10.1007/s10546-018-0374-2

Izett JG, Fennel K (2018b) Estimating the Cross-Shelf Export of Riverine Materials: Part 2. Estimates of Global Freshwater and Nutrient Export. Glob Biogeochem Cycle 32(2), doi:10.1002/2017GB005668

Izett JG, Fennel K (2018a) Estimating the Cross-Shelf Export of Riverine Materials: Part 1. General Relationships from an Idealized Numerical Model. Glob Biogeochem Cycle 32(2), doi:10.1002/2017GB005667

Co-author:

van Ramshorst JGV, Coenders-Gerrits M, Schilperoort B, van de Wiel BJH, Izett JG, Selker JS, Higgins CW, Savenije HHG, van de Giesen NC (2019) Wind speed measurements using distributed fiber optics: A windtunnel study. Atmos Meas Tech Discuss pp 1–21, doi:10.5194/amt-2019-63

MacGillivray A, McPherson C, McPherson G, Izett JG, Gosselin J, Li Z, Hannay D (2014) Modelling Underwater Shipping Noise in the Great Barrier Reef Marine Park Using AIS Vessel Track Data. In: InterNoise, Melbourne, Autralia

Miscellaneous:

Izett JG, Schilperoort B, Coenders-Gerrits M, van de Wiel BJH (2018b) High-Resolution DTS Temperature Measurements During Fog at Cabauw. Dataset doi:10.4121/uuid:e780eb4a-b53f-4482-a946-63994a41ef34

Izett JG, Schilperoort B, Coenders-Gerrits M, Baas P, Bosveld FC, van de Wiel BJH (2018a) High-Resolution Temperature and Visibility Observations During a Radiation Fog Event on 6 November, 2017. doi:10.5446/36212

Izett JG (2017) What does a river deliver? Current Tides

Izett JG (2016) Estimating the efficiency of cross-shelf transport of terrestrially derived materials in river plumes. Master's Thesis, Dalhousie University

Selected Presentations

Izett, JG, BJH van de Wiel, P Baas, RB Schulte, and JA van Hooft (2019c) The Observed Spatio-Temporal Variability of Dutch Fog. *EMS 2019*, Lyngby, Denmark, 12 Sept 2019.

Izett, JG, BJH van de Wiel, P Baas, RB Schulte, and JA van Hooft (2019b) A Comprehensive Observational Overview of Dutch Fog. *IFDA 2019*, Taipei, Taiwan, 16 Jul 2019.

Izett, JG, BJH van de Wiel, P Baas, RB Schulte, and JA van Hooft (2019a) Dutch Fog. *Ruisdael Science Day*, KNMI, De Bilt, The Netherlands, 19 Jun 2019.

Izett, JG, B Schilperoort, M Coenders-Gerrits, P Baas, FC Bosveld, and BJH van de Wiel (2018) Observing Shallow Fog at Very High Resolution. *23rd Symposium on Boundary Layers and Turbulence*, Oklahoma City, USA, 13 Jul 2018.

Izett, JG, BJH van de Wiel, P Baas, RB Schulte, and FC Bosveld (2018) Observed Regional Variability of Fog in the Netherlands. *23rd Symposium on Boundary Layers and Turbulence, Oklahoma City*, USA, 12 Jul 2018, 10.13140/RG.2.2.11733.12008.

Izett, JG (2018) Fog from the ground up. *GRS Open Seminar Series*, Delft, 13 Feb 2018. 10.13140/RG.2.2.32849.43364.

Izett, JG, BJH van de Wiel, P Baas, FC Bosveld (2017) Understanding the Cause of False Alarms in Observational Fog Prediction. *EMS 2017*, Dublin, Ireland, 8 Sep 2017.10.13140/RG.2.2.11733.12008.

Izett, JG, BJH van de Wiel, and P Baas, (2017) Fog at Cabauw: Using Observations to Inform Prediction. *CESAR Science Day*, KNMI, De Bilt, The Netherlands, 9 Jun 2017.

Curriculum Vitae

29 October, 1992	Born in Chester, United Kingdom
2006–2010	**Claremont Secondary School** Victoria, Canada
2010–2014	**Bachelor of Science in Physics and Ocean Sciences** (Ocean–Atmosphere Dynamics) University of Victoria, Canada
2014–2016	**Master of Science in Oceanography** Dalhousie University, Canada Thesis: "Estimating the efficiency of cross-shelf transport of terrestrially derived materials in river plumes." Supervisor: Prof. Katja Fennel
2016–present	**Doctoral Candidate** Delft University of Technology, The Netherlands